INFORMATION PROCESSING IN THE CEREBELLUM

EDITED BY: Richard Apps, Nadia Cerminara, Conor J. Houghton and Philippe Isope

PUBLISHED IN: Frontiers in Systems Neuroscience

frontiers Research Topics

frontiers

ISSN 1664-8714
ISBN 978-2-88971-590-9
DOI 10.3389/978-2-88971-590-9

About Frontiers

Frontiers is more than just an open-access publisher of scholarly articles: it is a pioneering approach to the world of academia, radically improving the way scholarly research is managed. The grand vision of Frontiers is a world where all people have an equal opportunity to seek, share and generate knowledge. Frontiers provides immediate and permanent online open access to all its publications, but this alone is not enough to realize our grand goals.

Frontiers Journal Series

The Frontiers Journal Series is a multi-tier and interdisciplinary set of open-access, online journals, promising a paradigm shift from the current review, selection and dissemination processes in academic publishing. All Frontiers journals are driven by researchers for researchers; therefore, they constitute a service to the scholarly community. At the same time, the Frontiers Journal Series operates on a revolutionary invention, the tiered publishing system, initially addressing specific communities of scholars, and gradually climbing up to broader public understanding, thus serving the interests of the lay society, too.

Dedication to Quality

Each Frontiers article is a landmark of the highest quality, thanks to genuinely collaborative interactions between authors and review editors, who include some of the world's best academicians. Research must be certified by peers before entering a stream of knowledge that may eventually reach the public - and shape society; therefore, Frontiers only applies the most rigorous and unbiased reviews.
Frontiers revolutionizes research publishing by freely delivering the most outstanding research, evaluated with no bias from both the academic and social point of view. By applying the most advanced information technologies, Frontiers is catapulting scholarly publishing into a new generation.

What are Frontiers Research Topics?

Frontiers Research Topics are very popular trademarks of the Frontiers Journals Series: they are collections of at least ten articles, all centered on a particular subject. With their unique mix of varied contributions from Original Research to Review Articles, Frontiers Research Topics unify the most influential researchers, the latest key findings and historical advances in a hot research area! Find out more on how to host your own Frontiers Research Topic or contribute to one as an author by contacting the Frontiers Editorial Office: frontiersin.org/about/contact

INFORMATION PROCESSING IN THE CEREBELLUM

Topic Editors:
Richard Apps, University of Bristol, United Kingdom
Nadia Cerminara, University of Bristol, United Kingdom
Conor J. Houghton, University of Bristol, United Kingdom
Philippe Isope, Centre National de la Recherche Scientifique (CNRS), France

Citation: Apps, R., Cerminara, N., Houghton, C. J., Isope, P., eds. (2021). Information Processing in the Cerebellum. Lausanne: Frontiers Media SA. doi: 10.3389/978-2-88971-590-9

Table of Contents

frontiers in Systems Neuroscience

EDITORIAL
published: 17 September 2021
doi: 10.3389/fnsys.2021.752719

Editorial: Information Processing in the Cerebellum

Conor Houghton[1], *Philippe Isope*[2], *Richard Apps*[3] *and Nadia L. Cerminara*[3]*

[1] Department of Computer Science, University of Bristol, Bristol, United Kingdom, [2] Institut des Neurosciences Cellulaires et Intégratives, CNRS, Université de Strasbourg, Strasbourg, France, [3] School of Physiology, Pharmacology and Neuroscience, University of Bristol, Bristol, United Kingdom

Keywords: cerebellum, computational modeling, forward model, timing, complex spike, oscillations, cerebellar learning, cerebellar circuitry

Editorial on the Research Topic

Information Processing in the Cerebellum

The cerebellum is involved in a wide range of behaviors including the coordination of reflex and voluntary movements, postural adjustments to maintain balance, and the learning of new motor skills. This is also increasing evidence that its role extends to cognition, affect and the control of the autonomic system. Amazingly, the cerebellum contains more than four-fifths of the brain's neurons (Herculano-Houzel, 2009) and so it has an incredible amount of computing power. Considering the cerebellum from a computational perspective has a long history going back to Albus (1971), Marr and Thach (1991), and Ito (1984) and the goal of linking theory to experiment through detailed modeling dates back to the early nineties (Tyrrell and Willshaw, 1992; De Schutter and Bower, 1994a,b). Now, new insights into the anatomy and physiology of cerebellar circuits are leading to revised thinking about how these circuits may process information: multiple sites of plasticity; heterogeneity in structure and function such as zebrin bands; variable complex spike wave form; synchronous activity.

It seems possible that the cerebellum is specialized to perform some specific types of computation. However, it is not known precisely what these might be and there are many, often overlapping, ideas: perceptron learning (Albus, 1971; Ito, 1984; Marr and Thach, 1991), Kalman filtering (Paulin, 1989; Tanaka et al., 2019), forward models (Miall and Wolpert, 1996), expansion coding (Billings et al., 2014), the approximation of cortical feedback (Pemberton et al., 2020), and computing with uncertainty (Palacios et al., 2021). Moreover, differences in cerebellar function are likely to be reflected within regional variations in cerebellar cytoarchitecture (for a review see Cerminara et al., 2015), that in turn reflect different computational roles. This is an important area for studying models of computation: models of cerebellar computation could be effective in describing not just the role of the cerebellum but could inspire universal theories of whole brain function. With this ambition in mind, the scope of this Research Topic was to bring together researchers to showcase recent experimental and computational studies exploring the computational dynamics of the cerebellum at levels from ions and microcircuits.

A fruitful approach to the cerebellum is to describe it using language and ideas borrowed from engineering control systems. Tanaka et al. reviews one such approach. A challenge in designing a control system is that the motor controls need to be based on a current estimate of position even though that estimate may not be available straight away because of the latency in sensory processing. A potential solution is to use a *forward model* (Miall and Wolpert, 1996) to predict the current position from the available, past, sensory data. This review describes evidence, computational and experimental, that cerebellar computation is a forward model. Holland et al. and

OPEN ACCESS

Edited and reviewed by:
Opher Donchin, Ben-Gurion University of the Negev, Israel

***Correspondence:**
Nadia L. Cerminara
n.cerminara@bristol.ac.uk

Received: *03 August 2021*
Accepted: *26 August 2021*
Published: *17 September 2021*

Citation:
Houghton C, Isope P, Apps R and Cerminara NL (2021) Editorial: Information Processing in the Cerebellum. Front. Syst. Neurosci. 15:752719. doi: 10.3389/fnsys.2021.752719

Anderson et al. consider cerebellar control for the specific example of image stabilization. Holland et al. presents a detailed forward model and compares their simulation to experimental data from mice. In a *filter* inputs are amplified or attenuated as part of processing and Anderson et al. has a cerebellar model of filter learning for an input, in this case the head velocity which eye movements need to compensate.

The exquisite organization of the cerebellar microcircuits and molecular architecture required to support computation has been well-described, however the mechanisms that guide developmental patterning of their afferent inputs is less well-understood. Lackey and Sillitoe show that the effector molecules ephrin-A2/A5 are needed for the parasagittal patterning of spinocerebellar mossy fibers but not the Purkinje cell zonal patterns themselves. Mossy fibers originate from a wide variety of locations in the brain and spinal cord and provide the cerebellum with a rich array of sensory and motor signals converging onto single granule cells (Shimuta et al., 2020). Whether ephrin-A2/A5 is specific to subsets of spinocerebellar mossy fibers or whether this mechanism is generalized across all types of mossy fiber input needs further exploration.

Many proposed mechanisms underlying cerebellar computations require perfectly controlled time processing to avoid any mismatch in comparisons, such as the comparison of predictions with sensory feedback. The cerebellar cortex integrates mossy fiber inputs at a very high frequency so synaptic short-term plasticity properties are important. Notably, Schmidt reviews recent reinvestigations of release properties underlying short-term plasticity at the parallel fiber to Purkinje cell synapse. He develops new hypotheses that can explain how these, the most numerous synapses in the brain, reliably handle inputs at very high frequency. Another critical issue is to understand how local oscillatory activity in cerebellar microcircuits influences incoming information channeling across the cerebellar cortex. Levesque et al. recorded both individual neurons and local field potential (LFP) in the granule cell layer (GCL) of the rat and shows that input driven oscillations in the GCL predict the timing of individual neurons suggesting that LFP may have a preparatory role for cerebellar computation. How this computation is communicated to the rest of the brain remains uncertain. Using dual recordings in the cerebellum and the prefrontal cortex, Tremblay et al. demonstrate that cerebellar stimulation can influence LFP in the prefrontal cortex and that frequency-dependent changes in stimulation drive synchronization of cerebello-cortical and cortico-cortical networks.

Central to cerebellar function are the climbing fibers and the complex spikes they induce in Purkinje cell: cerebellar learning theories suggest climbing fibers signal an error signal to drive depression of the parallel fiber synapses. However, plasticity can occur at multiple sites within the cerebellum and without the need for complex spikes, calling into question the role of climbing fibers in cerebellar learning. Additionally, multiple studies have shown that complex spikes are inherent variability (Najafi et al., 2014; Yang and Lisberger, 2014; Burroughs et al., 2017; Tang et al., 2017). The review paper of Zang and De Schutter highlights recent experimental and computational studies on how this analog complex spike error signal could integrate with cerebellar learning theories. Along similar lines, Yarden-Rabinowitz and Yarom present evidence from previous classical conditioning studies as well as original data that rather than encode an error signal, complex spikes encode the timing of movement initiation through the modification of cerebellar circuitry. Together, these two papers present new views on cerebellar learning based on the graded role of complex spikes.

Together these studies add weight to the notion that the cerebellum has a multiplicity of information processing capabilities. They also demonstrate a wide-diversity of novel insight into the nature and purpose of cerebellar computation, bringing us to the surprising realization that there is no dominant theory of cerebellar function; whether the range of cerebellar operations can be captured by a universal computational algorithm remains a question for the field.

AUTHOR CONTRIBUTIONS

All authors contributed to the drafting and editing of this editorial.

FUNDING

NC and RA were supported by the Medical Research Council UK (G1100626) and BBSRC (BB/P000959/1). PI was supported by the Centre National pour la Recherche Scientifique (CNRS), the Université de Strasbourg and the Agence Nationale pour la Recherche (ANR-2019-MultiMod, ANR-2019-NetOnTime).

REFERENCES

Albus, J. S. (1971). A theory of cerebellar function. *Math. Biosci.* 10, 25–61. doi: 10.1016/0025-5564(71)90051-4

Billings, G., Piasini, E., Lörincz, A., Nusser, Z., and Silver, R. A. (2014). Network structure within the cerebellar input layer enables lossless sparse encoding. *Neuron* 83, 960–974. doi: 10.1016/j.neuron.2014.07.020

Burroughs, A., Wise, A. K., Xiao, J., Houghton, C., Tang, T., Suh, C. Y., et al. (2017). The dynamic relationship between cerebellar Purkinje cell simple spikes and the spikelet number of complex spikes. *J. Physiol.* 595, 283–299. doi: 10.1113/JP272259

Cerminara, N. L., Lang, E. J., Sillitoe, R. V., and Apps, R. (2015). Redefining the cerebellar cortex as an assembly of non-uniform Purkinje cell microcircuits. *Nat. Rev. Neurosci.* 16, 79–93. doi: 10.1038/nrn3886

De Schutter, E., and Bower, J. M. (1994a). An active membrane model of the cerebellar Purkinje cell. i. simulation of current clamps in slice. *J. Neurophysiol.* 71, 375–400. doi: 10.1152/jn.1994.71.1.375

De Schutter, E., and Bower, J. M. (1994b). An active membrane model of the cerebellar Purkinje cell ii. simulation of synaptic responses. *J. Neurophysiol.* 71, 401–419. doi: 10.1152/jn.1994.71.1.401

Herculano-Houzel, S. (2009). The human brain in numbers: a linearly scaled-up primate brain. *Front. Hum. Neurosci.* 3:2009. doi: 10.3389/neuro.09.031.2009

Ito, M. (1984). *The Cerebellum and Neural Control*. New York, NY: Raven Press.

Marr, D., and Thach, W. T. (1991). "A theory of cerebellar cortex," in *From the Retina to the Neocortex*, ed L. M. Vaina (Boston, MA: Springer), 11–50. doi: 10.1007/978-1-4684-6775-8_3

Miall, R. C., and Wolpert, D. M. (1996). Forward models for physiological motor control. *Neural Netw.* 9, 1265–1279. doi: 10.1016/S0893-6080(96)00035-4

Najafi, F., Giovannucci, A., Wang, S. S., and Medina, J. F. (2014). Coding of stimulus strength via analog calcium signals in Purkinje cell dendrites of awake mice. *Elife* 3:e03663. doi: 10.7554/eLife.03663.010

Palacios, E. R., Houghton, C., and Chadderton, P. (2021). Accounting for uncertainty: inhibition for neural inference in the cerebellum. *Proc. R. Soc. B* 288:20210276. doi: 10.1098/rspb.2021.0276

Paulin, M. (1989). "A Kalman filter theory of the cerebellum," in *Dynamic Interactions in Neural Networks: Models and Data*, eds M. A. Arbib and A. Shun-ichi (New York, NY: Springer), 239–259. doi: 10.1007/978-1-4612-4536-0_15

Pemberton, J., Boven, E., Apps, R., and Costa, R. P. (2020). "Poster: cortico cerebellar networks as decoupled neural interfaces," in *Computational and Systems Neuroscience Meeting (CoSyNe)* (Denver, CO), 1–26.

Shimuta, M., Sugihara, I., and Ishikawa, T. (2020). Multiple signals evoked by unisensory stimulation converge onto cerebellar granule and Purkinje cells in mice. *Commun. Biol.* 3, 1–12. doi: 10.1038/s42003-020-1110-2

Tanaka, H., Ishikawa, T., and Kakei, S. (2019). Neural evidence of the cerebellum as a state predictor. *Cerebellum* 18, 349–371. doi: 10.1007/s12311-018-0996-4

Tang, T., Xiao, J., Suh, C. Y., Burroughs, A., Cerminara, N. L., Jia, L., et al. (2017). Heterogeneity of Purkinje cell simple spike–complex spike interactions: zebrin-and non-zebrin-related variations. *J. Physiol.* 595, 5341–5357. doi: 10.1113/JP274252

Tyrrell, T., and Willshaw, D. (1992). Cerebellar cortex: its simulation and the relevance of Marr's theory. *Philos. Trans. R. Soc. Lond. Ser. B Biol. Sci.* 336, 239–257. doi: 10.1098/rstb.1992.0059

Yang, Y., and Lisberger, S. G. (2014). Purkinje-cell plasticity and cerebellar motor learning are graded by complex-spike duration. *Nature* 510, 529–532. doi: 10.1038/nature13282

Conflict of Interest: The authors declare that the research was conducted in the absence of any commercial or financial relationships that could be construed as a potential conflict of interest.

Publisher's Note: All claims expressed in this article are solely those of the authors and do not necessarily represent those of their affiliated organizations, or those of the publisher, the editors and the reviewers. Any product that may be evaluated in this article, or claim that may be made by its manufacturer, is not guaranteed or endorsed by the publisher.

frontiers in Systems Neuroscience

MINI REVIEW
published: 17 July 2019
doi: 10.3389/fnsys.2019.00030

Control of Presynaptic Parallel Fiber Efficacy by Activity-Dependent Regulation of the Number of Occupied Release Sites

*Hartmut Schmidt**

Carl-Ludwig Institute for Physiology, Medical Faculty, University of Leipzig, Leipzig, Germany

Parallel fiber (PF) synapses show pronounced and lasting facilitation during bursts of high-frequency activity. They typically connect to their target neurons *via* a single active zone (AZ), harboring few release sites (∼2–8) with moderate initial vesicular release probability (∼0.2–0.4). In light of these biophysical characteristics, it seems surprising that PF synapses can sustain facilitation during high-frequency periods of tens of action potentials (APs). Recent findings suggest an increase in the number of occupied release sites due to ultra-rapid (∼180 s^{-1}), Ca^{2+} dependent recruitment of synaptic vesicles (SVs) from replenishment sites as major presynaptic mechanism of this lasting facilitation. On the molecular level, Synaptotagmin 7 or Munc13s have been suggested to be involved in mediating facilitation at PF synapses. The recruitment of SVs from replenishment sites appears to be reversible on a slower time-scale, thereby, explaining that PF synapses rapidly depress and ultimately become silent during low-frequency activity. Hence, PF synapses show high-frequency facilitation (HFF) but low-frequency depression (LFD). This behavior is explained by regulation of the number of occupied release sites at the AZ by AP frequency.

Keywords: parallel fiber, faciliatation, replenishment, release probability, vesicle pools, residual calcium, synaptotagmin 7, Munc13

OPEN ACCESS

Edited by:
Conor J. Houghton,
University of Bristol, United Kingdom

Reviewed by:
Stephen Rayport,
Columbia University, United States
Uri Ashery,
Tel Aviv University, Israel

***Correspondence:**
Hartmut Schmidt
hartmut.schmidt@medizin.uni-leipzig.de

Received: *11 April 2019*
Accepted: *01 July 2019*
Published: *17 July 2019*

Citation:
Schmidt H (2019) Control of Presynaptic Parallel Fiber Efficacy by Activity-Dependent Regulation of the Number of Occupied Release Sites. Front. Syst. Neurosci. 13:30. doi: 10.3389/fnsys.2019.00030

INTRODUCTION

Parallel fiber (PF) synapses are major sites for conveying sensory information to the cerebellar cortical output neurons, the Purkinje cells (PCs), and to interneurons. They are formed by granule cells, which fire bursts of action potentials (APs) over a broad range of frequencies up to ∼1 kHz in response to sensory input (Chadderton et al., 2004; Rancz et al., 2007; Ritzau-Jost et al., 2014). PF synapses in turn are adapted to reliably respond to these high-frequency bursts of APs with sustained and facilitating transmission (Valera et al., 2012). This puts substantial demands on the mechanisms of synaptic vesicle (SV) supply.

Abbreviations: A, amplitude of EPSC; AP, action potential; AZ, active zone; BC, Basket cell; EPSC, excitatory postsynaptic current; MLI, molecular layer interneuron; N, number of release sites; N_{occ}, number of release sites occupied by release-ready SVs; p_v, vesicular release probability; SV, synaptic vesicle; PC, Purkinje cell; PF, parallel fiber; PPR, paired pulse ratio; PPF, paired pulse facilitation; RRP, ready releasable pool.

Briefly, an AP invading a presynaptic terminal opens voltage-gated Ca^{2+} channels and the inflowing Ca^{2+} ions trigger the fusion of SVs with the presynaptic plasma membrane and transmitter release. Fusion of SVs is a probabilistic process that takes place at the presynaptic active zone (AZ). The AZ is thought to harbor one or more release sites (N) that constitute the individual entities at which a single SV can fuse with a certain vesicular release probability (p_v; Südhof, 2013; Kaeser and Regehr, 2017).

For a single AP, the presynaptic efficacy depends on the number of release sites occupied by release-ready SVs (N_{occ}) at the time of the AP and on the p_v of these SVs. The p_v, in turn, depends on several factors, including the diffusional distance between the Ca^{2+} channels and the SV and the intrinsic Ca^{2+} sensitivity of its release machinery (Eggermann et al., 2012; Bornschein and Schmidt, 2019). While in experiments typically only an average p_v can be estimated (Clements and Silver, 2000), the p_v need not be homogeneous across release sites (Neher, 2015).

During a train of APs, the regulation of presynaptic efficacy gets more complex. Occupied release sites are continuously emptied by the fusion processes, which, without further mechanisms, would result in synaptic depression due to progressive depletion of the pool of release-ready SVs. How effectively the information transfer can be maintained during an AP train now depends on the speed with which N_{occ} can be restored or newly recruited and on their p_v, which may increase. If the latter outcompetes SV consumption, the synapse may show facilitation rather than depression during the train (Jackman and Regehr, 2017; Neher and Brose, 2018).

This mini review article focusses on recent results from PF synapses suggesting that during high-frequency trains of APs the rate of restoration or recruitment of release sites exceeds the fusion rate, resulting in an activity-dependent increase in N_{occ} as major presynaptic mechanism of facilitation at PF synapses (Valera et al., 2012; Brachtendorf et al., 2015; Miki et al., 2016; Doussau et al., 2017).

PARALLEL-FIBER SYNAPSES

Biophysics of Parallel Fiber Terminals

The target neurons of PFs include PCs and molecular layer interneurons (MLIs). PFs contact their targets typically by a single presynaptic bouton harboring a single AZ only (Xu-Friedman et al., 2001). Presynaptic Ca^{2+} transients are reliably induced by single APs, show very little trial-to-trial variability for a given bouton and linear summation during a train of APs (Brenowitz and Regehr, 2007; Schmidt et al., 2013; Baur et al., 2015; Miki et al., 2016; Kusch et al., 2018). Mature PF terminals gate release with P/Q-type channel nanodomains (Schmidt et al., 2013; Kusch et al., 2018) that develop from P/Q- and N-type channel microdomains gating release from young terminals (Mintz et al., 1995; Baur et al., 2015). Depending on their target neuron, PFs release SVs with p_v ~0.25–0.4 in 2 mM extracellular Ca^{2+} concentration ($[Ca^{2+}]_e$; Sims and Hartell, 2005; Valera et al., 2012; Schmidt et al., 2013; Ishiyama et al., 2014; Baur et al., 2015). The number of release sites per synapse is small and has been estimated by amplitude fluctuation analysis of excitatory postsynaptic currents (EPSCs) to be on average in the range of ~2–5, perhaps with some target- or species-dependent differences (Schmidt et al., 2013; Ishiyama et al., 2014; Malagon et al., 2016). In electron microscopy ~8 docked vesicles were found in PF terminals (Xu-Friedman et al., 2001). These results indicate that single PF AZs harbor more than one release site, consistent with multi-vesicular release (Crowley et al., 2007).

High-Frequency Facilitation and Low-Frequency Depression

PF synapses show paired-pulse facilitation (PPF) with paired-pulse ratios (PPRs) between the first and the second EPSC amplitude (A_2/A_1) of ~2–3 at small interstimulus intervals (ISIs) of 5–10 ms (**Figure 1**). PPRs (A_i/A_1) remain at this level even during longer lasting high-frequency bursts and under conditions of elevated initial p_v (p_{v1}; Atluri and Regehr, 1996; Sims and Hartell, 2005; Valera et al., 2012; Ishiyama et al., 2014; Brachtendorf et al., 2015; Turecek and Regehr, 2018). In light of the above brief overview of biophysical characteristics, this is surprising at first glance. Assuming N of three, p_{v1} of 0.25 and p_{v2} of 0.84 as estimated for PF to PC synapses in 2 mM $[Ca^{2+}]_e$ (Valera et al., 2012; Schmidt et al., 2013; Brachtendorf et al., 2015), the theoretical maximum for the PPR between second and first pulse in the absence of SV replenishment [PPR = $(p_{v2}/p_{v1})^*(1 - p_{v1}) = 2.52$; the term $(1 - p_{v1})$ accounts for the reduction in N_{occ} during the first AP] is close to or even lower than the experimentally found values and subsequent pulses cannot be explained. Consistently, it has been suggested early that SV replenishment at PF terminals is very rapid (Crowley et al., 2007).

Rapid replenishment alone, however, is unlikely to fully account for PPF at PF synapses. It was recognized that even if p_{v2} of one and full replenishment between APs (i.e., $N_{occ,1} = N_{occ,2}$; PPR = p_{v2}/p_{v1}) are assumed the experimentally determined values frequently exceed the theoretical maxima (Valera et al., 2012; Ishiyama et al., 2014; Brachtendorf et al., 2015; Miki et al., 2016). Consistently, Valera et al. (2012) found evidence for changes in N during activity of PF to PC synapses. They found that N, as estimated by the binominal parameter in fluctuation analysis, increased during high-frequency trains of APs. In particular N during the second AP was larger than during the first AP ($N_2 > N_1$), suggesting incremental N as a substantial factor of PPF. These findings were subsequently confirmed by stationary fluctuation analysis at single PF to PC synapses in paired recordings (Brachtendorf et al., 2015).

In the latter study, it was proposed that the PPR of PF to PC synapses can be explained by a model with sequential SV pools originally proposed for crayfish motoneuron synapses (Millar et al., 2005). In the adaptation for the PF terminal, it was assumed that release sites are restored from replenishment sites in a Ca^{2+} dependent manner (Brachtendorf et al., 2015). The model well predicted the experimental PPF over a broad range of ISIs of 5 ms to 1 s if a transient increase in N between the two APs of a paired-pulse experiment was permitted rather than an increase in p_v alone. Morphologically, additional N appear possible since the area of the PF AZ (0.068 μm^2; Kusch et al., 2018) is sufficiently

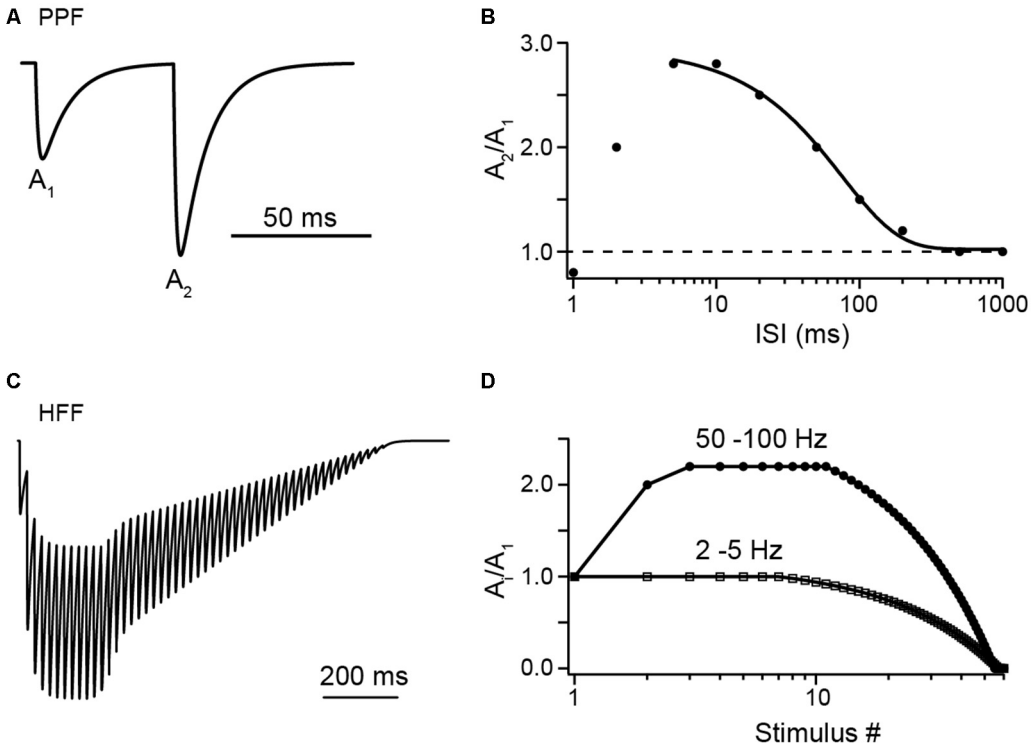

FIGURE 1 | Illustrations of facilitation vs. depression at Parallel fiber (PF) to Purkinje cell (PC) synapses with synthetic data. **(A)** A pair of excitatory postsynaptic currents (EPSCs), normalized to the first amplitude (A_1), as would be evoked by PF tract stimulation at an interstimulus interval (ISI) of 50 ms, illustrating paired-pulse facilitation (PPF). **(B)** Illustration of paired-pulse ratio (PPR) as a function of ISI. Synthetic data in the range of 5 ms to 1 s were fit by a sigmoidal function (see Valera et al., 2012). Note the decline in PPR at ISI <5 ms, which may indicate a limit in the speed of synaptic vesicle (SV) replenishment (see text for detail). **(C)** Illustration of high-frequency facilitation (HFF) of normalized EPSCs during a 50 Hz train of action potentials (APs). **(D)** Illustration of HFF (circles) and low-frequency depression (LFD; squares) as a function of stimulus number as would be observed at the indicated frequencies (see Doussau et al., 2017).

large to harbor more than 2–8 release-ready SVs (r = 21 nm; Wilhelm et al., 2014).

Two recent studies investigated the mechanisms of sustained release reliability at PF terminals during trains of APs in great depth (Miki et al., 2016; Doussau et al., 2017; **Figure 2**). Miki et al. (2016) challenged PF to MLI synapses with trains of eight APs delivered at small ISI of 5 ms in elevated $[Ca^{2+}]_e$ of 3 mM. Based on these data they suggest a sequential two-pool model (plus an implicit reserve pool) that explains facilitation mainly based on increasing N_{occ} (**Figure 2A**). They suggest an initially incomplete resting occupancy of release sites (referred to as docking sites), such that $N_{occ,1} < N_1$. N_1 was estimated to be ∼4–5 with a resting occupancy of 0.45, such that $N_{occ,1}$ is ∼2–3. Replenishment sites of about the same number (4–5) were considered to be fully occupied and the transition probability between the two pools was estimated to be 0.6 during activity. Based on EGTA effects, this high transition probability was Ca^{2+} dependent and gave rise to the increase in N_{occ} during the train.

Doussau et al. (2017) challenged PF synapses by long-lasting trains of 50 to >100 APs delivered either at high (ISI 10 or 20 ms) or low (ISI 0.2, 0.5 or 2 s) frequency. They found sustained high-frequency facilitation (HFF) for a large number of 20–30 APs before synapses progressively depressed and frequently became "silent." Remarkably, during low-frequency activation, synapses no longer facilitated but had A_i/A_1 PPRs of 1 for the first ∼7 APs. Subsequently, EPSC amplitudes progressively depressed over tens of APs and eventually the synapses became silent. Hence, PF terminals show HFF but low-frequency depression (LFD; **Figures 1C,D**). In agreement with the above studies, the authors provide evidence that these bidirectional short-term plasticity characteristics are explained by the presence of two sequential SV pools (termed fully releasable and reluctant pool, plus an implicit reserve pool). During high-frequency trains, N, which is equal to N_{occ} in this study, increased *via* rapid recruitment from the reluctant pool while release sites became progressively depleted during low-frequency stimulation. The results with EGTA and simulations indicated that this rapid recruitment is Ca^{2+} dependent and slowly reversible within ∼200 ms, such that it effectively increased N contributing to release with high-frequency but not low-frequency AP firing (**Figure 2B**).

In summary, while there is some controversy about the resting occupancy of release sites (Miki et al., 2016; Doussau et al., 2017), several lines of evidence from the recent literature suggest that facilitation at PF synapses mainly results

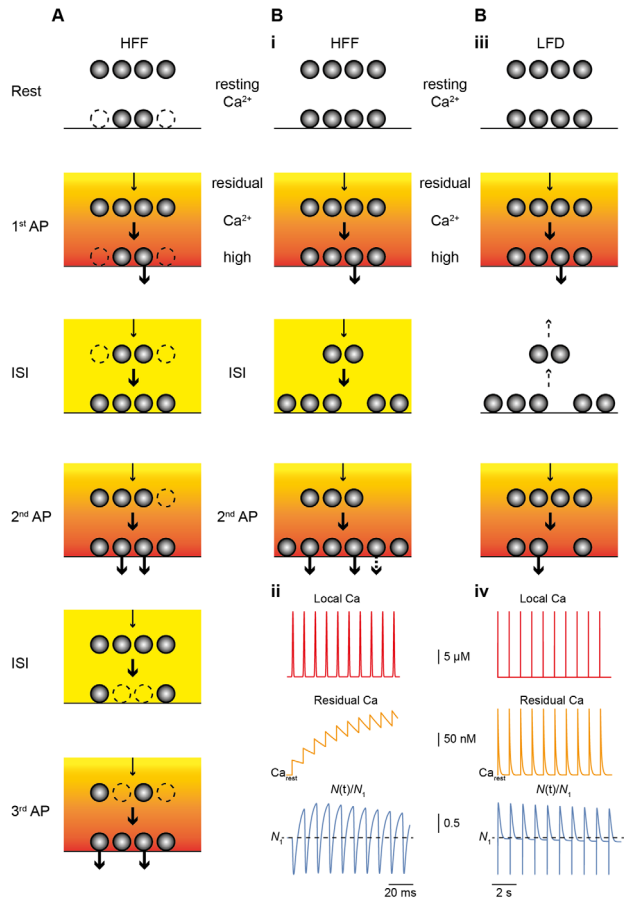

FIGURE 2 | Main mechanism of facilitation and depression. **(A)** Scheme of the model of HFF proposed by Miki et al. (2016). The resting occupancy of release sites (lower vesicles) is ∼50% (dashed vesicles; $N_{occ,1} < N$), while a replenishment pool (upper vesicles) is fully occupied. The reserve pool is not shown. During high-frequency stimulation N_{occ} increases ($N_{occ,train} = N$), thereby, giving rise to HFF. Release and the transition of vesicles from replenishment sites to release sites (arrows) is driven by the Ca^{2+} gradient (red to yellow gradient) and residual Ca^{2+} (orange to yellow). **(B)** As in **(A)** but for the model proposed by Doussau et al. (2017) for HFF and LFD. At rest, all release sites are occupied ($N_{occ,1} = N_1$). (i) During HFF, N increases ($N_{train} > N_1$); an increase in p_v makes a smaller contribution to HFF (indicated by the dashed arrow in the lower panel). (ii) Illustrations of local Ca^{2+} at the release sensor (red, *top*), build-up of residual Ca^{2+} (orange, *middle*), and $N(t)$ (blue, *bottom*), normalized to N_1 (dashed line), plotted over time for 10 APs at 100 Hz. Note the increase in N. (iii) During low-frequency activation Ca^{2+} drops back to resting level between pulses and vesicles return from release sites to replenishment sites (dashed arrows), giving rise to PPR of ∼1 in the second pulse. (iv) As in (ii) but for 10 APs at 2 Hz. Note that there is no build-up in residual Ca^{2+} (*middle*) and that N is no longer increased at the time of stimulation and progressively declines (*lower*), resulting in LFD during continuing activation.

from a presynaptic mechanism that increases the number of release sites or their occupancy during high-frequency trains of APs. This increase is the result of a very rapid, activity-dependent supply of SVs from replenishment sites, also referred to a "overfilling" of the ready releasable pool (RRP; Neher and Brose, 2018). The forward transition of SVs from replenishment sites is likely to be reversible on a slower time-scale, thereby, explaining the finding of LFD in addition to HFF at PF synapses.

Mechanisms of Rapid Replenishment

The very rapid, Ca^{2+} dependent forward transition of SVs from replenishment sites to release sites requires a mechanism that operates on the ms time-scale. PPR experiments indicate that the speed of the replenishment process reaches its limit at ISI <5 ms (**Figure 1B**). At shorter ISI PPF declined and eventually turned to depression (Valera et al., 2012).

Assuming an exponential process, Miki et al. (2016) estimate a very rapid rate constant of ∼180 s^{-1}, corresponding to τ of ∼5.5 ms per release site for an ISI of 5 ms. This is faster than would be obtained by mere diffusion of SVs, suggesting an active process. Consistently, they found evidence for an involvement of actin and myosin cytoskeleton in rapid replenishment based on the inhibitory effects of latrunculin B and blebbistatin. Additional experiments with EGTA-AM revealed the Ca^{2+} dependency of replenishment.

As detailed above, Doussau et al. (2017) found evidence that the replenishment process is reversible on a slower time scale of ∼200 ms. Interestingly, in a recent manuscript reporting results from electron microscopic analysis of hippocampal synapses, following stimulation and rapid freezing of cultured neurons, new SVs were recruited to the plasma membrane and fully replenished the docked pool of SVs within ∼10 ms after stimulation (Kusick et al., 2018). The docking of these SVs was transient and they either undocked or fused within 100 ms. These ultra structural results are in notable agreement with the findings at PF synapses, suggesting that recruitment of SVs to release sites is rapid and reversible.

Already 20 years ago it has been suggested that facilitation at PF synapses requires a Ca^{2+} dependent facilitation sensor separate from the release sensor (Atluri and Regehr, 1996). The molecular identity and mode of action of this sensor, however, remained elusive until recently. Recent results suggest that Synaptotagmin 7 (Syt7) acts as facilitation sensor at PF terminals. Syt7 knock-out mice displayed reduced PPF, while their p_v and presynaptic Ca^{2+} signaling were not affected (Turecek and Regehr, 2018). Mechanistically, Ca^{2+} binding to the C2A domain of Syt7 is required for facilitation at different synapses (Jackman et al., 2016). Interestingly, Syt7 was also found to promote SV replenishment during trains of APs in a Ca^{2+} dependent manner by interaction with Ca^{2+} bound calmodulin (Liu et al., 2014). For other functions of Syt7, e.g., in asynchronous release (Turecek and Regehr, 2018), and proposed relationships between different functions I refer the reader to recent reviews (e.g., Chen and Jonas, 2017; Bornschein and Schmidt, 2019; Volynski and Krishnakumar, 2018).

At Syt7 mutant PF synapses, a substantial amount of PPF remained at short ISI (Turecek and Regehr, 2018). This indicates that other mechanisms are operational in addition, which may involve other proteins with C2 domains such as Munc13s (Neher and Brose, 2018). The cerebellum-specific Munc13-3, for example, increases p_v and alters PPR by "superpriming" (Augustin et al., 2001; Ishiyama et al., 2014). Experiments in a developmental context indicated that Munc13-3 tightens

the coupling distance between SVs and P/Q-type channels (Kusch et al., 2018). Whether coupling distance tightening and Munc13-3 can establish newly occupied release sites during high-frequency activity is unclear at present. For further details on molecular mechanisms of short-term plasticity and the role of Synaptotagmins and other molecular players I refer the reader to recent comprehensive reviews (Jackman and Regehr, 2017; Bornschein and Schmidt, 2019; Neher and Brose, 2018; Volynski and Krishnakumar, 2018).

CONCLUDING REMARKS

PPF was discovered more than 70 years ago and its mechanisms may differ between synapses (Jackman and Regehr, 2017). At different synapses different conceptions were suggested to account for facilitation. Originally, it has been proposed that the "active Ca^{2+}," which is "Ca^{2+} remaining attached to specific sites on the inner axon membrane" causes facilitation (Katz and Miledi, 1968). Reminiscent of the active Ca^{2+} are slow Ca^{2+} unbinding from the release sensor (Bornschein et al., 2013) and Ca^{2+} binding to the facilitation sensor Syt7 (Atluri and Regehr, 1996; Jackman et al., 2016). In addition, elevated release site $[Ca^{2+}]_i$ due to AP broadening (Geiger and Jonas, 2000) or effects of endogenous Ca^{2+} buffers can cause facilitation (Rozov et al., 2001). Finally, the very rapid, activity-dependent increase in the number of occupied release sites added to the mechanisms of facilitation (Valera et al., 2012; Brachtendorf et al., 2015; Miki et al., 2016; Doussau et al., 2017). At PF synapses buffering by their major endogenous buffer Calretinin increases PPF by reducing p_{v1} (Schmidt et al., 2013; Brachtendorf et al., 2015). The effect is attenuated by the concomitant reduction in the Ca^{2+} dependent recruitment process such that the net effect of Calretinin on PPF is rather moderate (Schiffmann et al., 1999; Brachtendorf et al., 2015). Also, Ca^{2+} unbinding from the release sensor likely makes a small contribution (Brachtendorf et al., 2015; Doussau et al., 2017). The majority of facilitation, however, results from an ultra-rapid and reversible increase in occupied release sites during high-frequency activity (Miki et al., 2016; Doussau et al., 2017). Hence, release sites at AZs of PF synapses are very dynamic entities that can be reversibly recruited or replenished on a millisecond time scale.

AUTHOR CONTRIBUTIONS

HS wrote the manuscript.

FUNDING

This work was supported by the German Research Foundation (Deutsche Forschungsgemeinschaft, DFG, SCHM1838/2) and the DFG and University of Leipzig within the program of open access publishing.

ACKNOWLEDGMENTS

The author would like to thank Philippe Isope, Bernard Poulain, Takafumi Miki and Stefan Hallermann for their helpful comments and critical discussion of the manuscript.

REFERENCES

Atluri, P. P., and Regehr, W. G. (1996). Determinants of the time course of facilitation at the granule cell to Purkinje cell synapse. *J. Neurosci.* 16, 5661–5671. doi: 10.1523/JNEUROSCI.16-18-05661.1996

Augustin, I., Korte, S., Rickmann, M., Kretzschmar, H. A., Südhof, T. C., Herms, J. W., et al. (2001). The cerebellum-specific Munc13 isoform Munc13–3 regulates cerebellar synaptic transmission and motor learning in mice. *J. Neurosci.* 21, 10–17. doi: 10.1523/JNEUROSCI.21-01-00010.2001

Baur, D., Bornschein, G., Althof, D., Watanabe, M., Kulik, A., Eilers, J., et al. (2015). Developmental tightening of cerebellar cortical synaptic influx-release coupling. *J. Neurosci.* 35, 1858–1871. doi: 10.1523/JNEUROSCI.2900-14.2015

Bornschein, G., Arendt, O., Hallermann, S., Brachtendorf, S., Eilers, J., and Schmidt, H. (2013). Paired-pulse facilitation at recurrent Purkinje neuron synapses is independent of calbindin and parvalbumin during high-frequency activation. *J. Physiol.* 591, 3355–3370. doi: 10.1113/jphysiol.2013.254128

Bornschein, G., and Schmidt, H. (2019). Synaptotagmin Ca^{2+} sensors and their spatial coupling to presynaptic Ca_v channels in central cortical synapses. *Front. Mol. Neurosci.* 11:494. doi: 10.3389/fnmol.2018.00494

Brachtendorf, S., Eilers, J., and Schmidt, H. (2015). A use-dependent increase in release sites drives facilitation at calretinin-deficient cerebellar parallel-fiber synapses. *Front. Cell. Neurosci.* 9:27. doi: 10.3389/fncel.2015.00027

Brenowitz, S. D., and Regehr, W. G. (2007). Reliability and heterogeneity of calcium signaling at single presynaptic boutons of cerebellar granule cells. *J. Neurosci.* 27, 7888–7898. doi: 10.1523/JNEUROSCI.1064-07.2007

Chadderton, P., Margrie, T. W., and Häusser, M. (2004). Integration of quanta in cerebellar granule cells during sensory processing. *Nature* 428, 856–860. doi: 10.1038/nature02442

Chen, C., and Jonas, P. (2017). Synaptotagmins: that's why so many. *Neuron* 94, 694–696. doi: 10.1016/j.neuron.2017.05.011

Clements, J. D., and Silver, R. A. (2000). Unveiling synaptic plasticity: a new graphical and analytical approach. *Trends Neurosci.* 23, 105–113. doi: 10.1016/s0166-2236(99)01520-9

Crowley, J. J., Carter, A. G., and Regehr, W. G. (2007). Fast vesicle replenishment and rapid recovery from desensitization at a single synaptic release site. *J. Neurosci.* 27, 5448–5460. doi: 10.1523/JNEUROSCI.1186-07.2007

Doussau, F., Schmidt, H., Dorgans, K., Valera, A. M., Poulain, B., and Isope, P. (2017). Frequency-dependent mobilization of heterogeneous pools of synaptic vesicles shapes presynaptic plasticity. *Elife* 6:e28935. doi: 10.7554/elife.28935

Eggermann, E., Bucurenciu, I., Goswami, S. P., and Jonas, P. (2012). Nanodomain coupling between Ca^{2+} channels and sensors of exocytosis at fast mammalian synapses. *Nat. Rev. Neurosci.* 13, 7–21. doi: 10.1038/nrn3125

Geiger, J. R., and Jonas, P. (2000). Dynamic control of presynaptic Ca^{2+} inflow by fast-inactivating K^+ channels in hippocampal mossy fiber boutons. *Neuron* 28, 927–939. doi: 10.1016/s0896-6273(00)00164-1

Ishiyama, S., Schmidt, H., Cooper, B. H., Brose, N., and Eilers, J. (2014). Munc13–3 superprimes synaptic vesicles at granule cell-to-basket cell synapses in the mouse cerebellum. *J. Neurosci.* 34, 14687–14696. doi: 10.1523/JNEUROSCI.2060-14.2014

Jackman, S. L., and Regehr, W. G. (2017). The mechanisms and functions of synaptic facilitation. *Neuron* 94, 447–464. doi: 10.1016/j.neuron.2017.02.047

Jackman, S. L., Turecek, J., Belinsky, J. E., and Regehr, W. G. (2016). The calcium sensor synaptotagmin 7 is required for synaptic facilitation. *Nature* 529, 88–91. doi: 10.1038/nature16507

Kaeser, P. S., and Regehr, W. G. (2017). The readily releasable pool of synaptic vesicles. *Curr. Opin. Neurobiol.* 43, 63–70. doi: 10.1016/j.conb.2016.12.012

Katz, B., and Miledi, R. (1968). The role of calcium in neuromuscular facilitation. *J. Physiol.* 195, 481–492. doi: 10.1113/jphysiol.1968.sp008469

Kusch, V., Bornschein, G., Loreth, D., Bank, J., Jordan, J., Baur, D., et al. (2018). Munc13–3 is required for the developmental localization of Ca^{2+} channels to active zones and the nanopositioning of $Ca_v2.1$ near release sensors. *Cell Rep.* 22, 1965–1973. doi: 10.1016/j.celrep.2018.02.010

Kusick, G. F., Chin, M., Lippmann, K., Adula, K. P., Davis, M. W., Jorgensen, E. M., et al. (2018). Synaptic vesicles undock and then transiently dock after an action potential. *bioRxiv* [Preprint]. doi: 10.1101/509216

Liu, H., Bai, H., Hui, E., Yang, L., Evans, C. S., Wang, Z., et al. (2014). Synaptotagmin 7 functions as a Ca^{2+}-sensor for synaptic vesicle replenishment. *Elife* 3:e01524. doi: 10.7554/elife.01524

Malagon, G., Miki, T., Llano, I., Neher, E., and Marty, A. (2016). Counting vesicular release events reveals binomial release statistics at single glutamatergic synapses. *J. Neurosci.* 36, 4010–4025. doi: 10.1523/JNEUROSCI.4352-15.2016

Miki, T., Malagon, G., Pulido, C., Llano, I., Neher, E., and Marty, A. (2016). Actin- and myosin-dependent vesicle loading of presynaptic docking sites prior to exocytosis. *Neuron* 91, 808–823. doi: 10.1016/j.neuron.2016.07.033

Millar, A. G., Zucker, R. S., Ellis-Davies, G. C., Charlton, M. P., and Atwood, H. L. (2005). Calcium sensitivity of neurotransmitter release differs at phasic and tonic synapses. *J. Neurosci.* 25, 3113–3125. doi: 10.1523/JNEUROSCI.4717-04.2005

Mintz, I. M., Sabatini, B. L., and Regehr, W. G. (1995). Calcium control of transmitter release at a cerebellar synapse. *Neuron* 15, 675–688. doi: 10.1016/0896-6273(95)90155-8

Neher, E. (2015). Merits and limitations of vesicle pool models in view of heterogeneous populations of synaptic vesicles. *Neuron* 87, 1131–1142. doi: 10.1016/j.neuron.2015.08.038

Neher, E., and Brose, N. (2018). Dynamically primed synaptic vesicle states: key to understand synaptic short-term plasticity. *Neuron* 100, 1283–1291. doi: 10.1016/j.neuron.2018.11.024

Rancz, E. A., Ishikawa, T., Duguid, I., Chadderton, P., Mahon, S., and Hausser, M. (2007). High-fidelity transmission of sensory information by single cerebellar mossy fibre boutons. *Nature* 450, 1245–1248. doi: 10.1038/nature05995

Ritzau-Jost, A., Delvendahl, I., Rings, A., Byczkowicz, N., Harada, H., Shigemoto, R., et al. (2014). Ultrafast action potentials mediate kilohertz signaling at a central synapse. *Neuron* 84, 152–163. doi: 10.1016/j.neuron.2014.08.036

Rozov, A., Burnashev, N., Sakmann, B., and Neher, E. (2001). Transmitter release modulation by intracellular Ca^{2+} buffers in facilitating and depressing nerve terminals of pyramidal cells in layer 2/3 of the rat neocortex indicates a target cell-specific difference in presynaptic calcium dynamics. *J. Physiol.* 531, 807–826. doi: 10.1111/j.1469-7793.2001.0807h.x

Schiffmann, S. N., Cheron, G., Lohof, A., d'Alcantara, P., Meyer, M., Parmentier, M., et al. (1999). Impaired motor coordination and Purkinje cell excitability in mice lacking calretinin. *Proc. Natl. Acad. Sci. U S A* 96, 5257–5262. doi: 10.1073/pnas.96.9.5257

Schmidt, H., Brachtendorf, S., Arendt, O., Hallermann, S., Ishiyama, S., Bornschein, G., et al. (2013). Nanodomain coupling at an excitatory cortical synapse. *Curr. Biol.* 23, 244–249. doi: 10.1016/j.cub.2012.12.007

Sims, R. E., and Hartell, N. A. (2005). Differences in transmission properties and susceptibility to long-term depression reveal functional specialization of ascending axon and parallel fiber synapses to Purkinje cells. *J. Neurosci.* 25, 3246–3257. doi: 10.1523/JNEUROSCI.0073-05.2005

Südhof, T. C. (2013). Neurotransmitter release: the last millisecond in the life of a synaptic vesicle. *Neuron* 80, 675–690. doi: 10.1016/j.neuron.2013.10.022

Turecek, J., and Regehr, W. G. (2018). Synaptotagmin 7 mediates both facilitation and asynchronous release at granule cell synapses. *J. Neurosci.* 38, 3240–3251. doi: 10.1523/jneurosci.3207-17.2018

Valera, A. M., Doussau, F., Poulain, B., Barbour, B., and Isope, P. (2012). Adaptation of granule cell to Purkinje cell synapses to high-frequency transmission. *J. Neurosci.* 32, 3267–3280. doi: 10.1523/JNEUROSCI.3175-11.2012

Volynski, K. E., and Krishnakumar, S. S. (2018). Synergistic control of neurotransmitter release by different members of the synaptotagmin family. *Curr. Opin. Neurobiol.* 51, 154–162. doi: 10.1016/j.conb.2018.05.006

Wilhelm, B. G., Mandad, S., Truckenbrodt, S., Kröhnert, K., Schäfer, C., Rammner, B., et al. (2014). Composition of isolated synaptic boutons reveals the amounts of vesicle trafficking proteins. *Science* 344, 1023–1028. doi: 10.1126/science.1252884

Xu-Friedman, M. A., Harris, K. M., and Regehr, W. G. (2001). Three-dimensional comparison of ultrastructural characteristics at depressing and facilitating synapses onto cerebellar Purkinje cells. *J. Neurosci.* 21, 6666–6672. doi: 10.1523/jneurosci.21-17-06666.2001

Conflict of Interest Statement: The author declares that the research was conducted in the absence of any commercial or financial relationships that could be construed as a potential conflict of interest.

frontiers in Systems Neuroscience

REVIEW
published: 11 September 2019
doi: 10.3389/fnsys.2019.00046

Climbing Fibers Provide Graded Error Signals in Cerebellar Learning

Yunliang Zang and Erik De Schutter*

Computational Neuroscience Unit, Okinawa Institute of Science and Technology Graduate University, Okinawa, Japan

The cerebellum plays a critical role in coordinating and learning complex movements. Although its importance has been well recognized, the mechanisms of learning remain hotly debated. According to the classical cerebellar learning theory, depression of parallel fiber synapses instructed by error signals from climbing fibers, drives cerebellar learning. The uniqueness of long-term depression (LTD) in cerebellar learning has been challenged by evidence showing multi-site synaptic plasticity. In Purkinje cells, long-term potentiation (LTP) of parallel fiber synapses is now well established and it can be achieved with or without climbing fiber signals, making the role of climbing fiber input more puzzling. The central question is how individual Purkinje cells extract global errors based on climbing fiber input. Previous data seemed to demonstrate that climbing fibers are inefficient instructors, because they were thought to carry "binary" error signals to individual Purkinje cells, which significantly constrains the efficiency of cerebellar learning in several regards. In recent years, new evidence has challenged the traditional view of "binary" climbing fiber responses, suggesting that climbing fibers can provide graded information to efficiently instruct individual Purkinje cells to learn. Here we review recent experimental and theoretical progress regarding modulated climbing fiber responses in Purkinje cells. Analog error signals are generated by the interaction of varying climbing fibers inputs with simultaneous other synaptic input and with firing states of targeted Purkinje cells. Accordingly, the calcium signals which trigger synaptic plasticity can be graded in both amplitude and spatial range to affect the learning rate and even learning direction. We briefly discuss how these new findings complement the learning theory and help to further our understanding of how the cerebellum works.

Keywords: cerebellar learning, Purkinje cell, climbing fiber, complex spike (CS), error signal

OPEN ACCESS

Edited by:
Philippe Isope, Centre National de la Recherche Scientifique (CNRS), France

Reviewed by:
Christian Hansel, University of Chicago, United States
Jason M. Christie, Max Planck Florida Institute for Neuroscience, United States

****Correspondence:***
Yunliang Zang
zangyl1983@gmail.com

Received: *24 June 2019*
Accepted: *19 August 2019*
Published: *11 September 2019*

Citation:
Zang Y and De Schutter E (2019) Climbing Fibers Provide Graded Error Signals in Cerebellar Learning. Front. Syst. Neurosci. 13:46. doi: 10.3389/fnsys.2019.00046

INTRODUCTION

It is widely recognized that the cerebellum is critical in coordinating muscles and learning novel movements with highly accurate and temporal precision. Even for a simple finger-to-nose task, to make different segments of hand and arm interact smoothly, humans need the cerebellum to precisely modulate the sequence and duration of elementary movements. The cerebellum has a relatively simple anatomy and the anatomic connections involved in its associated functions are also well known. In this context, the cerebellum becomes an ideal structure to explore learning rules and it also opens a window for us to begin to comprehend how the brain works.

For decades, it has been of great interest to decipher cerebellar learning algorithms (De Schutter, 1995). The cerebellar learning theory was first systematically proposed by Marr (1969) and then Albus (1971), building upon previous knowledge of wiring connections and electrophysiological properties of the cerebellar cortex (Eccles et al., 1967). The basic structure of cerebellar circuitry is illustrated in **Figure 1**. Mossy fibers transmit sensory and cortical information to granule cells *via* excitatory synaptic connections. Small granule cells are electrically compact and they constitute the majority of neurons in the brain. Their axons project up into the molecular layer of the cerebellar cortex, bifurcate and form excitatory synapses onto Purkinje cell dendrites. As the sole output of the cerebellar cortex, each Purkinje cell is contacted by ∼150,000 parallel fiber (bifurcations of granule cell axons) synapses. Meanwhile, parallel fibers also activate stellate cells and basket cells, which form inhibitory synapses with Purkinje cells, establishing a stereotypical feed-forward-inhibition circuit. Stellate cells tend to locate in the outer part of the molecular layer and mainly target Purkinje cell distal dendrites. In contrast, basket cells locate in the inner part of the molecular layer and mainly target Purkinje cell somas and axon initial segments (AIS).

Each Purkinje cell is also innervated by a single climbing fiber, which spontaneously fires at ∼1 Hz and reliably triggers complex spikes. In Marr's theory (Marr, 1969), when a novel movement needs to be learned or an old one requires modification because of an error, the climbing fiber fires a spike. Then the simultaneously activated parallel fiber synapses in Purkinje cells are potentiated to learn. Albus extended Marr's model and proposed that synaptic weights between parallel fibers and Purkinje cells should be depressed rather than potentiated since Purkinje cells are inhibitory neurons (Albus, 1971). Amazingly, the idea of climbing fiber-induced plasticity at parallel fiber synapses being the cellular substrate of cerebellar learning was proposed before any experimental demonstration of climbing fiber-evoked parallel fiber plasticity. Ito and Kano (1982) found that the synapses between parallel fibers and Purkinje cells undergo long-term depression (LTD) when parallel fibers are activated in conjunction with climbing fibers. Since then, the Marr-Albus-Ito theory has dominated cerebellar learning research, although it has been challenged by emerging experimental data at molecular, cellular, and behavioral levels in recent years. First, this theory turns out to be incomplete after the discovery of long-term potentiation (LTP) at parallel fiber-Purkinje cell synapses (Sakurai, 1987) and synaptic plasticity at other sites. In the cerebellar cortex, mossy fiber-granule cell synapses, granule cell-Golgi cell synapses, Golgi cell-granule cell synapses, parallel fiber-molecular layer interneuron (MLI) synapses, and MLI-Purkinje cell synapses are all plastic (Gao et al., 2012). Mossy fiber-cerebellar nuclei neuron synapses can also be potentiated (Pugh and Raman, 2006). In theory, all these learning sites should work synergistically to optimize motor behaviors. Second, climbing fibers seemed to be inefficient teachers in cerebellar learning. Since multi-site learning was well summarized by Gao et al. (2012), we will review the history of climbing fiber physiology, summarize recent progress, and predict how climbing fibers may instruct cerebellar learning.

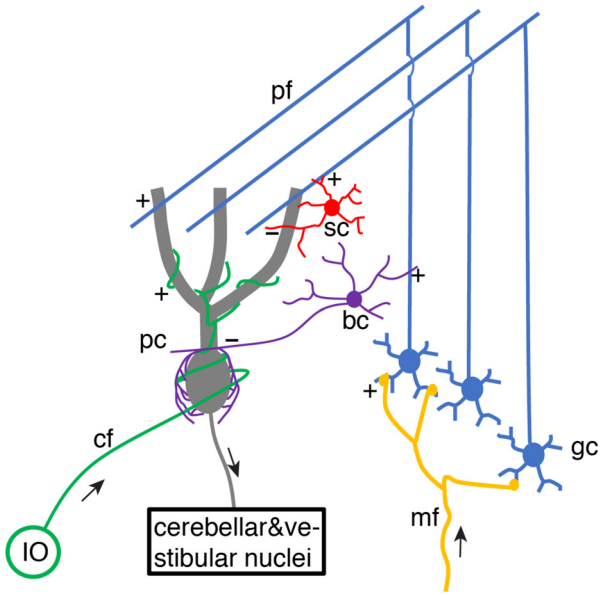

FIGURE 1 | Schematic of basic cerebellar circuitry. mf, gc, pf, pc, sc, bc, cf, IO designate mossy fiber, granule cell, parallel fiber, Purkinje cell, stellate cell, basket cell, climbing fiber and inferior olive neuron, respectively. "+" and "−" correspond to excitatory and inhibitory synaptic connections, respectively. pf → pc and pf → bc/sc → pc connections form a typical feed-forward-inhibition circuit. Some cell types and connections have been omitted for simplicity (Schematic, created by ourselves).

"ALL-OR-NONE" CLIMBING FIBER RESPONSES

After birth, each Purkinje cell is initially innervated by several climbing fibers (Hashimoto and Kano, 2003). With development, only one of the climbing fibers is selectively strengthened and preserved, while the weaker ones are eliminated. Thus, in the adult cerebellar cortex, preserved climbing fibers provide powerful synaptic inputs to Purkinje cells, with ∼300 synapses distributed on the soma and proximal parts of each dendritic tree (Llinas et al., 1969). More than 50 years ago, the climbing fiber response in Purkinje cells was described as "all-or-none" by Eccles et al. (1966). In response to a climbing fiber stimulus, stereotypical complex spikes occur at the soma with an initial fast spike and several spikelets driving on a plateau membrane potential (Eccles et al., 1966; Hounsgaard and Midtgaard, 1989; **Figure 2**). In the dendrite, the climbing fiber-evoked response is distinct from the somatic complex spike. The dendritic response was also found to be "all-or-none" (Llinás and Sugimori, 1980; Hounsgaard and Midtgaard, 1989), which corresponded to either global Ca^{2+} influx in the whole dendrite, triggered by a strong stimulus, or no Ca^{2+} influx from a weak, subthreshold stimulus (Miyakawa et al., 1992). The view of "all-or-none" climbing fiber responses in Purkinje cells continues to be emphasized in recent cerebellar research (Piochon et al., 2007; Nietz et al., 2017; Bouvier et al., 2018).

Unfortunately, "all-or-none" responses make the climbing fiber an inefficient teacher and this view has triggered heated

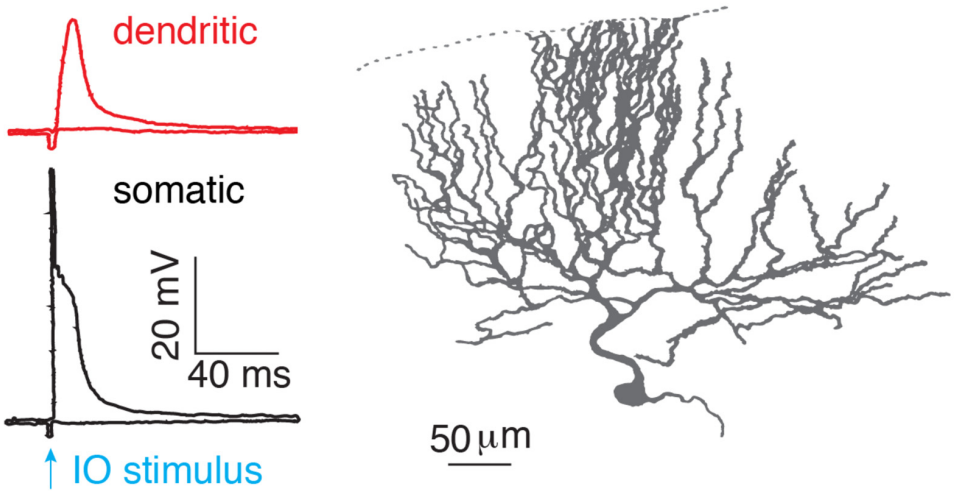

FIGURE 2 | "All-or-none" climbing fiber responses. Climbing fiber-evoked somatic (black) and dendritic (red) responses measured in the isolated cerebellum of turtles. The climbing fiber was activated by stimulating an inferior olive neuron (IO), reproduced from Hounsgaard and Midtgaard (1989). Somatic complex spikes are characterized by a fast spike followed by several spikelets on top of a plateau potential. ©1989 The Physiological Society, reproduced with permission from Wiley Publishing, Inc.

debates regarding its functional importance in cerebellar learning (Najafi and Medina, 2013). First, spontaneously firing climbing fibers provide "instruction" signals, even in the absence of errors, causing a signal-to-noise problem that is inherent in any spontaneously active system (Llinás et al., 1997). According to cell-attached recordings, granule cells fire at 4.8 ± 1.3 Hz under resting condition in awake mice (Chen et al., 2017). Thus, parallel fiber synapses coincident with spontaneous complex spikes become modified, since single Purkinje cells would seem unlikely to differentiate spontaneous "noise" complex spikes from "signal" complex spikes if their responses were "all-or-none." Second, unlike simple spikes, the firing rate of climbing fibers is low, implying that their capacity to increase the information transmission by changing spiking rates is limited (Kitazawa et al., 1998). Third, the plasticity of parallel fiber synapses occurs on Purkinje cell dendrites. "All-or-none" dendritic responses suggest that climbing fibers carry only qualitative rather than quantitative information, which significantly constrains the information capacity of climbing fibers and the learning capacity of single Purkinje cells. Finally, cerebellar learning suffers from the credit assignment problem (Minsky, 1961; Suvrathan et al., 2016; Bouvier et al., 2018). To learn well-timed and precise arbitrary movements, individual Purkinje cells most probably require specific error signals and learn heterogeneously. However, "all-or-none" climbing fiber responses would make individual Purkinje cells unable to extract specific error information from global error feedback.

GRADED CLIMBING FIBER RESPONSES IN PURKINJE CELLS

It is necessary to reassess a neglected aspect of experimental data reported in the last century that seemed to support "all-or-none" climbing fiber responses. Although neither climbing fiber-evoked somatic complex spikes nor dendritic spikes change by varying stimulus amplitude in the same cells *in vitro*, their firing patterns vary significantly among different cells and between recordings by different groups (Eccles et al., 1966; Llinás and Sugimori, 1980; Hounsgaard and Midtgaard, 1989). Observed complex spikes *in vivo* also show quite variable firing patterns (Bell and Kawasaki, 1972; Gilbert, 1976; Armstrong and Rawson, 1979). Theoretically, several factors can potentially reconcile these observations. Climbing fiber responses in Purkinje cells exhibit individual variability. The characteristics of Purkinje cells, such as excitability or voltage, varies. Presynaptic climbing fiber input varies, although Crill (1970) contested this. Do these factors really occur and grade climbing fiber responses?

In recent years, the veil obscuring the complex nature of climbing fiber responses has gradually lifted (**Figure 3**). The somatic complex spike is voltage-dependent and shows significant individual variability (Khaliq and Raman, 2005; Monsivais et al., 2005). Later, Tal et al. (2008) and Rokni et al. (2009) found that apart from somatic complex spike patterns, dendritic Ca^{2+} influx also shows strong voltage-dependence in slice preparations, characteristic of controversial bistability (Loewenstein et al., 2005; Schonewille et al., 2006), and suggesting that climbing fiber responses may be ternary rather than binary. Similar findings were later confirmed in anesthetized rats *in vivo* (Kitamura and Hausser, 2011). Ionic current modulation is also shown to grade the amplitude and spikelet number of dendritic spikes (Ohtsuki et al., 2012; Otsu et al., 2014). Interestingly, although both somatic and dendritic responses undergo modulation, conflicting observations have been made regarding their interactions. The variation of dendritic spikes had only a minimal role in regulating somatic output in

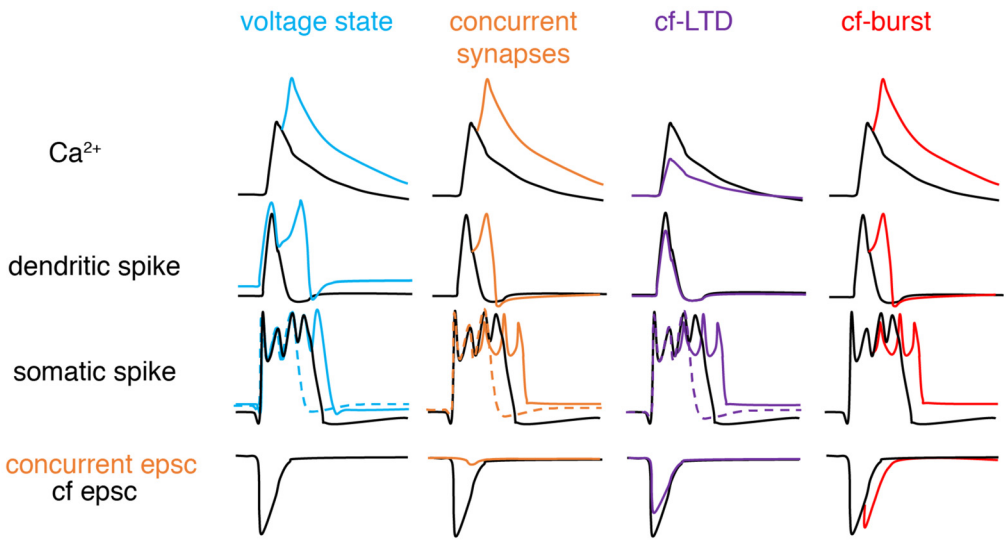

FIGURE 3 | Schematic of factors modifying climbing fiber responses. From left to right, climbing fiber (cf) responses can be graded by voltage states, concurrent synaptic input, cf-long-term depression (LTD), and spike numbers in a cf-burst. Compared with basal conditions (black): depolarization (blue), concurrent excitatory synapse (orange), cf-LTD (purple) and cf-burst (red, manifested by cf epsc) increases, increases, decreases and increases dendritic Ca^{2+} influx respectively, by modulating dendritic spikes. If concurrent synaptic input is inhibitory, changes are opposite (not illustrated here). For somatic complex spike changes, the existence of both dashed and solid-colored traces suggests that complex spikes can exhibit bidirectional changes depending on the "state," also implying that somatic complex spikes are poor proxies for dendritic responses. Sketched according to Zang et al. (2018; the authors' open access paper).

Callaway et al. (1995), Davie et al. (2008) and Rowan et al. (2018), but not in Ohtsuki et al. (2012) or Otsu et al. (2014). The climbing fiber-Purkinje cell synapses can also undergo LTD, which modulates complex spike waveforms by reduced synaptic current (Hansel and Linden, 2000). The capability of climbing fibers in generating analog signals was further demonstrated by Mathy et al. (2009). Depending on the phase of subthreshold oscillations, single somatic action potentials in olivary neurons can be translated into bursts of varying numbers of axonal spikes in climbing fibers and then reliably conveyed to Purkinje cells. Increasing spike numbers in climbing fibers modulate somatic spike patterns, enhances dendritic spikes, and consequently promote short-term and long-term plasticity at parallel fiber synapses in Purkinje cells. More recently, Gaffield et al. (2019) demonstrated that climbing fiber burst firing occurs *in vivo* and this response can be modulated by behaviorally relevant stimuli. Importantly, Purkinje cell dendrites can integrate this burst firing into a graded Ca^{2+} response. In addition, complex-spike doublets have been also shown to increase Ca^{2+} influx compared with single complex spikes and have been suggested to be "instruction" signals compared to spontaneous "noise" single complex spikes (Titley et al., 2019).

On one hand, a growing body of experimental evidence demonstrates the variability of climbing fiber responses, but on the other hand, it fails to provide a systematic explanation of somatic and dendritic spike initiation and variation and leads to many conflicting observations that stymie delineation of the functional role of climbing fibers in cerebellar learning. Furthermore, limited information extracted from noisy *in vivo* data by present experimental techniques (local field potential, calcium imaging, voltage imaging), adds to the confusion. In a recent experimental data-based theoretical study by Zang et al. (2018), the biophysical mechanism of climbing fiber responses at whole Purkinje cell scale was systematically investigated (**Figure 4**). The somatic complex spike is a result of climbing fiber synaptic current, intrinsic ionic currents, and axial currents from the dendritic spike. Accordingly, it is subject to regulation by climbing fiber firing patterns, voltage-dependent availability of Na^+ channels, and dendritic spike patterns.

In agreement with Ohtsuki et al. (2012) and Otsu et al. (2014), dendritic spike patterns can modulate somatic spike outputs in the model. The possible reason that Davie et al. (2008) and Rowan et al. (2018) observed a minimal role of dendritic spikes in regulating somatic firing patterns is that dendritic spikes measured by single-site patch-clamps do not reliably represent dendritic spike patterns in the complete dendrite. Zang et al. (2018) reproduced the data of Davie et al. (2008) and showed that the somatic complex spike hardly changes when a dendritic spike is either completely local or propagates along a branch. On the dendritic side, Ca^{2+} influx can be graded by climbing fiber firing patterns, coincident background synapses, and voltage states in an analog manner. The conflicting spatial range of Ca^{2+} influx observed in different experiments can be accounted for by different voltage states (Miyakawa et al., 1992; Zagha et al., 2010; Kitamura and Hausser, 2011; Ohtsuki et al., 2012; Otsu et al., 2014). On distal parts of Purkinje dendrites, there are not only P-type voltage-dependent Ca^{2+} channels, but also voltage-dependent K^+ channels. Climbing fibers directly excite and depolarize proximal smooth dendrites (Palay and Chan-Palay, 1974; Roth and Häusser, 2001; Zang et al., 2018), but not distal spiny parts. The axial current from the depolarization of proximal parts constitutes the sole current source to depolarize

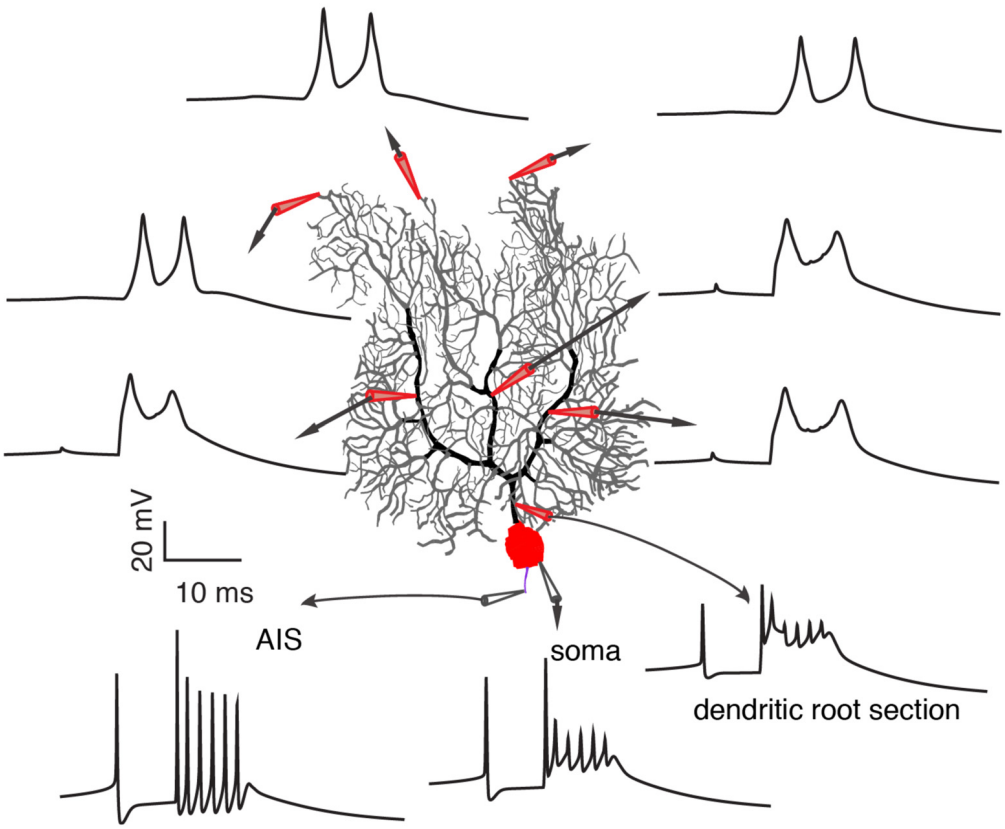

FIGURE 4 | Occurrence of somatic and dendritic spikes. Climbing fiber responses at different sites of the Purkinje cell, including axon initial segment (AIS), soma, proximal and distal dendrites. Each spikelet in the complex spike still initiates at the AIS. Reproduced from Zang et al. (2018; the authors' open access paper).

distal parts and to reach the activation threshold of P-type Ca^{2+} channels. When dendritic membrane potential is hyperpolarized, the large availability of K^+ currents outweighs P-type Ca^{2+} current to "brake" the initiation of dendritic spikes in distal parts. With depolarization, K^+ currents inactivate and axial currents can trigger dendritic spikes in the whole dendrite. Theoretically, voltage-dependent climbing fiber responses also endow single Purkinje cells with the ability to overcome the credit assignment problem. Individual Purkinje cells can extract specific instruction information according to their firing states (equivalent to voltage states *in vivo*; Jelitai et al., 2016), even when they receive the same climbing fiber signal.

GRADED ERROR SIGNALS IN CEREBELLAR LEARNING

Although Purkinje cells and climbing fibers are capable of encoding analog signals, does this really contribute to cerebellar learning? As reported by Najafi et al. (2014b), sensory event-triggered Ca^{2+} influx is larger than spontaneous Ca^{2+} spikes to signal the occurrence of an unexpected sensory event. Furthermore, Ca^{2+}-based instruction signals in Purkinje cell dendrites contain analog information that encodes the strength of instructive stimuli trial-by-trial (Najafi et al., 2014a). In another study, magnitudes of both plasticity and motor learning are correlated with durations of complex spikes measured in monkeys executing eye pursuit movements (Yang and Lisberger, 2014). On one hand, this finding is ground breaking, since it demonstrated for the first time that climbing fibers can adjust the instruction signal according to real-time movement errors. However, the mechanism that realizes the analog instruction signal remains unknown and requires further work. The authors assumed that the analog instruction signal is encoded by the number of spikes in climbing fibers (Mathy et al., 2009), ignoring other factors contributing to complex spike duration, such as firing states and background synapses in Purkinje cells (Kitamura and Hausser, 2011; Rowan et al., 2018; Zang et al., 2018). On the other hand, it remains unclear whether somatic complex spikes are reliable proxies of dendritic Ca^{2+} influx in Purkinje cells. Extracellular microelectrodes are usually used to extract simple spikes and complex spikes *in vivo*. Nonetheless, complex spike patterns are extremely variable in spikelet numbers and durations (Warnaar et al., 2015; Tang et al., 2017), and cannot be well separated, in most cases. Purkinje cell simple spike firing rates show bidirectional modulation (i.e., increased or decreased) during tasks (Yang and Lisberger, 2014; Herzfeld et al., 2015; Chen et al., 2016; Jelitai et al., 2016). At high voltage states (high firing rate), amplitudes of spikelets in complex

spikes tend to decrease (Warnaar et al., 2015; Zang et al., 2018) and they are prone to *in vivo* noise. Thus, it is easier to sort complex spikes from Purkinje cells with low firing rates compared to Purkinje cells with high firing rates, and this causes unavoidable bias in statistical analyses. Sometimes, it is even impossible to separate a complex spike with its subsequent simple spike, when the complex spike lacks a significant pause. This situation mainly occurs when there is only one dendritic spikelet that fails to hyperpolarize dendrites (see Figure 6A in Davie et al., 2008). Additionally, complex spike duration does not linearly correlate with dendritic Ca^{2+} influx (Zang et al., 2018), making the complex spike an unreliable proxy of dendritic response even if it can be well separated. Finally, and most importantly, the cellular mechanism of this short-term trial-by-trial learning is still unclear and how it correlates with long-term learning is unknown (Kimpo et al., 2014). Short-term plasticity of parallel fiber synapses and dendritic excitability plasticity may also be candidate mechanisms (Rancz and Häusser, 2006; Mathy et al., 2009; Ohtsuki et al., 2012; Regehr, 2012; Grangeray-Vilmint et al., 2018).

Noticeably, theoretical studies have also started to test the role of graded climbing fiber responses in cerebellar learning. Using a cerebellar network model with necessary climbing fiber-evoked burst-pause information in Purkinje cells (different with parallel fiber-evoked burst-pause by Steuber et al., 2007), Luque et al. (2019) found that parametric "pause" signals help to support both early and consolidated vestibulo-ocular reflex learning.

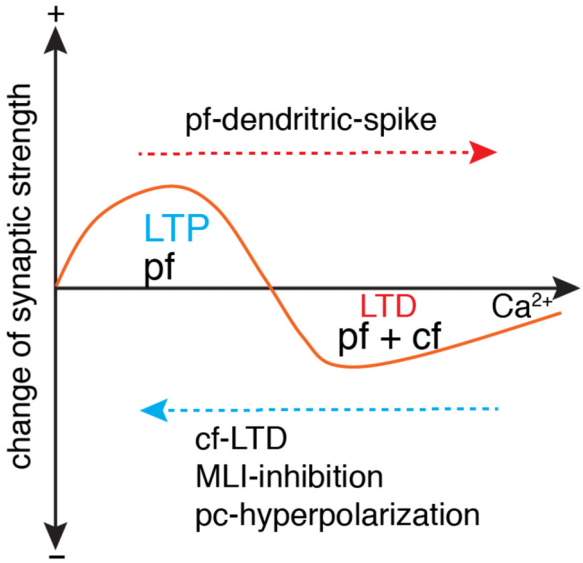

FIGURE 5 | Ca^{2+}-determined bidirectional plasticity of parallel fiber synapses. Parallel fiber (pf)-LTD has a higher Ca^{2+} induction threshold (usually induced by conjunctive pf and cf stimulation) than long-term potentiation (LTP; usually induced by pf stimulation in isolation). Depending on the dendritic Ca^{2+} influx, LTP can also be induced by conjunctive pf and cf activation under the condition of cf-LTD, conjunctive inhibition by molecular layer interneuron (MLI), or Purkinje cell (pc)-hyperpolarization. LTD can also be induced by pf in isolation when dendritic spikes occur with strong pf stimulation. Modified from Coesmans et al. (2004).

LTD AND LTP IN CEREBELLAR LEARNING

Parallel fiber synapses exhibit bidirectional long-term plasticity (Coesmans et al., 2004; Gallimore et al., 2018; Zamora Chimal and De Schutter, 2018), i.e., depression and potentiation. LTP is necessary to prevent suppression of all parallel fiber synapses due to spontaneous activation of parallel fibers and climbing fibers. Compared with LTP, LTD has a higher Ca^{2+} induction threshold, usually with a climbing fiber as the polarity switch (**Figure 5**). However, climbing fiber activation is neither sufficient nor necessary to trigger LTD, as evidenced by the LTP triggered by climbing fiber-LTD (Coesmans et al., 2004), and LTD triggered by strong parallel fiber stimulation alone (Hartell, 1996). Mathy et al. (2009) required an even higher threshold for LTD induction. Pairing of parallel fiber stimuli with a climbing fiber burst triggers LTD of parallel fiber synapses, but pairing of parallel fiber stimuli with a single climbing fiber stimulus induces LTP. Recently it was shown that the calcium threshold can slide rather than being constant (Piochon et al., 2016). Pooling the data together, it is easy to find that polarity of synaptic changes essentially depends on the amplitude of dendritic Ca^{2+} influx relative to the threshold, regardless of concurrent climbing fiber signals (**Figure 5**). In the Albus-Ito theory, LTD of parallel fiber synapses forms the unique cellular substrate of cerebellar learning, and LTP is largely ignored (Not by Marr, 1969). Nonetheless, whether LTD plays an essential role in cerebellar learning was questioned strongly in recent years. In mutant mice with deficits in parallel fiber-Purkinje cell LTD, there was no learning impairment in cerebellar coordination tasks, including adaptation of vestibulo-ocular reflex, eyeblink conditioning, and locomotion learning (Schonewille et al., 2011). The authors argued that LTD of parallel fiber synapses was not essential for cerebellar learning. However, Yamaguchi et al. (2016) demonstrated that LTD is inducible by intensified conjunctive stimulation in the same types of mutant mice, refuting previous arguments that questioned the function of LTD in cerebellar learning. Obviously, the lack of a standardized LTD stimulation protocol has caused many conflicting results (Suvrathan et al., 2016; Bouvier et al., 2018; Suvrathan and Raymond, 2018) and there is a lack of systematic experimental evaluation of the effect of stimulation parameters on the probability of plasticity induction (Zamora Chimal and De Schutter, 2018). In a more recent study, by developing a new optogenetic tool to transiently manipulate parallel fiber synaptic plasticity, Kakegawa et al. (2018) demonstrated that LTD is directly responsible for motor learning during horizontal optokinetic response and vestibulo-ocular reflex.

Although LTD is demonstrably critical in cerebellar learning, at least in some behavioral contexts, there is increasing awareness that it is not the sole mechanism. Accumulating evidence demonstrates that LTP of parallel fiber synapses also functions in procedural learning (Schonewille et al., 2011; Grasselli and Hansel, 2014; Gutierrez-Castellanos et al., 2017; Romano et al., 2018). Consistent with cerebellar plasticity rules in slice preparations [LTP usually induced by isolated parallel fiber activation (Coesmans et al., 2004)], potentiation

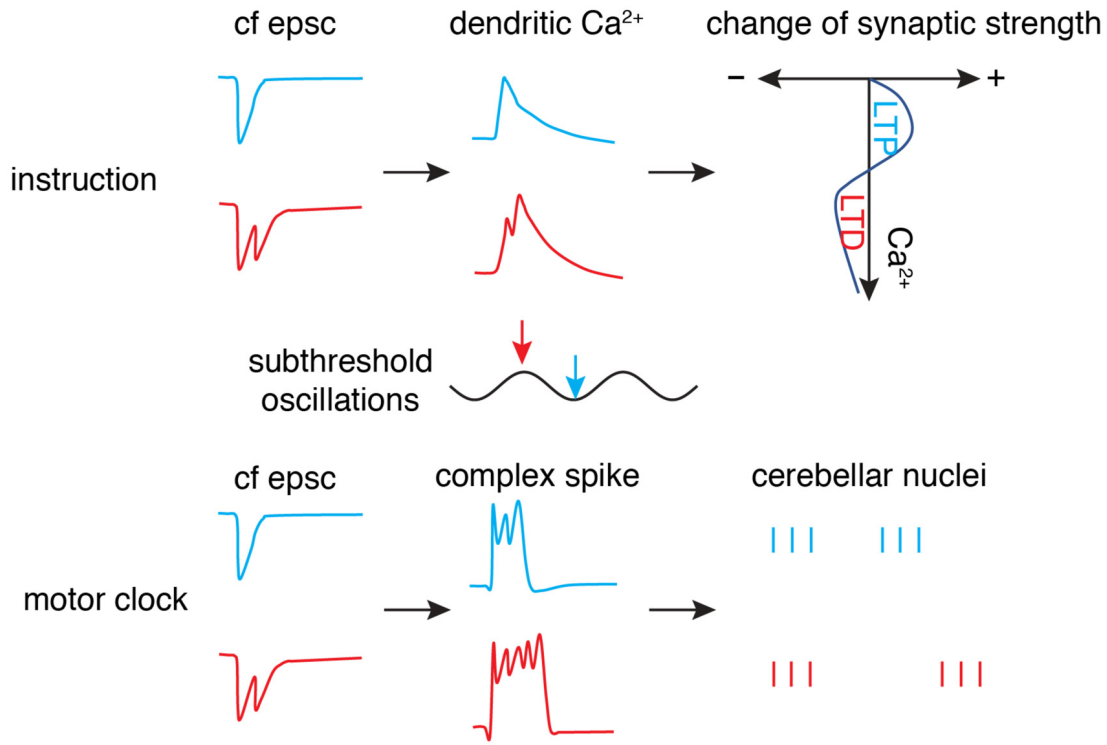

FIGURE 6 | "Motor clock" and "instruction" by climbing fibers. The phase (timing) of synaptic input in subthreshold oscillations is encoded by the number of axonal spikes in a climbing fiber (cf), manifested by cf epsc. The burst can convert to dendritic spikes and modulate the Ca^{2+} influx to shift the polarity of synaptic changes (top panel) as an "instruction" signal. Simultaneously, the burst can convert to somatic complex spikes and entrain downstream cerebellar nuclei neuron outputs to initiate or modulate movement as a "motor clock" (bottom panel; Schematic, created by ourselves).

of parallel fiber synapses is prominent in Purkinje cells with low complex activation probability (Romano et al., 2018). Interestingly in another study, optogenetic activation of molecular interneurons shifts the climbing fiber-induced depression of parallel fiber synapses to potentiation in vestibulo-ocular reflex learning (Rowan et al., 2018). This is the first evidence to support climbing fiber-triggered LTP during cerebellar learning, although abundant data support climbing fiber-induced LTP in slice preparations. It is mechanistically easy to understand that enhanced molecular interneuron spiking reduces climbing fiber-triggered dendritic Ca^{2+} influx and consequently shifts plasticity from LTD to LTP.

In cerebellum-related behaviors such as saccadic eye movement (Herzfeld et al., 2015; Hong et al., 2016), self-paced locomotion (Jelitai et al., 2016) and voluntary whisking (Chen et al., 2016), Purkinje cells show bidirectional modulation of their simple spike firing rates. Then a remaining, neglected, critical question is to measure whether climbing fiber-evoked Ca^{2+} influx is constrained to proximal dendrites in Purkinje cells showing decreased firing rates, as observed *in vitro* (Zagha et al., 2010; Otsu et al., 2014; Zang et al., 2018). Even if Ca^{2+} influx is still global in Purkinje cell dendrites, is it within the range of triggering LTP rather than LTD? In other words, does the directional change of Purkinje cell simple spike firing rates determine the polarity of parallel fiber synaptic strength changes, with LTD in "bursting" Purkinje cells, but LTP in "pause" Purkinje cells?

A recent study proposed synaptic plasticity rules that strikingly contradict the current consensus of plasticity induction to solve the credit assignment problem (Bouvier et al., 2018). In their new rule, parallel fiber stimulation requires both conjunctive perturbation (spontaneous) and post-erroneous climbing fiber signals to induce LTD. With only conjunctive perturbation or post-erroneous climbing fiber signals, parallel fiber synapses undergo LTP or no change. In theory, this new plasticity rule still works with the Ca^{2+} threshold-dependent plasticity rule (Coesmans et al., 2004), but obviously more experimental data are required to support this algorithm in motor learning, since existing oculomotor control data do not (Catz et al., 2005; Ke et al., 2009; Yang and Lisberger, 2014).

BRANCH-SPECIFIC DENDRITIC RESPONSES AND LEARNING

Conventionally, dendritic trees are thought to just receive synaptic inputs from presynaptic cells and to convey them to the soma. In recent years, more and more experimental data have uncovered local computation in neuronal dendrites (Branco and Häusser, 2010; Cichon and Gan, 2015). In Purkinje

cells, the parallel fiber synapses distributed on spiny dendrites undergo synaptic plasticity. The spatio-variability of dendritic Ca^{2+} influx determines the computational unit of climbing fiber responses and constrains the learning capacity of individual Purkinje cells. Although Ca^{2+} influx due to strong parallel fiber-triggered dendritic spikes is constrained to branchlets (Hartell, 1996; Rancz and Häusser, 2006), information about spatio-temporal patterns of climbing fiber-evoked dendritic responses has only become available in recent years. The amplitude of dendritic Ca^{2+} signals was first shown to increase with distance from the soma in anesthetized rats (Kitamura and Hausser, 2011). This can be explained either by increased surface-to-volume ratios or non-uniform distribution of Ca^{2+} channels with distance from the soma. In the physiologically detailed Purkinje cell model with homogeneous distributed Ca^{2+} channels, dendritic Ca^{2+} influx increases significantly with distance from the soma and shows significant variations in different branchlets at similar distances (Zang et al., 2018). As discussed above, the initiation of "out-of-territory" dendritic spikes on distal dendrites relies on the axial current from climbing fiber-depolarized proximal dendrites. The morphology-dependent ratio of spiny dendrite capacitance load to proximal climbing fiber input is uneven in Purkinje cell dendrites, which causes inhomogeneous excitability of individual branches. In agreement with this theoretical study, the spatiotemporal variability of dendritic spikes has also been observed in awake mice by voltage imaging (Roome and Kuhn, 2018). Many factors can enhance the intrinsic inhomogeneous excitability *in vivo*, including firing state-related availability of K^+ channels, concurrent synaptic input and compartment-specific dendritic excitability plasticity (Kitamura and Hausser, 2011; Ohtsuki et al., 2012; Zang et al., 2018). The significant spatio-temporal variability of dendritic Ca^{2+} influx implies that both LTP and LTD can occur coincidently at different dendritic branchlets of a Purkinje cell. This spatio-temporal variability can be fine-tuned to modulate the distribution of branchlet-specific synaptic changes, rather than a homogeneous change. Accordingly, the learning capacity of single Purkinje cells can be significantly increased, which may be necessary for complex and arbitrary movement learning (Bouvier et al., 2018).

THE OTHER SIDE OF THE SAME COIN—CLIMBING FIBERS AS MOTOR CLOCKS

In contrast to the idea of climbing fibers as teachers in the Marr-Albus-Ito theory, an alternative view of their role is to provide a "motor clock" function in the initiation and timing of movements (Welsh et al., 1995; Llinás et al., 1997). Olivary neurons exhibit subthreshold oscillations, and neighboring neurons are coupled by gap junctions to help synchronize their outputs (Leznik and Llinás, 2005). Each climbing fiber also forms synapses on 5–10 Purkinje cells along the parasagittal direction. All these factors facilitate synchronization of complex spikes among neighboring Purkinje cells and spatio-temporally organize the output of Purkinje cell "microzones" (targeting the same cerebellar nucleus neuron). The ability to initiate or modulate movement seems to depend on synchronization of complex spikes in the Purkinje cell "microzone" rather than changes of complex spike firing rates (Llinás et al., 1997; Hoogland et al., 2015). Powerful climbing fiber synaptic current guarantees reliable conversion from synchronous climbing fiber input ("timing" signal) to synchronous complex spikes in Purkinje cells. First, climbing fibers evoke complex spikes immediately, which fits perfectly the high temporal precision required for the cerebellum to initiate or coordinate muscles. Second, although complex spike duration and spikelet number vary significantly under different conditions, the timing of the first several spikelets is relatively constant (Warnaar et al., 2015; Zang et al., 2018). This enables the timing and rate of spikes of cerebellar nuclei neurons efficiently entrained by synchronized presynaptic inputs from their upstream Purkinje cell "microzone" (Person and Raman, 2011). The view of climbing fibers as "motor clocks" is supported by some recent data. By simultaneously recording cerebellar nuclei neuron activities and complex spikes, Tang et al. (2019) observed inhibition of cerebellar nuclei neurons after complex spikes, with the degree of inhibition dependent on the synchrony among complex spikes. Delayed and attenuated co-activation of complex spikes have also been suggested to cause changes in the timing and execution of both complex and reflex movements (Hoogland et al., 2015).

Is there any connection between the "motor clock" signal and instruction signal? The finding by Mathy et al. (2009) of climbing fiber bursting may well reconcile these two functions (**Figure 6**). The number of spikes in the climbing fiber burst depends on the phase of olivary subthreshold oscillations and can be read out by complex spike spikelet numbers and dendritic spikelet numbers in Purkinje cells. On one hand, the oscillatory phase of olivary neurons is converted to climbing fiber bursting and is then reliably transmitted to cerebellar nuclei neurons *via* complex spikes (Tang et al., 2019) to initiate or modulate movements. On the other hand, climbing fiber bursts can shift the probability of inducing short-term and long-term plasticity at parallel fiber synapses. However, this demonstrates what climbing fibers can do, rather than what they actually do. Further research is required to decipher whether the system is degenerate (Edelman and Gally, 2001), with both climbing fiber modes working simultaneously to improve motor performance, or whether the two modes are specific to particular cerebellar regions or distinct behaviors.

CONCLUSIONS

Despite the growing awareness of multisite learning (Gao et al., 2012), climbing fiber-induced LTD and LTP in the cerebellar cortex may still comprise the backbone of cerebellar learning, especially now that climbing fibers have been demonstrated to be a versatile instructor. The ongoing activity-dependent analog instruction signal undoubtedly increases the learning capacity of the cerebellum.

AUTHOR CONTRIBUTIONS

YZ wrote the initial draft and revised it. ED edited the draft and revised it.

ACKNOWLEDGMENTS

This work was supported by the Okinawa Institute of Science and Technology Graduate University.

REFERENCES

Albus, J. S. (1971). A theory of cerebellar function. *Math. Biosci.* 10, 25–61. doi: 10.1016/0025-5564(71)90051-4

Armstrong, D. M., and Rawson, J. A. (1979). Activity patterns of cerebellar cortical neurones and climbing fibre afferents in the awake cat. *J. Physiol.* 289, 425–448. doi: 10.1113/jphysiol.1979.sp012745

Bell, C. C., and Kawasaki, T. (1972). Relations among climbing fiber responses of nearby Purkinje cells. *J. Neurophysiol.* 35, 155–169. doi: 10.1152/jn.1972.35.2.155

Bouvier, G., Aljadeff, J., Clopath, C., Bimbard, C., Ranft, J., Blot, A., et al. (2018). Cerebellar learning using perturbations. *Elife* 7:e31599. doi: 10.7554/eLife.31599

Branco, T., and Häusser, M. (2010). The single dendritic branch as a fundamental functional unit in the nervous system. *Curr. Opin. Neurobiol.* 20, 494–502. doi: 10.1016/j.conb.2010.07.009

Callaway, J. C., Lasser-Ross, N., and Ross, W. N. (1995). IPSPs strongly inhibit climbing fiber-activated [Ca2+]i increases in the dendrites of cerebellar Purkinje neurons. *J. Neurosci.* 15, 2777–2787. doi: 10.1523/jneurosci.15-04-02777.1995

Catz, N., Dicke, P. W., and Thier, P. (2005). Cerebellar complex spike firing is suitable to induce as well as to stabilize motor learning. *Curr. Biol.* 15, 2179–2189. doi: 10.1016/j.cub.2005.11.037

Chen, S., Augustine, G. J., and Chadderton, P. (2016). The cerebellum linearly encodes whisker position during voluntary movement. *Elife* 5:e10509. doi: 10.7554/elife.10509

Chen, S., Augustine, G. J., and Chadderton, P. (2017). Serial processing of kinematic signals by cerebellar circuitry during voluntary whisking. *Nat. Commun.* 8:232. doi: 10.1038/s41467-017-00312-1

Cichon, J., and Gan, W. B. (2015). Branch-specific dendritic Ca^{2+} spikes cause persistent synaptic plasticity. *Nature* 520, 180–185. doi: 10.1038/nature14251

Coesmans, M., Weber, J. T., De Zeeuw, C. I., and Hansel, C. (2004). Bidirectional parallel fiber plasticity in the cerebellum under climbing fiber control. *Neuron* 44, 691–700. doi: 10.1016/j.neuron.2004.10.031

Crill, W. E. (1970). Unitary multiple-spiked responses in cat inferior olive nucleus. *J. Neurophysiol.* 33, 199–209. doi: 10.1152/jn.1970.33.2.199

Davie, J. T., Clark, B. A., and Häusser, M. (2008). The origin of the complex spike in cerebellar Purkinje cells. *J. Neurosci.* 28, 7599–7609. doi: 10.1523/jneurosci.0559-08.2008

De Schutter, E. (1995). Cerebellar long-term depression might normalize excitation of purkinje-cells: a hypothesis. *Trends Neurosci.* 18, 291–295. doi: 10.1016/0166-2236(95)93916-l

Eccles, J. C., Ito, M., and Szentágothai, J. N. (1967). *The Cerebellum As A Neuronal Machine.* Berlin, New York, NY: Springer-Verlag.

Eccles, J. C., Llinás, R., and Sasaki, K. (1966). The excitatory synaptic action of climbing fibres on the Purkinje cells of the cerebellum. *J. Physiol.* 182, 268–296. doi: 10.1113/jphysiol.1966.sp007824

Edelman, G. M., and Gally, J. A. (2001). Degeneracy and complexity in biological systems. *Proc. Natl. Acad. Sci. U S A* 98, 13763–13768. doi: 10.1073/pnas.231499798

Gaffield, M. A., Bonnan, A., and Christie, J. M. (2019). Conversion of graded presynaptic climbing fiber activity into graded postsynaptic Ca^{2+} signals by purkinje cell dendrites. *Neuron* 102, 762–769. doi: 10.1016/j.neuron.2019.03.010

Gallimore, A. R., Kim, T., Tanaka-Yamamoto, K., and De Schutter, E. (2018). Switching on depression and potentiation in the cerebellum. *Cell Rep.* 22, 722–733. doi: 10.1016/j.celrep.2017.12.084

Gao, Z., van Beugen, B. J., and De Zeeuw, C. I. (2012). Distributed synergistic plasticity and cerebellar learning. *Nat. Rev. Neurosci.* 13, 619–635. doi: 10.1038/nrn3312

Gilbert, P. F. (1976). Simple spike frequency and the number of secondary spikes in the complex spike of the cerebellar Purkinje cell. *Brain Res.* 114, 334–338. doi: 10.1016/0006-8993(76)90676-4

Grangeray-Vilmint, A., Valera, A. M., Kumar, A., and Isope, P. (2018). Short-term plasticity combines with excitation-inhibition balance to expand cerebellar purkinje cell dynamic range. *J. Neurosci.* 38, 5153–5167. doi: 10.1523/jneurosci.3270-17.2018

Grasselli, G., and Hansel, C. (2014). Cerebellar long-term potentiation: cellular mechanisms and role in learning. *Int. Rev. Neurobiol.* 117, 39–51. doi: 10.1016/b978-0-12-420247-4.00003-8

Gutierrez-Castellanos, N., Da Silva-Matos, C. M., Zhou, K. K., Canto, C. B., Renner, M. C., Koene, L. M. C., et al. (2017). Motor learning requires Purkinje cell synaptic potentiation through activation of AMPA-receptor subunit GluA3. *Neuron* 93, 409–424. doi: 10.1016/j.neuron.2016.11.046

Hansel, C., and Linden, D. J. (2000). Long-term depression of the cerebellar climbing fiber—Purkinje neuron synapse. *Neuron* 26, 473–482. doi: 10.1016/s0896-6273(00)81179-4

Hartell, N. A. (1996). Strong activation of parallel fibers produces localized calcium transients and a form of LTD that spreads to distant synapses. *Neuron* 16, 601–610. doi: 10.1016/s0896-6273(00)80079-3

Hashimoto, K., and Kano, M. (2003). Functional differentiation of multiple climbing fiber inputs during synapse elimination in the developing cerebellum. *Neuron* 38, 785–796. doi: 10.1016/s0896-6273(03)00298-8

Herzfeld, D. J., Kojima, Y., Soetedjo, R., and Shadmehr, R. (2015). Encoding of action by the Purkinje cells of the cerebellum. *Nature* 526, 439–442. doi: 10.1038/nature15693

Hong, S., Negrello, M., Junker, M., Smilgin, A., Thier, P., and De Schutter, E. (2016). Multiplexed coding by cerebellar Purkinje neurons. *Elife* 5:e13810. doi: 10.7554/elife.13810

Hoogland, T. M., De Gruijl, J. R., Witter, L., Canto, C. B., and De Zeeuw, C. I. (2015). Role of synchronous activation of cerebellar Purkinje cell ensembles in multi-joint movement control. *Curr. Biol.* 25, 1157–1165. doi: 10.1016/j.cub.2015.03.009

Hounsgaard, J., and Midtgaard, J. (1989). Synaptic control of excitability in turtle cerebellar Purkinje cells. *J. Physiol.* 409, 157–170. doi: 10.1113/jphysiol.1989.sp017490

Ito, M., and Kano, M. (1982). Long-lasting depression of parallel fiber Purkinje-cell transmission induced by conjunctive stimulation of parallel fibers and climbing fibers in the cerebellar cortex. *Neurosci. Lett.* 33, 253–258. doi: 10.1016/0304-3940(82)90380-9

Jelitai, M., Puggioni, P., Ishikawa, T., Rinaldi, A., and Duguid, I. (2016). Dendritic excitation-inhibition balance shapes cerebellar output during motor behaviour. *Nat. Commun.* 7:13722. doi: 10.1038/ncomms13722

Kakegawa, W., Katoh, A., Narumi, S., Miura, E., Motohashi, J., Takahashi, A., et al. (2018). Optogenetic control of synaptic AMPA receptor endocytosis reveals roles of LTD in motor learning. *Neuron* 99, 985.e6–998.e6. doi: 10.1016/j.neuron.2018.07.034

Ke, M. C., Guo, C. C., and Raymond, J. L. (2009). Elimination of climbing fiber instructive signals during motor learning. *Nat. Neurosci.* 12, 1171–1179. doi: 10.1038/nn.2366

Khaliq, Z. M., and Raman, I. M. (2005). Axonal propagation of simple and complex spikes in cerebellar Purkinje neurons. *J. Neurosci.* 25, 454–463. doi: 10.1523/jneurosci.3045-04.2005

Kimpo, R. R., Rinaldi, J. M., Kim, C. K., Payne, H. L., and Raymond, J. L. (2014). Gating of neural error signals during motor learning. *Elife* 3:e02076. doi: 10.7554/elife.02076

Kitamura, K., and Hausser, M. (2011). Dendritic calcium signaling triggered by spontaneous and sensory-evoked climbing fiber input to cerebellar Purkinje cells *in vivo*. *J. Neurosci.* 31, 10847–10858. doi: 10.1523/jneurosci.2525-10.2011

Kitazawa, S., Kimura, T., and Yin, P. B. (1998). Cerebellar complex spikes encode both destinations and errors in arm movements. *Nature* 392, 494–497. doi: 10.1038/33141

Leznik, E., and Llinás, R. (2005). Role of gap junctions in synchronized neuronal oscillations in the inferior olive. *J. Neurophysiol.* 94, 2447–2456. doi: 10.1152/jn.00353.2005

Llinás, R., and Sugimori, M. (1980). Electrophysiological properties of *in vitro* Purkinje cell dendrites in mammalian cerebellar slices. *J. Physiol.* 305, 197–213. doi: 10.1113/jphysiol.1980.sp013358

Llinas, R., Bloedel, J. R., and Hillman, D. E. (1969). Functional characterization of neuronal circuitry of frog cerebellar cortex. *J. Neurophysiol.* 32, 847–870. doi: 10.1152/jn.1969.32.6.847

Llinás, R., Lang, E. J., and Welsh, J. P. (1997). The cerebellum, LTD, and memory: alternative views. *Learn. Mem.* 3, 445–455. doi: 10.1101/lm.3.6.445

Loewenstein, Y., Mahon, S., Chadderton, P., Kitamura, K., Sompolinsky, H., Yarom, Y., et al. (2005). Bistability of cerebellar Purkinje cells modulated by sensory stimulation. *Nat. Neurosci.* 8, 202–211. doi: 10.1038/nn1393

Luque, N. R., Naveros, F., Carrillo, R. R., Ros, E., and Arleo, A. (2019). Spike burst-pause dynamics of Purkinje cells regulate sensorimotor adaptation. *PLoS Comput. Biol.* 15:e1006298. doi: 10.1371/journal.pcbi.1006298

Marr, D. (1969). A theory of cerebellar cortex. *J. Physiol.* 202, 437–470. doi: 10.1113/jphysiol.1969.sp008820

Mathy, A., Ho, S. S., Davie, J. T., Duguid, I. C., Clark, B. A., and Häusser, M. (2009). Encoding of oscillations by axonal bursts in inferior olive neurons. *Neuron* 62, 388–399. doi: 10.1016/j.neuron.2009.03.023

Minsky, M. (1961). "Steps toward artificial intelligence," in *Proceedings of the Institute of Radio Engineers (IEEE)*, 8–30.

Miyakawa, H., Lev-Ram, V., Lasser-Ross, N., and Ross, W. N. (1992). Calcium transients evoked by climbing fiber and parallel fiber synaptic inputs in guinea pig cerebellar Purkinje neurons. *J. Neurophysiol.* 68, 1178–1189. doi: 10.1152/jn.1992.68.4.1178

Monsivais, P., Clark, B. A., Roth, A., and Hausser, M. (2005). Determinants of action potential propagation in cerebellar Purkinje cell axons. *J. Neurosci.* 25, 464–472. doi: 10.1523/JNEUROSCI.3871-04.2005

Najafi, F., Giovannucci, A., Wang, S. S., and Medina, J. F. (2014a). Coding of stimulus strength *via* analog calcium signals in Purkinje cell dendrites of awake mice. *Elife* 3:e03663. doi: 10.7554/elife.03663

Najafi, F., Giovannucci, A., Wang, S. S., and Medina, J. F. (2014b). Sensory-driven enhancement of calcium signals in individual Purkinje cell dendrites of awake mice. *Cell Rep.* 6, 792–798. doi: 10.1016/j.celrep.2014.02.001

Najafi, F., and Medina, J. F. (2013). Beyond "all-or-nothing" climbing fibers: graded representation of teaching signals in Purkinje cells. *Front. Neural Circuits* 7:115. doi: 10.3389/fncir.2013.00115

Nietz, A. K., Vaden, J. H., Coddington, L. T., Overstreet-Wadiche, L., and Wadiche, J. I. (2017). Non-synaptic signaling from cerebellar climbing fibers modulates Golgi cell activity. *Elife* 6:e29215. doi: 10.7554/elife.29215

Ohtsuki, G., Piochon, C., Adelman, J. P., and Hansel, C. (2012). SK2 channel modulation contributes to compartment-specific dendritic plasticity in cerebellar Purkinje cells. *Neuron* 75, 108–120. doi: 10.1016/j.neuron.2012.05.025

Otsu, Y., Marcaggi, P., Feltz, A., Isope, P., Kollo, M., Nusser, Z., et al. (2014). Activity-dependent gating of calcium spikes by A-type K^+ channels controls climbing fiber signaling in Purkinje cell dendrites. *Neuron* 84, 137–151. doi: 10.1016/j.neuron.2014.08.035

Palay, S. L., and Chan-Palay, V. (1974). *Cerebellar Cortex: Cytology and Organization.* Berlin, Heidelberg, New York, NY: Springer.

Person, A. L., and Raman, I. M. (2011). Purkinje neuron synchrony elicits time-locked spiking in the cerebellar nuclei. *Nature* 481, 502–505. doi: 10.1038/nature10732

Piochon, C., Irinopoulou, T., Brusciano, D., Bailly, Y., Mariani, J., and Levenes, C. (2007). NMDA receptor contribution to the climbing fiber response in the adult mouse Purkinje cell. *J. Neurosci.* 27, 10797–10809. doi: 10.1523/jneurosci.2422-07.2007

Piochon, C., Titley, H. K., Simmons, D. H., Grasselli, G., Elgersma, Y., and Hansel, C. (2016). Calcium threshold shift enables frequency-independent control of plasticity by an instructive signal. *Proc. Natl. Acad. Sci. U S A* 113, 13221–13226. doi: 10.1073/pnas.1613897113

Pugh, J. R., and Raman, I. M. (2006). Potentiation of mossy fiber EPSCs in the cerebellar nuclei by NMDA receptor activation followed by postinhibitory rebound current. *Neuron* 51, 113–123. doi: 10.1016/j.neuron.2006.05.021

Rancz, E. A., and Häusser, M. (2006). Dendritic calcium spikes are tunable triggers of cannabinoid release and short-term synaptic plasticity in cerebellar Purkinje neurons. *J. Neurosci.* 26, 5428–5437. doi: 10.1523/jneurosci.5284-05.2006

Regehr, W. G. (2012). Short-term presynaptic plasticity. *Cold Spring Harb. Perspect. Biol.* 4:a005702. doi: 10.1101/cshperspect.a005702

Rokni, D., Tal, Z., Byk, H., and Yarom, Y. (2009). Regularity, variability and bi-stability in the activity of cerebellar purkinje cells. *Front. Cell. Neurosci.* 3:12. doi: 10.3389/neuro.03.012.2009

Romano, V., De Propris, L., Bosman, L. W. J., Warnaar, P., Ten Brinke, M. M., Lindeman, S., et al. (2018). Potentiation of cerebellar Purkinje cells facilitates whisker reflex adaptation through increased simple spike activity. *Elife* 7:e38852. doi: 10.7554/elife.38852

Roome, C. J., and Kuhn, B. (2018). Simultaneous dendritic voltage and calcium imaging and somatic recording from Purkinje neurons in awake mice. *Nat. Commun.* 9:3388. doi: 10.1038/s41467-018-05900-3

Roth, A., and Häusser, M. (2001). Compartmental models of rat cerebellar Purkinje cells based on simultaneous somatic and dendritic patch-clamp recordings. *J. Physiol.* 535, 445–472. doi: 10.1111/j.1469-7793.2001.00445.x

Rowan, M. J. M., Bonnan, A., Zhang, K., Amat, S. B., Kikuchi, C., Taniguchi, H., et al. (2018). Graded control of climbing-fiber-mediated plasticity and learning by inhibition in the cerebellum. *Neuron* 99, 999.e6–1015.e6. doi: 10.1016/j.neuron.2018.07.024

Sakurai, M. (1987). Synaptic modification of parallel fibre-Purkinje cell transmission in *in vitro* guinea-pig cerebellar slices. *J. Physiol.* 394, 463–480. doi: 10.1113/jphysiol.1987.sp016881

Schonewille, M., Gao, Z., Boele, H. J., Veloz, M. F., Amerika, W. E., Simek, A. A., et al. (2011). Reevaluating the role of LTD in cerebellar motor learning. *Neuron* 70, 43–50. doi: 10.1016/j.neuron.2011.02.044

Schonewille, M., Khosrovanl, S., Winkelman, B. H. J., Hoebeek, F. E., De Jeu, M. T. G., Larsen, I. M., et al. (2006). Purkinje cells in awake behaving animals operate at the upstate membrane potential. *Nat. Neurosci.* 9, 459–461. doi: 10.1038/nn0406-459

Steuber, V., Mittmann, W., Hoebeek, F. E., Silver, R. A., De Zeeuw, C. I., Häusser, M., et al. (2007). Cerebellar LTD and pattern recognition by Purkinje cells. *Neuron* 54, 121–136. doi: 10.1016/j.neuron.2007.03.015

Suvrathan, A., and Raymond, J. L. (2018). Depressed by learning-heterogeneity of the plasticity rules at parallel fiber synapses onto Purkinje cells. *Cerebellum* 17, 747–755. doi: 10.1007/s12311-018-0968-8

Suvrathan, A., Payne, H. L., and Raymond, J. L. (2016). Timing rules for synaptic plasticity matched to behavioral function. *Neuron* 92, 959–967. doi: 10.1016/j.neuron.2016.10.022

Tal, Z., Chorev, E., and Yarom, Y. (2008). State-dependent modification of complex spike waveforms in the cerebellar cortex. *Cerebellum* 7, 577–582. doi: 10.1007/s12311-008-0058-4

Tang, T., Blenkinsop, T. A., and Lang, E. J. (2019). Complex spike synchrony dependent modulation of rat deep cerebellar nuclear activity. *Elife* 8:e40101. doi: 10.7554/elife.40101

Tang, T., Xiao, J., Suh, C. Y., Burroughs, A., Cerminara, N. L., Jia, L., et al. (2017). Heterogeneity of Purkinje cell simple spike-complex spike interactions: zebrin- and non-zebrin-related variations. *J. Physiol.* 595, 5341–5357. doi: 10.1113/jp274252

Titley, H. K., Kislin, M., Simmons, D. H., Wang, S. S., and Hansel, C. (2019). Complex spike clusters and false-positive rejection in a cerebellar supervised learning rule. *J. Physiol.* 597, 4387–4406. doi: 10.1113/jp278502

Warnaar, P., Couto, J., Negrello, M., Junker, M., Smilgin, A., Ignashchenkova, A., et al. (2015). Duration of Purkinje cell complex spikes increases with their firing frequency. *Front. Cell. Neurosci.* 9:122. doi: 10.3389/fncel.2015.00122

Welsh, J. P., Lang, E. J., Sugihara, I., and Llinás, R. (1995). Dynamic organization of motor control within the olivocerebellar system. *Nature* 374, 453–457. doi: 10.1038/374453a0

Yamaguchi, K., Itohara, S., and Ito, M. (2016). Reassessment of long-term depression in cerebellar Purkinje cells in mice carrying mutated GluA2 C terminus. *Proc. Natl. Acad. Sci. U S A* 113, 10192–10197. doi: 10.1073/pnas.1609957113

Yang, Y., and Lisberger, S. G. (2014). Purkinje-cell plasticity and cerebellar motor learning are graded by complex-spike duration. *Nature* 510, 529–532. doi: 10.1038/nature13282

Zagha, E., Manita, S., Ross, W. N., and Rudy, B. (2010). Dendritic Kv3.3 potassium channels in cerebellar Purkinje cells regulate generation and spatial dynamics of dendritic Ca^{2+} spikes. *J. Neurophysiol.* 103, 3516–3525. doi: 10.1152/jn.00982.2009

Zamora Chimal, C. G., and De Schutter, E. (2018). Ca^{2+} requirements for long-term depression are frequency sensitive in purkinje cells. *Front. Mol. Neurosci.* 11:438. doi: 10.3389/fnmol.2018.00438

Zang, Y., Dieudonné, S., and De Schutter, E. (2018). Voltage- and branch-specific climbing fiber responses in purkinje cells. *Cell Rep.* 24, 1536–1549. doi: 10.1016/j.celrep.2018.07.011

Conflict of Interest: The authors declare that the research was conducted in the absence of any commercial or financial relationships that could be construed as a potential conflict of interest.

frontiers in Systems Neuroscience

PERSPECTIVE
published: 09 October 2019
doi: 10.3389/fnsys.2019.00050

Delayed Complex Spike Response Evoked by Conditioned Stimulus Encodes Movement Onset Time and Is Determined by Intrinsic Inferior Olive Properties

Yasmin Yarden-Rabinowitz[1,2]* *and Yosef Yarom*[1,2]

[1]*Department of Neurobiology, Institute of Life Sciences, Hebrew University of Jerusalem, Jerusalem, Israel,* [2]*Edmond & Lily Safra Center for Brain Sciences, Hebrew University of Jerusalem, Jerusalem, Israel*

Recent studies demonstrate that after classical conditioning the conditioned stimulus (CS) triggers a delayed complex spike. This new finding revolutionizes our view on the role of complex spike activity. The classical view of the complex spike as an error signal has been replaced by a signal that encodes for expectation, prediction and reward. In this brief perspective, we review some of these works, focusing on the characteristic delay of the response (~80 ms), its independence on the time interval between CS and the unconditioned stimulus (US) and its relationship to movement onset. In view of these points, we suggest that the generation of complex spike activity following learning, encodes for timing of movements onset. We then provide original data recorded from Purkinje and cerebellar nuclei neurons, demonstrating that delayed complex spike activity is an intrinsic property of the cerebellar circuit. We, therefore, suggest that learning of classical conditioning involves modulation of cerebellar circuitry where timing is provided by the inferior olive and the movement kinematic is delivered by the cerebellar nuclei projection neurons.

Keywords: cerebellum, classical conditioning, complex spike, inferior olive, Purkinje neurons

OPEN ACCESS

Edited by:
Nadia Cerminara,
University of Bristol, United Kingdom

Reviewed by:
José M. Delgado-García,
Universidad Pablo de Olavide, Spain
Jianfeng Sui,
Department of Physiology, Third Military Medical University, China

***Correspondence:**
Yasmin Yarden-Rabinowitz
yasmin.yarden@mail.huji.ac.il

Received: *02 June 2019*
Accepted: *09 September 2019*
Published: *09 October 2019*

Citation:
Yarden-Rabinowitz Y and Yarom Y (2019) Delayed Complex Spike Response Evoked by Conditioned Stimulus Encodes Movement Onset Time and Is Determined by Intrinsic Inferior Olive Properties. Front. Syst. Neurosci. 13:50. doi: 10.3389/fnsys.2019.00050

INTRODUCTION

Classical conditioning is a wildly studied paradigm in cerebellar research. Numerous studies have shown that the conditioned stimulus (CS) is transmitted by mossy fibers (MFs) to the cerebellar cortex whereas the unconditioned stimulus (US) is delivered by climbing fibers. Furthermore, the probability for climbing fiber response to the US is significantly reduced after learning. This learning-dependent modification gave rise to the idea that complex spike is an error signal. In recent years, new evidence show that after learning complex spikes appear after the CS and before the US (Nicholson and Freeman, 2003; Ohmae and Medina, 2015; ten Brinke et al., 2015, 2017, 2019), suggesting that the complex spike evoked by the CS provides additional information (Ohmae and Medina, 2015; Heffley et al., 2018; Popa et al., 2019; Streng et al., 2018).

Ohmae and Medina (2015) and ten Brinke et al. (2019) both recorded Purkinje neuron (PN) activity in head restrained mice before and after eye-blink conditioning. PNs were considered to be eyelid-related if they reliably responded with complex spikes to the US. In both studies, after training the CS was followed by a complex spike with a delay of ~80 ms (**Figures 1A1–A3**). Moreover, Ohmae and Medina (2015) show that the delay to the complex spike is independent of the interval between the CS and the US (**Figure 1B**) and this is further supported by the work of

ten Brinke et al. (2019) that used a different interval between the CS and the US. Together, these two studies show that the delay of the complex spike evoked by the CS is not related to the ***timing*** of the US.

In our view, this interesting finding sets the stage for two questions: first, of course, is what is this signal telling the brain? Is it a prediction signal that an US is about to occur? Is it a reward signal, if you behave you will avoid unpleasantness? Or is it an instruction signal: start to move now or else! Second, what and how is the circuit modified during learning to enable a complex spike response after the CS. Ohmae and Medina (2015) addressed the first question and suggested that before training the complex spike signals the novelty of a stimulus and after training it serves as a prediction error signal. ten Brinke et al. (2017) addressed the second question and suggested that the formation of MF axon collaterals is the necessary circuit modulation responsible for the generation of the CS evoked complex spike (ten Brinke et al., 2017).

In this brief perspective, we scan trough classical conditioning studies, focusing on two points. First, the initiation of movement that like the timing of the CS evoked complex spikes, is independent of the CS-US interval. Second, the kinematics of the movement is highly correlated with both the reduction in firing of PN and the increased firing of cerebellar nuclei (CN) neurons and that both are modified by the CS-US interval. We then show some results demonstrating that in anesthetized naïve animals delayed complex spikes can be elicited by stimulating either the MFs or the inferior olive (IO). Finally, we propose that the learning of classical conditioning involves modulation of the cerebellar circuitry where the climbing fibers provide timing of movement **onset** while PN *via* cerebellar projection neurons, provide the necessary information for movement kinematics.

CEREBELLAR ACTIVITY DURING LEARNED CONDITIONED RESPONSE

Cerebellar Activity Preceding Movement Onset

A thorough analysis of the eyelid movement during classical conditioning have been performed in many studies (Chettih et al., 2011; Halverson et al., 2015; ten Brinke et al., 2017), focusing on the time of the peak response and/or the time of maximal velocity or acceleration. Only few studies directly address the time of movement **onset**. On one hand this is rather surprising as there is a general consensus that the cerebellum is deeply involved in movement coordination, namely providing timing information. On the other hand, successful learning implies that the eyelid will close at the time of the US and therefore time of maximal closer seems more appropriate. However, we carefully examined published traces of eyelid movements and the impression is that the onset time of the movement is independent of the CS-US interval and seems to occur at a delay of ∼100 ms from the CS (Heiney et al., 2014; Ohmae and Medina, 2015; Siegel et al., 2015; ten Brinke et al., 2015). This impression is supported by the work of Chettih et al. (2011), one of the few works that studied the kinematic of the response. In their study they conclude that "*. . . mice appear to achieve precise timing by regulating the velocity, but not the onset latency of the eyelid movement.*" This is demonstrated in **Figure 1C**, where traces of eyelid position in four different CS-US intervals are superimposed. Indeed, the movement onset latency (∼100 ms) is independent of the CS-US interval. In a later work Ohmae and Medina (2015) differentiate early and late onset of movement (**Figure 1D**) where movement onset was defined by a threshold of eyelid velocity. However, careful examination of their results reveals that the time of movement onset of both early and late response is very similar. Thus, it seems likely that after learning, both the complex spike and the onset time of the eyelid movement occur after a relatively constant delay that is independent of the CS-US interval. Consequently, it is tempting to suggest that the CS evoked complex spike actually provide timing for movement initiation. This possibility is further supported by the results presented in **Figure 1B**, demonstrating a rear case where two different CS-US intervals where used and the movement onset time of the longer interval is somewhat delayed. Surprisingly, the time of the complex spike is also delayed and to a similar extent (Movement onset delayed by ∼15 ms and peak of histogram is delayed by a single 10 ms bin).

Cerebellar Control of Movement Kinematics

Large body of electrophysiological studies demonstrate that learning of eye blink response is associated with a reduction in simple spike activity of PN (ten Brinke et al., 2015; Jirenhed and Hesslow, 2016; Jirenhed et al., 2017; Halverson et al., 2018). Whether it is due to long term depression of parallel fibers input (Alba et al., 1994; Kim and Thompson, 1997; Koekkoek et al., 2003) or increase activity of molecular layer inhibitory interneurons (ten Brinke et al., 2015) or both, is still debated (Schonewille et al., 2011), but the relationship with movement kinematic is highly correlated. This is best demonstrated in the work of Mauk and his colleagues (Halverson et al., 2015) where the reduction in PN simple spike activity was correlated with the movement kinematics. An example shown in **Figure 1E**, where PN simple spike activity was measured in four different CS-US intervals. It is clear that the slower movement (longer CS-US interval) is associated with slower reduction in PN firing. However, the reduction in simple spike activity starts at the same delay from the CS (∼90 ms) and again independent of the CS-US interval.

The reduction in simple spike firing should affect the firing of CN projection neurons. Indeed, ten Brinke et al. (2019) characterized the firing pattern of CN in response to CS. As shown in **Figures 1F1,F2** the CN neurons respond to CS with a characteristic short pause in firing that occurs after a delay of 70–100 ms and is followed by an increase in firing rate that lasts up to the US and beyond, highly correlated with the movement parameters. They suggest that the pause elicits rebound excitation that has been shown to mediate motor activity (Witter et al., 2013). However, the pause seems identical while the firing rate is highly variable along with the movement, suggesting a significant contribution from the reduction in PN simple spike activity. The interesting

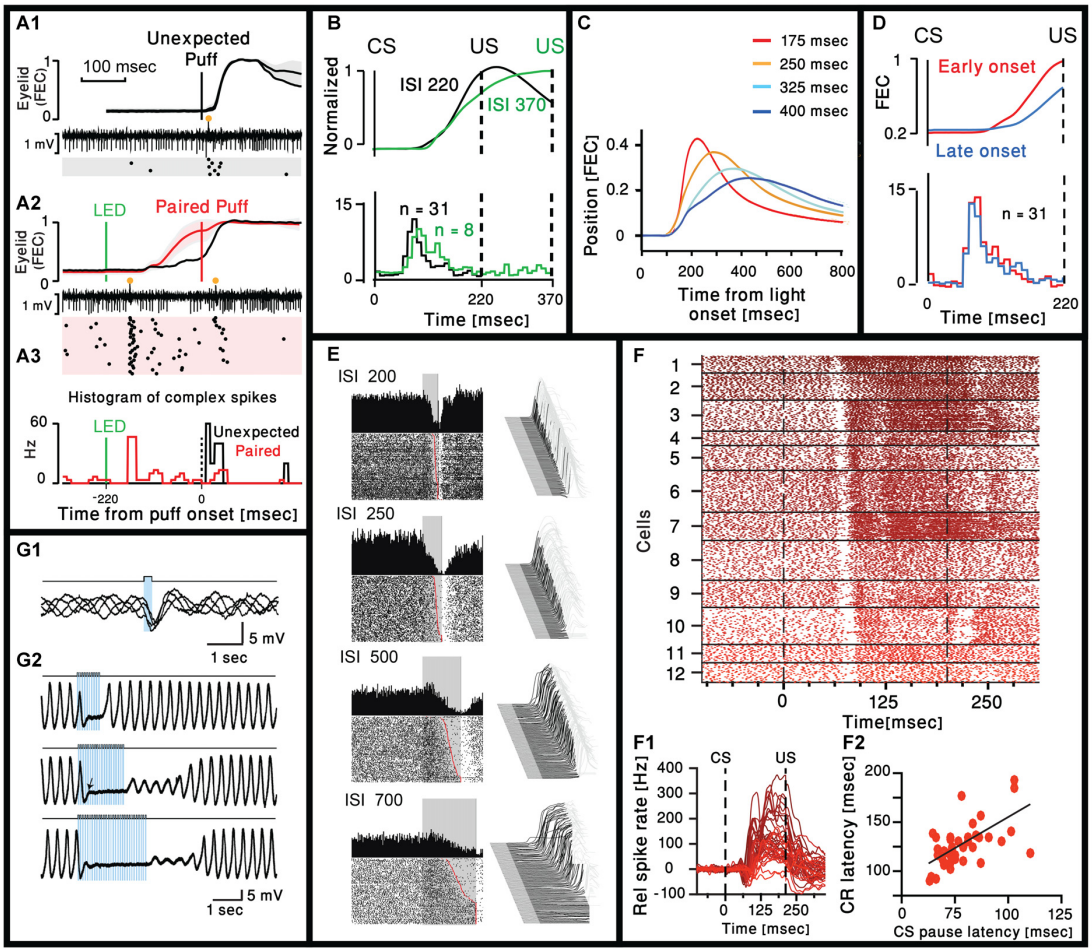

FIGURE 1 | Cerebellar activity after eye-blink conditioning and related movement kinematics. **(A1)** Eyelid movements (FEC, fraction eyelid closure, presenting mean ± standard deviation, SD as shaded region) and example of simultaneously recorded Purkinje neuron (PN) activity in trials with unexpected periocular air puff. Complex spikes are marked with orange circle and their corresponding raster plot is presented below. **(A2)** Similar to **(A1)** but using paired LED and periocular air puff. **(A3)** Peristimulus time histograms (bin size = 10 ms) for the complex spikes fired in the trials corresponding to the two raster plots in **(A1)** and (**A2**; Ohmae and Medina, 2015). **(B)** Upper panel: normalized eyelid traces. Lower panel: comparison of population-averaged complex spike activity in mice trained with a 220-ms inter spike interval (ISI 220) and a mouse trained with a 370-ms ISI (ISI 370). Adapted from Ohmae and Medina (2015). **(C)** Average eyelid position, for mice trained with four different ISIs. Adapted from Chettih et al. (2011). **(D)** Upper panel: normalized eyelid traces. Lower panel: comparison of population-averaged complex spike activity in trials with early-onset and late-onset CR movements. Numbers in parentheses indicate the number of cells recorded. Adapted from Ohmae and Medina (2015). **(E)** Representative examples of eyelid (Right) and Purkinje recordings during four behavioral conditions that involved single ISIs of 200, 250, 500 and 700 ms. For each panel, a waterfall plot of all behavioral responses in the session is shown at right. For these plots, each sweep represents the response from an individual trial, first trial in front. Upward deflection represents closure of the eyelids. For each sweep the pre-conditioned stimulus (CS) portion is shown in dark gray, the time during which the CS was present is shown in black, with the post-unconditioned stimulus (US) portion of each response shown in light gray. With this arrangement, all eyelid responses during the black portions of the trace are CRs. The average response during the paired CS-US trials over the entire session is shown as a single sweep above the raster plots. For the raster plots, where the first trial is on the bottom row, each dot represents the simple-spike recording from that PN. The trials are aligned such that the CS duration is shown by the gray rectangle. These data are from four different PNs and their responses are representative of those observed for the four different ISIs. Adapted from Halverson et al. (2015). **(F1)** Combined raster plot for 12 CN neurons, ordered by the latency of their CS pause in spike activity. **(F2)** Relative spike rates corresponding to the cells shown in **(F1)**. **(F3)** CS pause latency plotted against the latency at which the CR passes 5% eyelid closure for 45 cells (ten Brinke et al., 2017). **(G1)** Superimposed voltage traces from an oscillating IO neuron. Single pulse of light elicits an IPSP in different phases of the subthreshold oscillations. **(G2)**. Three traces with trains of light stimulation given at 12.5 Hz for three different durations (0.8, 1.6 and 2.4 s). Sub-threshold oscillations were blocked for the entire duration of the train. With longer trains, the complete recovery of the sub-threshold oscillations amplitude occurs after variable delays (Lefler et al., 2014).

observation is that delay to the pause is highly correlated with movement latency (**Figure 1F3**), thus strongly supporting the possibility that complex spikes triggered by the CS encode movement initiation.

Summary and Suggestions

Summarizing this brief review demonstrates that classical conditioning is associated with the appearance of a complex spike in response to the CS. All these studies agree that

these findings argue against the error signal paradigm and propose an additional or alternative role for the complex spike. We focus our review on the movement kinematic, providing evidence, whereas movement velocity is higher at shorter CS-US intervals, and movement initiation is independent of the interval. Thus, we propose that cerebellar learning of classical conditioning involve two mechanisms: learning to initiate a movement and learning the kinematics of the movement. The CS evoked complex spike signals movement onset that occurs 20 ms after the complex spike. This delay can easily be accounted for by the path from the CN neurons to the motor system that activates the eyelid muscles. The decrease in simple spike activity and the resultant increase activity of CN neurons control movement kinematics, where longer intervals are associated with slower movement, insuring eyelid closer at the right time.

CEREBELLAR CIRCUITRY ENABLING CS EVOKED DELAYED COMPLEX SPIKE RESPONSE

Understanding the circuitry that is responsible for the CS evoked complex spikes shall pave the way to decipher at least one aspect of the learning mechanisms, the timing of movement initiation. The two main inputs to the cerebellum are the MFs originating in the pontine nucleus, and the climbing fibers, originating in the IO. It is commonly accepted that the CS mainly activates MFs and that the US primarily activates the IO. Thus, the appearance of a complex spike in response to a CS represents changes within the olivo-cerebellar system.

In their work, ten Brinke et al. (2019) review different circuit pathways that may explain the circuit modifications giving rise to the CS evoked delayed complex spike. Their main suggestion is that during learning there is an outgrowth of MF collaterals to the CN (Boele et al., 2013). Thus, after learning, the MFs that are activated by the CS strongly activate specific CN projection neurons. These CN neurons activate the IO indirectly *via* the mesodiencephalic junction (MDJ). They support this hypothesis by showing that electrical stimulation in the CN can elicit EPSPs in IO neurons with a delay of 38.2 ± 14.2 ms (Bazzigaluppi et al., 2012). Although this suggestion is indeed intriguing, it requires synaptic specificity that has not been demonstrated. Moreover, if learning involves generation of new connections, how can it explain the observed fast extinction? (Medina et al., 2002). In addition, the delay from CN stimulation to the generation of complex spike is insuffcient to account for the 80 ms delay observed. Even if we add about 15 ms to account for the delay between the CS and the activation of the CN and 5 ms for the delay between the IO and PN, we are still too short.

We, therefore, suggest that the generation of the delayed complex spike reflects changes within the CN, particularly in the inhibitory projection neurons, and that the delayed complex spike is due to resetting of the olivary activity by the inhibitory input. To examine this possibility, we characterized the responses of PN and CN neurons to either MF or IO stimulation in anesthetized (Ketamine/Xylazine) mice. The MF and the IO were either electrically or optogenetically stimulated, the MF at the medial cerebellar peduncle and the IO was directly stimulated.

Recording from PNs reveals that as expected, stimulating the MF triggered simple spikes that appear after a delay of 4.75 ± 0.89 ms (n = 8). Interestingly, similar to the work of Bazzigaluppi et al. (2012), on some occasions, this response was followed by a complex spike after a delay of 37.56 ± 7.74 ms (n = 3, **Figure 2A**). This relatively prolonged delay, is likely to represent recurrent circuitry *via* the MDJ (see **Figure 2B**) as suggested by ten Brinke et al. (2019). However, as stated above, it can not account for the 80 ms delay of complex spikes evoked by the CS (see table in **Figure 2B**). Similarly, stimulating the IO resulted in direct activation of the climbing fibers evoking complex spikes after a short delay (5.15 ± 1.23 ms, **Figure 2C1**). Unexpectedly, in several cases an additional complex spike appeared after prolonged delay of ∼75 ms (**Figure 2C2**, n = 7; mean ± standard deviation 76.22 ± 17.25 ms). This delayed response was observed also in PNs that did not directly respond to the stimulus (**Figure 2C3**). Furthermore, in few occasions the response was characterized by rhythmic activity at a frequency of ∼5 Hz, well within the frequency of olivary subthreshold activity (**Figure 2D**).

To further characterize this rhythmic IO response and keeping in mind that several tens of PNs converge onto one CN neuron (Najac and Raman, 2017; Yarden-Rabinowitz and Yarom, 2017), we recorded intracellularly from CN neurons while activating the IO. Indeed, rhythmic bursts of inhibition were occasionally observed in response to IO stimulation (**Figure 2E**). In accordance with the delayed complex spikes in PNs, the delay to the first peak of inhibitory response was ∼70 ms (**Figure 2E1**). It should be noted that the frequency of these events (∼7 Hz) within the frequency of olivary subthreshold activity. In the presented example IO stimulation directly activated the CN neuron (**Figure 2E1**, black arrow). Moreover, each of the delayed inhibitory response is always preceded by small, depolarizing signal (black arrow, **Figure 2E2**) that represent direct olivary input to CN neurons (van der Want et al., 1989). The absence of strong inhibitory response following direct activation of the IO suggests that only a small number of olivary neurons were activated by the stimulus. On the other hand, the inhibitory delayed response suggests that it is associated with a large number of IO neurons. Thus, robust delayed olivary activity can be triggered by direct olivary stimulation and it is likely to reflect feedback activation of a larger population of neurons compared to the directly activated neurons.

PROPOSED MECHANISM OF CLASSICAL CONDITIONING

In view of this brief description, it is tempting to consider the possibility that the delayed complex spike is an intrinsic property of the olivo-cerebellar network. However, the olivo-cerebellar loop is a rather temporally compact system, hence, where in the circuit can such a long delay emerge? One possible candidate is

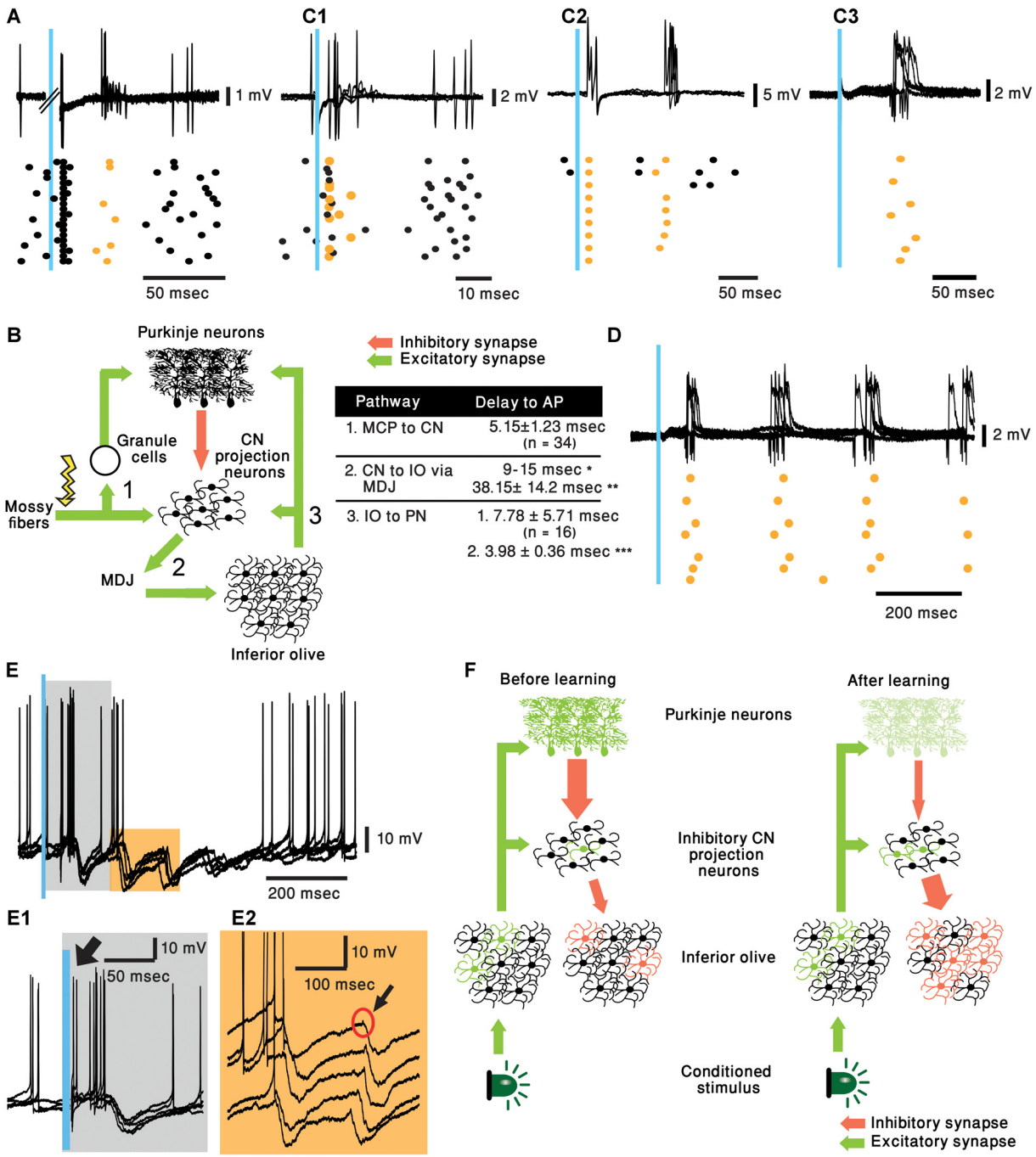

FIGURE 2 | Cerebellar activity in response to mossy fiber (MF) and IO stimulation in naive mice and proposed mechanism. **(A)** five superimposed voltage responses recorded from a PN during MF stimulation (Blue bar) placed at the medial cerebellar peduncle and the corresponding raster plot. In all the panels orange stars and black circles represent complex spikes and simple spikes, respectively. **(B)** Possible pathway of MF evoked delayed complex spike response as suggested by ten Brinke et al. (2019) and a table summarizing the delays in the diagram. Delay values are collected from our recordings unless indicated otherwise. *(Ruigrok and Voogd, 1995) **(Bazzigaluppi et al., 2012) and ***(Shinoda et al., 2000). MDJ, mesodiencephalic junction. **(C1–C3)** Three different types of PN responses to IO stimulation (Blue bar), five superimposed traces and the corresponding raster plots are plotted for each type of response. Direct complex spike activation (**C1**, ~5 ms delay), direct complex spike activation and a delayed response (**C2**, ~5 and ~75 ms delay) and only delayed complex spike (**C3**, ~80 ms). **(D)** Rhythmic complex spike response to IO stimulation (Blue bar), five superimposed traces and the corresponding raster plots are plotted. **(E)** Rhythmic inhibitory bursts recorded from CN neurons in response to IO stimulation (Blue bar), five superimposed traces and the corresponding raster plots are plotted. **(E1)** Higher resolution of the gray rectangle displayed in **(E)**. Black arrow indicates direct activation of CN neuron (~5 ms). **(E2)** Higher resolution of the orange rectangle displayed in **(E)**. Black arrow indicates short excitation preceding burst of inhibitory inputs. **(F)** Suggested pathway of CS evoking delayed complex spike response after learning.

the inhibitory input from CN inhibitory projection neurons (also referred to as nucleo-olivary neurons, NO) that innervate the IO. This inhibition closely controls the functional architecture of the nucleus as was shown in an *in vitro* study (Lefler et al., 2014). This study demonstrated that the activation of the inhibitory input is sufficient to block the subthreshold activity in the IO as well as to reset the rhythm phase (**Figures 1G1,G2**), thereby introducing a significant delay between activation time of NO neurons and the spiking activity in the IO.

Accordingly, we propose the following sequence of events that lead to classical conditioning. In a nutshell, CS activates the IO neurons (Ju et al., 2019; Rasmussen, 2019) but the number of activated cells, as well as the reliability of the response, is rather weak. After training the same stimulus reliably activates, after a considerable delay and *via* the NO, a large population of olivary neurons. This possibility is schematically illustrated in **Figure 2F**. Before training (left panel) the CS (Light) activates a small number of olivary neurons (Green), that in addition to activating the PNs, also innervate the NO projection neurons (De Zeeuw et al., 1997). However, under naïve conditions, the NO neurons are inhibited by the PN preventing them from delivering a significant output to the IO. After learning (right panel), there is a reduction in PN activity, commonly accepted paradigm of cerebellar learning. This reduction relieves the NO neurons from inhibition, consequently, the IO input to the NO neurons becomes more efficient and more reliably activates the NO neurons. Again, the involvement of the inhibitory feedback of the NO in cerebellar learning processes has been well established (Andersson and Hesslow, 1987; Andersson et al., 1988; Llinás and Welsh, 1993). As a result, the feedback inhibition to the IO resets the olivary activity and thus, synchronously activates a large population of IO neurons (red cells) at a delay of 70–80 ms.

To conclude, recent classical conditioning studies presented the emergence of a delayed complex spike response following a CS. Reviewing evidence in the literature implies that this delayed complex spike response signals the initiation of movement whereas the kinematics of the movement that is acquired during learning is determined by Purkinje and CN neuronal activity. Our presented data argue that the delayed complex spike is a result of modifications in the activity of CN inhibitory projection neurons and not a result of a feedforward excitation *via* MFs.

DATA AVAILABILITY STATEMENT

All datasets generated for this study are included in the manuscript.

ETHICS STATEMENT

The animal study was reviewed and approved by Hebrew University of Jerusalem Animal Care Committee.

AUTHOR CONTRIBUTIONS

YY-R recorded from PN and CN neurons and analyzed the data. YY-R and YY conceived the idea and wrote the manuscript.

FUNDING

This work was supported by the Israeli Science Foundation (Israel Society for Neuroscience), Grant Number: 1496/16, and by the Gatsby Charitable Foundation.

REFERENCES

Alba, A., Kano, M., Chen, C., Stanton, M. E., Fox, G. D., Herrup, K., et al. (1994). Deficient cerebellar long-term depression and impaired motor learning in mGluR1 mutant mice. *Cell* 79, 377–388. doi: 10.1016/0092-8674(94)90205-4

Andersson, G., Garwicz, M., and Hesslow, G. (1988). Evidence for a GABA-mediated cerebellar inhibition of the inferior olive in the cat. *Exp. Brain Res.* 72, 450–456. doi: 10.1007/bf00250590

Andersson, G., and Hesslow, G. (1987). Inferior olive excitability after high frequency climbing fibre activation in the cat. *Exp. Brain Res.* 67, 523–532. doi: 10.1007/bf00247285

Bazzigaluppi, P., Ruigrok, T., Saisan, P., de Zeeuw, C. I., and de Jeu, M. (2012). Properties of the nucleo-olivary pathway: an *in vivo* whole-cell patch clamp study. *PLoS One* 7:e46360. doi: 10.1371/journal.pone.0046360

Boele, H.-J., Koekkoek, S. K. E., De Zeeuw, C. I., and Ruigrok, T. J. H. (2013). Axonal sprouting and formation of terminals in the adult cerebellum during associative motor learning. *J. Neurosci.* 33, 17897–17907. doi: 10.1523/JNEUROSCI.0511-13.2013

Chettih, S. N., McDougle, S. D., Ruffolo, L. I., and Medina, J. F. (2011). Adaptive timing of motor output in the mouse: the role of movement oscillations in eyelid conditioning. *Front. Integr. Neurosci.* 5:72. doi: 10.3389/fnint.2011.00072

De Zeeuw, C. I., Van Alphen, A. M., Hawkins, R. K., and Ruigrok, T. J. H. (1997). Climbing fibre collaterals contact neurons in the cerebellar nuclei that provide a GABAergic feedback to the inferior olive. *Neuroscience* 80, 981–986. doi: 10.1016/s0306-4522(97)00249-2

Halverson, H. E., Khilkevich, A., and Mauk, M. D. (2015). Relating cerebellar purkinje cell activity to the timing and amplitude of conditioned eyelid responses. *J. Neurosci.* 35, 7813–7832. doi: 10.1523/JNEUROSCI.3663-14.2015

Halverson, H. E., Khilkevich, A., and Mauk, M. D. (2018). Cerebellar processing common to delay and trace eyelid conditioning. *J. Neurosci.* 38, 7221–7236. doi: 10.1523/JNEUROSCI.0430-18.2018

Heffley, W., Song, E. Y., Xu, Z., Taylor, B. N., Hughes, M. A., McKinney, A., et al. (2018). Coordinated cerebellar climbing fiber activity signals learned sensorimotor predictions. *Nat. Neurosci.* 21, 1431–1441. doi: 10.1038/s41593-018-0228-8

Heiney, S. A., Wohl, M. P., Chettih, S. N., Ruffolo, L. I., and Medina, J. F. (2014). Cerebellar-dependent expression of motor learning during eyeblink conditioning in head-fixed mice. *J. Neurosci.* 34, 14845–14853. doi: 10.1523/JNEUROSCI.2820-14.2014

Jirenhed, D. A., and Hesslow, G. (2016). Are purkinje cell pauses drivers of classically conditioned blink responses? *Cerebellum* 15, 526–534. doi: 10.1007/s12311-015-0722-4

Jirenhed, D.-A., Rasmussen, A., Johansson, F., and Hesslow, G. (2017). Learned response sequences in cerebellar Purkinje cells. *Proc. Natl. Acad. Sci. U S A* 114, 6127–6132. doi: 10.1073/pnas.1621132114

Ju, C., Bosman, L. W. J., Hoogland, T. M., Velauthapillai, A., Murugesan, P., Warnaar, P., et al. (2019). Neurons of the inferior olive respond to broad classes of sensory input while subject to homeostatic control. *J. Physiol.* 597, 2483–2514. doi: 10.1113/jp277413

Kim, J. J., and Thompson, R. F. (1997). Cerebellar circuits and synaptic mechanisms involved in classical eyeblink conditioning. *Trends Neurosci.* 20, 177–181. doi: 10.1016/s0166-2236(96)10081-3

Koekkoek, S. K. E., Hulscher, H. C., Dortland, B. R., Hensbroek, R. A., Elgersma, Y., Ruigrok, T. J. H., et al. (2003). Cerebellar LTD and learning-dependent timing of conditioned eyelid responses. *Science* 301, 1736–1739. doi: 10.1126/science.1088383

Lefler, Y., Yarom, Y., and Uusisaari, M. (2014). Cerebellar inhibitory input to the inferior olive decreases electrical coupling and blocks subthreshold oscillations. *Neuron* 81, 1389–1400. doi: 10.1016/j.neuron.2014.02.032

Llinás, R., and Welsh, J. P. (1993). On the cerebellum and motor learning. *Curr. Opin. Neurobiol.* 3, 958–965. doi: 10.1016/0959-4388(93)90168-X

Medina, J. F., Nores, W. L., and Mauk, M. D. (2002). Inhibition of climbing fibres is a signal for the extinction of conditioned eyelid responses. *Nature* 416, 330–333. doi: 10.1038/416330a

Najac, M., and Raman, I. M. (2017). Synaptic excitation by climbing fibre collaterals in the cerebellar nuclei of juvenile and adult mice. *J. Physiol.* 595, 6703–6718. doi: 10.1113/jp274598

Nicholson, D. A., and Freeman, J. H. Jr. (2003). Addition of inhibition in the olivocerebellar system and the ontogeny of a motor memory. *Nat. Neurosci.* 6, 532–537. doi: 10.1038/nn1042

Ohmae, S., and Medina, J. F. (2015). Climbing fibers encode a temporal-difference prediction error during cerebellar learning in mice. *Nat. Neurosci.* 18, 1798–1803. doi: 10.1038/nn.4167

Popa, L. S., Streng, M. L., and Ebner, T. J. (2019). Purkinje cell representations of behavior: diary of a busy neuron. *Neuroscientist* 25, 241–257. doi: 10.1177/1073858418785628

Rasmussen, A. (2019). Graded error signals in eyeblink conditioning. *Neurobiol. Learn. Mem.* doi: 10.1016/j.nlm.2019.04.011 [Epub ahead of print].

Ruigrok, T. J. H., and Voogd, J. (1995). Cerebellar influence on olivary excitability in the cat. *Eur. J. Neurosci.* 7, 679–693. doi: 10.1111/j.1460-9568.1995.tb00672.x

Schonewille, M., Gao, Z., Boele, H. J., Veloz, M. F. V., Amerika, W. E., Šimek, A. A. M., et al. (2011). Reevaluating the role of LTD in cerebellar motor learning. *Neuron* 70, 43–50. doi: 10.1016/j.neuron.2011.02.044

Shinoda, Y., Sugihara, I., Wu, H. S., and Sugiuchi, Y. (2000). The entire trajectory of single climbing and mossy fibers in the cerebellar nuclei and cortex. *Prog. Brain Res.* 124, 173–186. doi: 10.1016/s0079-6123(00)24015-6

Siegel, J. J., Taylor, W., Gray, R., Kalmbach, B., Zemelman, B. V., Desai, N. S., et al. (2015). Trace eyeblink conditioning in mice is dependent upon the dorsal medial prefrontal cortex, cerebellum, and amygdala: behavioral characterization and functional circuitry. *eNeuro* 2:ENEURO.0051-14.2015. doi: 10.1523/eneuro.0051-14.2015

Streng, M. L., Popa, L. S., and Ebner, T. J. (2018). Complex spike wars: a new hope. *Cerebellum* 17, 735–746. doi: 10.1007/s12311-018-0960-3

ten Brinke, M. M., Boele, H. J., and De Zeeuw, C. I. (2019). Conditioned climbing fiber responses in cerebellar cortex and nuclei. *Neurosci. Lett.* 688, 26–36. doi: 10.1016/j.neulet.2018.04.035

ten Brinke, M. M., Boele, H. J., Spanke, J. K., Potters, J. W., Kornysheva, K., Wulff, P., et al. (2015). Evolving models of pavlovian conditioning: cerebellar cortical dynamics in awake behaving mice. *Cell Rep.* 13, 1977–1988. doi: 10.1016/j.celrep.2015.10.057

ten Brinke, M. M., Heiney, S. A., Wang, X., Proietti-Onori, M., Boele, H. J., Bakermans, J., et al. (2017). Dynamic modulation of activity in cerebellar nuclei neurons during pavlovian eyeblink conditioning in mice. *Elife* 6:e28132. doi: 10.7554/elife.28132

van der Want, J. J. L., Wiklund, L., Guegan, M., Ruigrok, T., and Voogd, J. (1989). Anterograde tracing of the rat olivocerebellar system with phaseolus vulgaris leucoagglutinin (PHA-L). Demonstration of climbing fiber collateral innervation of the cerebellar nuclei. *J. Comp. Neurol.* 288, 1–18. doi: 10.1002/cne.902880102

Witter, L., Canto, C. B., Hoogland, T. M., de Gruijl, J. R., and De Zeeuw, C. I. (2013). Strength and timing of motor responses mediated by rebound firing in the cerebellar nuclei after Purkinje cell activation. *Front. Neural Circuits* 7:133. doi: 10.3389/fncir.2013.00133

Yarden-Rabinowitz, Y., and Yarom, Y. (2017). *In vivo* analysis of synaptic activity in cerebellar nuclei neurons unravels the efficacy of excitatory inputs. *J. Physiol.* 595, 5945–5963. doi: 10.1113/jp274115

Conflict of Interest: The authors declare that the research was conducted in the absence of any commercial or financial relationships that could be construed as a potential conflict of interest.

frontiers in Systems Neuroscience

ORIGINAL RESEARCH
published: 29 October 2019
doi: 10.3389/fnsys.2019.00060

State-Dependent Entrainment of Prefrontal Cortex Local Field Potential Activity Following Patterned Stimulation of the Cerebellar Vermis

*Stéfanie A. Tremblay[1], C. Andrew Chapman[2] and Richard Courtemanche[1]**

[1] Department of Health, Kinesiology, and Applied Physiology, Center for Studies in Behavioral Neurobiology, Concordia University, Montreal, QC, Canada, [2] Department of Psychology, Center for Studies in Behavioral Neurobiology, Concordia University, Montreal, QC, Canada

The cerebellum is involved in sensorimotor, cognitive, and emotional functions through cerebello-cerebral connectivity. Cerebellar neurostimulation thus likely affects cortical circuits, as has been shown in studies using cerebellar stimulation to treat neurological disorders through modulation of frontal EEG oscillations. Here we studied the effects of different frequencies of cerebellar stimulation on oscillations and coherence in the cerebellum and prefrontal cortex in the urethane-anesthetized rat. Local field potentials were recorded in the right lateral cerebellum (Crus I/II) and bilaterally in the prefrontal cortex (frontal association area, FrA) in adult male Sprague-Dawley rats. Stimulation was delivered to the cerebellar vermis (lobule VII) using single pulses (0.2 Hz for 60 s), or repeated pulses at 1 Hz (30 s), 5 Hz (10 s), 25 Hz (2 s), and 50 Hz (1 s). Effects of stimulation were influenced by the initial state of EEG activity which varies over time during urethane-anesthesia; 1 Hz stimulation was more effective when delivered during the slow-wave state (Stage 1), while stimulation with single-pulse, 25, and 50 Hz showed stronger effects during the activated state (Stage 2). Single-pulses resulted in increases in oscillatory power in the delta and theta bands for the cerebellum, and in frequencies up to 80 Hz in cortical sites. 1 Hz stimulation induced a decrease in 0–30 Hz activity and increased activity in the 30–200 Hz range, in the right FrA. 5 Hz stimulation reduced power in high frequencies in Stage 1 and induced mixed effects during Stage 2. 25 Hz stimulation increased cortical power at low frequencies during Stage 2, and increased power in higher frequency bands during Stage 1. Stimulation at 50 Hz increased delta-band power in all recording sites, with the strongest and most rapid effects in the cerebellum. 25 and 50 Hz stimulation also induced state-dependent effects on cerebello-cortical and cortico-cortical coherence at high frequencies. Cerebellar stimulation can therefore entrain field potential activity in the FrA and drive synchronization of cerebello-cortical and cortico-cortical networks in a frequency-dependent manner. These effects highlight the role of the cerebellar vermis in modulating large-scale synchronization of neural networks in non-motor frontal cortex.

Keywords: oscillations, synchrony, cerebellum, vermis, prefrontal cortex, stimulation

OPEN ACCESS

Edited by:
Conor J. Houghton, University of Bristol, United Kingdom

Reviewed by:
Krystal Lynn Parker, The University of Iowa, United States
Mario Rosanova, University of Milan, Italy

***Correspondence:**
Richard Courtemanche
richard.courtemanche@concordia.ca

Received: *01 June 2019*
Accepted: *08 October 2019*
Published: *29 October 2019*

Citation:
Tremblay SA, Chapman CA and Courtemanche R (2019) State-Dependent Entrainment of Prefrontal Cortex Local Field Potential Activity Following Patterned Stimulation of the Cerebellar Vermis. Front. Syst. Neurosci. 13:60. doi: 10.3389/fnsys.2019.00060

INTRODUCTION

There has been growing evidence supporting cerebellar involvement in cognitive and affective functions (Hoppenbrouwers et al., 2008; Strick et al., 2009; Bostan et al., 2013). The cerebellum may promote synchronization of large-scale networks and influence extra-cerebellar networks through multiple cortical and subcortical projections (Courtemanche et al., 2013; Farzan et al., 2016). The cerebellum shows regional variations in its relatively uniform circuitry (Cerminara et al., 2015) and, through its wide connectivity, can modulate specific circuits involved in motor control, cognition, and affect (Schmahmann, 2004, 2019). Because of its contribution to several neurological disorders and its extensive connectivity with extra-cerebellar structures, the cerebellum has been used as a therapeutic target for non-invasive stimulation techniques such as transcranial magnetic stimulation (TMS) and transcranial direct current stimulation (tDCS) (Hoppenbrouwers et al., 2008; van Dun et al., 2017, 2018). Stimulation of the vermis, the most medial region of the cerebellum, results in positive effects on cognition and mood associated with modulation of frontal oscillations (Schutter et al., 2003; Schutter and van Honk, 2006, 2009; Demirtas-Tatlidede et al., 2010). Stimulation of the fastigial nucleus (FN) following middle cerebral artery occlusion and chronic mild stress in rats also improves neuroprotection by suppressing death of cerebellar Purkinje cells and alleviates depressive-like behaviors (Zhang et al., 2017). Stimulation of the FN also affects local field potential (LFP) oscillations in the frontal cortex of anesthetized cats, where high frequency stimulation attenuates slow rhythms, and enhances 20–40 Hz oscillations (Steriade, 1995). Low frequency FN stimulation (1 Hz) was also shown to inhibit epileptogenic activity in the rat (Wang et al., 2008), while stimulating lateral cerebellar projections at 2 Hz has been shown to rescue medial frontal cortex delta activity in a rat model of schizophrenia (Parker et al., 2017).

Brain imaging studies in humans have demonstrated functional connectivity between the cerebellum and prefrontal cortex (PFC) (O'Reilly et al., 2009; Buckner et al., 2011; Sang et al., 2012; Farzan et al., 2016). The underlying connections have also been well characterized in non-human primates (Kelly and Strick, 2003; Strick et al., 2009) and rodents (Watson et al., 2009, 2014; Suzuki et al., 2012) using neuroanatomical and electrophysiological approaches. In the urethane-anesthetized rat, stimulation of the medial PFC (prelimbic cortex; PrL) evoked responses in the contralateral vermis (lobule VII), while stimulation of the fastigial nucleus resulted in evoked potentials in the PrL, indicating reciprocal long-range interactions between the medial PFC and medial cerebellum (Watson et al., 2009, 2014). Watson et al. (2014) also observed synchronous LFP activity in the theta range (5–10 Hz) between the fastigial nucleus and PrL during active locomotion and at rest.

Coherent synchronization of rhythmic neuronal population activity between distant cortical regions is thought to reflect mechanisms that enhance communication between structures, and that coordinate contributions of brain regions to sensorimotor integration and cognitive function (Engel et al., 2001; Fries, 2015). There is growing interest in understanding how cerebello-cortical network interactions synchronize to modulate higher-order functions. The dorsolateral PFC and the vermis have been implicated in the pathogenesis of several neurological disorders (Baxter et al., 1989; Andreasen et al., 1996; Maeda et al., 2000a; Andreasen and Pierson, 2008; Koenigs and Grafman, 2009; Fatemi et al., 2012). Anatomical evidence in monkeys (Kelly and Strick, 2003) and functional connectivity studies in humans (Buckner et al., 2011; Farzan et al., 2016) have demonstrated pathways mediating communication between the vermal lobule VII and dorsolateral PFC. However, little is known concerning the frequencies of activity that promote coherent LFP oscillations in these structures most effectively, and to what extent the induction of coherent LFP activity may depend on the initial oscillatory state.

In the current study, we investigated the effects of various frequencies of cerebellar vermis stimulation on the power and coherence of LFP oscillations in Crus I/II of the right lateral cerebellum (RCb) and bilateral dorsolateral PFC (frontal association area; FrA) in the urethane-anesthetized rat. Urethane is permissive to oscillations, and results in cyclic alternations between states similar to slow-wave nREM sleep and active REM sleep (Clement et al., 2008; Ros et al., 2009). Based on previous anatomical and functional connectivity studies (Akgören et al., 1996; Kelly and Strick, 2003; Buckner et al., 2011; Farzan et al., 2016), stimulation of the vermis was expected to strongly modulate LFP activity in the FrA and in the RCb. Stimulation was delivered to the most superficial layer of the cerebellar cortex to activate Purkinje cells (PCs) that project to the fastigial nucleus, which can modulate cortical areas via the thalamus and the cerebellar hemispheres via parallel fibers (Akgören et al., 1996; Lisberger and Thach, 2013). Inhibitory interneurons would also likely be activated by stimulation, which could result in complex frequency-specific interactions (Dugué et al., 2009). The goals of this study were to (1) characterize spontaneous LFP activity in the lateral Cb and bilateral dorsolateral PFC [FrA in the rat; (Uylings et al., 2003)] as well as coherence within this network during urethane-anesthesia, (2), assess the effectiveness of different frequencies of vermal stimulation in inducing changes in power and coherence in LFP activity in the lateral Cb and FrA, and (3), determine how slow-wave and activated stages of urethane anesthesia may modulate the responsivity of the network to stimulation. Lower frequencies of stimulation were expected to have a greater impact on slow oscillatory activity and coherence, and higher frequencies were expected to drive cortical beta and gamma oscillations (Steriade, 1995; Schutter et al., 2003; Schutter and van Honk, 2006; Wang et al., 2008; Parker et al., 2017).

MATERIALS AND METHODS

Surgery

Six adult male Sprague-Dawley rats were used in this study. The anesthesia procedures were the same as used by Frederick et al. (2014). Briefly, rats were anesthetized with a 5% isoflurane and 95% oxygen mixture, and a catheter was placed in the jugular vein. Urethane (0.8 g/ml) was then administered intravenously to maintain anesthesia, and level of anesthesia was verified by

ensuring that the foot-withdrawal reflex was absent throughout the experiment. Rats were placed in a stereotaxic apparatus and a regulated heating pad and insulating blanket were used to maintain body temperature near 37°C. All procedures were in accordance with the guidelines of the Canadian Council on Animal Care and approved by the Concordia University Animal Research Ethics Committee.

The skin was cut to expose the skull and a 2–2.5 mm craniotomy was performed in the occipital bone over the right cerebellar Crus I/II lobule. Holes were also drilled bilaterally over the FrA, and over the cerebellar vermis lobule VII. Bipolar electrodes, constructed from Teflon-coated stainless-steel twisted wire (125 μm tip diameter, with tips 1 mm apart in depth), were anchored to the stereotaxic apparatus. The stimulation electrode was inserted into the vermis lobule VII (AP -13.0; ML 0; V 3.3), and recording electrodes were inserted into the FrA (AP 4.7; ML ± 1.8; V 2.2). The recording electrode in the right Crus I/II was inserted at a 45° angle, 3.2 mm lateral from the midline, to a depth of 1 mm from the surface of the cerebellum (**Figure 1A**). The stereotaxic apparatus was grounded, and a bare stainless-steel reference electrode (5 mm long) was placed between the skull and the surface of the temporal lobe. Two monopolar recordings and one bipolar differential recording were obtained from each site. Both types of recordings can be used to record LFP activity yet electrode placement must be aligned to a dipole to obtain an optimal bipolar signal (Buzsaki et al., 2012). Bipolar recordings were thus used when the signal amplitude was optimal, otherwise monopolar recordings were used.

Recording Procedures

Recordings in each animal were initiated with a 2 min recording of spontaneous baseline LFP activity in the RCb and FrA. LFP signals were band-pass filtered between 0.01 and 500 Hz, amplified (x1000; A-M Systems Model 1700), and digitized onto the computer's hard drive at a sampling rate of 1024 Hz using SciWorks software (Datawave Technologies, Loveland, CO, United States). LFPs were recorded bilaterally in the FrA in three animals, in the left FrA (LFrA) in one animal, and in the right FrA (RFrA) in two animals. Each recording trial, in which a different stimulation frequency was tested, lasted 2 min. Following a 30 s baseline period, stimulation was delivered for 1–60 s, depending on the frequency of stimulation, and this was followed by a post-stimulus recording (**Figure 1B**). Biphasic square-wave pulses (0.1 ms duration) were delivered to the vermis using a stimulus generator (A-M Systems, Model 2100; Sequim, WA, United States). In addition to a single-pulse condition, in which pulses were delivered every 5 s for 60 s, stimulation frequencies were selected within all major frequency bands. Repeated pulses were delivered at 1 Hz (30 s duration, delta), 5 Hz (10 s, theta), 25 Hz (2 s, beta), and 50 Hz (1 s, gamma). Stimulation was delivered in ascending order (from lowest to highest frequency) in three animals and was delivered in randomized order in the other three animals. There were no significant effects of testing order on measures of power or coherence. Each frequency of stimulation was delivered at an intensity of 500, 750, and 1000 μA resulting in three trials at each stimulation frequency (two trials at each intensity were obtained in one animal; **Table 1**). Following recordings, animals were euthanized with an intravenous overdose of urethane.

Signal Processing and Analysis

Recordings were imported into MATLAB (Mathworks, Natick, MA, United States) for analysis. Signals were filtered using the function *filtfilt*, with a FIR equiripple low-pass at 250 Hz. Power spectral density analyses (short-time Fourier transform) were conducted using the spectrogram function with windows of 512 samples (0.5 s) and a 50% overlap. This resulted in good temporal resolution (0.25 s), allowing slow components of the signal to be quantified. Spectrograms were constructed to represent the frequency content of the signal as a function of time.

For coherence analysis, the filtered signals were divided into epochs of 2 s. The magnitude-squared coherence, which indicates how closely related two signals (x and y) are in power across frequencies and the consistency of the phase relationship between the two signals at each frequency, was computed for each electrode pair using the mscohere function:

$$C_{xy}(f) = \frac{|P_{xy}(f)|^2}{P_{xx}(f)P_{yy}(f)}$$

where Pxx(f) and Pyy(f) are the power spectral densities of x and y, and Pxy(f) is the cross power spectral density.

Each bipolar recording electrode provided two monopolar channels and one differential recording channel for each recording site (RCb, RfrA, and LFrA). One channel was chosen for analysis for each recording site. The differential bipolar recordings were chosen when possible, but the largest amplitude monopolar recording channel was used when similarity of the monopolar channels resulted in very low power in bipolar recordings. Coherence was calculated between RCb-LfrA (contra Cb-FrA), RCb-RfrA (ipsi Cb-FrA), and LfrA-RfrA (FrA-FrA), using the selected channels.

Power and coherence values were integrated within each frequency band: delta (Δ, 0.01–3 Hz), theta (θ, 3–8 Hz), alpha (α, 8–15 Hz), beta (β, 15–30 Hz), low gamma (low γ, 30–55 Hz), high gamma (65–80 Hz), and fast (80–200 Hz), and normalized by dividing by the number of frequency bins within each band. Frequencies between 55 and 65 Hz were left out to eliminate 60 Hz noise. Spectrograms and coherograms were inspected to assess the time-course of changes following stimulation, and power and coherence values were averaged across periods of 6 s. This resulted in five pre-stimulation periods (30 s period), 4 post-stimulation periods for single-pulse stimulation, and 8 post-stimulation periods for all other conditions. The relative changes in post-stimulation values of power and coherence were calculated from the mean pre-stimulation values for each period.

Neocortical activity at ∼1°Hz (delta) is associated with the slow-wave state under urethane anesthesia, and low-amplitude faster cortical oscillations are present during the activated state (Clement et al., 2008). To address the impact of the state-changes during anesthesia, we divided the trials into either the slow-wave state (Stage 1) or the activated state (Stage 2) based on the amount of power in the delta band in cortical channels during the pre-stimulation period. The z-scores of cortical power in the

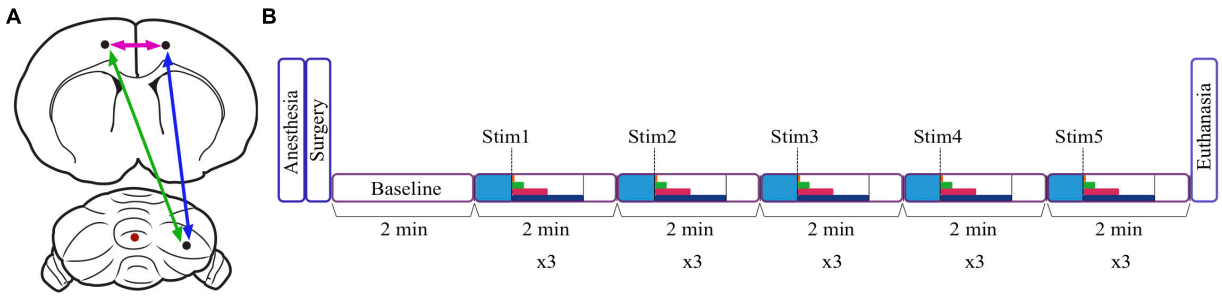

FIGURE 1 | Schematic diagram of the location of stimulation and recording sites, and the experimental timeline. **(A)** Recording sites in the right cerebellum and the left and right frontal association area are represented by black dots, and the stimulation site in the cerebellar vermis is indicated by a red dot. Arrows represent coherence between sites. **(B)** After anesthetizing the animal, electrodes were inserted stereotaxically during surgery, and a baseline period of 2 min was recorded. There was also a baseline period of 30 s (blue) at the start of each 2 min trial. The duration of the stimulation depended on stimulation frequency and varied from 1 to 60 s (dark blue = 60 s, pink = 30 s, green = 10 s, orange = 2 s, dashed line = 1 s). Three trials were conducted for each of the five stimulation frequencies, and the animal was euthanized following recordings.

TABLE 1 | Recording sites, number of trials per stimulation pattern and order of stimulation pattern delivery for each animal.

Rat	Recording sites	# trials/stim type	Order of stim delivery
1	RCb, RFrA	3	Low to high frequency
2	RCb, RFrA	3	Low to high frequency
3	RCb, LFrA	3	Low to high frequency
4	RCb, LFrA, RFrA	3	Randomized
5	RCb, LFrA, RFrA	6	Randomized
6	RCb, LFrA, RFrA	3	Randomized

delta band for all trials were plotted on a histogram (**Figure 2A**) and trials above the 60th percentile were classified as slow-wave, and trials below the 50th percentile were classified as activated state. Trials between the 50th and the 60th percentiles were considered as being in transition and were excluded from the stage analysis (see example in **Figure 2B**). The two subgroups of trials formed for each animal were used to determine if the stage of anesthesia has an impact on frequency-dependent effects of stimulation. Effects of stimulation did not typically outlast the 2 min trial duration, and this state-dependent analysis ensured that only trials representative of the slow-wave or activated state were included in the respective analyses.

Statistical Analysis

Repeated-measures ANOVAs were conducted using Tibco Statistica (Dell Software, Round Rock, TX, United States). Stimulation intensity had no significant effect on power [one rat in which 2 trials per intensity per stimulation frequency were obtained: $F_{(2,288)} = 1.92$, $p = 0.15$]. Therefore, trials of different intensities were grouped together for each stimulation frequency. The order in which the stimulation patterns were delivered also had no significant effect on measures of power [StimOrder: $F_{(1,\ 230)} = 0.31$, $p = 0.860$; Stim by StimOrder interaction: $F_{(4,\ 230)} = 0.485$, $p = 0.747$] or coherence [StimOrder: $F_{(1,\ 211)} = 0.008$, $p = 0.927$; Stim by StimOrder interaction: $F_{(4,\ 211)} = 0.410$, $p = 0.802$]. The data were therefore combined together.

For initial analyses, the dependent variables were LFP power and LFP-LFP coherence, while the independent variable was the type of stimulation. Repeated measures ANOVAs, with 7 levels of frequency bands and levels of time (1 Baseline and 4–8 Post windows, depending on the condition) as repeated measures, and stimulation type (Stim-SP, Stim-1 Hz, Stim-5 Hz, Stim-25 Hz, and Stim-50 Hz) and site (RCb, LfrA, RfrA) as categorical factors, were performed on the relative changes from baseline for LFP power. A similar analysis was done for coherence but included the pair of recording sites (contra Cb-FrA, ipsi Cb-FrA, and FrA-FrA) as a categorical factor. Results were considered statistically significant if $p < 0.05$.

To assess state-dependent differences in response to stimulation, separate repeated-measures ANOVAs for each stimulation frequency assessed changes in power or coherence in a given frequency band relative to baseline as a function of the time window and stage. These analyses were performed within each recording site for LFP power, and between each pair of recording sites for coherence (site or comparison type as categorical factor). Fisher's *post hoc* analyses ($p < 0.05$) were used to identify which components differed in statistically significant interactions.

RESULTS

Spontaneous Power and Coherence

Prior to assessing the effects of cerebellar rhythmic stimulation, spontaneous LFP power within each recording site, and coherence between each pair of recording sites were evaluated. Power was typically highest in the delta band in all animals, consistent with the slow-wave activity reported in urethane-anesthetized rats (Clement et al., 2008; Frederick et al., 2014). Baseline power spectra in all sites showed peaks in the delta band at about 2 Hz. This activity co-occurred with activity in the beta, low gamma and high gamma bands, which was superimposed on the slow waves. This higher-frequency activity was not always clear in power measures but was readily evident in coherence measures. The example in **Figures 3A–C** shows

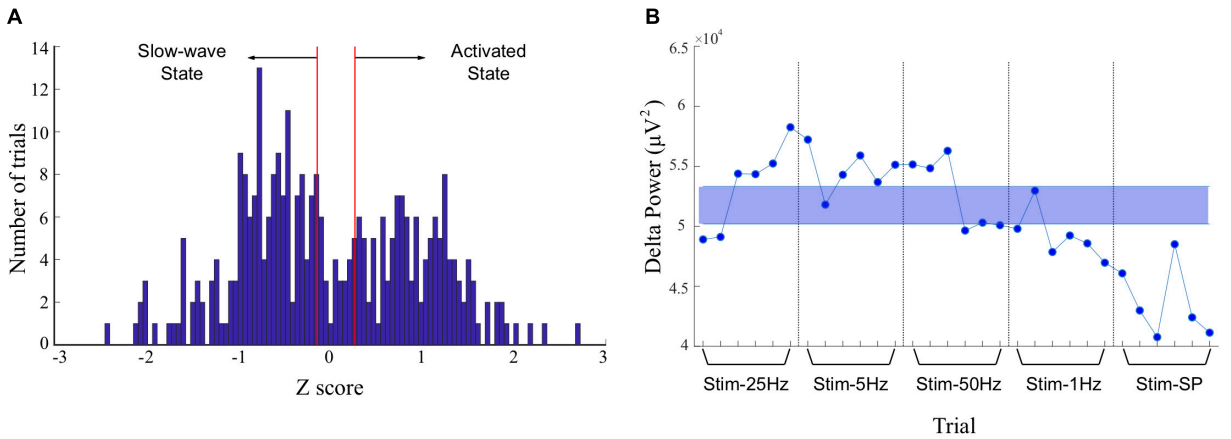

FIGURE 2 | Discrimination of trials recorded during slow-wave and activated states. **(A)** Histogram of z-scores of power in the delta band in cortical recordings during the 30 s baseline period, for all trials. The peak on the right represents greater delta power during the slow-wave state, and the peak on the left represents lower delta power during the activated state. The area between the red lines was identified as a transition period and corresponds to the median and to the 60th percentile of the distribution. The trials between the 50th and 60th percentiles were excluded from the stage-based analyses. **(B)** Example of trials attributed to the slow-wave or activated states in one animal (rat 5). Power in the delta band is plotted for a monopolar recording in the left frontal association area, and stimulation frequencies tested during each consecutive trial are indicated on the x-axis. Trials with values within the shaded blue area were excluded from analysis, and trials above and below the shaded areas were classified as representing the slow-wave, or activated states, respectively. SP, single-pulse.

coherent activity in both delta and low gamma bands between the left and right FrA.

LFP recordings also showed periods in which delta band activity was weaker, and there was a more broadband distribution that sometimes included periods of increased power and coherence around 8–10 Hz. The example in **Figures 3D–F** shows marked coherence in the alpha band (10 Hz) between the cerebellum and contralateral cortex, consistent with previous electrophysiological evidence in the cerebellum and neocortex (O'Connor et al., 2002). These periods when slow-wave activity subsides to give way to faster activity in neocortical sites are consistent with the activated state described by Clement et al. (2008).

Effects of Stimulation

An initial analysis was used to evaluate how LFP power and coherence were modulated by different frequencies of stimulation across all recorded trials. The time by stimulation frequency interaction was significant [$F_{16,\ 980)} = 2.28$, $p = 0.003$], with 50 Hz stimulation inducing more rapid effects on power, and single-pulse stimulation inducing more delayed effects. There was also a trend for a stimulation type by site interaction [$F_{(8,\ 245)} = 1.84$, $p = 0.071$], with the cerebellar site differing from cortical sites in the responses to stimulation frequencies, and a significant time by site interaction [$F_{8,\ 980)} = 2.44$, $p = 0.013$] due to earlier responses of the cerebellar recording to stimulation compared to the two cortical sites. No main effects or interactions were seen for coherence in this overall analysis.

Stage-Dependent Effects of Stimulation

The initial analysis indicated that vermal stimulation had frequency-dependent effects on LFP activity in both cerebellum and cortical sites, but baseline LFP activity differed markedly between the slow-wave state and the activated states. We therefore separated trials between the slow-wave (Stage 1) and activated (Stage 2) states and conducted ANOVAs to evaluate specific effects of stimulation frequency during each stage, on LFP and coherence measures in specific sites for each frequency band.

Overall, the stimulation patterns affected power to a greater extent than coherence. Stimulation at 1 Hz had larger effects when delivered during the slow-wave state (Stage 1), while single-pulse, 25 and 50 Hz stimulation had stronger effects in the activated state (Stage 2). **Figure 4** indicates maximal post-stimulus changes in power in each frequency band induced by each stimulation frequency for all sites; the left panels show power changes during slow-wave activity, and those on the right show changes during the activated state. Relative % change for the different stimulation patterns, in numerical values, are given in the **Supplementary Material**.

Single-Pulse Stimulation

Single-pulse stimulation (slow-wave: $n = 10$ trials from 4 rats; activated state: $n = 8$ trials from 3 rats) had several effects on power in cerebellar and cortical sites, but no significant effect on cerebello-cortical or cortico-cortical coherence. In general, single-pulse stimulation had a more robust effect on LFP power when delivered in the activated state (Stage 2). Single-pulse stimulation in Stage 2 resulted in increases in power in the Δ and θ bands in the cerebellum, and in a broader range of frequency bands in cortical sites (up to low γ in the LFrA and up to high γ in the RFrA). On the other hand, single-pulse stimulation during Stage 1 activity resulted in mixed effects on power in all sites. Maximal changes in power ranged between 5 and 15% from baseline (see **Figure 4**, Stim-SP).

Statistical comparisons showed main effects of Stage in Δ [$F_{(1,\ 39)} = 11.21$, $p = 0.002$], θ [$F_{(1,\ 39)} = 6.65$, $p = 0.014$], and β [$F_{(1,\ 39)} = 5.04$, $p = 0.031$], with Stage 2 being affected to a greater extent in all cases. During Stage 1, Δ was reduced in the

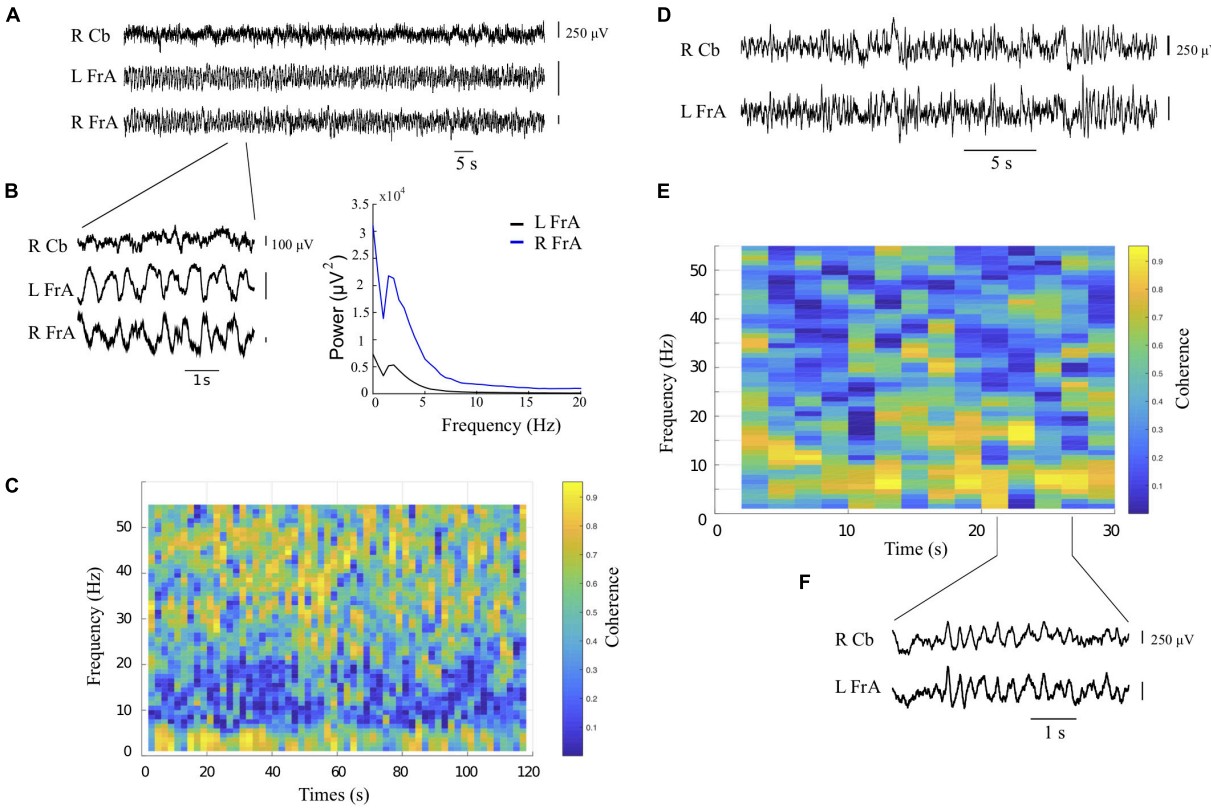

FIGURE 3 | Spontaneous oscillatory activity and coherence during baseline recordings from the right cerebellum (RCb) and left and right frontal association area (LFrA, RFrA). **(A)** Local field potential (LFP) recordings are shown for each recording site (rat 4). **(B)** Expanded view of LFP signals in **(A)** shows fast activity on top of slow-wave oscillatory activity in cortical sites. The corresponding power spectra reflect dominant rhythms at 2 Hz in the LFrA and RFrA during slow-wave activity. **(C)** The coherogram for the LFrA and RFrA shows periods of coherent activity at frequencies near 2 Hz and in the low gamma band (30–50 Hz). **(D)** Additional example of LFP traces in the RCb and LFrA (rat 3, 2 recording sites). **(E)** The coherogram shows coherence at 10 Hz, in the theta/alpha bands, between the RCb and LFrA. **(F)** Expanded LFP traces from the RCb and LFrA show prominent 10 Hz activity in both sites (lines indicate the time in **E** at which recordings were obtained).

cerebellum and in the RFrA, but during Stage 2, Δ power was increased in all sites. The main effect of stage in θ and β, was also due to increases in power during Stage 2, especially for the RFrA. Single pulse stimulation therefore induced the greatest increases in cortical power when delivered in the activated state, in a wide range of frequencies (**Figures 4D,F**). There was also a main effect of site in Δ [$F_{(2,\ 39)} = 3.87$, $p = 0.029$], θ [$F_{(2,\ 39)} = 4.80$, $p = 0.014$], and β [$F_{(2,39)} = 3.75$, $p = 0.032$], with the RFrA showing the greatest changes. Overall, there were more increases in power in the RFrA following single-pulse stimulation, and those increases were mainly in the activated state.

1 Hz Stimulation

Stimulation at 1 Hz had a much stronger effect on power during the slow-wave state than during the activated state. There were several changes in power in all sites in Stage 1 but very few in Stage 2 (**Figure 4**, Stim-1 Hz). We did not find any main effects or interactions in the ANOVA for coherence.

1 Hz stimulation during Stage 1 increased power in the RCb in the α and β bands, but decreased RCb θ power in Stage 2. In Stage 1, there were decreases in θ, α, β and high γ in the LFrA. In the RFrA, power in slow frequencies (Δ, θ, α, and β) decreased, while power in faster frequencies (low γ, high γ, and Fast) increased (**Figure 4C**). These changes ranged between 33% decreases (in Δ) and 15% increases (low γ). **Figure 5** shows example LFP traces and power spectra of 1 Hz stimulation trials in the slow-wave state (**Figures 5A,C**), examples in the activated state (**Figures 5B,D**), and the mean percent changes in power relative to baseline in the delta (**Figure 5E**) and low gamma bands (**Figure 5F**) for the group of rats (slow-wave: $n = 7$ trials from 4 rats; activated state: $n = 14$ trials from 6 rats). These state-dependent effects on power were supported by statistically significant Stage by site interactions in the Δ band, with the RFrA showing a reduction during Stage 1 [$F_{(2,\ 45)} = 5.31$, $p = 0.009$], and in the θ band, with reductions in the R and LFrA during Stage 1 [$F_{(2,\ 45)} = 3.52$, $p = 0.038$]. Overall, the RFrA showed the greatest change between stages. This implies that 1 Hz stimulation during the slow-wave state can shift LFP activity to higher frequencies, decreasing 0–30 Hz activity while increasing activity in the 30–200 Hz range.

5 Hz Stimulation

5 Hz stimulation (slow-wave: $n = 8$ trials from 3 rats; activated state: $n = 8$ trials from 4 rats) led to marked changes in power during both Stage 1 and Stage 2, but there were no main effects

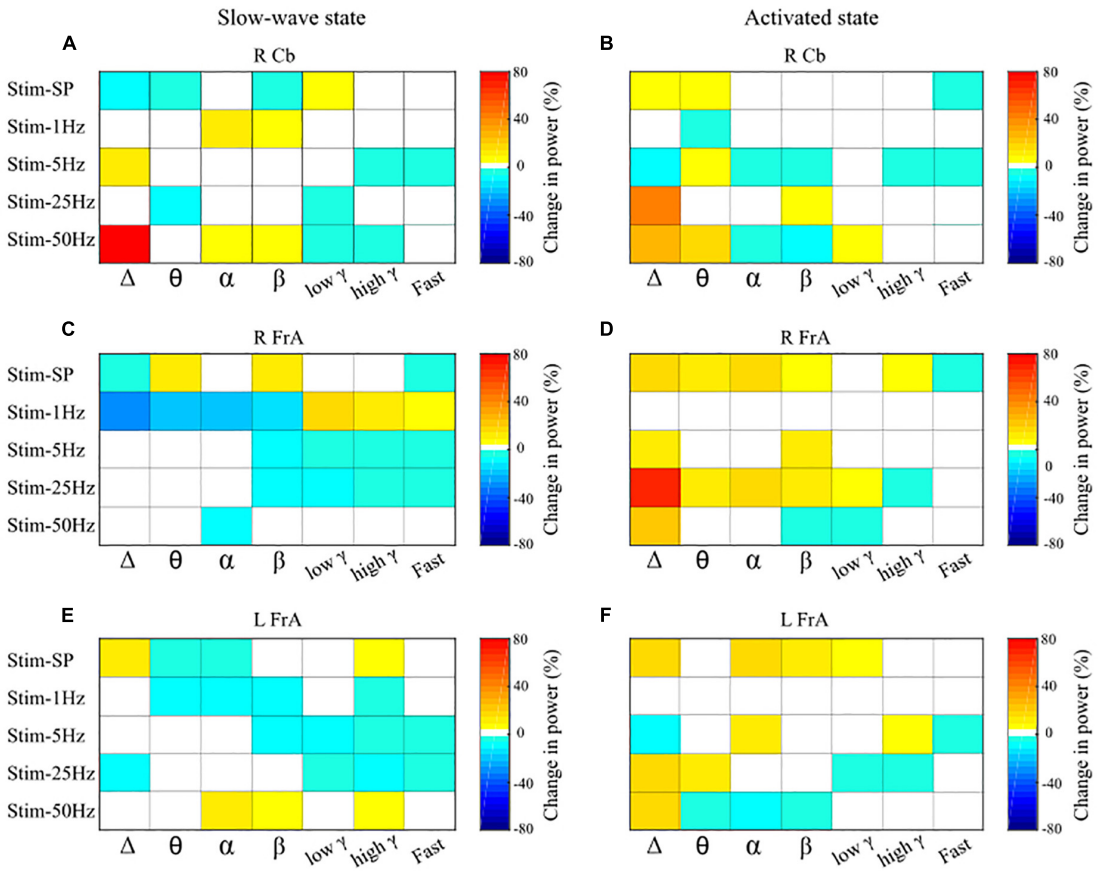

FIGURE 4 | Overall effects of the various stimulation types on power across the different frequency bands, by site. Maximal increases and decreases in mean power within each frequency band induced by stimulation of the cerebellar vermis are summarized here for the different frequencies of stimulation. Panels on the left show changes in mean power relative to the pre-stimulus baseline in the trials when stimulation was delivered during the slow-wave state, and panels on the right show changes in power induced during the activated state. The magnitude of relative changes in power from baseline in percent are represented by the color scales at the right of each panel; white indicates no significant change. Results are shown for the power of LFP activity in the right cerebellum (RCb; **A,B**), right frontal association area (RFrA; **C,D**), and left frontal association area (LFrA; **E,F**). Note the different patterns of changes in power induced by cerebellar stimulation that were dependent upon the presence of either the slow-wave or the activated state. SP, single-pulse; Δ, delta; θ, theta; α, alpha; β, beta; γ, gamma.

of stimulation or interactions for the coherence measures. In Stage 1, stimulation at 5 Hz led mainly to decreases in power, especially in high frequency bands (β, low γ, high γ, and Fast for cortical sites; high γ, and Fast for the RCb). During Stage 2, there were both increases and decreases in power at different recordings sites distributed across all frequency bands (**Figure 4**, Stim-5 Hz**).** There was a main effect of time for the low γ band [$F_{(8,\ 288)} = 2.47$, $p = 0.013$], due to a more pronounced drop in power at Post4, indicating a strong decrease in 30–55 Hz oscillatory power about 25 s post-stimulus. There also was a Stage by time interaction for β [$F_{(8,\ 288)} = 2.12$, $p = 0.034$] with greater power during Stage 2 than during Stage 1 at all delays except Post3; Stage 2 had an increase in β power while Stage 1 had a decrease. Overall, stimulation at 5 Hz decreased high frequency (15–200 Hz) power in cortical sites during slow-wave activity.

25 Hz Stimulation

Stimulation at 25 Hz induced greater effects on power and coherence during the activated state. During Stage 2, there were large increases in the Δ band in all sites (66% in the RFrA, 13% in the LFrA, and 41% in the RCb). Power also increased in θ in the LFrA and in θ, α, β, and low γ in the RFrA. In Stage 1, stimulation at 25 Hz decreased cortical power in high frequency bands (LFrA: 30–200 Hz; RFrA: 15–200 Hz). 25 Hz stimulation therefore had strong, state-dependent effects on LFP activity in cortical sites, with an increase of lower frequency activity in the activated state and a decreased activity in faster bands in the slow-wave state (**Figures 4C–F**, Stim-25 Hz). These state-dependent effects of 25 Hz stimulation are illustrated in **Figure 6** where example LFP traces and power spectra in both stages (**Figures 6A–D**), and the mean percent changes in power relative to baseline in the delta (**Figure 6E**), theta (**Figure 6F**), and low gamma bands (**Figure 6G**), for the group of rats (slow-wave: $n = 7$ trials from 4 rats; activated state: $n = 7$ trials from 5 rats), are shown.

State-dependent effects of 25 Hz stimulation were reflected by main effects of Stage in Δ [$F_{(1,\ 30)} = 13.81$, $p = 0.001$], θ [$F_{(1,\ 30)} = 10.78$, $p = 0.003$], β [$F_{(1,\ 30)} = 5.96$, $p = 0.021$], and Fast [$F_{(1,\ 30)} = 5.56$, $p = 0.025$], with Stage 2 being higher in all cases.

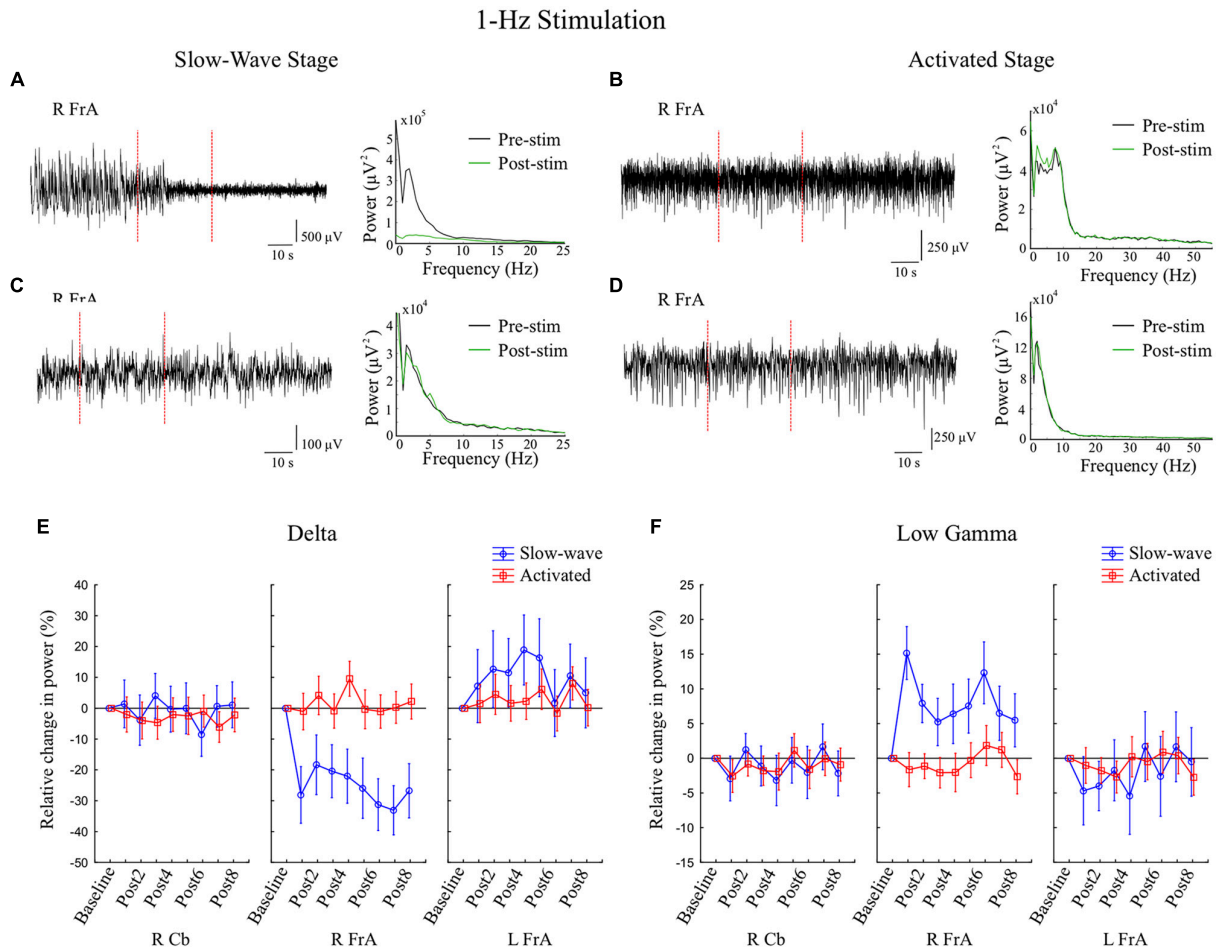

FIGURE 5 | Stimulation at 1 Hz for 30 s during the slow-wave state decreases delta activity and increases low gamma activity in the right frontal association area (RFrA). **(A,C)** Examples are shown in which 1 Hz stimulation (during the period between the vertical red dashed lines) was followed by either greatly reduced slow-wave activity (A, rat 2), or a more moderate reduction in slow-wave activity (**C**, rat 6). Power spectra show corresponding reductions in power in the delta band from pre-stimulation (Pre-stim, black line) to post-stimulation (Post-stim, green line). **(B,D)** During the activated state, 1 Hz stimulation did not significantly affect power in the delta band in the RFrA. Examples of LFP traces in the RFrA and corresponding power spectra are shown for two animals (**B**, rat 2; **D**, rat 4) in which there were minimal changes post-stimulation. **(E,F)** The mean percent changes in power relative to baseline are shown for the group of animals (slow-wave: $n = 7$ trials from 4 rats; activated state: $n = 14$ trials from 6 rats) for the delta band **(E)** and for the low gamma band **(F)** for all three recording sites. Results are shown for the eight 6 s time windows following stimulation (Post1–Post8). The reduction in power in the delta band, and the increase in power in the low gamma band occurred only during the slow-wave state (blue lines) in the RFrA.

A Stage by time interaction in Δ [$F_{(8,\ 240)} = 2.21$, $p = 0.028$], with greater increases in power during Stage 2 at multiple time points (Post3–6), also indicates the sensitivity of the activated state to 25 Hz stimulation. There was a main effect of time in β [$F_{(8,\ 240)} = 2.44$, $p = 0.015$], low γ [$F_{(8,\ 240)} = 1.98$, $p = 0.049$], high γ [$F_{(8,\ 240)} = 3.68$, $p = 0.001$], and Fast [$F_{(8,\ 240)} = 4.33$, $p = 0.00007$] frequency bands with mostly decreases post-stimulus, meaning that there was a general decrease in high frequency power after stimulation. A time by site interaction in Δ [$F_{(16,\ 240)} = 2.33$, $p = 0.003$] was also present, with the cerebellar site showing an early increase, and the RFrA showing a later increase.

Analysis of changes in coherence following 25 Hz stimulation showed a main effect of Stage in β [$F_{(1,\ 24)} = 6.61$, $p = 0.017$], with greater increases in coherence during Stage 2. We also found a Stage by Comparison effect in β [$F_{(2,\ 24)} = 4.84$, $p = 0.017$] in which the contra Cb-FrA comparison showed the greatest difference between Stages. 25 Hz stimulation therefore induced larger increases in coherence in the activated state, especially in the contra Cb-FrA comparison where coherence was increased during Stage 2 and decreased during Stage 1. This shows that 25 Hz stimulation can entrain and synchronize activity in the β band in cerebello-cortical networks when delivered in the activated state.

50 Hz Stimulation

Overall, stimulation at 50 Hz (slow-wave: $n = 9$ trials from 4 rats; activated state: $n = 9$ trials from 5 rats) had a greater effect on power during the activated state. Once again, more effects were noted for power than for coherence. There were increases in Δ power in all sites in Stage 2 and a large increase in the RCb (80%)

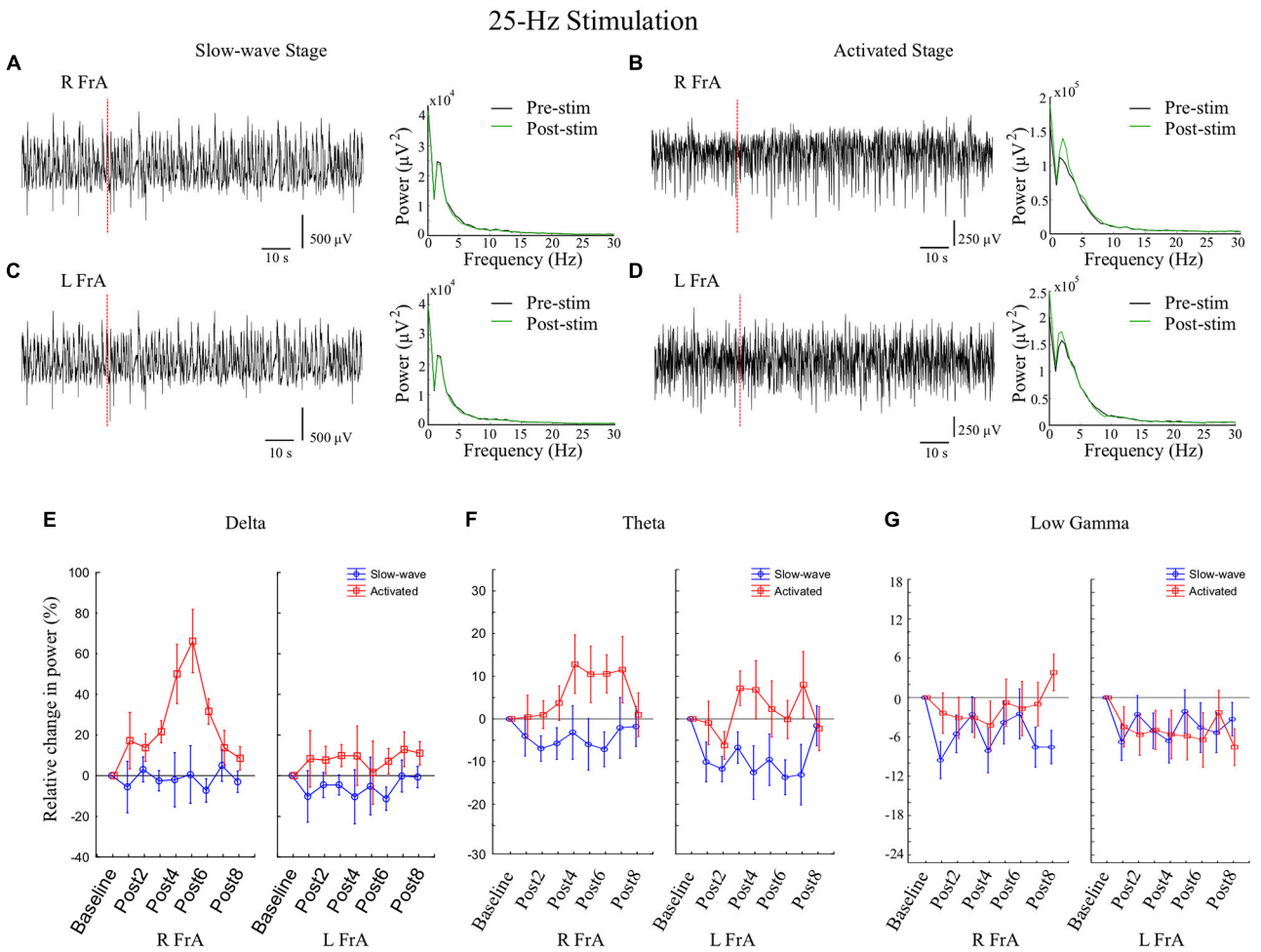

FIGURE 6 | In cortical sites, stimulation at 25 Hz for 2 s increases power in low frequency bands in the activated state and decreases low gamma activity in the slow-wave state. **(A,C)** During the slow-wave state, representative examples of local field potential (LFP) traces and power spectra in the right frontal association area (RFrA) **(A)** and LFrA **(C)** showing no marked changes in response to 25 Hz stimulation (vertical red dashed line; rat 5) as clear peaks in the power spectrum at high frequencies were rarely visible. **(B,D)** During the activated state, LFP traces and power spectra in the RFrA **(B)** and LFrA **(D)** showed increased power in the delta band following stimulation (Post-stim, green line) compared to pre-stimulation (black line; rat 4). **(E–G)** The mean percent changes in power in cortical sites relative to baseline are shown for the group of animals (slow-wave: $n = 7$ trials from 4 rats; activated state: $n = 7$ trials from 5 rats) for the delta band **(E)**, theta band **(F)**, and low gamma band **(G)**. Results are shown for the eight 6 s time windows following stimulation (Post1–Post8). Increases in power in the delta and theta bands occurred in the activated state (red line), while reductions in power in the low gamma band were more reliable in the slow-wave state (blue line).

in Stage 1. Power also increased in α, β, and high γ in the LFrA in Stage 1, while it decreased in the 3–30 Hz range in Stage 2 (**Figure 4**, Stim-50 Hz).

There was a main effect of Stage in Δ [$F_{(1,\ 36)} = 6.47$, $p = 0.015$] with increases in power being greater in Stage 2, suggesting that the activated state was the most responsive within the 0–3 Hz range. A significant Stage by time interaction in Δ [$F_{(8,\ 288)} = 2.11$, $p = 0.035$] showed that power increased at Post1 in both stages, but then decreased slightly below baseline in Stage 1 while remaining elevated in Stage 2. There was also a time by site interaction in Δ [$F_{(16,\ 288)} = 2.06$, $p = 0.010$], indicating the cerebellar site was affected earlier and more strongly by the stimulation. We also saw a Stage by site interaction for low γ [$F_{(2,\ 36)} = 4.18$, $p = 0.023$], in which the power in the cerebellum was also affected more strongly than cortical sites. This implies that the effects 50 Hz stimulation differed the most as a function of stage in the cerebellar site.

Analysis of coherence showed that there was a main effect of time in high γ [$F_{(8,\ 248)} = 2.49$, $p = 0.013$], with an early increase, followed by a slight decrease in coherence. When exploring specific Stage by site by frequency interactions for high γ, it was found that ipsi Cb-FrA and FrA-FrA coherence increased and contra Cb-FrA coherence decreased following 50 Hz stimulation.

DISCUSSION

The cerebellum is thought to play an important role in cognitive function through its interactions with the prefrontal cortex (Hoppenbrouwers et al., 2008; Strick et al., 2009;

Bostan et al., 2013). Both slow and fast oscillatory rhythms are thought to coordinate interactions between the cerebellum and cortical sites (O'Connor et al., 2002; Courtemanche and Lamarre, 2005; Ros et al., 2009; Courtemanche et al., 2013; Popa et al., 2013; Chen et al., 2016), and rhythmic cerebellar stimulation has been used as a therapeutic intervention in some disorders (Schutter et al., 2003; Schutter and van Honk, 2006, 2009; Demirtas-Tatlidede et al., 2010). The present study has examined the effects of cerebellar vermal stimulation at various rhythms on the entrainment of cerebellar and cortical LFPs under urethane anesthesia. Our results show that there are frequency-specific effects of cerebellar stimulation on both cerebellar and cerebral cortical LFP spectral properties, and that cerebellar stimulation at high frequencies (25 and 50 Hz) can also promote coherence in this cerebello-cortical network. Our findings also indicate that the effects of vermal stimulation are highly dependent upon the initial state of the networks, and that markedly different patterns of results were obtained, particularly for cortical sites, when stimulation was applied during the slow-wave versus the activated state.

Cerebellar vermal stimulation during either the slow-wave state or activated state produced different effects on cerebellar hemispheric LFPs. Single-pulse and 50 Hz stimulation led to opposite changes in LFP power when delivered during the slow-wave state as opposed to the activated state (**Figures 4A,B**). For this site, stimulation at a low rate would produce variable effects on the slower frequency bands; at higher rates, the effect was mostly to decrease the power at low gamma frequency and higher. This effect was clear for the 5, 25, and 50 Hz stimulations, and was most potent during slow-wave activity. There was also an effect of the 25 and 50 Hz stimulation in increasing power in the delta band.

Stimulation of the vermis induced markedly different effects on the prefrontal cortex LFPs depending on the initial state. In the slow-wave state, 5 and 25 Hz stimulation induced a strong decrease in power in the beta to Fast frequency bands in both the right and left FrA. Stimulation at 1 Hz during the slow-wave state also had a strong effect: delta-to-beta activity decreased, while the low gamma-to-fast activity increased in the right FrA. In the activated state, however, stimulation using single pulses, and at 5, 25, and 50 Hz resulted in an overall increase in power across the delta-to-beta bands.

State-Dependent Effects of Stimulation

One of the main findings in our study is that the effects of stimulation were influenced by the stage of urethane anesthesia (Clement et al., 2008). This highlights the importance of the initial oscillatory state in determining the susceptibility of target structures for changes in LFP oscillations and entrainment within different frequency bands. Previous research investigating the effects of vermal stimulation on frontal oscillations in humans, cats, and rodents showed that low frequency stimulation mainly affects slow activity, while stimulating at higher frequencies increased activity in faster bands (Steriade, 1995; Schutter et al., 2003; Schutter and van Honk, 2006; Parker et al., 2017). Experiments reported here used various stimulation frequencies, and demonstrated a range of effects that were dependent on baseline oscillatory state.

Pathways Mediating the Effects of Stimulation

Reciprocal anatomical connections have been well established between the cerebellum and prefrontal cortex, via cerebello-thalamo-cortical and cortico-ponto-cerebellar pathways (Kelly and Strick, 2003; Strick et al., 2009; Watson et al., 2009, 2014; Buckner et al., 2011; Farzan et al., 2016), but how rhythmic cerebellar output modulates cortical activity is still an open question. The stimulation in the cerebellar vermis, in reaching the prefrontal cortex, likely coursed through the fastigial nucleus and then to the thalamus (Bostan et al., 2013; Lisberger and Thach, 2013). Stimulation of Purkinje cells, in the outermost layer of the cerebellum, leads to changes in the cerebellar output, which in turn modulates the output of deep cerebellar nuclei (DCN) (Oulad Ben Taib and Manto, 2013, 2016; Das et al., 2017). Because inputs from Purkinje cells to the DCN are inhibitory, increased activation of Purkinje cells with high frequency stimulation (Maeda et al., 2000b; Hallett, 2007) inhibits the tonic activity of the DCN. This would in turn decrease excitation in the thalamus. However, it is also quite possible that DCN neurons could also show rebound excitation (Buzsaki, 2006). Subsequent activation of extra-cerebellar areas via the thalamus may thus occur through rebound excitation within the DCN (Buzsaki, 2006; Hoebeek et al., 2010). This phenomenon has been reported mainly in thalamic, cortical, and DCN neurons (Grenier et al., 1998; Buzsaki, 2006; Hoebeek et al., 2010; Boehme et al., 2011). After the initial inhibition induced by stimulation, the T-channel is activated causing Ca^{2+} influx, which leads to a slow rebound spike. Thus, the initial hyperpolarization of the fastigial nuclei, induced by electrical stimulation of the vermis, would lead to a burst of rebound spikes in the DCN up to 100 ms after the hyperpolarization ceases. If these spikes occur in synchrony and interact with the necessary opposing currents (mixed cation current, I_h), oscillations could be generated and would then propagate to thalamocortical pathways (McCormick and Pape, 1990; Buzsaki, 2006). The emergence of different oscillatory patterns thus depends not only on the strength and frequency of the applied stimuli, but also on factors regulating the intrinsic excitability and rhythmicity of neurons. Indeed, in this mode, when the effects of stimulation on oscillations rely on rebound excitation mechanisms (high frequency stimulation), the initial state of the neuron strongly impacts the effects of inputs (Buzsaki, 2006). This is in line with the state-dependent effects of stimulation that we have found here, with stimulation at high frequencies (25 and 50 Hz) leading to greater changes when initially in the activated state, and stimulation at 1 Hz inducing more effects in the slow-wave state.

Low frequency stimulation on the other hand may cause a decrease in activity of Purkinje cells (Chen et al., 1997), which would reduce inhibitory input to the fastigial nucleus, and result in greater excitatory drive to the thalamus. In a study investigating responses to different types of stimulation, single-pulse stimulation of the cerebellar cortex (paravermal lobules VI/VII) increased the chance of spiking for a short period post-stimulation (after a latency of ∼8 ms), but did not alter the firing

frequency of DCN neurons (Hoebeek et al., 2010). Although the mechanisms are not fully understood, this effect on spike timing occurred in the absence of rebound excitation.

In this study, vermal stimulation could entrain cerebello-cortical networks. However, given the duration of the changes observed, stimulation was unlikely to have induced long-term potentiation (LTP). For instance, high frequency stimulation (100 Hz in bursts of 15 pulses, for a total of 1500 pulses) applied to the parallel fibers, in the most superficial layer of the cerebellar cortex, has been shown to induce LTP at synapses between parallel fibers and Purkinje cells (Jörntell and Ekerot, 2002). Therefore, although we did not assess induction of LTP in this study, the number of pulses delivered in our study was likely too low to lead to lasting plastic changes.

Cortical Effects

Our results show that the effects of stimulation are state-dependent. Indeed, LFP activity fluctuates in urethane-anesthetized rats in cyclic alternations that are similar to sleep stages (Clement et al., 2008). When applied in the slow-wave state, the faster (5, 25, and 50 Hz) stimulations produced a noticeable decrease in cortical power for the faster frequency bands. In the activated state, the same stimulations produced an overall increase in power across the slower bands. The bands most affected were thus markedly different between the two states. The influence of the initial brain state on the effects of stimulation has been investigated in humans, in studies using TMS or direct cortical stimulation, as well as in rats (Jackson et al., 2008; Alagapan et al., 2016; Connolly et al., 2016; Silvanto et al., 2017).

The effects of the stimulation at 1 and 25 Hz provide good examples of this modulation by state. During the slow-wave state, 1 Hz stimulation would increase power in the 30–200 Hz range, while decreasing power in the 0–30 Hz band, however, 1 Hz stimulation did not show any effects in cortical sites during the activated state. The effects produced by 1 Hz stimulation can be interpreted partially by the mechanism of generation of slow-wave activity in thalamocortical networks, modulated by thalamic neuronal activity. Delta activity in the brain, sleeping and anesthetized, stems from an interaction between thalamic and cortical oscillators (Steriade, 2003). Optogenetic stimulation of thalamocortical neurons at 1 Hz triggers their firing of bursts of action potentials, and is also an optimal frequency for inducing cortical slow waves; stimulations at 1.5 Hz or higher on the other hand failed to entrain EEG activity (David et al., 2013). It is possible that 1 Hz stimulation of the cerebellar cortex in our recordings disrupted thalamic mechanisms that mediate delta activity, in a manner specific to the slow-wave state. This could decrease activity in the delta range while increasing activity in faster frequency bands. Optogenetic stimulation of cerebellar projections at 2 Hz was also shown to re-establish normal levels of delta activity in an awake rat model of schizophrenia, which shows lower delta activity in the medial frontal cortex similar to observations in schizophrenic patients (Parker et al., 2017). The threshold stimulation frequency for the cerebellar cortex to entrain delta activity would likely then be affected by the initial state in the cerebral cortex. As our results show, the initial state strongly affects the optimal stimulation pattern for entrainment at various frequencies.

Conversely, in the slow-wave state, 25 Hz stimulation produced a decrease of power in a wide range of higher frequencies (15–200 Hz), while inducing a strong increase in the 0–55 Hz band in cortical sites during the activated state. This can be compared to the work of Steriade (1995), who used 300 Hz stimulation of the fastigial nucleus in ketamine/xylazine anesthetized cats, and showed an attenuation of slow rhythms, and an enhancement of 20–40 Hz oscillatory activity in the frontal cortex. We did not find this strong effect of high-frequency stimulation in decreasing slow-wave activity in our recordings, but we did find an increase in beta/gamma power following 25 Hz stimulation in the activated state. In addition, using stimulation at 100–200 Hz of the brachium conjunctivum (i.e., afferents to the thalamus from the cerebellar nuclei), the same team (Timofeev and Steriade, 1997) found an activation of the cat EEG at 30–100 Hz during ketamine/xylazine anesthesia. Again, we found a similar increase in power in these bands only during 25 Hz stimulation in the activated state. Differences in these results could be due in part to the type of anesthetic used, or to the different axon conduction speed and synaptic delays characteristic of different species (Buzsáki et al., 2013). Differences could also be due to the much higher stimulation frequencies used in those studies (Steriade, 1995; Timofeev and Steriade, 1997). In the rat, in order to increase motor cortical excitability, stimulation of the lateral cerebellar nucleus at different frequencies showed a greater facilitation at 30 Hz, similar to our effects at 25 Hz in the activated state (Baker et al., 2010). Similarly, stimulation of the same nucleus at 30–50 Hz increased contralateral cortical excitability, measured as motor evoked potentials, in a rat model of stroke (Park et al., 2015). It would be interesting to monitor the oscillatory state differences prior to stimulation in these awake animals, as it could have played a role in the optimal responsivity to stimulation. Overall, it does appear that prefrontal cortex networks can generate and resonate with beta and gamma rhythms and that activity in these bands can be modulated by cerebellar output (Sherfey et al., 2018).

Cerebellar Effects and Minimal Effects on Cerebello-Cortical Coherence

We assessed here whether different frequencies of patterned stimulation can entrain cerebellar frequency-specific patterns that have been previously described (Courtemanche et al., 2013). In the slow-wave state, stimulation at 1 and 50 Hz produced more effects on cerebellar oscillatory activity. These stimulation frequencies caused an augmentation of 8–30 Hz power, which corresponds to the range of oscillatory activity in the granule cell layer (GCL) of the cerebellum, and this effect could have been mediated directly, or through pathways projecting to the GCL such as the parallel fibers. In addition, stimulation at 50 Hz also caused a strong increase in delta power, which could be due in part by the brief nature of this stimulation train, which may have activated multiple cerebellar units in-phase, likely through parallel fibers, especially if the

stimulation was timed with the ascending phase or peak of a slow rhythm. In the activated state, effects within the 8–30 Hz range were mostly absent, but stimulations at 25 and 50 Hz had strong effects on the 0–8 Hz activity in the cerebellum. This could be again due to a phasic increase in excitation timed with a slow cerebellar rhythm. The 5 Hz stimulation also increased power in the theta band, potentially affecting a theta-related oscillatory pattern already present in the cerebellum (Courtemanche et al., 2013).

Our results showed significant effects of stimulation mainly for measures of power across frequency bands, and less so for coherence measures. Synchronized activity between the cerebellum and cortex has been observed in a variety of contexts. Coherent activity in the alpha and beta frequency ranges occurs in the cerebellum and sensorimotor cortex during actions requiring somatosensory monitoring (O'Connor et al., 2002; Courtemanche and Lamarre, 2005). Functionally as well, synchronization of LFPs between the medial prefrontal cortex and the cerebellum at 5–12 Hz has been linked with adaptive performance in eyeblink conditioning during the early stages of learning (Chen et al., 2016). Multiple brain regions, including the amygdala, hippocampus, medial prefrontal cortex, and cerebellum must coordinate to acquire a variety of learned responses, such as the conditioned eyelid response in the eyeblink conditioning paradigm (Lee and Kim, 2004). Coherent activity between the cerebellum and prefrontal cortex across a variety of bands may thus contribute to acquiring appropriate behaviors through associative learning and during performance. There are other clear indications that the cerebellum is important in cortical synchronization (Courtemanche et al., 2013). The functional role of the cerebellum in gamma-band coherence between areas of the cerebral cortex has been demonstrated in rats; inactivating the cerebellum with a muscimol injection disrupted cortical coherence in gamma between the sensory and motor cortices, potentially interrupting transmission of sensorimotor information between these areas (Popa et al., 2013). Finally, a recent study also showed Purkinje cell simple spike timing is related to coherent cerebral cortical oscillatory activity (McAfee et al., 2019).

Why did we not find clear effects on coherence? An obvious first consideration is the anesthetic state. The anesthetic state carries with it clearly different patterns of large-scale oscillations and coherence than the awake state (Steriade, 2003), but urethane anesthesia has been shown to be permissive to network oscillations (Maggi and Meli, 1986; Clement et al., 2008; Frederick et al., 2014; Robinson et al., 2017). Coherent activity in our preparation was abundant (see **Figure 3**), and the coherent slow-wave state represented a majority of the total duration of our recordings (e.g., see **Figure 2**). Ros et al. (2009) have shown that the cerebellum can generate slow oscillations that are synchronized with those of the neocortex, and that neocortical oscillations drive cerebellar rhythms. The strong slow-wave state throughout the recordings may have hindered our capacity to detect coherence effects. The state of the network in this study was likely similar to a resting-state condition, first described in idling states and during early stages of sleep in fMRI studies, but also in the anesthetized state in humans, monkeys, and rodents (Lu et al., 2007; Raichle, 2015). It is thus quite possible that during anesthesia, as in sleep, large-scale coherent slow-wave mechanisms protect the cortical circuits from outside disturbance via the thalamocortical circuit isolation properties (Steriade, 2003), and that this may reduce effects of stimulation on coherence. It is possible that over our particular anesthesia modes, coherent activity between sites acts as a filtering mechanism to suppress external inputs, as happens during functional inhibition to optimize performance (Courtemanche et al., 2003; Jensen and Mazaheri, 2010). Another consideration is that the placement of our frontal lobe recording electrodes and/or our cerebellar stimulation electrodes was perhaps not optimal to evaluate between-site synchrony. The methodological approach of evaluating the location of cerebral cortical best response to stimulation through evoked potentials could help determine an optimal electrode alignment (Watson et al., 2009, 2014) and might further help in finding coherent sites.

Effects of Cerebellar Stimulation on Frontal Cortical Networks

Cerebro-cerebellar loops involving prefrontal cortical areas have received increased attention over the last few decades. The initial explorations concerned cerebro-cerebellar relationships in sensorimotor circuits (Allen and Tsukahara, 1974; Sasaki, 1979; Bloedel and Courville, 1981; Morissette and Bower, 1996; Courtemanche and Lamarre, 2005). In parallel, the identification of cognitive roles for the cerebellum was being progressively characterized through neuropsychological testing and studies in patients (Leiner et al., 1991; Akshoomoff and Courchesne, 1992; Courchesne et al., 1994; Akshoomoff et al., 1997; Mangels et al., 1998). Advances in brain imaging also indicated a cerebellar role in cognition (Roland, 1993; Allen et al., 1997, 2005; Schmahmann, 1997; Allen and Courchesne, 2003; Buckner, 2013; Schmahmann, 2019). Anatomical reports showed precise functional connections between the cerebellum and prefrontal cortex in the primate (Schmahmann and Pandya, 1997a,b; Kelly and Strick, 2003) which could mediate cerebro-cerebellar loops involved in cognitive operations. The cerebello-cerebral connectivity displays multiple parallel loops mediating processes related to sensation, movement, and thought (Middleton and Strick, 2000; Strick et al., 2009; Bostan et al., 2013; Bostan and Strick, 2018). Even though the nature of the prefrontal cortex in rodents is the object of some debate, multiple cognitive and executive functions are performed by prefrontal cortex or similar regions in rats (Kolb, 1984; Uylings et al., 2003; Dalley et al., 2004; Kesner and Churchwell, 2011; Leonard, 2016). Cerebello-prefrontal cortex connectivity has also been confirmed using physiological and anatomical measures (Suzuki et al., 2012), and has been explored electrophysiologically, by evaluating cerebellar evoked potential and cellular responses obtained through medial prefrontal cortical stimulation, as well as through measures of prefrontal cortex neurophysiological activity following fastigial nucleus stimulation (Watson et al., 2009; Watson et al., 2014). In addition, related to the results

presented here, Watson et al. (2014) found a cerebello-cerebral directed coherence pattern in the theta range that was prominent during active locomotion, showing that these connections could support cerebello-cerebral communication. Our current study has contributed to understanding how different frequencies of cerebellar oscillations modulate oscillations and coherent activity within cerebello-cortical networks (Courtemanche et al., 2013).

The effects of cerebellar stimulation on the activity of cerebello-prefrontal loops remains largely unexplored in the rat, in which the underlying neuronal pathways and mechanisms can be assessed. Our findings show that even under anesthesia, cerebello-cortical network interactions can be modulated through cerebellar stimulation. A multi-site multi-electrode approach could enhance the fine-grained mapping through evoked responses and/or unit activity to study the spatio-temporal properties of cerebello-cortical connectivity. Such an approach would also allow changes in evoked synaptic responses to be monitored in association with ongoing EEG rhythms and state (Ozen et al., 2010; Marquez-Ruiz et al., 2014), to provide some insight into the strength of synaptic pathways during oscillations (Timofeev et al., 1996; Rosanova and Timofeev, 2005). Future studies could also investigate the effects of cerebellar stimulation in awake animals, during behavior or rest. These would require the study of oscillatory and synchronous networks at smaller timescales, with analytical methods able to follow fast changes in network configuration, such as phase synchrony analysis (Lachaux et al., 1999). The initial oscillatory or activation state can be expected to strongly impact the effects of stimulation. In the activated state, the cerebellar stimulation with single-pulses, as well as with repeated pulses at 25 Hz, was optimal in generating increased delta-gamma band activity, which could correspond to an analog of cortical cross-frequency entrainment (Helfrich et al., 2014, 2016). It would also be interesting to test the physiological effects of cross-frequency coupled nested rhythms in the awake-behaving animal. As the cerebellum contributes to higher-order functions, understanding how cerebello-cerebral loops operate and respond to stimulation is essential in uncovering the underlying physiology, but also in developing new methods to address numerous disorders.

DATA AVAILABILITY STATEMENT

The datasets generated for this study are available on request to the corresponding author.

ETHICS STATEMENT

The animal study was reviewed and approved by Concordia University Animal Research Ethics Committee.

AUTHOR CONTRIBUTIONS

ST, CC, and RC designed and prepared the experiments, acquired the data, and wrote the manuscript. ST and RC analyzed the data.

FUNDING

Funding for this study was provided by a grant from the Concordia VPRGS to RC and CC, and from grants from the FRQS (Québec) to the Center for Studies in Behavioral Neurobiology. CC was funded by NSERC. ST received the William R. Sellers graduate award for this thesis work.

ACKNOWLEDGMENTS

We thank Dr. Thanh Dang-Vu for comments on the design and data analysis of the study, to Dr. Jennifer Robinson for support in some experiments, to Ariana Frederick for graphical examples, and to Marie-Ève Dumas for providing some coding support in the analysis.

SUPPLEMENTARY MATERIAL

The Supplementary Material for this article can be found online at: https://www.frontiersin.org/articles/10.3389/fnsys.2019.00060/full#supplementary-material

REFERENCES

Akgören, N., Dalgaard, P., and Lauritzen, M. (1996). Cerebral blood flow increases evoked by electrical stimulation of rat cerebellar cortex: relation to excitatory synaptic activity and nitric oxide synthesis. *Brain Res.* 710, 204–214.

Akshoomoff, N. A., and Courchesne, E. (1992). A new role for the cerebellum in cognitive operations. *Behav. Neurosci.* 106, 731–738.

Akshoomoff, N. A., Courchesne, E., and Townsend, J. (1997). Attention coordination and anticipatory control. *Int. Rev. Neurobiol.* 41, 575–598.

Alagapan, S., Schmidt, S. L., Lefebvre, J., Hadar, E., Shin, H. W., and Fröhlich, F. (2016). Modulation of cortical oscillations by low-frequency direct cortical stimulation is state-dependent. *PLoS Biol.* 14:e1002424. doi: 10.1371/journal.pbio.1002424

Allen, G., Buxton, R. B., Wong, E. C., and Courchesne, E. (1997). Attentional activation of the cerebellum independent of motor involvement. *Science* 275, 1940–1943.

Allen, G., and Courchesne, E. (2003). Differential effects of developmental cerebellar abnormality on cognitive and motor functions in the cerebellum: an fMRI study of autism. *Am. J. Psychiatry* 160, 262–273.

Allen, G., McColl, R., Barnard, H., Ringe, W. K., Fleckenstein, J., Cullum, C. M., et al. (2005). Magnetic resonance imaging of cerebellar-prefrontal and cerebellar-parietal functional connectivity. *Neuroimage* 28, 39–48.

Allen, G. I., and Tsukahara, N. (1974). Cerebrocerebellar communication systems. *Physiol. Rev.* 54, 957–1006.

Andreasen, N. C., O'Leary, D. S., Cizadlo, T., Arndt, S., Rezai, K., Ponto, L., et al. (1996). Schizophrenia and cognitive dysmetria: a positron-emission tomography study of dysfunctional prefrontal-thalamic-cerebellar circuitry. *Proc. Natl. Acad. Sci. U.S.A.* 93, 9985–9990.

Andreasen, N. C., and Pierson, R. (2008). The role of the cerebellum in schizophrenia. *Biol. Psychol.* 64, 81–88.

Baker, K. B., Schuster, D., Cooperrider, J., and Machado, A. G. (2010). Deep brain stimulation of the lateral cerebellar nucleus produces frequency-specific

alterations in motor evoked potentials in the rat in vivo. *Exp. Neurol.* 226, 259–264. doi: 10.1016/j.expneurol.2010.08.019

Baxter, L. R., Schwartz, J. M., Phelps, M. E., Mazziotta, J. C., Guze, B. H., Selin, C. E., et al. (1989). Reduction of prefrontal cortex glucose metabolism common to three types of depression. *Arch.Gen.Psychiatry* 46:243.

Bloedel, J. R., and Courville, J. (1981). "Cerebellar afferent systems," in *Handbook of Physiology. Section 1: The Nervous System. Volume II. Motor Control, Part 2*, ed. V. B. Brooks (Bethesda: American Physiological Society), 735–829.

Boehme, R., Uebele, V. N., Renger, J. J., and Pedroarena, C. (2011). Rebound excitation triggered by synaptic inhibition in cerebellar nuclear neurons is suppressed by selective T-type calcium channel block. *J. Neurophysiol.* 106, 2653–2661. doi: 10.1152/jn.00612.2011

Bostan, A. C., Dum, R. P., and Strick, P. L. (2013). Cerebellar networks with the cerebral cortex and basal ganglia. *Trends Cogn. Sci.* 17, 241–254. doi: 10.1016/j.tics.2013.03.003

Bostan, A. C., and Strick, P. L. (2018). The basal ganglia and the cerebellum: nodes in an integrated network. *Nat. Rev. Neurosci.* 19, 338–350. doi: 10.1038/s41583-018-0002-7

Buckner, R. L. (2013). The cerebellum and cognitive function: 25 years of insight from anatomy and neuroimaging. *Neuron* 80, 807–815. doi: 10.1016/j.neuron.2013.10.044

Buckner, R. L., Krienen, F. M., Castellanos, A., Diaz, J. C., and Yeo, B. T. T. (2011). The organization of the human cerebellum estimated by intrinsic functional connectivity. *J. Neurophysiol.* 106, 2322–2345. doi: 10.1152/jn.00339.2011

Buzsaki, G. (2006). *Rhythms of the Brain*. New York, NY: Oxford University Press.

Buzsaki, G., Anastassiou, C. A., and Koch, C. (2012). The origin of extracellular fields and currents–EEG, ECoG, LFP and spikes. *Nat. Rev. Neurosci.* 13, 407–420. doi: 10.1038/nrn3241

Buzsáki, G., Logothetis, N., and Singer, W. (2013). Scaling brain size, keeping timing: evolutionary preservation of brain rhythms. *Neuron* 80, 751–764. doi: 10.1016/j.neuron.2013.10.002

Cerminara, N. L., Lang, E. J., Sillitoe, R. V., and Apps, R. (2015). Redefining the cerebellar cortex as an assembly of non-uniform Purkinje cell microcircuits. *Nat. Rev. Neurosci.* 16, 79–93. doi: 10.1038/nrn3886

Chen, H., Wang, Y.-J., Yang, L., Sui, J.-F., Hu, Z.-A., Hu, B., et al. (2016). Theta synchronization between medial prefrontal cortex and cerebellum is associated with adaptive performance of associative learning behavior. *Sci. Rep.* 6:20960. doi: 10.1038/srep20960

Chen, R., Classen, J., Gerloff, C., Celnik, P., Wassermann, E., Hallett, M., et al. (1997). Depression of motor cortex excitability by low-frequency transcranial magnetic stimulation. *Neurology* 48, 1398–1403.

Clement, E. A., Richard, A., Thwaites, M., Ailon, J., Peters, S., Dickson, C. T., et al. (2008). Cyclic and sleep-like spontaneous alternations of brain state under urethane anaesthesia. *PLoS One* 3:e2004. doi: 10.1371/journal.pone.0002004

Connolly, M. J., Gross, R. E., and Mahmoudi, B. (2016). The influence of the pre-stimulation neural state on the post-stimulation neural dynamics via distributed microstimulation of the hippocampus. *Conf. Proc. IEEE Eng. Med. Biol. Soc.* 2016, 1810–1813. doi: 10.1109/EMBC.2016.7591070

Courchesne, E., Townsend, J., Akshoomoff, N. A., Saitoh, O., Yeung-Courchesne, R., Lincoln, A. J., et al. (1994). Impairment in shifting attention in autistic and cerebellar patients. *Behav. Neurosci.* 108, 848–865.

Courtemanche, R., Fujii, N., and Graybiel, A. M. (2003). Synchronous, focally modulated beta-band oscillations characterize local field potential activity in the striatum of awake behaving monkeys. *J. Neurosci.* 23, 11741–11752.

Courtemanche, R., and Lamarre, Y. (2005). Local field potential oscillations in primate cerebellar cortex: synchronization with cerebral cortex during active and passive expectancy. *J. Neurophysiol.* 93, 2039–2052.

Courtemanche, R., Robinson, J. C., and Aponte, D. I. (2013). Linking oscillations in cerebellar circuits. *Front. Neural. Circ.* 7:125. doi: 10.3389/fncir.2013.00125

Dalley, J. W., Cardinal, R. N., and Robbins, T. W. (2004). Prefrontal executive and cognitive functions in rodents: neural and neurochemical substrates. *Neurosci. Biobehav. Rev.* 28, 771–784.

Das, S., Spoor, M., Sibindi, T. M., Holland, P., Schonewille, M., De Zeeuw, C. I., et al. (2017). Impairment of long-term plasticity of cerebellar purkinje cells eliminates the effect of anodal direct current stimulation on vestibulo-ocular reflex habituation. *Front. Neurosci.* 11:44. doi: 10.3389/fnins.2017.00444

David, F., Schmiedt, J. T., Taylor, H. L., Orban, G., Di Giovanni, G., Uebele, V. N., et al. (2013). Essential thalamic contribution to slow waves of natural sleep. *J. Neurosci.* 33, 19599–19610. doi: 10.1523/JNEUROSCI.3169-13.2013

Demirtas-Tatlidede, A., Freitas, C., Cromer, J. R., Safar, L., Ongur, D., Stone, W. S., et al. (2010). Safety and proof of principle study of cerebellar vermal theta burst stimulation in refractory schizophrenia. *Schizophr. Res.* 124, 91–100. doi: 10.1016/j.schres.2010.08.015

Dugué, G. P., Brunel, N., Hakim, V., Schwartz, E., Chat, M., Lévesque, M., et al. (2009). Electrical coupling mediates tunable low-frequency oscillations and resonance in the cerebellar golgi cell network. *Neuron* 61, 126–139. doi: 10.1016/j.neuron.2008.11.028

Engel, A. K., Fries, P., and Singer, W. (2001). Dynamic predictions: oscillations and synchrony in top–down processing. *Nat. Rev. Neurosci.* 2:704.

Farzan, F., Pascual-Leone, A., Schmahmann, J. D., and Halko, M. (2016). Enhancing the temporal complexity of distributed brain networks with patterned cerebellar stimulation. *Sci. Rep.* 6:23599. doi: 10.1038/srep23599

Fatemi, S. H., Aldinger, K. A., Ashwood, P., Bauman, M. L., Blaha, C. D., Blatt, G. J., et al. (2012). Consensus paper: pathological role of the cerebellum in autism. *Cerebellum* 11, 777–807. doi: 10.1007/s12311-012-0355-9

Frederick, A., Bourget-Murray, J., Chapman, C. A., Amir, S., and Courtemanche, R. (2014). Diurnal influences on electrophysiological oscillations and coupling in the dorsal striatum and cerebellar cortex of the anesthetized rat. *Front. Syst. Neurosci.* 8:145. doi: 10.3389/fnsys.2014.00145

Fries, P. (2015). Rhythms for cognition: communication through coherence. *Neuron* 88, 220–235. doi: 10.1016/j.neuron.2015.09.034

Grenier, F., Timofeev, I., and Steriade, M. (1998). Leading role of thalamic over cortical neurons during postinhibitory rebound excitation. *Proc. Natl. Acad. Sci. U.S.A.* 95, 13929–13934.

Hallett, M. (2007). Transcranial magnetic stimulation: a primer. *Neuron* 55, 187–199.

Helfrich, R. F., Herrmann, C. S., Engel, A. K., and Schneider, T. R. (2016). Different coupling modes mediate cortical cross-frequency interactions. *Neuroimage* 140, 76–82. doi: 10.1016/j.neuroimage.2015.11.035

Helfrich, R. F., Schneider, T. R., Rach, S., Trautmann-Lengsfeld, S. A., Engel, A. K., and Herrmann, C. S. (2014). Entrainment of brain oscillations by transcranial alternating current stimulation. *Curr. Biol.* 24, 333–339. doi: 10.1016/j.cub.2013.12.041

Hoebeek, F. E., Witter, L., Ruigrok, T. J., and De Zeeuw, C. I. (2010). Differential olivo-cerebellar cortical control of rebound activity in the cerebellar nuclei. *Proc. Natl. Acad. Sci. U.S.A.* 107, 8410–8415. doi: 10.1073/pnas.0907118107

Hoppenbrouwers, S. S., Schutter, D. J. L. G., Fitzgerald, P. B., Chen, R., and Daskalakis, Z. J. (2008). The role of the cerebellum in the pathophysiology and treatment of neuropsychiatric disorders: a review. *Brain Res. Brain Res. Rev.* 59:185. doi: 10.1016/j.brainresrev.2008.07.005

Jackson, J., Dickson, C. T., and Bland, B. H. (2008). Median raphe stimulation disrupts hippocampal theta via rapid inhibition and state-dependent phase reset of theta-related neural circuitry. *J. Neurophysiol.* 99, 3009–3026. doi: 10.1152/jn.00065.2008

Jensen, O., and Mazaheri, A. (2010). Shaping functional architecture by oscillatory alpha activity: gating by inhibition. *Front. Human Neurosci.* 4:186. doi: 10.3389/fnhum.2010.00186

Jörntell, H., and Ekerot, C.-F. (2002). Reciprocal bidirectional plasticity of parallel fiber receptive fields in cerebellar Purkinje cells and their afferent interneurons. *Neuron* 34, 797–806.

Kelly, R. M., and Strick, P. L. (2003). Cerebellar loops with motor cortex and prefrontal cortex of a nonhuman primate. *J. Neurosci.* 23, 8432–8444.

Kesner, R. P., and Churchwell, J. C. (2011). An analysis of rat prefrontal cortex in mediating executive function. *Neurobiol. Learn. Mem.* 96, 417–431. doi: 10.1016/j.nlm.2011.07.002

Koenigs, M., and Grafman, J. (2009). The functional neuroanatomy of depression: distinct roles for ventromedial and dorsolateral prefrontal cortex. *Behav. Brain Res.* 201, 239–243. doi: 10.1016/j.bbr.2009.03.004

Kolb, B. (1984). Functions of the frontal cortex of the rat: a comparative review. *Brain Res.* 320, 65–98.

Lachaux, J. P., Rodriguez, E., Martinerie, J., and Varela, F. J. (1999). Measuring phase synchrony in brain signals. *Hum. Brain Mapp.* 8, 194–208.

Lee, T., and Kim, J. J. (2004). Differential effects of cerebellar, amygdalar, and hippocampal lesions on classical eyeblink conditioning in rats. *J. Neurosci.* 24, 3242–3250.

Leiner, H. C., Leiner, A. L., and Dow, R. S. (1991). The human cerebro-cerebellar system: its computing, cognitive, and language skills. *Behav. Brain Res.* 44, 113–128.

Leonard, C. M. (2016). Finding prefrontal cortex in the rat. *Brain Res.* 1645, 1–3. doi: 10.1016/j.brainres.2016.02.002

Lisberger, S. G., and Thach, W. T. (2013). "The Cerebellum," in *Principles of Neural Science*, 5th Edn, eds E. R. Kandel, J. H. Schwartz, T. M. Jessell, S. A. Siegelbaum, and A. J. Hudspeth (New York, NY: McGraw-Hill), 960–981.

Lu, H., Zuo, Y., Gu, H., Waltz, J. A., Zhan, W., Scholl, C. A., et al. (2007). Synchronized delta oscillations correlate with the resting-state functional MRI signal. *Proc. Natl. Acad. Sci. U.S.A.* 104, 18265–18269.

Maeda, F., Keenan, J. P., and Pascual-Leone, A. (2000a). Interhemispheric asymmetry of motor cortical excitability in major depression as measured by transcranial magnetic stimulation. *Br. J. Psychiatry* 177:169.

Maeda, F., Keenan, J. P., Tormos, J. M., Topka, H., and Pascual-Leone, A. (2000b). Interindividual variability of the modulatory effects of repetitive transcranial magnetic stimulation on cortical excitability. *Exp. Brain Res.* 133:425.

Maggi, C. A., and Meli, A. (1986). Suitability of urethane anesthesia for physiopharmacological investigations in various systems. Part 1: general considerations. *Experientia* 42, 109–114.

Mangels, J. A., Ivry, R. B., and Shimizu, N. (1998). Dissociable contributions of the prefrontal and neocerebellar cortex to time perception. *Cogn. Brain Res.* 7, 15–39.

Marquez-Ruiz, J., Leal-Campanario, R., Wendling, F., Ruffini, G., Gruart, A., Delgado-Garcia, J. M., et al. (2014). "Transcranial electrical stimulation in animals," in *The Stimulated Brain*, ed. R. C. Kadosh (London, UK: Academic Press), 117–144.

McAfee, S. S., Liu, Y., Sillitoe, R. V., and Heck, D. H. (2019). Cerebellar lobulus simplex and crus I differentially represent phase and phase difference of prefrontal cortical and hippocampal oscillations. *Cell Rep.* 27:2328-2334.e3. doi: 10.1016/j.celrep.2019.04.085

McCormick, D. A., and Pape, H. C. (1990). Properties of a hyperpolarization-activated cation current and its role in rhythmic oscillation in thalamic relay neurones. *J. Physiol.* 431, 291–318.

Middleton, F. A., and Strick, P. L. (2000). Basal ganglia and cerebellar loops: motor and cognitive circuits. *Brain Res. Brain Res. Rev.* 31, 236–250.

Morissette, J., and Bower, J. M. (1996). Contribution of somatosensory cortex to responses in the rat cerebellar granule cell layer following peripheral tactile stimulation. *Exp. Brain Res.* 109, 240–250.

O'Connor, S., Berg, R. W., and Kleinfeld, D. (2002). Coherent electrical activity between vibrissa sensory areas of cerebellum and neocortex is enhanced during free whisking. *J. Neurophysiol.* 87, 2137–2148.

O'Reilly, J. X., Beckmann, C. F., Tomassini, V., Ramnani, N., and Johansen-Berg, H. (2009). Distinct and overlapping functional zones in the cerebellum defined by resting state functional connectivity. *Cereb. Cortex* 20, 953–965. doi: 10.1093/cercor/bhp157

Oulad Ben Taib, N., and Manto, M. (2013). Trains of epidural DC stimulation of the cerebellum tune corticomotor excitability. *Neural Plast.* 2013:613197. doi: 10.1155/2013/613197

Oulad Ben Taib, N., and Manto, M. (2016). The in vivo reduction of afferent facilitation induced by low frequency electrical stimulation of the motor cortex is antagonized by cathodal direct current stimulation of the cerebellum. *Cereb. Ataxias* 3:15. doi: 10.1186/s40673-016-0053-3

Ozen, S., Sirota, A., Belluscio, M. A., Anastassiou, C. A., Stark, E., Koch, C., et al. (2010). Transcranial electric stimulation entrains cortical neuronal populations in rats. *J. Neurosci.* 30, 11476–11485. doi: 10.1523/JNEUROSCI.5252-09.2010

Park, H.-J., Furmaga, H., Cooperrider, J., Gale, J. T., Baker, K. B., Machado, A. G., et al. (2015). Modulation of cortical motor evoked potential after stroke during electrical stimulation of the lateral cerebellar nucleus. *Brain Stimul.* 8, 1043–1048. doi: 10.1016/j.brs.2015.06.020

Parker, K., Kim, Y., Kelley, R., Nessler, A., Chen, K., Muller-Ewald, V., et al. (2017). Delta-frequency stimulation of cerebellar projections can compensate for schizophrenia-related medial frontal dysfunction. *Mol. Psychiatry* 22:647. doi: 10.1038/mp.2017.50

Popa, D., Spolidoro, M., Proville, R. D., Guyon, N., Belliveau, L., and Léna, C. (2013). Functional role of the cerebellum in gamma-band synchronization of the sensory and motor cortices. *J. Neurosci.* 33, 6552–6556. doi: 10.1523/JNEUROSCI.5521-12.2013

Raichle, M. E. (2015). The brain's default mode network. *Ann. Rev. Neurosci.* 38, 433–447.

Robinson, J. C., Chapman, C. A., and Courtemanche, R. (2017). Gap junction modulation of low-frequency oscillations in the cerebellar granule cell layer. *Cerebellum* 16, 802–811. doi: 10.1007/s12311-017-0858-5

Roland, P. E. (1993). Partition of the human cerebellum in sensory-motor activities, learning and cognition. *Can. J. Neurol. Sci.* 20(Suppl. 3), S75–S77.

Ros, H., Sachdev, R. N., Yu, Y., Sestan, N., and McCormick, D. A. (2009). Neocortical networks entrain neuronal circuits in cerebellar cortex. *J. Neurosci.* 29, 10309–10320. doi: 10.1523/JNEUROSCI.2327-09.2009

Rosanova, M., and Timofeev, I. (2005). Neuronal mechanisms mediating the variability of somatosensory evoked potentials during sleep oscillations in cats. *J. Physiol.* 562, 569–582.

Sang, L., Qin, W., Liu, Y., Han, W., Zhang, Y., Jiang, T., et al. (2012). Resting-state functional connectivity of the vermal and hemispheric subregions of the cerebellum with both the cerebral cortical networks and subcortical structures. *Neuroimage* 61, 1213–1225. doi: 10.1016/j.neuroimage.2012.04.011

Sasaki, K. (1979). "Cerebro-cerebellar interconnections in cats and monkeys," in *Cerebro-Cerebellar Interactions*, eds J. Massion, and K. Sasaki (Amsterdam: Elsevier/North-Holland Biomedical Press), 105–124.

Schmahmann, J. D. (1997). *The Cerebellum and Cognition - International Review of Neurobiology*. San Diego, CA: Academic Press.

Schmahmann, J. D. (2004). Disorders of the cerebellum: ataxia, dysmetria of thought, and the cerebellar cognitive affective syndrome. *J. Neuropsychiatry Clin. Neurosci.* 16:367.

Schmahmann, J. D. (2019). The cerebellum and cognition. *Neurosci. Lett.* 688, 62–75. doi: 10.1016/j.neulet.2018.07.005

Schmahmann, J. D., and Pandya, D. N. (1997a). Anatomic organization of the basilar pontine projections from prefrontal cortices in rhesus monkey. *J. Neurosci.* 17, 438–458.

Schmahmann, J. D., and Pandya, D. N. (1997b). The cerebrocerebellar system. *Int. Rev. Neurobiol.* 41:31–60.

Schutter, D. J., van Honk, J., d'Alfonso, A. A., Peper, J. S., and Panksepp, J. (2003). High frequency repetitive transcranial magnetic over the medial cerebellum induces a shift in the prefrontal electroencephalography gamma spectrum: a pilot study in humans. *Neurosci. Lett.* 336, 73–76.

Schutter, D. J. L. G., and van Honk, J. (2006). An electrophysiological link between the cerebellum, cognition and emotion: frontal theta EEG activity to single-pulse cerebellar TMS. *NeuroImage* 33, 1227–1331.

Schutter, D. J. L. G., and van Honk, J. (2009). The cerebellum in emotion regulation: a repetitive transcranial magnetic stimulation study. *Cerebellum* 8, 28–34. doi: 10.1007/s12311-008-0056-6

Sherfey, J. S., Ardid, S., Hass, J., Hasselmo, M. E., and Kopell, N. J. (2018). Flexible resonance in prefrontal networks with strong feedback inhibition. *PLoS Comput. Biol.* 14:e1006357. doi: 10.1371/journal.pcbi.1006357

Silvanto, J., Bona, S., and Cattaneo, Z. (2017). Initial activation state, stimulation intensity and timing of stimulation interact in producing behavioral effects of TMS. *Neuroscience* 363, 134–141. doi: 10.1016/j.neuroscience.2017.09.002

Steriade, M. (1995). Two channels in the cerebellothalamocortical system. *J. Comp. Neurol.* 354, 57–70.

Steriade, M. (2003). *Neuronal Substrates of Sleep and Epilepsy*. Cambridge: Cambridge University Press.

Strick, P. L., Dum, R. P., and Fiez, J. A. (2009). Cerebellum and nonmotor function. *Ann. Rev. Neurosci.* 32, 413–434.

Suzuki, L., Coulon, P., Sabel-Goedknegt, E. H., and Ruigrok, T. J. (2012). Organization of cerebral projections to identified cerebellar zones in the posterior cerebellum of the rat. *J. Neurosci.* 32, 10854–10869. doi: 10.1523/JNEUROSCI.0857-12.2012

Timofeev, I., Contreras, D., and Steriade, M. (1996). Synaptic responsiveness of cortical and thalamic neurones during various phases of slow sleep oscillation in cat. *J. Physiol.* 494(Pt 1), 265–278.

Timofeev, I., and Steriade, M. (1997). Fast (mainly 30-100 Hz) oscillations in the cat cerebellothalamic pathway and their synchronization with cortical potentials. *J. Physiol.* 504, 153–168.

Uylings, H. B., Groenewegen, H. J., and Kolb, B. (2003). Do rats have a prefrontal cortex? *Behav. Brain Res.* 146, 3–17.

van Dun, K., Bodranghien, F., Manto, M., and Marien, P. (2017). Targeting the cerebellum by noninvasive neurostimulation: a review. *Cerebellum* 16, 695–741. doi: 10.1007/s12311-016-0840-7

van Dun, K., Mitoma, H., and Manto, M. (2018). Cerebellar cortex as a therapeutic target for neurostimulation. *Cerebellum* 17, 777–787. doi: 10.1007/s12311-018-0976-8

Wang, S., Wu, D.-C., Ding, M.-P., Li, Q., Zhuge, Z.-B., Zhang, S.-H., et al. (2008). Low-frequency stimulation of cerebellar fastigial nucleus inhibits amygdaloid kindling acquisition in sprague-dawley rats. *Neurobiol. Dis.* 29, 52–58.

Watson, T. C., Becker, N., Apps, R., and Jones, M. W. (2014). Back to front: cerebellar connections and interactions with the prefrontal cortex. *Front. Syst. Neurosci.* 8:4. doi: 10.3389/fnsys.2014.00004

Watson, T. C., Jones, M. W., and Apps, R. (2009). Electrophysiological mapping of novel prefrontal-cerebellar pathways. *Front. Integ. Neurosci.* 3:18. doi: 10.3389/neuro.07.018.2009

Zhang, L., Zhao, M., and Sui, R.-B. (2017). Cerebellar fastigial nucleus electrical stimulation alleviates depressive-like behaviors in post-stroke depression rat model and potential mechanisms. *Cell Physiol. Biochem.* 41, 1403–1412. doi: 10.1159/000467940

Conflict of Interest: The authors declare that the research was conducted in the absence of any commercial or financial relationships that could be construed as a potential conflict of interest.

frontiers in Systems Neuroscience

ORIGINAL RESEARCH
published: 13 February 2020
doi: 10.3389/fnsys.2020.00007

Eph/ephrin Function Contributes to the Patterning of Spinocerebellar Mossy Fibers Into Parasagittal Zones

Elizabeth P. Lackey[1,2,3] *and Roy V. Sillitoe*[1,2,3,4,5]*

[1]Department of Pathology & Immunology, Baylor College of Medicine, Houston, TX, United States, [2]Department of Neuroscience, Baylor College of Medicine, Houston, TX, United States, [3]Jan and Dan Duncan Neurological Research Institute at Texas Children's Hospital, Houston, TX, United States, [4]Development, Disease Models & Therapeutics Graduate Program, Baylor College of Medicine, Houston, TX, United States, [5]Developmental Biology Graduate Program, Baylor College of Medicine, Houston, TX, United States

Purkinje cell microcircuits perform diverse functions using widespread inputs from the brain and spinal cord. The formation of these functional circuits depends on developmental programs and molecular pathways that organize mossy fiber afferents from different sources into a complex and precisely patterned map within the granular layer of the cerebellum. During development, Purkinje cell zonal patterns are thought to guide mossy fiber terminals into zones. However, the molecular mechanisms that mediate this process remain unclear. Here, we used knockout mice to test whether Eph/ephrin signaling controls Purkinje cell-mossy fiber interactions during cerebellar circuit formation. Loss of *ephrin-A2* and *ephrin-A5* disrupted the patterning of spinocerebellar terminals into discrete zones. Zone territories in the granular layer that normally have limited spinocerebellar input contained ectopic terminals in *ephrin-A2*$^{-/-}$;*ephrin-A5*$^{-/-}$ double knockout mice. However, the overall morphology of the cerebellum, lobule position, and Purkinje cell zonal patterns developed normally in the *ephrin-A2*$^{-/-}$;*ephrin-A5*$^{-/-}$ mutant mice. This work suggests that communication between Purkinje cell zones and mossy fibers during postnatal development allows contact-dependent molecular cues to sharpen the innervation of sensory afferents into functional zones.

Keywords: cerebellum, mossy fiber, Purkinje cells, development, patterning, zebrinII

OPEN ACCESS

Edited by:
Nadia Cerminara, University of Bristol, United Kingdom

Reviewed by:
Rachel M. Sherrard, Sorbonne Universités, France
Taisuke Miyazaki, Hokkaido University, Japan
Izumi Sugihara, Tokyo Medical and Dental University, Japan

***Correspondence:**
Roy V. Sillitoe
sillitoe@bcm.edu

Received: *11 September 2019*
Accepted: *24 January 2020*
Published: *13 February 2020*

Citation:
Lackey EP and Sillitoe RV (2020) Eph/ephrin Function Contributes to the Patterning of Spinocerebellar Mossy Fibers Into Parasagittal Zones. Front. Syst. Neurosci. 14:7. doi: 10.3389/fnsys.2020.00007

INTRODUCTION

Brain function requires precise input and output connections between neurons. In the cerebellar cortex, mossy fibers carry input from more than three dozen brain and spinal cord nuclei and terminate in a reproducible pattern of parasagittal zones within the granular layer (for reviews, see Sillitoe and Joyner, 2007; Apps and Hawkes, 2009; Voogd, 2014; Apps et al., 2018). The mossy fiber termination patterns of the spinocerebellar projections have been particularly well-characterized in adult and developing rodents (Grant, 1962; Voogd et al., 1969; Matsushita and Ikeda, 1980; Matsushita and Okado, 1981; Matsushita and Hosoya, 1982; Robertson et al., 1983; Arsénio Nunes et al., 1985; Gravel and Hawkes, 1990; Grishkat and Eisenman, 1995; Reeber et al., 2011b; Sillitoe, 2016; Luo et al., 2018). These studies showed that immature spinocerebellar mossy fibers

segregate into the adult pattern of zones during postnatal development. However, the molecular mechanisms that guide the patterning of mossy fiber inputs into zones are not fully understood.

Data from different models led Sotelo and colleagues to propose that Purkinje cells act as organizer elements for the patterning of inputs to the cerebellar cortex (Wassef et al., 1985; Sotelo and Wassef, 1991). The Purkinje cell zonal architecture is now also thought to control zone formation of all other cerebellar components (Apps and Hawkes, 2009; Miterko et al., 2018). Developing and adult Purkinje cells express a wide variety of molecules in distinct parasagittal zones that could potentially mediate zone formation in the different cerebellar cell types (White and Sillitoe, 2013; Hawkes, 2014), while Purkinje cell zone formation itself is thought to be intrinsically driven (Leclerc et al., 1988; Wassef et al., 1990; Seil et al., 1995; Apps and Hawkes, 2009). Though adult mossy fibers terminate on granule cells, the adjacent Purkinje cell zonal boundaries have a reproducible relationship with those of mossy fiber terminals in the granular layer (Gravel and Hawkes, 1990; Matsushita et al., 1991; Ji and Hawkes, 1994; Quy et al., 2011; Luo et al., 2018) such that different Purkinje cell zones align with and/or subdivide neighboring mossy fiber zones. However, during postnatal development in the mouse and kitten, developing mossy fiber terminals form transient contacts with Purkinje cells before displacing to innervate their postsynaptic granule cell targets that subsequently invade the granular layer (Mason and Gregory, 1984; Takeda and Maekawa, 1989; Kalinovsky et al., 2011), potentially providing an opportunity for Purkinje cells to communicate directly with mossy fibers during circuit development. More recent work showed that the transient spinocerebellar mossy fiber contacts on Purkinje cells are refined to Purkinje cell zones at around postnatal day (P) 4 in the mouse (Sillitoe, 2016), suggesting that cell-cell contacts with Purkinje cells could be essential for the formation of mossy fiber parasagittal zones. This idea is consistent with data from mutant mice in which mossy fiber zones were disrupted in the absence of Purkinje cells but developed normally in the absence of granule cells (Arsénio Nunes et al., 1988). These findings suggest that mossy fiber patterning does not require synaptogenesis with their target granule cells but does require the presence of Purkinje cells, *via* an unknown mechanism. Analyses of mutant mice whose Purkinje cells are present in the cerebellum but lack organization into zones also show abnormal spinocerebellar termination patterns (Vogel et al., 1996; Sillitoe et al., 2010; Reeber et al., 2013; White et al., 2014), suggesting that the mechanism by which Purkinje cells influence mossy fiber patterning likely relies on the positional framework of Purkinje cell zones. Hawkes and colleagues ablated the spinocerebellar tract in the neonatal rat and showed that cuneocerebellar mossy fibers, which terminate in zones that interdigitate with the spinocerebellar zones, still respected the zonal boundaries and did not invade the "open" spinocerebellar territories of the granular layer despite the lack of competition (Ji and Hawkes, 1995). These data support a mechanism whereby mossy fibers recognize molecular cues in a zone. Sotelo and colleagues also proposed that the biochemical heterogeneity of Purkinje cell zones could reflect positional molecular cues that match with molecular cues on the incoming climbing fibers and mossy fibers; the effector molecules were, at the time, unknown but were postulated to act as guides for parasagittal zonation (Wassef et al., 1985; Sotelo and Wassef, 1991; Sotelo, 2004; Sotelo and Chédotal, 2005; Apps and Hawkes, 2009), perhaps through chemoaffinity (Sperry, 1963).

One family of molecules that could satisfy this role is the ephrin receptor tyrosine kinases (Eph) and ephrin molecules. *Eph/ephrin* genes encode membrane-bound molecules that mediate attraction and repulsion between cells (for reviews, see Flanagan and Vanderhaeghen, 1998; Wilkinson, 2001; Kania and Klein, 2016). The roles of the ephrin-A and EphA subfamilies as effector molecules that pattern neural circuit topography through chemoaffinity has been well-described in different sensory (Cheng et al., 1995; Drescher et al., 1995; Huffman and Cramer, 2007) and motor systems (Kania and Jessell, 2003; Iwasato et al., 2007). Analyses of Eph/ephrin expression in the developing chick and mouse have shown that the Purkinje cell layer and the external granular layer express ephrin-A ligands in the anterior and posterior cerebellum (Rogers et al., 1999; Karam et al., 2000; Saywell et al., 2014). Interestingly, immature granule cells in the external granular layer inhibit the growing mossy fibers from invading beyond the Purkinje cell layer (Manzini et al., 2006). Importantly, Bothwell and colleagues showed that ephrin-A2 expression and ephrin-A5 expression are arranged in parasagittal zones of Purkinje cells in the developing chick cerebellum (Karam et al., 2000) and related family members are also expressed in zones in the mouse cerebellum (Karam et al., 2002). Ephrin-A2 and ephrin-A5 are ligands for EphA receptors (Gale et al., 1996), and expression of EphA receptors has been documented in the pre-cerebellar nuclei where mossy fiber and climbing fiber inputs to the cerebellar cortex originate (Lin and Cepko, 1998; Rogers et al., 1999; Karam et al., 2000, 2002; Blanco et al., 2002; Nishida et al., 2002; Hashimoto et al., 2012; Saywell et al., 2014). *In vitro* work in the developing chick showed that overexpression of ephrin-A2 in the cerebellum repels climbing fiber inputs that express EphA receptors (Nishida et al., 2002). However, Bothwell and colleagues examined knockout mice that lack the *EphA4* gene expressed in Purkinje cells and reported that the Purkinje cell zones developed normally (Karam et al., 2002). Therefore, it is still unclear whether Eph/ephrin signaling mediates the formation of Purkinje cell zones or whether they control the patterning of cerebellar afferents *in vivo*. We hypothesized that zonal expression of the ephrin-A subfamily in Purkinje cells refines cell-cell contacts with mossy fiber terminals into parasagittal zones. The idea that specific Eph/ephrin molecules or combinations of the different subtypes could influence cerebellar patterning is appealing because an ephrin combinatorial code organizes visual maps (Cang et al., 2005). The likely functional redundancy established by the many overlapping Eph/ephrin subtypes in the cerebellum may require multiple genes to be deleted in order to observe a dramatic effect. Here, we used a combination of anterograde spinocerebellar tract-tracing and double knockout *ephrin-A2*$^{-/-}$;*ephrin-A5*$^{-/-}$ mice (Feldheim et al., 2000) to test the role of Eph/ephrin signaling in patterning

spinocerebellar mossy fiber terminal fields into cerebellar parasagittal zones.

MATERIALS AND METHODS

Animals

We performed all experiments in accordance with a protocol approved by the Institutional Animal Care and Use Committee at Baylor College of Medicine and the National Institutes of Health guidelines. We purchased *ephrin-A2*$^{-/-}$*;ephrin-A5*$^{-/-}$ double knockout mice (Feldheim et al., 2000) from The Jackson Laboratory (*Efna2*^{tm1Jgf} *Efna5*^{tm1Ddmo}/J, Bar Harbor, ME, USA; #005992). We used a combination of C57BL/6J control mice purchased from The Jackson Laboratory (#000664) and littermate controls generated from breeding the alleles. We used both types of controls due to breeding difficulties of the mutant line. During breeding, we considered the day a vaginal plug was visible as embryonic day (E) 0 and the day of birth as P0. All mice were analyzed for cerebellar zonal patterns between 1 and 2 months of age.

Neural Tract Tracing Using Sterile Surgery

We performed anterograde tracing of spinocerebellar afferents with WGA-Alexa 555 as we have previously described (Reeber et al., 2011a,b; Levy et al., 2017). WGA-Alexa 555 tracers travel quickly after injection, and they are robust when visualized in axons and terminals. Moreover, the Alexa fluorescent tag allows them to be easily combined with immunohistochemistry so that axon and terminal labeling can be examined in reference to neighboring cells. Briefly, we administered a 1 mg/kg dose of sustained-release buprenorphine and a 5 mg/kg dose of meloxicam by subcutaneous injections as preoperative analgesics. We anesthetized mice with Avertin (2,2,2-Tribromoethanol, Sigma-Aldrich, St. Louis MO, USA; #T48402) or with 1–4% isoflurane and administered a mixture of lidocaine and bupivacaine by intradermal injection as a local anesthetic. We made an incision in the skin above the lower thoracic-upper lumbar spinal cord. We cut the soft tissue connecting the T10 and T11 vertebral segments to expose the T13 and L1 spinal cord segments using the curvature of the spine as a guide (Harrison et al., 2013). We used a Nanoject II (Drummond Scientific, Broomall, PA, USA; #3-000-204) secured with a stereotaxic frame (David Kopf Instruments, Tujunga, CA, USA; Model 940) to pressure inject 0.2–1 μl of 2% WGA-Alexa 555 (Thermo Fisher Scientific, Waltham, MA, USA; #W32464) diluted in 0.1 M phosphate-buffered saline (PBS, Sigma-Aldrich; Cat #P4417; pH 7.4) just right of the dorsal spinal vein and approximately 1 mm below the dorsal surface of the spinal cord. We supplemented the tracer solution with 0.5% Fast Green (Sigma-Aldrich; #F7252) to visualize tracer injection during surgery. We applied antibiotic ointment and closed the incision with wound clips (Fine Science Tools, Foster City, CA, USA; #12032-07) and VetBond (3M, Maplewood, MN, USA; #1469SB). We placed 31M diet gel and hydrogel on the floor of the cage and carefully monitored the mice during the post-operative recovery period. We administered a 5 mg/kg dose of meloxicam by subcutaneous injection as a postoperative analgesic every 24 h and provided additional analgesic as needed. After a survival period of 48 h to allow the anterograde transport of WGA-Alexa 555 from the spinal cord to the cerebellum, we anesthetized the mice with Avertin and performed cardiac perfusion with PBS followed by 4% paraformaldehyde (PFA, pH 7.4) diluted in PBS. We sectioned and mounted brain and spinal cord tissue to image the tracer signal at the site of injection and in the terminals located in the cerebellum (see below).

Tissue Preparation

We obtained free-floating frozen cut tissue sections as previously described (Reeber et al., 2011a,b; Levy et al., 2017). Briefly, we post-fixed brains and spinal cords for 24–48 h in 4% PFA and then cryoprotected the tissue stepwise in 15% and 30% sucrose solutions (diluted in PBS) at 4°C. We embedded the tissue in Tissue-Tek Optimal Cutting Temperature Compound (Sakura Finetek, Torrance, CA, USA; #4583) and froze the tissue at −80°C. We cut 40 μm sections on a cryostat at −20°C and collected them in PBS. We performed free-floating immunohistochemistry (see below) or immediately mounted sections on electrostatically coated slides with Fluoro-gel (Electron Microscopy Sciences, Hatfield, PA, USA; #17985-10).

Immunohistochemistry

We performed free-floating immunohistochemistry as we have previously described (Sillitoe et al., 2010; Reeber et al., 2011b; White et al., 2014). Briefly, we blocked free-floating tissue sections for 1–2 h in 10% normal donkey serum (Sigma-Aldrich; #D9663) and 0.2% Triton-X 100 (Thermo Fisher Scientific #BP151-100) in PBS while gently shaking at room temperature, and then we incubated the free-floating tissue sections in primary antibodies for 16–18 h while shaking at room temperature. We used mouse monoclonal anti-zebrinII antibody (kind gift from Dr. Richard Hawkes, University of Calgary, Alberta, Canada) or rabbit polyclonal anti-Hsp25 antibody (Enzo Life Sciences, Farmingdale, NY, USA; #ADI-SPA-801-F) at concentrations of 1:500 diluted in blocking solution. After 3 × 5 min washes in PBS, we incubated the free-floating tissue sections in anti-mouse (Donkey anti-mouse IgG Alexa Fluor 488, Thermo Fisher Scientific #A21202) or anti-rabbit (Donkey anti-rabbit IgG Alexa Fluor 488, Thermo Fisher Scientific #A21206) Alexa fluorophore-conjugated secondary antibodies at concentrations of 1:1,500, again diluted in the blocking solution, for 2 h while shaking at room temperature. We then washed the sections 3 × 5 min in PBS before mounting on the electrostatically coated slides with Fluoro-gel.

Microscopy

We captured photomicrographs of tissue sections with AxioCam MRm and MRc5 cameras (Zeiss, Oberkochen, DE) mounted on a Zeiss Axio Imager.M2 microscope. We acquired the images of tissue sections using Zeiss Zen software (2012 edition). We captured photomicrographs of whole-mount brains and spinal cords with Zeiss AxioCam MRm and MRc5 cameras mounted on a Zeiss Axio Zoom.V16 microscope. We acquired the whole-mount images using Zeiss AxioVision software (release 4.8). We pseudocolored WGA-Alexa 555 to magenta for better

visualization. We imported the raw data into Adobe Photoshop CC and corrected the images for brightness and contrast levels.

Image Analysis

We examined the WGA-Alexa 555 signal in matched coronal sections from the anterior, central, posterior, and nodular transverse domains (see **Figure 1**) based on the known regionalization and transitions between spinocerebellar mossy fiber zones (Grant, 1962; Voogd et al., 1969; Robertson et al., 1983; Gravel and Hawkes, 1990; Reeber et al., 2011b). To characterize the zones based on the previously described spinocerebellar termination pattern in rodents, we designated the spinocerebellar zones as "S" starting from the midline moving laterally as "S1, S2, + ..." We used an "a" or "p" to distinguish between the anterior zones (S1a, S2a, + ...) and the posterior zones (S1p, S2p, + ...) since the exact relationship between the spinocerebellar mossy fiber terminal fields in anterior and posterior zones remains unclear, though it has been demonstrated that individual spinal projection neurons can collateralize to terminate in the anterior and posterior cerebellar lobules (Heckroth and Eisenman, 1988; Luo et al., 2018). Therefore, it is unclear to what extent a given anterior mossy fiber zone is anatomically equivalent or linked to a posterior zone beyond sharing the originating fiber. Please refer to the Results for additional information about nomenclature. We observed occasional background WGA-Alexa 555 labeling in the molecular and Purkinje cell layers that we have previously observed with this technique due to leakage of WGA-Alexa 555 into the cerebrospinal fluid during surgery (Sillitoe et al., 2010). We further examined adjacent matched sections with immunohistochemistry to detect the Purkinje cells.

We measured the WGA-Alexa 555 signal intensity in the granular layer using the Plot Profile function in ImageJ, and we wrote custom MATLAB (MathWorks, Natick, MA, USA) code to calculate the intensity relative to the mean in the negative zones (lacking spinocerebellar terminals) for each genotype. The region of interest included S1a, S2a, and the negative zones between S1a and S2a in left and right lobule III, ±350 microns from the cerebellar midline. For all measurements, we calculated the intensity relative to the section mean to control for differences in intensity between sections. In order to calculate the relative intensities in the negative zones, we defined the boundaries between the zones as the positions where the second derivative of the intensity vector changed sign. Each boundary reflected a local minimum or maximum in the slope of the relative intensity vector along the mediolateral axis. We smoothed the data with a moving average filter when calculating the derivatives. We then plotted the boundary position values on the original unsmoothed relative intensity data and found that our approach reliably isolated the zones. We calculated the mean relative intensity in the negative zones for each genotype using the original unsmoothed data. We analyzed three sections per animal for a total of six negative zones per animal (n) and three animals per genotype (N). We performed all statistical analyses on the unsmoothed relative intensity data.

In order to measure the molecular layer thickness, we used the line measurement tool in ImageJ to measure the distance from the top of the Purkinje cell soma to the top of the Purkinje cell dendritic tree on images of coronal sections immunostained with the anti-zebrinII antibody. We obtained the measurements from the midline of posterior lobule VIII and anterior lobule IX in three sections per lobule for a total of six measurements per animal (n) and three animals per genotype (N).

For all statistical tests, we calculated the mean for each genotype and compared the genotypes using a two-tailed unpaired t-test with N as the number of animals and a significance threshold of $p < 0.05$. We reported the error as the standard error of the mean.

RESULTS

Spinocerebellar Mossy Fiber Zones Are Disrupted in ephrin-A2$^{-/-}$;ephrin-A5$^{-/-}$ Mutant Mice

We asked whether ephrin-A2/ephrin-A5 are effector molecules by which Purkinje cells organize mossy fiber zones downstream of the Purkinje cell zonal framework. If ephrin-A2 and ephrin-A5 are necessary for guiding mossy fibers into zones, then the loss of *ephrin-A2* and *ephrin-A5* should disrupt mossy fiber termination patterns. To test this, we used mice that lack the genes encoding ephrin-A2 and ephrin-A5 to examine the patterning of spinocerebellar terminal fields. The *ephrin-A2*$^{-/-}$*;ephrin-A5*$^{-/-}$ double knockout mice showed generally normal motor function with no gross abnormalities in locomotion, coordination, or balance (N = 6). We injected wheat germ agglutinin tracer conjugated to Alexa 555 fluorophores (WGA-Alexa 555) into the lower thoracic-upper lumbar spinal cord of *ephrin-A2*$^{-/-}$*;ephrin-A5*$^{-/-}$ double knockout mice (N = 6) and control mice (N = 6) to anterogradely trace and label spinocerebellar projections (Reeber et al., 2011a,b; Levy et al., 2017; **Figure 1A**) and then examined the labeled profiles in matched sections from the cerebellar cortex. We examined the WGA-Alexa 555 signal at the injection sites and found that we likely targeted spinocerebellar neurons arising from the dorsal nucleus of Clarke as well as neurons in laminae IV–VII and border cells of the upper thoracic to the lower lumbar spinal cord segments (**Figures 1B,C**). In the granular layer, we examined for the traced and labeled spinocerebellar mossy fibers in coronal sections (**Figures 1D–Q**). In order to characterize the traced and labeled spinocerebellar zones with reference to the previously characterized termination pattern (Grant, 1962; Voogd et al., 1969; Robertson et al., 1983; Gravel and Hawkes, 1990; Reeber et al., 2011b) for the purpose of this study, we designated the spinocerebellar zones as "S" starting from the midline moving laterally as "S1, S2, + ..." We used an "a" or "p" to distinguish between the anterior zones (S1a, S2a, + ...) and the posterior zones (S1p, S2p, + ...) because the relationship between the spinocerebellar mossy fiber terminals in anterior and posterior zones has not been fully defined, though single spinal neurons do collateralize to terminate in both anterior and posterior cerebellar lobules (Heckroth and Eisenman, 1988; Luo et al., 2018). In both mutant and control mice, we found that the

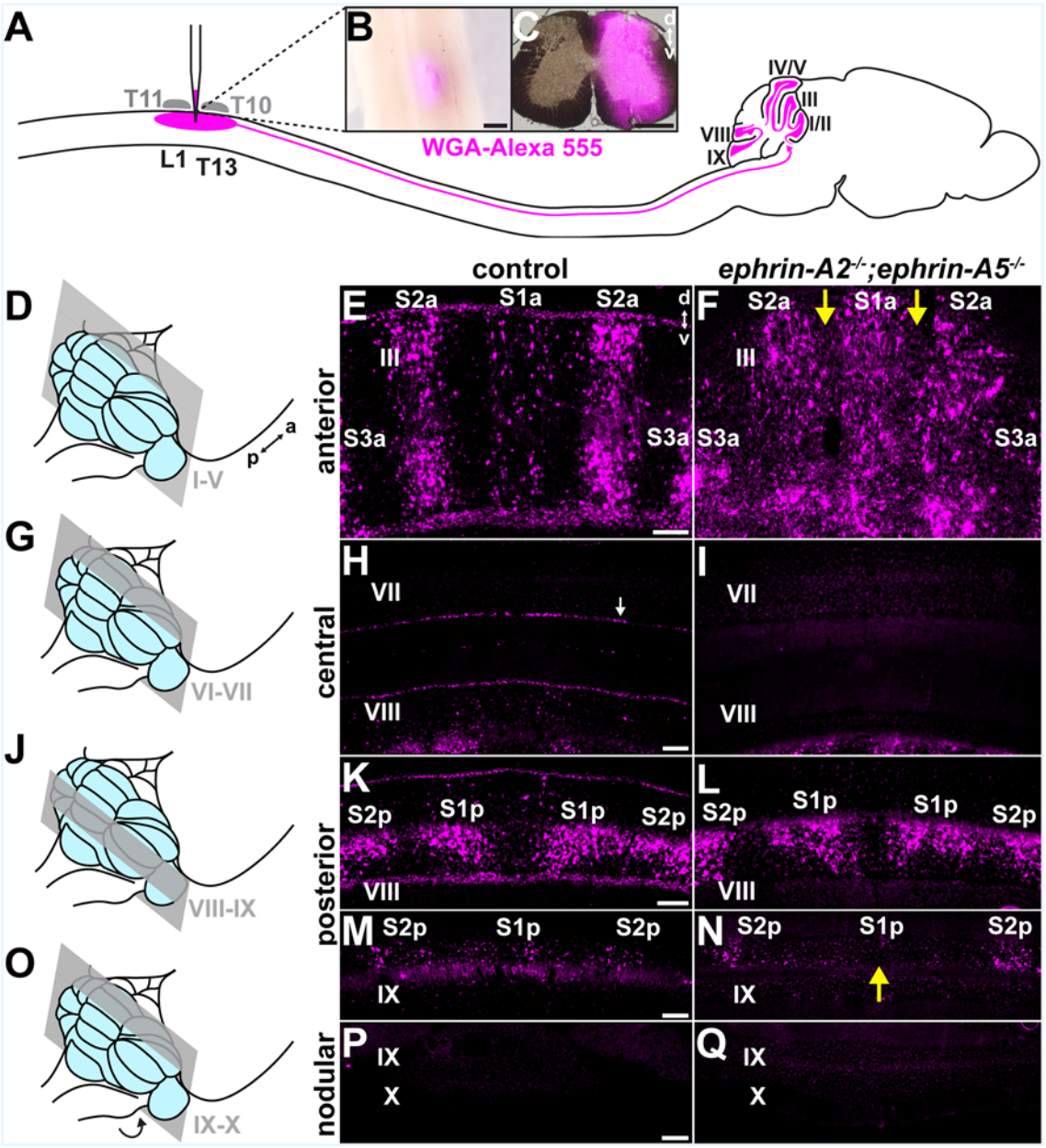

FIGURE 1 | Spinocerebellar mossy fiber patterning is disrupted in *ephrin-A2*$^{-/-}$;*ephrin-A5*$^{-/-}$ mice. **(A)** Strategy for labeling spinocerebellar mossy fiber terminals in the cerebellar cortex of *ephrin-A2*$^{-/-}$; *ephrin-A5*$^{-/-}$ double knockout mice and control mice. We injected wheat germ agglutinin conjugated to Alexa fluorophores (WGA-Alexa 555) into the lower thoracic-upper lumbar spinal cord. Based on the curvature of the spine, we used vertebral segments T10 and T11 as landmarks to inject tracer into the underlying spinal cord segments of T13 to L1 (Harrison et al., 2013). **(B)** Whole-mount image of a dorsal view of a lower thoracic-upper lumbar spinal cord. A fluorescent image is overlaid on a bright-field image. The WGA-Alexa 555 tracer injection site is visible just lateral to the midline. a, anterior; p, posterior. Scale = 500 μm. **(C)** The A coronal section adjacent to a large injection site located in the lower thoracic-upper lumbar spinal cord. A fluorescent image is overlaid on a bright-field image. d, dorsal; v, ventral. Scale = 500 μm. **(D)** Schematic depicting a mouse brain with the cerebellum highlighted in blue and a coronal section through lobules I-V highlighted in gray. **(E)** Image of the WGA-Alexa 555 signal in the anterior cerebellum of a control mouse (*N* = 6). A midline parasagittal zone (S1a) and two zones lateral to the midline (S2a and S3a) are visible in lobule III. d, dorsal; v, ventral. Scale = 100 μm. **(F)** Image of the WGA-Alexa 555 signal in spinocerebellar mossy fibers in the anterior cerebellum of an *ephrin-A2*$^{-/-}$;*ephrin-A5*$^{-/-}$ double knockout mouse (*N* = 6). The boundaries of S1a and S2a in lobule III are less defined, and territories of the granular layer that have a limited termination of spinocerebellar mossy fiber terminals in control mice contain ectopic spinocerebellar mossy fiber terminals (yellow arrows). **(G)** Schematic depicting a mouse brain with the cerebellum highlighted in blue and a coronal section through lobules VI-VII highlighted in gray. **(H)** Image after WGA-Alexa 555 tracing to test for spinocerebellar mossy fibers in the central cerebellum of a control mouse (*N* = 6). Spinocerebellar mossy fiber terminals are not present in lobule VII. The background staining in the Purkinje cells is likely due to leakage of the WGA-Alexa 555 tracer from the cerebrospinal fluid that accumulates from the injection in the spinal cord (Sillitoe et al., 2010; white arrow). Scale = 100 μm. **(I)** Image after tracing to test for

(*Continued*)

FIGURE 1 | Continued
WGA-Alexa 555 signal in spinocerebellar mossy fibers in the central cerebellum of an *ephrin-A2*$^{-/-}$;*ephrin-A5*$^{-/-}$ double knockout mouse (N = 6). Spinocerebellar mossy fibers are not present in lobule VII. **(J)** Schematic depicting a mouse brain with the cerebellum highlighted in blue and a coronal section through lobules VIII and IX highlighted in gray. **(K)** Image of the WGA-Alexa 555 signal in spinocerebellar mossy fibers in the posterior cerebellum of a control mouse (N = 6). Two symmetrical pairs of parasagittal zones are visible in lobule VIII (S1p and S2p). Scale = 100 μm. **(L)** Image of the WGA-Alexa 555 signal in spinocerebellar mossy fibers in the posterior cerebellum of an *ephrin-A2*$^{-/-}$;*ephrin-A5*$^{-/-}$ double knockout mouse (N = 6). The two symmetrical pairs of parasagittal zones in lobule VIII are visible and relatively well-defined (S1p and S2p). **(M)** Image of the WGA-Alexa 555 signal in spinocerebellar mossy fibers in the posterior cerebellum of a control mouse (N = 6). A midline parasagittal zone and a zone lateral to the midline are visible in anterior lobule IX (S1p and S2p). Scale = 100 μm. **(N)** Image of the WGA-Alexa 555 signal in spinocerebellar mossy fibers in the posterior cerebellum of an *ephrin-A2*$^{-/-}$;*ephrin-A5*$^{-/-}$ double knockout mouse (N = 6). The midline parasagittal zone (S1p) and the zone lateral to the midline (S2p) are visible in anterior lobule IX. However, the S1p zone terminals are poorly organized compared to those in control mice (yellow arrow). **(O)** Schematic depicting a mouse brain with the cerebellum highlighted in blue and a coronal section through the nodular cerebellum (lobules posterior IX–X) highlighted in gray. The arrow indicates that lobule X is located underneath the posterior cerebellum, out of view. **(P)** Image after WGA-Alexa 555 tracing to examine for spinocerebellar mossy fibers in the nodular cerebellum of a control mouse (N = 6). Spinocerebellar mossy fibers are not present in posterior lobule IX or lobule X. Scale = 200 μm. **(Q)** Image after WGA-Alexa 555 tracing to examine for spinocerebellar mossy fibers in the nodular cerebellum of an *ephrin-A2*$^{-/-}$;*ephrin-A5*$^{-/-}$ double knockout mouse (N = 6). Spinocerebellar mossy fibers are not present in posterior lobule IX or lobule X.

traced spinocerebellar mossy fibers terminated in the granular layer of the anterior lobules (I–V; **Figures 1D–F**) and the posterior lobules (VIII-anterior IX; **Figures 1J–N**) and did not terminate in the central lobules (VI–VII; **Figures 1G–I**) or the nodular lobules (posterior IX–X; **Figures 1O–Q**). While *ephrin-A2*/*ephrin-A5* deletion did not disrupt the targeting of mossy fibers to the granular layer or to the correct lobules, it did disrupt the refinement of the parasagittal spinocerebellar zones. In the vermis of the anterior lobules, the traced spinocerebellar mossy fibers terminated in a midline zone (S1a) and two zones that are lateral to the midline (S2a and S3a; **Figure 1E**). We found that the deletion of *ephrin-A2* and *ephrin-A5* disrupted the mediolateral segregation of spinocerebellar terminal fields in the anterior zones (**Figure 1F**). Territories of the granular layer in lobule III that have limited spinocerebellar mossy fiber input in control mice contained ectopic spinocerebellar mossy fibers in the *ephrin-A2*$^{-/-}$;*ephrin-A5*$^{-/-}$ mutant mice (**Figure 1F**). Spinocerebellar mossy fiber terminals normally occupy complementary zones to the cuneocerebellar mossy fibers (Quy et al., 2011; Gebre et al., 2012). We observed labeled spinocerebellar terminals arranged into crude zones in *ephrin-A2*$^{-/-}$;*ephrin-A5*$^{-/-}$ mice, and their boundaries were less sharply defined due to the ectopic terminals that we observed to invade the adjacent granule cell territory that normally would be occupied by the cuneocerebellar terminals (**Figure 1F**). We detected the effect on mossy fiber zones in vermal lobule III but not in the zones of other anterior lobules or in the hemispheres where the known termination pattern is less clearly segregated in control mice (**Supplementary Figure S1**). We did not observe ectopic spinocerebellar mossy fibers terminating in the central lobules (VI–VII; **Figures 1G–I**). In the vermis of the posterior lobules, the overall pattern of the traced spinocerebellar mossy fiber zones in the double mutants was normal compared to that in controls, and the boundaries that define each zone were easily distinguished (**Figures 1J–N**). However, we observed poorly defined zonal clusters within the S1p of lobule IX (**Figure 1N**). We did not observe ectopic spinocerebellar mossy fibers terminating in the nodular lobules (posterior IX–X; **Figures 1O–Q**). In order to quantify the effect of *ephrin-A2*/*ephrin-A5* deletion on spinocerebellar mossy fiber zones, we measured the WGA-Alexa 555 signal intensity in the negative zones (lacking spinocerebellar terminals) of the granular layer between the S1a zone and the left and right S2a zones in lobule III (**Figure 2A**). We calculated the intensity relative to the mean to control for differences in intensity between sections, and we defined the boundaries between zones as the distances from the midline where the second derivative of the smoothed intensity vector changed the sign at each zone transition (**Figure 2A**). We found that the WGA-Alexa 555 relative intensity was increased in the negative zones of the granular layer between S1a and S2a in the mutants compared to that of the controls (control = 56.1% ± 0.21%; *ephrin-A2*$^{-/-}$;*ephrin-A5*$^{-/-}$ = 91.2% ± 10.3%; n = 6 negative zones per animal, N = 3 animals per genotype, p = 0.0267; **Figure 2B**). These results show that the genetic deletion of *ephrin-A2*/*ephrin-A5* caused a significantly increased number of spinocerebellar mossy fibers to terminate in the zones between S1a and S2a that normally lack spinocerebellar terminals in controls. These data suggest that Eph/ephrin signaling is required for refining spinocerebellar mossy fiber zones. Our data also show that *ephrin-A2* and *ephrin-A5* are not required for specifically targeting spinocerebellar axons and terminals into the granular layer or to the correct lobules in the anterior-posterior axis of the cerebellum.

ephrin-A2 and ephrin-A5 Are Not Required for the Formation of Purkinje Cell Zones

We next asked whether ephrin-A2/ephrin-A5 are also required for the formation of Purkinje cell zones. If ephrin-A2/ephrin-A5 mediate the formation of Purkinje cell zones, then we would expect the loss of *ephrin-A2* and *ephrin-A5* to disrupt Purkinje cell zonal patterning. To test whether loss of *ephrin-A2* and *ephrin-A5* disrupts Purkinje cell zones, we used immunohistochemistry to detect molecular markers of Purkinje cell zones in order to label and examine their expression patterns in matched coronal sections from each of the four transverse domains of the cerebellar cortex (anterior, central, posterior, and nodular; Ozol et al., 1999; Sillitoe et al., 2005) in *ephrin-A2*$^{-/-}$;*ephrin-A5*$^{-/-}$ mice (N = 6) and control mice (N = 6; **Figures 3A–L**). In the anterior (I–V) and posterior (VIII-anterior IX) lobules of control mice, zebrinII/AldolaseC marks a striking array of Purkinje cell zones (Brochu et al., 1990; Gravel and Hawkes, 1990; Ji and Hawkes, 1994; Ozol et al., 1999). In contrast, the small 25 kDa heat shock protein (Hsp25) marks Purkinje cell zones in the central (VI–VII) and

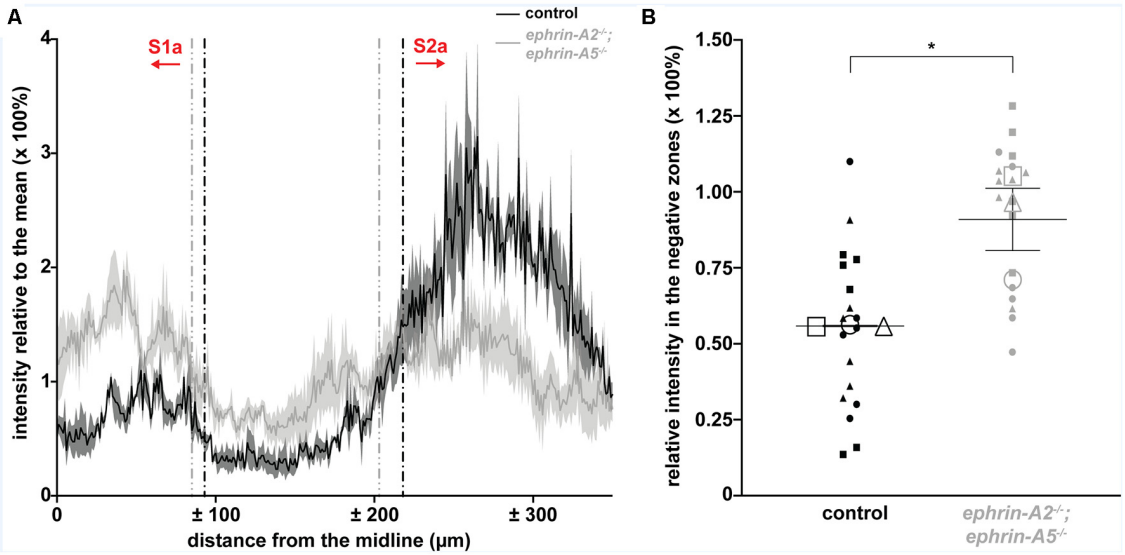

FIGURE 2 | *ephrin-A2*$^{-/-}$;*ephrin-A5*$^{-/-}$ mice have ectopic spinocerebellar terminals. **(A)** Plot of the WGA-Alexa 555 relative intensity in the granular layer of lobule III for control and *ephrin-A2*$^{-/-}$;*ephrin-A5*$^{-/-}$ mice [n = 3 sections (six left/right negative zones) per animal, N = 3 animals per genotype]. The y-axis values indicate a ratio of the intensity to the mean intensity for the section, which directly represents a percentage of the mean intensity value. The x-axis values indicate the distance from the cerebellar midline as measured per pixel and scaled for µm per pixel. Vertical dotted lines indicate the boundaries of the negative zones between S1a and S2a calculated as where the second derivative of the smoothed intensity vector changes sign. The calculated zone boundaries are plotted on the original unsmoothed intensity data. Error bands indicate the standard error of the mean. **(B)** The WGA-Alexa 555 relative intensity in the negative zones between S1a and S2a is increased in the *ephrin-A2*$^{-/-}$;*ephrin-A5*$^{-/-}$ mice [control = 56.1% ± 0.21%; *ephrin-A2*$^{-/-}$;*ephrin-A5*$^{-/-}$ = 91.2% ± 10.3%; n = 6 negative zones per animal (small data points), N = 3 animals per genotype (large data points, each shape represents a different animal), p = 0.0267]. Error bars indicate the standard error of the mean. *$p < 0.05$.

nodular (posterior IX–X) lobules of control mice, where zebrinII is uniformly expressed in all Purkinje cells (Armstrong et al., 2000). Anti-Hsp25 immunohistochemistry also weakly labels blood vessels and ependymal cells throughout the cerebellum (Armstrong et al., 2000). We tested zebrinII and Hsp25 because their Purkinje cell expression patterns are a sensitive readout of developmental and disease-associated defects that disrupt Purkinje cell zones (Sillitoe et al., 2008; White et al., 2016). Along the mediolateral axis of vermal lobules I–V (**Figure 3A**), zebrinII is expressed in a medial zone of Purkinje cells (P1+) and a zone that is lateral to the midline (P2+; **Figure 3B**). We found that the deletion of *ephrin-A2* and *ephrin-A5* did not disrupt the pattern of anterior Purkinje cell zones (**Figure 3C**). We also observed occasional weak labeling of Purkinje cell axon collaterals in the granular layer with zebrinII immunohistochemistry in mutants and controls, as previously reported (Brochu et al., 1990). Posteriorly in the central lobules VI and VII (**Figure 3D**), Hsp25 is expressed by a medial zone of Purkinje cells (1; **Figure 3E**) and two zones that are lateral to the midline (the complete Hsp25 map is described in Armstrong et al., 2000). We found that the deletion of *ephrin-A2* and *ephrin-A5* does not disrupt the central Purkinje cell zones (**Figure 3F**). Moving more posteriorly into the vermis of lobules VIII and anterior IX (**Figure 3G**), zebrinII expression is again patterned, with a medial zone (P1+) flanked by two zones (P2+ and P3+; **Figure 3H**). We found that deletion of *ephrin-A2* and *ephrin-A5* does not disrupt the posterior Purkinje cell zones (**Figure 3I**), Note that for clarity we have only described the most medial and prominent zebrinII zones in the anterior and posterior lobules (for a full description see Ozol et al., 1999; Sillitoe and Hawkes, 2002). In the nodular lobules (**Figure 3J**), Hsp25 is expressed by a medial zone of Purkinje cells (1) and a zone lateral to the midline (2) in posterior lobule IX and similarly in a medial zone (1) and a zone lateral to the midline (2) in lobule X (**Figure 3K**; Armstrong et al., 2000). We found that deletion of *ephrin-A2* and *ephrin-A5* does not disrupt the nodular Purkinje cell zones (**Figure 3L**). For two well-described Purkinje cell markers, zebrinII and Hsp25, we showed that deletion of *ephrin-A2* and *ephrin-A5* did not disrupt the Purkinje cell zones in the anterior, central, posterior, or nodular lobules. In the mutants, the zonal expression patterns were restricted to the expected Purkinje cell subsets and arranged in the same distribution with clear zone boundaries as observed in control mice. The data suggest that *ephrin-A2* and *ephrin-A5* are not required for the formation or maintenance of sharp Purkinje cell zones in mice.

The Relationship Between Purkinje Cell Zones and Spinocerebellar Mossy Fiber Zones Is Disrupted in ephrin-A2$^{-/-}$; ephrin-A5$^{-/-}$ Mutant Mice

We examined the relationship between the pattern of WGA-Alexa 555 anterogradely labeled spinocerebellar mossy fiber terminal fields and the pattern of Purkinje cell zones that were marked using zebrinII immunohistochemistry in

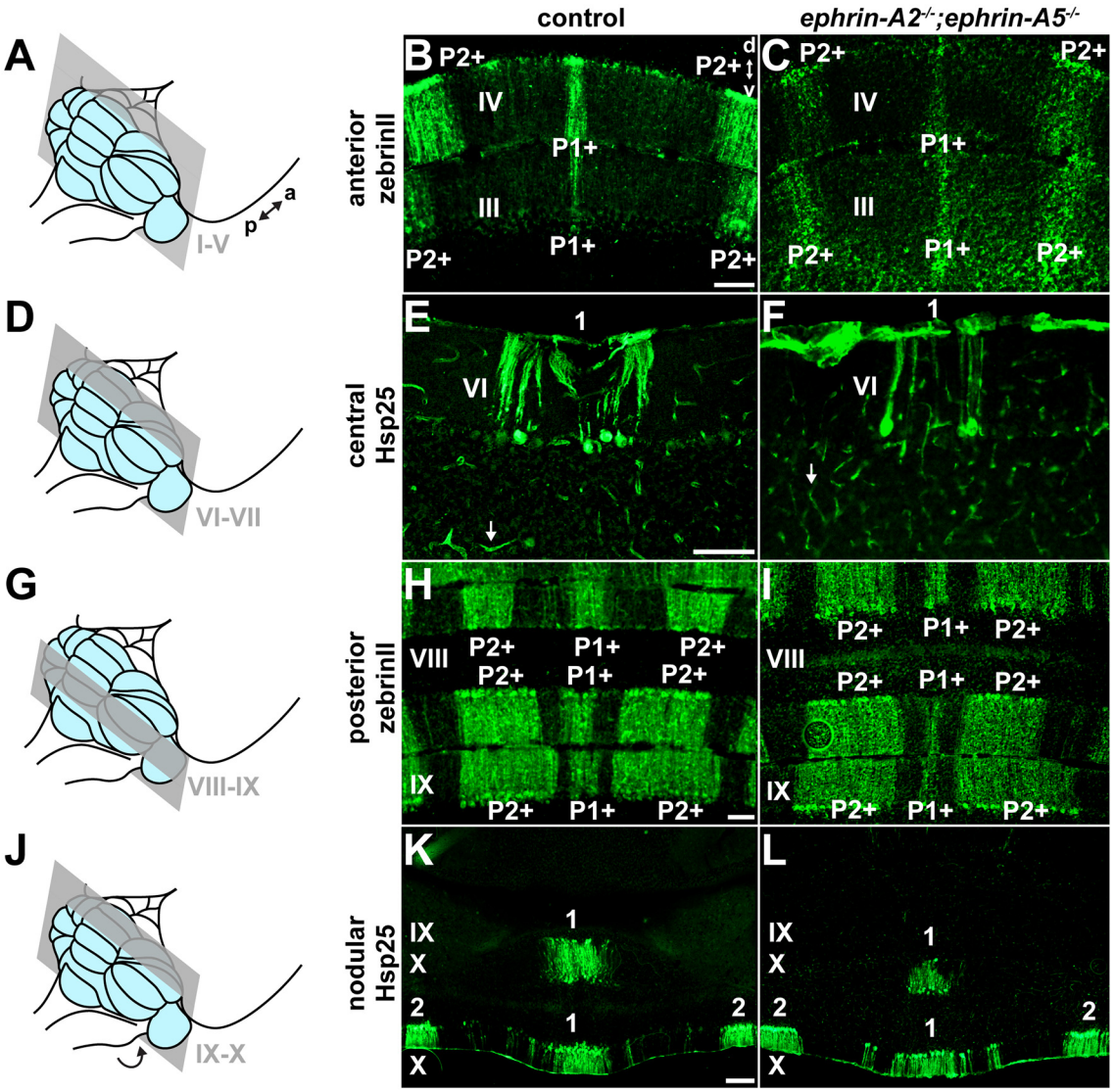

FIGURE 3 | *ephrin-A2* and *ephrin-A5* are not required for the formation of Purkinje cell zones. **(A)** Schematic depicting a mouse brain with the cerebellum highlighted in blue and a coronal section through the anterior cerebellum (lobules I-V) highlighted in gray. a, anterior; p, posterior. **(B)** Image of zebrinII expression in the anterior cerebellum of a control mouse (N = 6). A medial zone of Purkinje cells (P1+) and a zone lateral to the midline (P2+) are visible. d, dorsal; v, ventral. Scale = 100 μm. **(C)** Image of zebrinII expression in the anterior cerebellum of an *ephrin-A2*$^{-/-}$;*ephrin-A5*$^{-/-}$ double knockout mouse (N = 6). The medial zone of Purkinje cells (P1+) and the zone lateral to the midline (P2+) are visible and correctly organized. **(D)** Schematic depicting a mouse brain with the cerebellum highlighted in blue and a coronal section through the central cerebellum (lobules VI-VII) highlighted in gray. **(E)** Image of Hsp25 expression in the central cerebellum of a control mouse (N = 6). The focus is on the medial zone of Purkinje cells (1). Blood vessels are also immunoreactive for Hsp25 (white arrow). Scale = 100 μm. **(F)** Image of Hsp25 expression in the central cerebellum of an *ephrin-A2*$^{-/-}$;*ephrin-A5*$^{-/-}$ double knockout mouse (N = 6). The medial zone of Purkinje cells (1) has sharp boundaries. Blood vessels are also immunoreactive for Hsp25 (white arrow). **(G)** Schematic depicting a mouse brain with the cerebellum highlighted in blue and a coronal section through the posterior cerebellum (lobules VIII and anterior IX) highlighted in gray. **(H)** Image of zebrinII expression in the posterior cerebellum of a control mouse (N = 6). A medial zone of Purkinje cells (P1+) and a zone lateral to the midline (P2+) are visible. Scale = 100 μm. **(I)** Image of zebrinII expression in the posterior cerebellum of an *ephrin-A2*$^{-/-}$;*ephrin-A5*$^{-/-}$ double knockout mouse (N = 6). The medial zone of Purkinje cells (P1+) and the zone lateral to the midline (P2+) are correctly organized. **(J)** Schematic depicting a mouse brain with the cerebellum highlighted in blue and a coronal section through the nodular cerebellum (lobules posterior IX–X) highlighted in gray. The arrow indicates that lobule X is located underneath the posterior cerebellum and is therefore out of view. **(K)** Image of Hsp25 expression in the nodular cerebellum of a control mouse (N = 6). A medial zone of Purkinje cells (1) and a zone lateral to the midline (2) are labeled. Scale = 200 μm. **(L)** Image of Hsp25 expression in the nodular cerebellum of an *ephrin-A2*$^{-/-}$;*ephrin-A5*$^{-/-}$ double knockout mouse (N = 6). The medial zone of Purkinje cells (1) and the zone lateral to the midline (2) have a normal distribution pattern.

ephrin-A2$^{-/-}$;*ephrin-A5*$^{-/-}$ mice (N = 3) and control mice (N = 6). In control mice, the boundaries of the mossy fiber terminal fields have a reproducible relationship with Purkinje cell zones, which match or subdivide the afferent zones (Gravel and Hawkes, 1990; Matsushita et al., 1991; Ji and Hawkes, 1994; Reeber et al., 2011b; **Figures 4A–C**). We found that

while zebrinII expression in the cerebellar cortex of *ephrin-A2*$^{-/-}$;*ephrin-A5*$^{-/-}$ double knockout mice is restricted to Purkinje cells similar to the distribution of zones in control mice, the relationship between spinocerebellar terminal fields and how far they extend beyond the boundaries of Purkinje cell zones is disrupted (**Figures 4D–F**). The granular layer contained ectopic spinocerebellar terminals adjacent to zebrinII-negative Purkinje cell zones that normally align with mossy fibers originating from the external cuneate nucleus (Gebre et al., 2012; **Figures 4D–F**). These data suggest that the topographical relationship between Purkinje cell zones and the mossy fiber subsets that normally reside below them requires Eph/ephrin signaling.

Cerebellar Gross Morphology and Cerebellar Cortical Thickness Are Unaltered in Adult ephrin-A2$^{-/-}$/ephrin-A5$^{-/-}$ Mutant Mice

One possible explanation for the defective mapping of spinocerebellar terminals in the *ephrin-A2*$^{-/-}$;*ephrin-A5*$^{-/-}$ double knockout mice is that the cerebellar cortical layers may have developed abnormally, which could mean that spinocerebellar mossy fibers found their correct positions but in different locations. Purkinje cells express *ephrin-A2* and *ephrin-A5* in the positions of future lobules along the anteroposterior axis of the embryonic cerebellum before the lobules form (Rogers et al., 1999; Karam et al., 2000), further raising the question of whether they have a role in shaping the cerebellum. We, therefore, tested whether *ephrin-A2/ephrin-A5* are required for the formation of cerebellar morphological features that could interfere with the proper establishment of afferent termination patterns. We examined the gross morphology of *ephrin-A2*$^{-/-}$;*ephrin-A5*$^{-/-}$ mouse brains compared to control brains ($N = 6$ for each genotype). We found that the shape of the cerebellum, based on the surface structural identity of the 10 lobules (Larsell, 1970), was normal in *ephrin-A2*$^{-/-}$/*ephrin-A5*$^{-/-}$ mutant mice (**Figures 5A–F**). The cerebellum and the 10 lobules were fully represented and in their correct locations (**Figures 5A–F**). To examine whether there were more subtle morphological changes to the laminar structure of the cerebellar cortex, we measured the thickness of the molecular layer. Molecular layer thickness is a sensitive and straightforward measure for developmental and disease-associated defects that disrupt Purkinje cell dendrites or the placement of Purkinje cells into a monolayer (Hansen et al., 2013; White et al., 2014, 2016; White and Sillitoe, 2017). Such defects could be predicted to influence the patterning of mossy fibers, likely through their direct contacts (Mason and Gregory, 1984; Sillitoe, 2016). We did not detect a difference in molecular layer thickness between *ephrin-A2*$^{-/-}$;*ephrin-A5*$^{-/-}$ mice and control mice (control mean = 97.9 μm ± 2.55 μm; *ephrin-A2*$^{-/-}$;*ephrin-A5*$^{-/-}$ mean = 100.9 μm ± 0.373 μm; $n = 6$ measurements per animal, $N = 3$ animals per genotype, $p = 0.3088$; **Figure 5G**). These data suggest that *ephrin-A2* and *ephrin-A5* are not required for establishing the basic cerebellar foliation plan, cerebellar cortical lamination, or for the general expansion of Purkinje cell dendrites.

DISCUSSION

Multiple studies have provided compelling evidence that Purkinje cells may act as organizer elements for the patterning of incoming cerebellar afferents (Wassef et al., 1985; Sotelo and Wassef, 1991; Ji and Hawkes, 1995; Sotelo, 2004; Sotelo and Chédotal, 2005; Sillitoe and Joyner, 2007; Apps and Hawkes, 2009; White and Sillitoe, 2013). Additional data have pointed to Eph/ephrin signaling as a potential molecular mechanism by which Purkinje cells could guide afferent terminals into zones (Cheng et al., 1995; Drescher et al., 1995; Lin and Cepko, 1998; Rogers et al., 1999; Karam et al., 2000, 2002; Blanco et al., 2002; Nishida et al., 2002; Saywell et al., 2014). In order to investigate the role of Eph/ephrin signaling in the formation of mossy fiber terminal zones, we performed anterograde neural tract-tracing of spinocerebellar mossy fibers in *ephrin-A2*$^{-/-}$;*ephrin-A5*$^{-/-}$ double knockout mice and examined the topography of labeled terminal fields in the cerebellar cortex. We found that loss of *ephrin-A2* and *ephrin-A5* disrupted the parasagittal patterning of spinocerebellar mossy fibers. Loss of *ephrin-A2* and *ephrin-A5* did not disrupt the organization of Purkinje cell zones or the basic morphology of the cerebellum. These data suggest that Eph/ephrin signaling is required for the patterning of spinocerebellar mossy fiber zones and, more broadly, that an abnormal Purkinje cell zonal map *per se* is not required for insults in Eph/ephrin signaling to consequently disrupt the precision of mossy fiber patterning.

Our data address a distinction between the molecular mechanisms that form parasagittal zones in Purkinje cells vs. mossy fibers. Purkinje cell patterning has been thought to control the topography of all other cerebellar components, with the idea that they accomplish this *via* intercellular communication mediated by cell-to-cell contact and/or molecular cues. We show that loss of specific Eph/ephrin molecular signals leaves the Purkinje cell map intact but nevertheless alters spinocerebellar afferent patterns. How then do Purkinje cells control afferent mapping? We speculate that Purkinje cell zones are not disrupted by deleting the *ephrin-A2* and *ephrin-A5* genes or by deleting the *EphA4* gene (Karam et al., 2002) because there are multiple stages of constructing the complete zonal module, which would include patterning of afferents and efferents around the Purkinje cell. We suggest that the genes encoding patterned Eph/ephrin positional cues in Purkinje cells are expressed as factors for executing the Purkinje cell program that shapes the module around an existing plan of zones—at those early stages, the module is likely exclusively made up of Purkinje cells. In this scenario, patterned Eph/ephrin combinations would function as effector molecules for matching incoming circuit projections with Purkinje cell zones, but these specific Eph/ephrin codes would not be required for forming the Purkinje cell zones themselves. This argument is supported by the timing of Purkinje cell zonal development. Viral-mediated marking of Purkinje cells at the time of their birth, between E10-E13 (Miale and Sidman, 1961), demonstrates

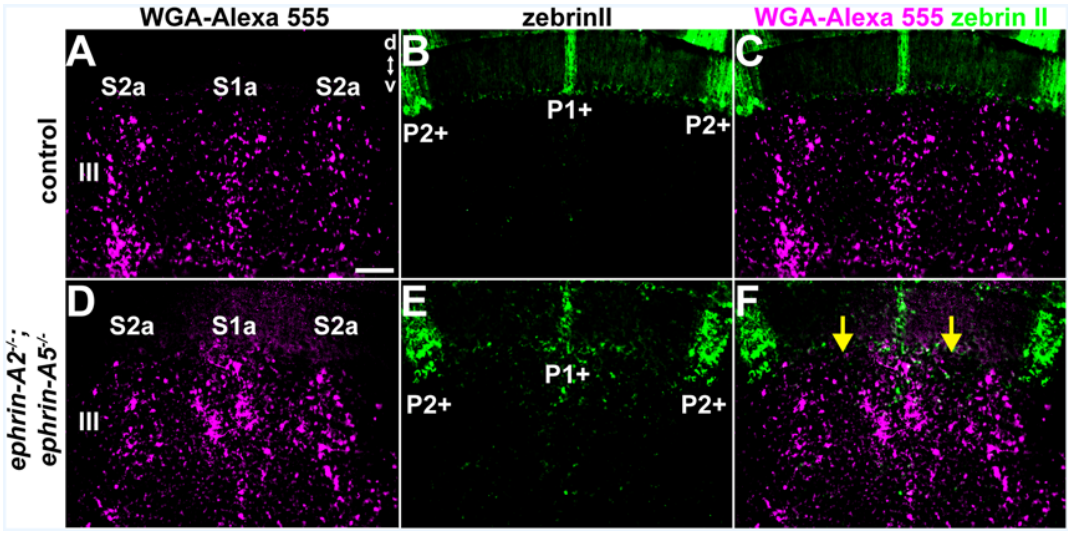

FIGURE 4 | The relationship between Purkinje cell zones and spinocerebellar mossy fiber zones is disrupted in *ephrin-A2*$^{-/-}$;*ephrin-A5*$^{-/-}$ mutant mice. **(A–C)** Image of the WGA-Alexa 555 signal and zebrinII expression in the anterior cerebellum of a control mouse (*N* = 6). The patterning of the spinocerebellar mossy fiber zones has a systematic relationship to the map defined by the Purkinje cell zones. d, dorsal, v, ventral. Scale = 100 μm. **(D–F)** Image of the WGA-Alexa 555 signal and zebrinII expression in the anterior cerebellum of an *ephrin-A2*$^{-/-}$;*ephrin-A5*$^{-/-}$ double knockout mouse (*N* = 3). The relationship between spinocerebellar terminal field zones (S1a and S2a) and the boundaries of the Purkinje cell zones (P1+ and P2+) is disrupted due to the poorly defined spinocerebellar zone boundaries (yellow arrows).

an early assembly of zones (Hashimoto and Mikoshiba, 2003) which are further defined by gene expression starting at ∼E14 (Oberdick et al., 1993; Millen et al., 1995; Larouche et al., 2006; Yaguchi et al., 2009; Wilson et al., 2011; Fujita et al., 2012; Vibulyaseck et al., 2017). There is strong evidence that the establishment of Purkinje cell zones is dependent on the *early B-cell factor 2* (*Ebf2*) gene that encodes a non-basic helix-loop-helix transcription factor and the homeobox-containing *Engrailed* (*En1/2*) genes. *Ebf2* plays a role in establishing the zebrinII-positive vs. negative identity of Purkinje cells (Croci et al., 2006; Chung et al., 2008), and *En1/2* are required for the early stages of patterning Purkinje cell zones (Baader et al., 1999; Sillitoe et al., 2008). Interestingly, *En1/2* acts upstream of *ephrin-A2* and *ephrin-A5* in the tectum to establish positional cues and guide the patterning of afferents from the retina that express *Eph* receptors (Logan et al., 1996; Shigetani et al., 1997). In the cerebellum, loss of *ephrin-A2* and *ephrin-A5* in Purkinje cells could lead to afferent termination defects because the absence of these cues affects the full composite of signals that define the cerebellar internal map, which would cause a failure in the ability of the mossy fibers to interpret the "zip code." However, it is also possible that the many other Eph/ephrin molecules expressed in the cerebellum during development (Lin and Cepko, 1998; Rogers et al., 1999; Karam et al., 2000, 2002; Blanco et al., 2002; Nishida et al., 2002; Saywell et al., 2014) compensate for a potential role of ephrin-A2 and/or ephrin-A5 in establishing Purkinje zones. Indeed, future work would need to resolve the exact timing of the onset of Eph/ephrin expression in different embryonic cerebellar neurons in order to fully appreciate how these molecules influence patterning. In any case, altering the Purkinje cell map has proven very difficult with several molecular and injury methods, and likely reflects the intrinsic control of Purkinje cell patterning (Apps and Hawkes, 2009). It is, therefore, striking that loss of *ephrin-A2* and *ephrin-A5* disrupts spinocerebellar mossy fiber zones but not the Purkinje cell molecular code since the relationship between afferent identity and Purkinje cell molecular identity is resistant even to experimental manipulations that dramatically alter cerebellar morphology (Vogel and Prittle, 1994; Vig et al., 2005; Reeber et al., 2013). We showed that the relationship between Purkinje cell molecular zone identity and the mossy fiber termination pattern is disrupted in the absence of *ephrin-A2* and *ephrin-A5* and is not the result of a gross morphologic displacement of circuitry. These data lead us to ask whether the refinement of mossy fiber zones by ephrin-A2/ephrin-A5 is specific to the spinocerebellar subset or generalizes to other mossy fiber inputs. We suspect that a given set of Purkinje cell zones would guide multiple cerebellar inputs into zones depending on the molecular tags expressed at the axons/terminals. For instance, spinocerebellar and cuneocerebellar terminals likely share some molecular targeting signals, whereas the more posteriorly located vestibular mossy fiber afferent terminals could use at least some unique cues compared to the anteriorly projecting afferents. It is also possible that at a finer level, even the different cerebellar-projecting cell classes from the spinal cord (Clarke's column, border cells, etc.) could use different Eph/ephrin molecules for patterning, which could explain the lobule-specific and overall circumscribed effects that we observed. Therefore, we speculate that dedicated, and probably combinatorial, Eph/ephrin signaling mechanism(s) could contribute to coordinating the organization of inputs and outputs of Purkinje cells during circuit formation.

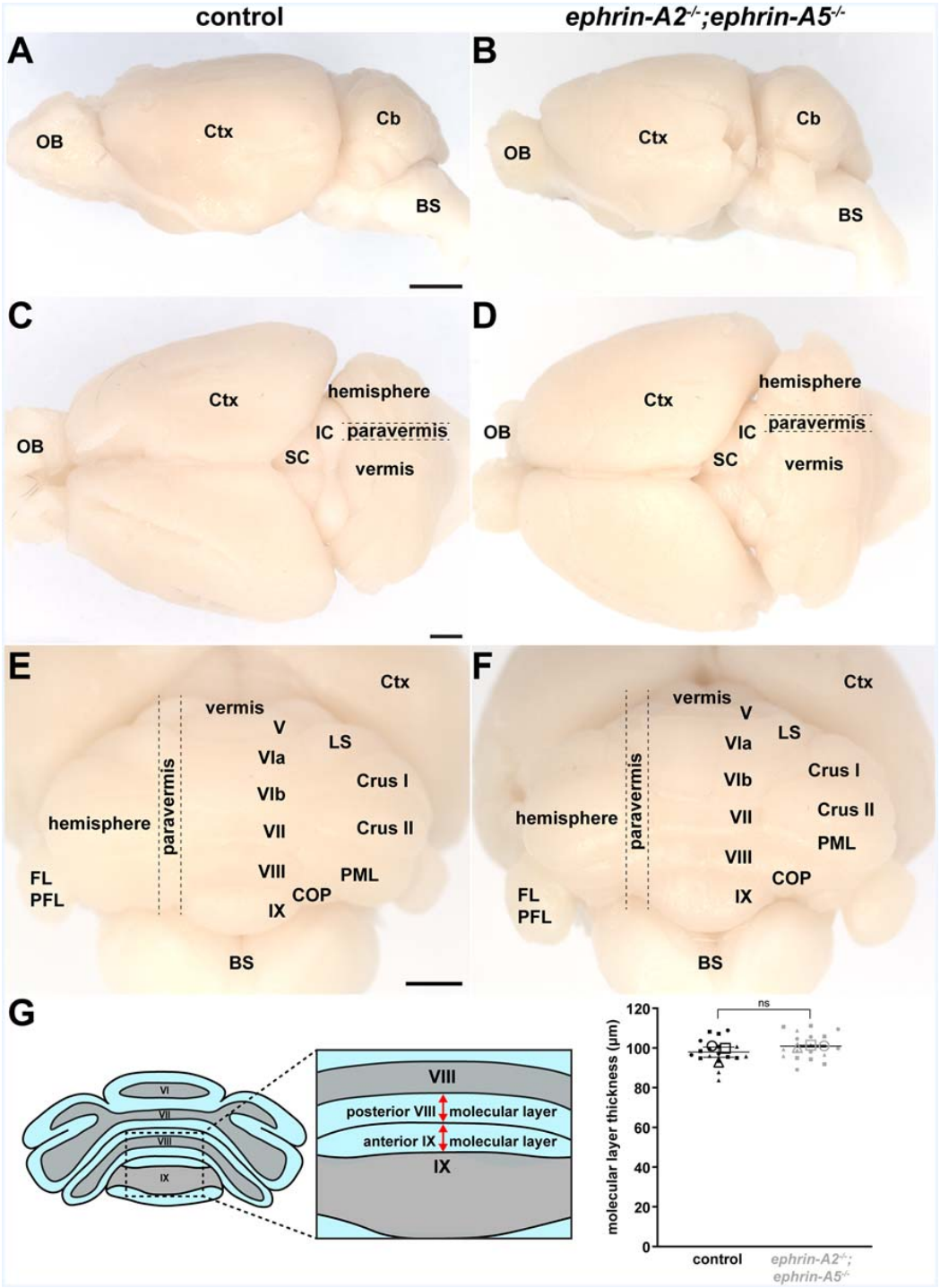

FIGURE 5 | Cerebellar lobule position and cerebellar cortical thickness are unaltered in adult *ephrin-A2*$^{-/-}$*/ephrin-A5*$^{-/-}$ mutant mice. **(A)** Whole-mount image of a lateral view of a control mouse brain (*N* = 6). OB, olfactory bulb; Ctx, cerebral cortex; Cb, cerebellum; BS, brain stem. Scale = 2 mm. **(B)** Whole-mount image of a lateral view of an *ephrin-A2*$^{-/-}$*;ephrin-A5*$^{-/-}$ double knockout mouse brain (*N* = 6). The cerebellum is in the correct location and proportional to the rest of the brain. **(C)** Whole-mount image of a dorsal view of a control mouse brain (*N* = 6). The gross mediolateral subdivisions of the cerebellum are visible (vermis, paravermis, hemisphere). OB, olfactory bulb; Ctx, cerebral cortex; SC, superior colliculus; IC, inferior colliculus. Scale = 1 mm. **(D)** Whole-mount image of a dorsal view of an *ephrin-A2*$^{-/-}$*;ephrin-A5*$^{-/-}$ double knockout mouse brain (*N* = 6). The gross mediolateral subdivisions of the cerebellum are fully represented and in their correct locations (vermis, paravermis, hemisphere). **(E)** Whole-mount image of a posterior view of a control mouse brain (*N* = 6). The cerebellar lobules are visible. Note that lobules I–IV and X of the vermis are located underneath the other lobules and out of view in this orientation. Ctx, cerebral cortex; LS, lobulus simplex;

(*Continued*)

FIGURE 5 | Continued
PML, paramedian lobule; COP, copula pyramidis; FL/PFL, flocculus and paraflocculus; BS, brain stem. Scale = 1 mm. **(F)** Whole-mount image of a posterior view of an *ephrin-A2*$^{-/-}$*;ephrin-A5*$^{-/-}$ double knockout mouse brain ($N = 6$). The main lobules are fully represented and in their correct locations. **(G)** Quantification of the molecular layer thickness measured from lobules VIII and IX. Molecular layer thickness is unaltered in the mutant mice [control = 97.9 μm ± 2.55 μm; *ephrin-A2*$^{-/-}$*;ephrin-A5*$^{-/-}$ = 100.9 μm ± 0.373 μm; $n = 6$ measurements per animal (small data points), $N = 3$ animals per genotype (large data points, each shape represents a different animal), $p = 0.3088$]. Error bars indicate the standard error of the mean. ns = not significant.

Despite the reproducible defects we observed in spinocerebellar zonal targeting, a map, albeit altered, did form, and individual clusters of terminals were represented in the mutants. During nervous system development, the processes of axon guidance, target recognition, and map formation are controlled by a growing list of overlapping molecular mechanisms including Netrin/Unc/DCC, Slit/Robo, Semaphorins/Plexins, and the different Cadherin family members. Therefore, the partial segregation of spinocerebellar mossy fibers we observed in *ephrin-A2*$^{-/-}$*;ephrin-A5*$^{-/-}$ mice could be due to the overlapping expression and function of other molecules in the cerebellum, such as cell-adhesion molecules (Arndt et al., 1998; Luo et al., 2004), additional Eph/ephrin family members (Lin and Cepko, 1998; Rogers et al., 1999; Karam et al., 2000, 2002; Blanco et al., 2002; Nishida et al., 2002; Saywell et al., 2014), or perhaps direct guidance by *En1/2* (Brunet et al., 2005). The loss of *ephrin-A2* or *ephrin-A5* could also cause more subtle or synaptic level changes to spinocerebellar mossy fiber topography that were not detected by the methods used here. We also expect that the loss of *ephrin-A2* or *ephrin-A5* could also disrupt the development of other components of the cerebellar circuit that were not tested here—for example, the different classes of interneurons. Because spinocerebellar mossy fiber zones have not been examined in *ephrin-A2* or *ephrin-A5* single knockout mice, our findings in the double knockout mice do not distinguish whether either gene is essential for refining mossy fiber zones independent of the other gene. However, there is a high level of redundancy in the Eph/ephrin family of signaling molecules (Gale et al., 1996; Feldheim et al., 2000), and we postulate that there is not a single master regulator of mossy fiber zone formation. Future experiments will hopefully reveal how ephrin-A2 and ephrin-A5, in concert with other molecules and pathways, precisely coordinate the attraction and repulsion of intrinsic and extrinsic fibers into precise cerebellar zonal maps.

CONCLUSION

The cerebellum is organized around a pleated array of parasagittal zones. Purkinje cells are the central component of zones. Recent work has shown that Purkinje cell zones have distinct neuronal firing properties, which could determine how they control different motor and non-motor behaviors. However, the mechanisms that assemble zones are still unclear. There is a long-standing hypothesis that perhaps Purkinje cell zones provide the platform upon which all other cerebellar components establish their topography. The activity of a molecular cue that mediates cell-to-cell communication would satisfy this hypothesis. Here, we provide evidence that Eph/ephrin signaling contributes to spinocerebellar mossy fiber zones. We also show that while Purkinje cells may indeed guide incoming afferents and shape their terminal field patterns, they likely employ cell intrinsic cues to first set up their own zones and then express cues to direct the fibers. We anticipate that the full molecular profile for cues that generate mossy fibers zones includes a large number of proteins with diverse functions.

DATA AVAILABILITY STATEMENT

All datasets generated for this study are included in the article/**Supplementary Material**.

ETHICS STATEMENT

The animal study was reviewed and approved by the Institutional Animal Care and Use Committee at Baylor College of Medicine.

AUTHOR CONTRIBUTIONS

EL and RS designed the experiments, performed the experiments, analyzed the data, wrote the article, and edited the article.

FUNDING

This work was supported by funds from Baylor College of Medicine (BCM) and Texas Children's Hospital. RS also received support from The Hamill Foundation, BCM IDDRC U54HD083092 (Neuropathology sub-Core), and the National Institutes of Neurological Disorders and Stroke (NINDS) R01NS089664 and R01NS100874.

ACKNOWLEDGMENTS

We thank Samri Gebre for help with histology.

SUPPLEMENTARY MATERIAL

The Supplementary Material for this article can be found online at: https://www.frontiersin.org/articles/10.3389/fnsys.2020.00007/full#supplementary-material.

FIGURE S1 | WGA-Alexa 555 tracing of spinocerebellar mossy fibers. **(A)** Representative image of the WGA-Alexa 555 signal in lobules I/II of a control mouse ($N = 6$). d, dorsal, v, ventral. Scale = 200 μm. **(B)** Representative image of the WGA-Alexa 555 signal in lobules I/II of an *ephrin-A2*$^{-/-}$*;ephrin-A5*$^{-/-}$ mouse ($N = 6$). **(C)** Representative image of the WGA-Alexa 555 signal in lobules IV/V of a control mouse ($N = 6$). d, dorsal, v, ventral. Scale = 100 μm. **(D)** Representative image of the WGA-Alexa 555 signal in lobules IV/V of an *ephrin-A2*$^{-/-}$*;ephrin-A5*$^{-/-}$ mouse ($N = 6$). **(E)** Representative image of the WGA-Alexa 555 signal in the copula pyramidis of a control mouse ($N = 6$). Scale = 200 μm. **(F)** Representative image of the WGA-Alexa 555 signal in the copula pyramidis of an *ephrin-A2*$^{-/-}$*;ephrin-A5*$^{-/-}$ mouse ($N = 6$).

REFERENCES

Apps, R., and Hawkes, R. B. (2009). Cerebellar cortical organization: a one-map hypothesis. *Nat. Rev. Neurosci.* 10, 670–681. doi: 10.1038/nrn2698

Apps, R., Hawkes, R. B., Aoki, S., Bengtsson, F., Brown, A. M., Chen, G., et al. (2018). Cerebellar modules and their role as operational cerebellar processing units. *Cerebellum* 17, 683–684. doi: 10.1007/s12311-018-0959-9

Armstrong, C. L., Krueger-Naug, A. M., Currie, R. W., and Hawkes, R. B. (2000). Constitutive expression of the 25-kDa heat shock protein Hsp25 reveals novel parasagittal bands of Purkinje cells in the adult mouse cerebellar cortex. *J. Comp. Neurol.* 416, 383–397. doi: 10.1002/(sici)1096-9861(20000117)416:3<383::aid-cne9>3.0.co;2-m

Arndt, K., Nakagawa, S., Takeichi, M., and Redies, C. (1998). Cadherin-defined segments and parasagittal cell ribbons in the developing chicken cerebellum. *Mol. Cell. Neurosci.* 10, 211–228. doi: 10.1006/mcne.1998.0665

Arsénio Nunes, M. L., Sotelo, C., Nunes, M. L. A., and Sotelo, C. (1985). Development of the spinocerebellar system in the postnatal rat. *J. Comp. Neurol.* 237, 291–306. doi: 10.1002/cne.902370302

Arsénio Nunes, M. L., Sotelo, C., and Wehrlé, R. (1988). Organization of spinocerebellar projection map in three types of agranular cerebellum: Purkinje cells vs. granule cells as organizer element. *J. Comp. Neurol.* 273, 120–136. doi: 10.1002/cne.902730110

Baader, S. L., Vogel, M. W., Sanlioglu, S., Zhang, X., and Oberdick, J. (1999). Selective disruption of "late onset" sagittal banding patterns by ectopic expression of engrailed-2 in cerebellar purkinje cells. *J. Neurosci.* 19, 5370–5379. doi: 10.1523/JNEUROSCI.19-13-05370.1999

Blanco, M. J., Peña-Melián, A., and Nieto, M. A. (2002). Expression of EphA receptors and ligands during chick cerebellar development. *Mech. Dev.* 114, 225–229. doi: 10.1016/s0925-4773(02)00065-5

Brochu, G., Maler, L., and Hawkes, R. B. (1990). Zebrin II: a polypeptide antigen expressed selectively by Purkinje cells reveals compartments in rat and fish cerebellum. *J. Comp. Neurol.* 291, 538–552. doi: 10.1002/cne.902910405

Brunet, I., Weinl, C., Piper, M., Trembleau, A., Volovitch, M., Harris, W., et al. (2005). The transcription factor Engrailed-2 guides retinal axons. *Nature* 438, 94–98. doi: 10.1038/nature04110

Cang, J., Kaneko, M., Yamada, J., Woods, G., Stryker, M. P., and Feldheim, D. A. (2005). Ephrin-as guide the formation of functional maps in the visual cortex. *Neuron* 48, 577–589. doi: 10.1016/j.neuron.2005.10.026

Cheng, H.-J., Nakamoto, M., Bergemann, A. D., and Flanagan, J. G. (1995). Complementary gradients in expression and binding of ELF-1 and Mek4 in development of the topographic retinotectal projection map. *Cell* 82, 371–381. doi: 10.1016/0092-8674(95)90426-3

Chung, S. H., Marzban, H., Croci, L., Consalez, G. G., and Hawkes, R. B. (2008). Purkinje cell subtype specification in the cerebellar cortex: early B-cell factor 2 acts to repress the zebrin II-positive Purkinje cell phenotype. *Neuroscience* 153, 721–732. doi: 10.1016/j.neuroscience.2008.01.090

Croci, L., Chung, S. H., Masserdotti, G., Gianola, S., Bizzoca, A., Gennarini, G., et al. (2006). A key role for the HLH transcription factor EBF2COE2,O/E-3 in Purkinje neuron migration and cerebellar cortical topography. *Development* 133, 2719–2729. doi: 10.1242/dev.02437

Drescher, U., Kremoser, C., Handwerker, C., Löschinger, J., Noda, M., and Bonhoeffer, F. (1995). *In vitro* guidance of retinal ganglion cell axons by RAGS, a 25 kDa tectal protein related to ligands for Eph receptor tyrosine kinases. *Cell* 82, 359–370. doi: 10.1016/0092-8674(95)90425-5

Feldheim, D. A., Kim, Y. I., Bergemann, A. D., Frisén, J., Barbacid, M., and Flanagan, J. G. (2000). Genetic analysis of ephrin-A2 and ephrin-A5 shows their requirement in multiple aspects of retinocollicular mapping. *Neuron* 25, 563–574. doi: 10.1016/s0896-6273(00)81060-0

Flanagan, J. G., and Vanderhaeghen, P. (1998). The ephrins and Eph receptors in neural development. *Annu. Rev. Neurosci.* 21, 309–345. doi: 10.1146/annurev.neuro.21.1.309

Fujita, H., Morita, N., Furuichi, T., and Sugihara, I. (2012). Clustered fine compartmentalization of the mouse embryonic cerebellar cortex and its rearrangement into the postnatal striped configuration. *J. Neurosci.* 32, 15688–15703. doi: 10.1523/JNEUROSCI.1710-12.2012

Gale, N. W., Holland, S. J., Valenzuela, D. M., Flenniken, A., Pan, L., Ryan, T. E., et al. (1996). Eph receptors and ligands comprise two major specificity subclasses and are reciprocally compartmentalized during embryogenesis. *Neuron* 17, 9–19. doi: 10.1016/s0896-6273(00)80276-7

Gebre, S. A., Reeber, S. L., and Sillitoe, R. V. (2012). Parasagittal compartmentation of cerebellar mossy fibers as revealed by the patterned expression of vesicular glutamate transporters VGLUT1 and VGLUT2. *Brain Struct. Funct.* 217, 165–180. doi: 10.1007/s00429-011-0339-4

Grant, G. (1962). Spinal course and somatotopically localized termination of the spinocerebellar tracts. An experimental study in the cat. *Acta Physiol. Scand. Suppl.* 56, 1–61.

Gravel, C., and Hawkes, R. B. (1990). Parasagittal organization of the rat cerebellar cortex: direct comparison of purkinje cell compartments and the organization of the spinocerebellar projection. *J. Comp. Neurol.* 291, 79–102. doi: 10.1002/cne.902910107

Grishkat, H. L., and Eisenman, L. M. (1995). Development of the spinocerebellar projection in the prenatal mouse. *J. Comp. Neurol.* 363, 93–108. doi: 10.1002/cne.903630109

Hansen, S. T., Meera, P., Otis, T. S., and Pulst, S. M. (2013). Changes in Purkinje cell firing and gene expression precede behavioral pathology in a mouse model of SCA2. *Hum. Mol. Genet.* 22, 271–283. doi: 10.1093/hmg/dds427

Harrison, M., O'Brien, A., Adams, L., Cowin, G., Ruitenberg, M. J., Sengul, G., et al. (2013). Vertebral landmarks for the identification of spinal cord segments in the mouse. *NeuroImage* 68, 22–29. doi: 10.1016/j.neuroimage.2012.11.048

Hashimoto, M., Ito, R., Kitamura, N., Namba, K., and Hisano, Y. (2012). Epha4 controls the midline crossing and contralateral axonal projections of inferior olive neurons. *J. Comp. Neurol.* 520, 1702–1720. doi: 10.1002/cne.23008

Hashimoto, M., and Mikoshiba, K. (2003). Mediolateral compartmentalization of the cerebellum is determined on the "birth date" of Purkinje cells. *J. Neurosci.* 23, 11342–11351. doi: 10.1523/JNEUROSCI.23-36-11342.2003

Hawkes, R. B. (2014). Purkinje cell stripes and long-term depression at the parallel fiber-Purkinje cell synapse. *Front. Syst. Neurosci.* 8, 41. doi: 10.3389/fnsys.2014.00041

Heckroth, J. A., and Eisenman, L. M. (1988). Parasagittal organization of mossy fiber collaterals in the cerebellum of the mouse. *J. Comp. Neurol.* 270, 385–394. doi: 10.1002/cne.902700307

Huffman, K. J., and Cramer, K. S. (2007). EphA4 misexpression alters tonotopic projections in the auditory brainstem. *Dev. Neurobiol.* 67, 1655–1668. doi: 10.1002/dneu.20535

Iwasato, T., Katoh, H., Nishimaru, H., Ishikawa, Y., Inoue, H., Saito, Y. M., et al. (2007). Rac-GAP α-chimerin regulates motor-circuit formation as a key mediator of EphrinB3/EphA4 forward signaling. *Cell* 130, 742–753. doi: 10.1016/j.cell.2007.07.022

Ji, Z., and Hawkes, R. B. (1994). Topography of Purkinje cell compartments and mossy fiber terminal fields in lobules II and III of the rat cerebellar cortex: spinocerebellar and cuneocerebellar projections. *Neuroscience* 61, 935–954. doi: 10.1016/0306-4522(94)90414-6

Ji, Z., and Hawkes, R. B. (1995). Developing mossy fiber terminal fields in the rat cerebellar cortex may segregate because of Purkinje cell compartmentation and not competition. *J. Comp. Neurol.* 359, 197–212. doi: 10.1002/cne.903590202

Kalinovsky, A., Boukhtouche, F., Blazeski, R., Bornmann, C., Suzuki, N., Mason, C. A., et al. (2011). Development of axon-target specificity of ponto-cerebellar afferents. *PLoS Biol.* 9:e1001013. doi: 10.1371/journal.pbio.1001013

Kania, A., and Jessell, T. M. (2003). Topographic motor projections in the limb imposed by LIM homeodomain protein regulation of ephrin-A:EphA interactions. *Neuron* 38, 581–596. doi: 10.1016/s0896-6273(03)00292-7

Kania, A., and Klein, R. (2016). Mechanisms of ephrin-Eph signalling in development, physiology and disease. *Nat. Rev. Mol. Cell Biol.* 17, 240–256. doi: 10.1038/nrm.2015.16

Karam, S. D., Burrows, R. C., Logan, C., Koblar, S., Pasquale, E. B., and Bothwell, M. (2000). Eph receptors and ephrins in the developing chick cerebellum: relationship to sagittal patterning and granule cell migration. *J. Neurosci.* 20, 6488–6500. doi: 10.1523/JNEUROSCI.20-17-06488.2000

Karam, S. D., Dottori, M., Ogawa, K., Henderson, J. T., Boyd, A. W., Pasquale, E. B., et al. (2002). EphA4 is not required for Purkinje cell compartmentation. *Dev. Brain Res.* 135, 29–38. doi: 10.1016/s0165-3806(02)00278-x

Larouche, M., Che, P. M., and Hawkes, R. (2006). Neurogranin expression identifies a novel array of Purkinje cell parasagittal stripes during mouse cerebellar development. *J. Comp. Neurol.* 494, 215–227. doi: 10.1002/cne.20791

Larsell, O. (1970). *The Comparative Anatomy and Histology of the Cerebellum: From Monotremes through Apes.* Minneapolis, MN: University of Minnesota Press.

Leclerc, N., Gravel, C., and Hawkes, R. B. (1988). Development of parasagittal zonation in the rat cerebellar cortex: MabQ113 antigenic bands are created postnatally by the suppression of antigen expression in a subset of Purkinje cells. *J. Comp. Neurol.* 273, 399–420. doi: 10.1002/cne.902730310

Levy, S. L., White, J. J., Lackey, E. P., Schwartz, L., and Sillitoe, R. V. (2017). WGA-alexa conjugates for axonal tracing. *Curr. Protoc. Neurosci.* 79, 1.28.1–1.28.24. doi: 10.1002/cpns.28

Lin, J. C., and Cepko, C. L. (1998). Granule cell raphes and parasagittal domains of Purkinje cells: complementary patterns in the developing chick cerebellum. *J. Neurosci.* 18, 9342–9353. doi: 10.1523/JNEUROSCI.18-22-09342.1998

Logan, C., Wizenmann, A., Drescher, U., Monschau, B., Bonhoeffer, F., and Lumsden, A. (1996). Rostral optic tectum acquires caudal characteristics following ectopic engrailed expression. *Curr. Biol.* 6, 1006–1014. doi: 10.1016/s0960-9822(02)00645-0

Luo, Y., Patel, R. P., Sarpong, G. A., Sasamura, K., and Sugihara, I. (2018). Single axonal morphology and termination to cerebellar aldolase C stripes characterize distinct spinocerebellar projection systems originating from the thoracic spinal cord in the mouse. *J. Comp. Neurol.* 526, 681–706. doi: 10.1002/cne.24360

Luo, J., Treubert-Zimmermann, U., and Redies, C. (2004). Cadherins guide migrating Purkinje cells to specific parasagittal domains during cerebellar development. *Mol. Cell. Neurosci.* 25, 138–152. doi: 10.1016/j.mcn.2003.10.003

Manzini, M. C., Ward, M. S., Zhang, Q., Lieberman, M. D., and Mason, C. A. (2006). The stop signal revised: immature cerebellar granule neurons in the external germinal layer arrest pontine mossy fiber growth. *J. Neurosci.* 26, 6040–6051. doi: 10.1523/JNEUROSCI.4815-05.2006

Mason, C. A., and Gregory, E. (1984). Postnatal maturation of cerebellar mossy and climbing fibers: transient expression of dual features on single axons. *J. Neurosci.* 4, 1715–1735. doi: 10.1523/JNEUROSCI.04-07-01715.1984

Matsushita, M., and Hosoya, Y. (1982). Spinocerebellar projections to lobules III to V of the anterior lobe in the cat, as studied by retrograde transport of horseradish peroxidase. *J. Comp. Neurol.* 208, 127–143. doi: 10.1002/cne.902080203

Matsushita, M., and Ikeda, M. (1980). Spinocerebellar projections to the vermis of the posterior lobe and the paramedian lobule in the cat, as studied by retrograde transport of horseradish peroxidase. *J. Comp. Neurol.* 192, 143–162. doi: 10.1002/cne.901920110

Matsushita, M., and Okado, N. (1981). Spinocerebellar projections to lobules I and II of the anterior lobe in the cat, as studied by retrograde transport of horseradish peroxidase. *J. Comp. Neurol.* 197, 411–424. doi: 10.1002/cne.901970305

Matsushita, M., Ragnarson, B., and Grant, G. (1991). Topographic relationship between sagittal Purkinje cell bands revealed by a monoclonal antibody to zebrin I and spinocerebellar projections arising from the central cervical nucleus in the rat. *Exp. Brain Res.* 84, 133–141. doi: 10.1007/bf00231768

Miale, I. L., and Sidman, R. L. (1961). An autoradiographic analysis of histogenesis in the mouse cerebellum. *Exp. Neurol.* 4, 277–296. doi: 10.1016/0014-4886(61)90055-3

Millen, K. J., Hui, C. C., and Joyner, A. L. (1995). A role for En-2 and other murine homologues of Drosophila segment polarity genes in regulating positional information in the developing cerebellum. *Development* 121, 3935–3945.

Miterko, L. N., Lackey, E. P., Heck, D. H., and Sillitoe, R. V. (2018). Shaping diversity into the brain's form and function. *Front. Neural Circuits* 12:83. doi: 10.3389/fncir.2018.00083

Nishida, K., Flanagan, J. G., and Nakamoto, M. (2002). Domain-specific olivocerebellar projection regulated by the EphA-ephrin-A interaction. *Development* 129, 5647–5658. doi: 10.1242/dev.00162

Oberdick, J., Schilling, K., Smeyne, R., Corbin, J., Bocchiaro, C., and Morgan, J. (1993). Control of segment-like patterns of gene expression in the mouse cerebellum. *Neuron* 10, 1007–1018. doi: 10.1016/0896-6273(93)90050-2

Ozol, K., Hayden, J. M., Oberdick, J., and Hawkes, R. B. (1999). Transverse zones in the vermis of the mouse cerebellum. *J. Comp. Neurol.* 412, 95–111. doi: 10.1002/(sici)1096-9861(19990913)412:1<95::aid-cne7>3.0.co;2-y

Quy, P. N., Fujita, H., Sakamoto, Y., Na, J., and Sugihara, I. (2011). Projection patterns of single mossy fiber axons originating from the dorsal column nuclei mapped on the aldolase C compartments in the rat cerebellar cortex. *J. Comp. Neurol.* 519, 874–899. doi: 10.1002/cne.22555

Reeber, S. L., Gebre, S. A., Filatova, N., and Sillitoe, R. V. (2011a). Revealing neural circuit topography in multi-color. *J. Vis. Exp.* 57:e3371. doi: 10.3791/3371

Reeber, S. L., Gebre, S. A., and Sillitoe, R. V. (2011b). Fluorescence mapping of afferent topography in three dimensions. *Brain Struct. Funct.* 216, 159–169. doi: 10.1007/s00429-011-0304-2

Reeber, S. L., Loeschel, C. A., Franklin, A., and Sillitoe, R. V. (2013). Establishment of topographic circuit zones in the cerebellum of scrambler mutant mice. *Front. Neural Circuits* 7:122. doi: 10.3389/fncir.2013.00122

Robertson, B., Grant, G., and Björkeland, M. (1983). Demonstration of spinocerebellar projections in cat using anterograde transport of WGA-HRP, with some observations on spinomesencephalic and spinothalamic projections. *Exp. Brain Res.* 52, 99–104. doi: 10.1007/bf00237154

Rogers, J. H., Ciossek, T., Menzel, P., and Pasquale, E. B. (1999). Eph receptors and ephrins demarcate cerebellar lobules before and during their formation. *Mech. Dev.* 87, 119–128. doi: 10.1016/s0925-4773(99)00154-9

Saywell, V., Cioni, J.-M., and Ango, F. (2014). Developmental gene expression profile of axon guidance cues in purkinje cells during cerebellar circuit formation. *Cerebellum* 13, 307–317. doi: 10.1007/s12311-014-0548-5

Seil, F. J., Johnson, M. L., and Hawkes, R. B. (1995). Molecular compartmentation expressed in cerebellar cultures in the absence of neuronal activity and neuron-glia interactions. *J. Comp. Neurol.* 356, 398–407. doi: 10.1002/cne.903560307

Shigetani, Y., Funahashi, J. I., and Nakamura, H. (1997). En-2 regulates the expression of the ligands for Eph type tyrosine kinases in chick embryonic tectum. *Neurosci. Res.* 27, 211–217. doi: 10.1016/s0168-0102(96)01151-0

Sillitoe, R. V. (2016). Mossy fibers terminate directly within purkinje cell zones during mouse development. *Cerebellum* 15, 14–17. doi: 10.1007/s12311-015-0712-6

Sillitoe, R. V., and Hawkes, R. B. (2002). Whole-mount immunohistochemistry: a high-throughput screen for patterning defects in the mouse cerebellum. *J. Histochem. Cytochem.* 50, 235–244. doi: 10.1177/002215540205000211

Sillitoe, R. V., and Joyner, A. L. (2007). Morphology, molecular codes, and circuitry produce the three-dimensional complexity of the cerebellum. *Annu. Rev. Cell Dev. Biol.* 23, 549–577. doi: 10.1146/annurev.cellbio.23.090506.123237

Sillitoe, R. V., Marzban, H., Larouche, M., Zahedi, S., Affanni, J., and Hawkes, R. B. (2005). Conservation of the architecture of the anterior lobe vermis of the cerebellum across mammalian species. *Prog. Brain Res.* 148, 283–297. doi: 10.1016/s0079-6123(04)48022-4

Sillitoe, R. V., Stephen, D., Lao, Z., and Joyner, A. L. (2008). Engrailed homeobox genes determine the organization of purkinje cell sagittal stripe gene expression in the adult cerebellum. *J. Neurosci.* 28, 12150–12162. doi: 10.1523/JNEUROSCI.2059-08.2008

Sillitoe, R. V., Vogel, M. W., and Joyner, A. L. (2010). Engrailed homeobox genes regulate establishment of the cerebellar afferent circuit map. *J. Neurosci.* 30, 10015–10024. doi: 10.1523/JNEUROSCI.0653-10.2010

Sotelo, C. (2004). Cellular and genetic regulation of the development of the cerebellar system. *Prog. Neurobiol.* 72, 295–339. doi: 10.1016/j.pneurobio.2004.03.004

Sotelo, C., and Chédotal, A. (2005). Development of the olivocerebellar system: migration and formation of cerebellar maps. *Prog. Brain Res.* 148, 1–20. doi: 10.1016/S0079-6123(04)48001-7

Sotelo, C., and Wassef, M. (1991). Cerebellar development: afferent organization and Purkinje cell heterogeneity. *Philos. Trans. R. Soc. London. Ser. B Biol. Sci.* 331, 307–313. doi: 10.1098/rstb.1991.0022

Sperry, R. W. (1963). Chemoaffinity in the orderly growth of nerve fiber patterns and connections. *Proc. Natl. Acad. Sci. U S A* 50, 703–710. doi: 10.1073/pnas.50.4.703

Takeda, T., and Maekawa, K. (1989). Transient direct connection of vestibular mossy fibers to the vestibulocerebellar Purkinje cells in early postnatal development of kittens. *Neuroscience* 32, 99–111. doi: 10.1016/0306-4522(89)90110-3

Vibulyaseck, S., Fujita, H., Luo, Y., Tran, A. K., Oh-Nishi, A., Ono, Y., et al. (2017). Spatial rearrangement of Purkinje cell subsets forms the transverse

and longitudinal compartmentalization in the mouse embryonic cerebellum. *J. Comp. Neurol.* 525, 2971–2990. doi: 10.1002/cne.24250

Vig, J., Goldowitz, D., Steindler, D. A., and Eisenman, L. M. (2005). Compartmentation of the reeler cerebellum: segregation and overlap of spinocerebellar and secondary vestibulocerebellar fibers and their target cells. *Neuroscience* 130, 735–744. doi: 10.1016/j.neuroscience.2004.09.051

Vogel, M. W., Ji, Z., Millen, K., and Joyner, A. L. (1996). The Engrailed-2 homeobox gene and patterning of spinocerebellar mossy fiber afferents. *Dev. Brain Res.* 96, 210–218. doi: 10.1016/0165-3806(96)00122-8

Vogel, M. W., and Prittle, J. (1994). Topographic spinocerebellar mossy fiber projections are maintained in the Lurcher mutant. *J. Comp. Neurol.* 343, 341–351. doi: 10.1002/cne.903430212

Voogd, J. (2014). What we do not know about cerebellar systems neuroscience. *Front. Syst. Neurosci.* 8:227. doi: 10.3389/fnsys.2014.00227

Voogd, J., Broere, G., and van Rossum, J. (1969). The medio-lateral distribution of the spinocerebellar projection in the anterior lobe and the simple lobule in the cat and a comparison with some other afferent fibre systems. *Psychiatr. Neurol. Neurochir.* 72, 137–151.

Wassef, M., Sotelo, C., Thomasset, M., Granholm, A.-C., Leclerc, N., Rafrafi, J., et al. (1990). Expression of compartmentation antigen zebrin I in cerebellar transplants. *J. Comp. Neurol.* 294, 223–234. doi: 10.1002/cne.902940207

Wassef, M., Zanetta, J. P., Brehier, A., and Sotelo, C. (1985). Transient biochemical compartmentalization of Purkinje cells during early cerebellar development. *Dev. Biol.* 111, 129–137. doi: 10.1016/0012-1606(85)90441-5

White, J. J., Arancillo, M., King, A., Lin, T., Miterko, L. N., Gebre, S. A., et al. (2016). Pathogenesis of severe ataxia and tremor without the typical signs of neurodegeneration. *Neurobiol. Dis.* 86, 86–98. doi: 10.1016/j.nbd.2015.11.008

White, J. J., Arancillo, M., Stay, T. L., George-Jones, N. A., Levy, S. L., Heck, D. H., et al. (2014). Cerebellar zonal patterning relies on purkinje cell neurotransmission. *J. Neurosci.* 34, 8231–8245. doi: 10.1523/JNEUROSCI.0122-14.2014

White, J. J., and Sillitoe, R. V. (2013). Development of the cerebellum: from gene expression patterns to circuit maps. *Wiley Interdiscip. Rev. Dev. Biol.* 2, 149–164. doi: 10.1002/wdev.65

White, J. J., and Sillitoe, R. V. (2017). Genetic silencing of olivocerebellar synapses causes dystonia-like behaviour in mice. *Nat. Commun.* 8:14912. doi: 10.1038/ncomms14912

Wilkinson, D. G. (2001). Multiple roles of eph receptors and ephrins in neural development. *Nat. Rev. Neurosci.* 2, 155–164. doi: 10.1038/35058515

Wilson, S. L., Kalinovsky, A., Orvis, G. D., and Joyner, A. L. (2011). Spatially restricted and developmentally dynamic expression of engrailed genes in multiple cerebellar cell types. *Cerebellum* 10, 356–372. doi: 10.1007/s12311-011-0254-5

Yaguchi, Y., Yu, T., Ahmed, M. U., Berry, M., Mason, I., and Basson, M. A. (2009). Fibroblast growth factor (FGF) gene expression in the developing cerebellum suggests multiple roles for FGF signaling during cerebellar morphogenesis and development. *Dev. Dyn.* 238, 2058–2072. doi: 10.1002/dvdy.22013

Conflict of Interest: The authors declare that the research was conducted in the absence of any commercial or financial relationships that could be construed as a potential conflict of interest.

frontiers in Systems Neuroscience

ORIGINAL RESEARCH
published: 25 March 2020
doi: 10.3389/fnsys.2020.00013

A Neuroanatomically Grounded Optimal Control Model of the Compensatory Eye Movement System in Mice

Peter J. Holland [1,2,3†], Tafadzwa M. Sibindi [1,2,4†], Marik Ginzburg [2†], Suman Das [1,2], Kiki Arkesteijn [1,5,6], Maarten A. Frens [1‡] and Opher Donchin [1,2,7‡]*

[1] Department of Neuroscience, Erasmus MC, Rotterdam, Netherlands, [2] Department of Biomedical Engineering, Zlotowski Centre for Neuroscience, Ben Gurion University, Beer-Sheva, Israel, [3] School of Psychology, University of Birmingham, Birmingham, United Kingdom, [4] Singapore Institute for Neurotechnology, Singapore, Singapore, [5] Department of Experimental and Applied Psychology, Vrije Universiteit Amsterdam, Amsterdam, Netherlands, [6] Department of Human Movement Sciences, Vrije Universiteit Amsterdam, Amsterdam, Netherlands, [7] ABC Centre for Robotics, Ben Gurion University, Beer-Sheva, Israel

OPEN ACCESS

Edited by:
Nadia Cerminara,
University of Bristol, United Kingdom

Reviewed by:
Thomas Haslwanter,
University of Applied Sciences Upper Austria, Austria
Jean Laurens,
Baylor College of Medicine, United States
Chris Harris,
University of Plymouth, United Kingdom

***Correspondence:**
Maarten A. Frens
m.frens@erasmusmc.nl

[†] These authors have contributed equally to this work

[‡] These authors have contributed equally to this work and share last authorship

Received: 28 May 2019
Accepted: 28 February 2020
Published: 25 March 2020

Citation:
Holland PJ, Sibindi TM, Ginzburg M, Das S, Arkesteijn K, Frens MA and Donchin O (2020) A Neuroanatomically Grounded Optimal Control Model of the Compensatory Eye Movement System in Mice. Front. Syst. Neurosci. 14:13. doi: 10.3389/fnsys.2020.00013

We present a working model of the compensatory eye movement system in mice. We challenge the model with a data set of eye movements in mice (n =34) recorded in 4 different sinusoidal stimulus conditions with 36 different combinations of frequency (0.1–3.2 Hz) and amplitude (0.5–8°) in each condition. The conditions included vestibular stimulation in the dark (vestibular-ocular reflex, VOR), optokinetic stimulation (optokinetic reflex, OKR), and two combined visual/vestibular conditions (the visual-vestibular ocular reflex, vVOR, and visual suppression of the VOR, sVOR). The model successfully reproduced the eye movements in all conditions, except for minor failures to predict phase when gain was very low. Most importantly, it could explain the interaction of VOR and OKR when the two reflexes are activated simultaneously during vVOR stimulation. In addition to our own data, we also reproduced the behavior of the compensatory eye movement system found in the existing literature. These include its response to sum-of-sines stimuli, its response after lesions of the nucleus prepositus hypoglossi or the flocculus, characteristics of VOR adaptation, and characteristics of drift in the dark. Our model is based on ideas of state prediction and forward modeling that have been widely used in the study of motor control. However, it represents one of the first quantitative efforts to simulate the full range of behaviors of a specific system. The model has two separate processing loops, one for vestibular stimulation and one for visual stimulation. Importantly, state prediction in the visual processing loop depends on a forward model of residual retinal slip after vestibular processing. In addition, we hypothesize that adaptation in the system is primarily adaptation of this model. In other words, VOR adaptation happens primarily in the OKR loop.

Keywords: VOR, OKR, mouse, forward model, state estimation, adaptation

INTRODUCTION

Compensatory eye movement (CEM) is a general term for several reflexes whose goal is to maintain a stable image on the retina during movements of the head by moving the eyes in the opposite direction (Delgado-García, 2000). In other words, these reflexes serve to reduce retinal slip (movement of the visual image across the retina). In afoveate animals like mice, the CEM comprises two reflexes: the vestibulo-ocular reflex (VOR) uses vestibular input to predictively compensate retinal slip and the optokinetic reflex (OKR) is driven by the retinal slip itself. The two reflexes have roughly complementary properties: the OKR performs well in low velocities and the VOR works well at high frequencies. The existence of these reflexes allows accurate compensation of retinal slip velocities experienced in normal behavior. However, a challenge for any model of the CEM is to explain the interaction between VOR and OKR. In many conditions, the combined action, with a gain of almost exactly one, is much less than the sum of the two reflexes driven separately. The main aim of this paper is to produce a model of the system and that can simulate the behavior of the VOR, OKR and their interaction. Importantly, the model should be able to reproduce these behaviors with a single set of parameters and be based on the known neuroanatomy. The model must also function in the presence of motor and sensory noise as well as including realistic delays involved in visual sensation.

The CEM system has a number of properties that make it a popular candidate for quantitative modeling of sensorimotor processes (for review see Glasauer, 2007). First, its goal, minimizing retinal slip, is clear and invariant over time (Robinson, 1981). Second, the dynamics of the system as a whole are close to linear. Third, the output only has three degrees of freedom. Moreover, horizontal CEM can be isolated from the other two degrees of freedom and treated as a system with a single degree of freedom. There is a rich tradition in developing models of the CEM (Raphan et al., 1979; Robinson, 1981; Kawato and Gomi, 1992; Merfeld and Young, 1995; Laurens and Droulez, 2007; Lisberger, 2009; Karmali and Merfeld, 2012; Clopath et al., 2014; Laurens and Angelaki, 2017). The different models address different aspects of the CEM system, and we discuss here two key features shared by some of the models: containing an internal model that is used to predict sensory feedback and explaining the interactions of VOR and OKR.

One of the most enduring models is based on the Merfled Observer Model (Merfeld and Young, 1995; Karmali and Merfeld, 2012). In this model the brain uses forward modeling and sensory prediction error to appropriately compensate for unexpected perturbations. However, they only model VOR leaving open the question of the interaction of VOR and OKR. Laurens and Angelaki (2017) similarly propose a model based on internal models and sensory prediction. Their focus is on comparing active and passive movements, but, like Merfeld, they do not concentrate on the interaction of OKR and VOR and they do not consider the actual motor signals that reach the eye and the way that feedback from the eyes influences eye movements. Our model is in the spirit of these two earlier models in that it is based on the hypothesis that the brain uses internal models to predict upcoming sensory signals and make appropriate corrections. However, we are not primarily concerned with estimate of the movements of the body, but rather with reduction of retinal slip. This means we must consider both the VOR and the OKR, their interactions, and the way the system is driven by visual input.

The only models that attempt to combine VOR and OKR, to our knowledge, are Raphan et al. (1979) and the related model of Laurens and Angelaki (2017). While our model has some strong similarities to Raphan et al. (1979), their approach lacks the explicit notion of internal modeling which characterized more recent approaches. Our own model, while similar in important ways to other approaches, is originally based in efforts to connect the CEM with the ideas borrowed from optimal control theory that have been productive in the study of reaching movements (Shadmehr and Krakauer, 2008; Frens and Donchin, 2009; Haar and Donchin, 2019). Optimal control suggests that the motor system operates in a "full feedback" mode: generating motor commands in response to the best guess regarding the current situation as opposed to using a pre-defined plan (Todorov and Jordan, 2002). However, it has proved very difficult to build optimal control models that make specific predictions for real, physiological motor circuits. Our original thinking was that the CEM was a sufficiently simple motor system to allow for the use of this framework. In the end, our model is consistent with earlier models in the field but extends them by combining VOR and OKR and internal modeling in a manner consistent with the optimal feedback approach used in other motor fields.

We build a working quantitative model (**Figure 1**) of the compensatory eye movement system (CEM) starting from the ideas developed in the Frens and Donchin state predicting feedback control (SPFC) scheme (Frens and Donchin, 2009). It explains data collected from CEM in mice across a broad range of frequencies and amplitudes and different stimulation conditions. The model reproduces the main characteristics of mouse vVOR (rotation of the animal in the light, providing simultaneous visual and vestibular stimulation). Importantly, the same set of parameters also results in good predictions of responses in VOR, OKR and additional conditions, i.e., suppressed VOR (sVOR; simultaneous rotation of the animal and its visual surroundings), and responses to sum-of-sines (SOS) stimuli. To test a hypothetical mapping of the model onto the underlying anatomy, we simulate lesions in specific parts of the model and compare the results with actual lesion studies in mice. Finally, the model also successfully captures VOR adaptation. We introduce the novel proposal that VOR adaptation actually occurs through changes in the way OKR predicts inaccuracies in the VOR.

The interaction of the VOR and OKR might be explained if OKR is capable of predicting the retinal slip not compensated by VOR. This is at the core of the model that we present. The current model is essentially hierarchical, with the vestibular and the visual components of the CEM handled in two distinct loops (see **Figure 1**). This is close to the traditional view of CEM which also incorporates two, more or less separate, mechanisms for the VOR and OKR (Wakita et al., 2017). The VOR operates in a partially open-loop fashion with feedback used to drive only

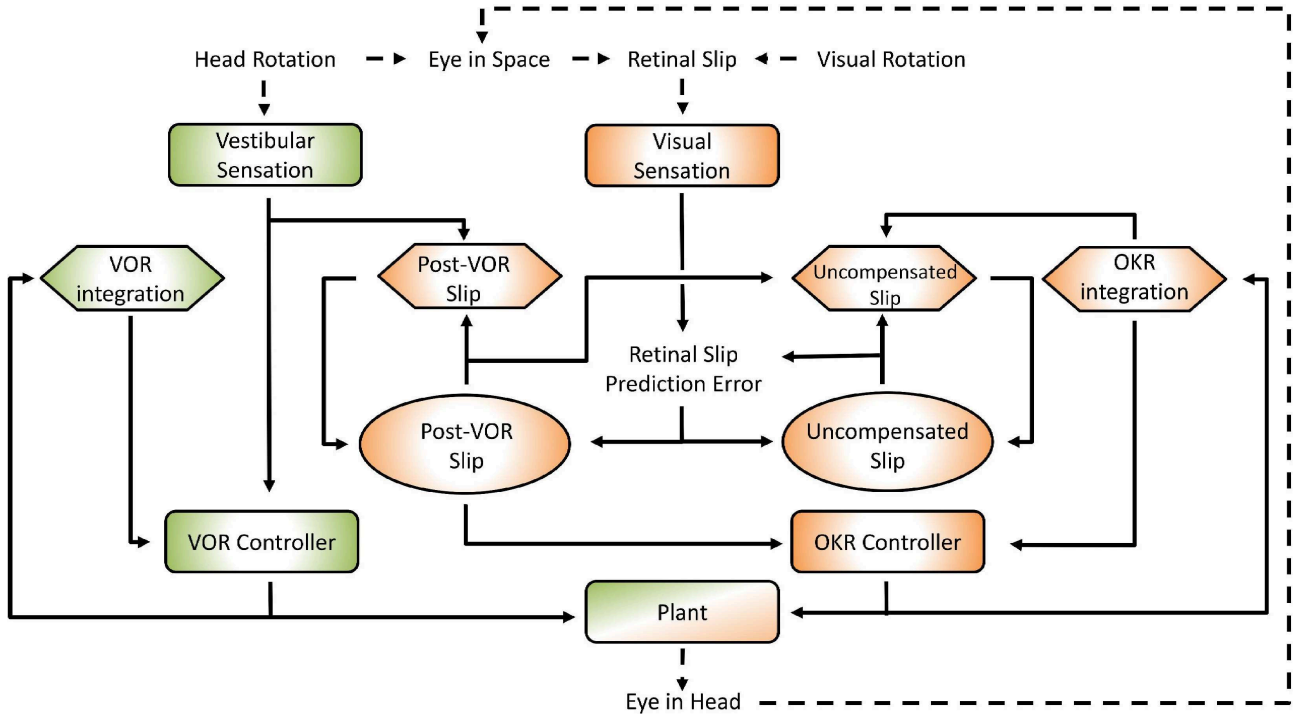

FIGURE 1 | General layout of the model. Green areas are vestibular, orange areas are optokinetic. Hexagons represent Forward Models, ellipses are State Estimators. Dashed arrows indicate processes in the real world, solid arrows are neural processes. Details of the model are specified in the text and **Supplementary Material**. The connection between the vestibular sensation and the Post-VOR Slip forward model is one of the main innovations in the model and represents the OKR modeling the inaccuracies in the VOR loop.

the forward model of the eye without modifying processing of the vestibular state itself. In our model the OKR loop, on the other hand, incorporates forward models of the eye, the visual input, and also the VOR system. That is, the OKR not only predicts current retinal slip based on models of the environment and the eye movements, it also incorporates a model of the residual retinal slip that remains after the actions of the VOR loop. This represents a crucial expansion of previous models in which sensory systems and plant dynamics have been included in the internal model, so that now the VOR reflex itself is modeled by the OKR system (Post-VOR Slip, **Figure 1**). The sensitivity of the OKR loop's estimate of inaccuracies in the VOR loop is determined by a single parameter, ζ (see Equation 5, Equation 29 in **Supplementary Material**). An additional test of our model is that it should be possible to set the value of ζ adaptively, thus mimicking VOR adaptation. Thus, adaptation of the CEM system (at least to first approximation) is mostly adaptation of the OKR model of VOR inaccuracies (**Figure 1**; Post-VOR Slip). This is consistent with experimental findings (as reviewed in the discussion) and also with our hypothesis that the OKR loop is more dependent on forward model prediction than the VOR.

We chose to model and perform experiments in mice because mice, being afoveate, lack a confounding smooth pursuit system. Moreover, we concern ourselves only with the horizontal CEM as is commonly done in the experimental literature. However, since rotations are non-commutative, expanding the model to three dimensions is not trivial and this is an area that has been tackled in other models (Merfeld and Young, 1995; Laurens and Angelaki, 2017). We ultimately decided to constrain ourselves to modeling only the horizontal CEM as there exists a great deal more literature on this than the vertical or torsional responses in mice. In order to compare our model to data, we collected from mice in a large set of conditions (VOR, OKR, vVOR, sVOR, SOS), frequencies and amplitudes. Such a data set was lacking in the literature so that our contribution in this work, beyond a model that fits all existing data, is a comprehensive data set showing CEM behavior across a complete array of stimuli. Importantly, the Matlab code for implementing the model as well as the behavioral data and analysis code are all freely available online to encourage the extension of the model into untested conditions.

MATERIALS AND METHODS

Model

The model was implemented in Matlab (version 2016a; The MathWorks, Natick, MA, USA) and calculations were performed via matrix multiplication with a time step of 1 ms. In describing the model we first provide a brief outline of the neuroanatomical basis and subsequently outline our approach to modeling. We do this separately for the VOR and OKR parts of the model (green and orange areas in **Figure 1**, respectively). In the Model Specification section we provide a summary of the mathematical

specification of the model, with full details provided in the **Supplementary Material**.

VOR

The mouse VOR uses vestibular input from the semi-circular canals (labyrinth) to compensate head movement (Delgado-García, 2000). Vestibular afferents from the labyrinth project directly to VN with a small delay (2 ms; Sohmer et al., 1999). Their activity accurately reflects head velocity at high frequencies but not at low frequencies (Robinson, 1981) due to filtering properties of the vestibular labyrinth (Yang and Hullar, 2007).

Thus, in modeling VOR, the processing is quite simple (green areas in **Figure 1**). Since the system has no access to the actual head velocity, we use the vestibular signal as an approximation of the head velocity. Neither system dynamics nor the oculomotor command affect head dynamics. Note, therefore, that this model currently does not distinguish between active and passive head movements, i.e., it does not incorporate efference copy or proprioceptive information about head movement.

OKR

In the mouse, the OKR originates in velocity sensitive neurons of the retina, which project through the Accessory Optic System (AOS) and Nucleus Reticularis Tegmenti Pontis (NRTP) to the vestibular nucleus (VN) and the vestibulo-cerebellum (Gerrits et al., 1984; Langer et al., 1985; Glickstein et al., 1994). The VN output is sent to the brainstem nuclei, which drive the extra-ocular muscles. In the case of horizontal eye movements, these are the abducens nucleus (Ab), the oculomotor nucleus (OMN), and nucleus prepositus hypoglossi (NPH; Büttner-Ennever and Büttner, 1992). The OKR has a species-dependent response delay of 70–120 ms (Collewijn, 1969; van Alphen et al., 2001; Winkelman and Frens, 2006) primarily caused by the visual processing in the pathway from retina to VN (Graf et al., 1988). The retinal afferents saturate at high velocities (Oyster et al., 1972; Soodak and Simpson, 1988), causing non-linearities in the OKR in this range (Collewijn, 1969; van Alphen et al., 2001). Thus, the OKR is ineffective in compensating high velocity (and thus often high frequency) visual stimuli.

One main innovation in our model is that the OKR system assumes that the VOR only compensates for some proportion of the head movement. The role of the rest of the control system (orange areas in **Figure 1**) is to estimate the retinal slip that will remain after the action of the VOR loop (Post-VOR Slip) and provide this information for the OKR controller. Post-VOR slip arises from two sources: from changes in the velocity of the visual stimulus and from head movements not compensated by the VOR. Thus, our forward model estimate of movement of the visual surrounding (Post-VOR Slip; left orange hexagon in **Figure 1**) will be updated by a factor proportional to head acceleration (Equation 5, See also Equation 29 in **Supplementary Material**). The specific constant of proportionality, ζ, is discussed in the section on VOR adaptation below. The combination of this predicted retinal slip (Post-VOR Slip) combined with an estimate of how much the OKR is moving the eye, gives the OKR's forward model prediction of uncompensated retinal slip (right orange hexagon in **Figure 1**).

As one can see in **Figure 1**, state estimation produces estimates of both Post-VOR slip, and uncompensated retinal slip (oval boxes). Post-VOR slip is retinal slip after VOR compensation and uncompensated slip is that remaining after the action of both systems. In both cases, we chose to use an approximation of a Kalman filter to perform state estimation. Kalman filters estimate state using an optimal combination of previous state and incoming sensory data, optimized relative to the variance associated with each of them (Porrill et al., 2013). That is, they generate the estimate which is most likely to be closest to the true value, given their inputs. In our case, the two inputs were not optimally mixed, but rather the mixing was chosen to match the data (see **Supplementary Material**, Equation 42). We are not claiming that the mouse brain implements a true optimal Kalman filter, but rather some weighted mixing of sensory input and forward model prediction. Thus, through the model architecture, vestibular input only affects our estimate of the head velocity, and retinal input affects both our estimate of retinal slip and our estimate of uncompensated retinal slip.

VOR Adaptation

VOR adaptation occurs when gaze consistently fails to compensate head movement (Blazquez et al., 2004; Schonewille et al., 2010; Shin et al., 2014). In a laboratory environment, a rotating visual environment can lead such failure (as described in the Methods below). This causes persistent changes in the VOR, such that retinal slip is reduced in the new situation. In our model, such a mismatch would affect the proportionality constant ζ. This is because the OKR system's assumption that retinal slip is the result of inaccuracies in the VOR loop.

Summary of Model Specification

What follows is a brief description of the mathematical specification of the model. A full description is available in the **Supplementary Material**. We use a standard linear systems formulation (Frens and Donchin, 2009):

$$\begin{aligned} x_{k+1} &= Ax_k + Bu_k + z_k + n_k \\ y_k &= Dx_k \end{aligned} \tag{1}$$

with dynamics A applied to system state, x_k, which is also affected by the command signal, u_k, the external state of the world, z_k, and noise, n_k. Finally, this state leads to sensory input, y_k. z_k is the external input and includes the change in the actual head velocity, vestibular sensory signal, and movement of the visual stimulus.

The state vector includes some easily recognizable quantities like head state (position, H, and velocity, $\dot{H}$), eye state (E and $\dot{E}$) and state of the visual scene (T and $\dot{T}$). However, it also includes two enigmatic variables (V and R). One is the filtered head velocity signal that represents vestibular input. The semicircular canals are described as a high pass filter that acts on head velocity:

$$\dot{V} = -\frac{1}{T_v}V + \dot{H} \tag{2}$$

Where V is the neural signal generated by the velocity sensitive vestibular afferents (as can be seen by comparing with the

Supplementary Material, the equations here are simplified for clarity). T_V is the time constant of the filter.

The other more abstract quantity is the combination of head, eye, and visual input that creates retinal slip ($R = \dot{H} + \dot{E} - \dot{T}$ with a saturation cutoff at $R_{\max} = 0.65$ deg/sec). Input delays are represented by including time delayed versions of retinal slip and vestibular input in the state vector and only the delayed versions are available to the internal state estimation. Thus, the state vector is:

$$x = \left[H\ \dot{H}\ V\ E\ \dot{E}\ T\ \dot{T}\ R\ \cdots\right] \tag{3}$$

with the three dots indicating extra time-delayed copies of vestibular and retinal signals.

In modeling the noise, we opted for model simplicity over realistic modeling of the noise. We followed Todorov (2004) and Harris and Wolpert (1998) in making noise magnitude proportional to the signal. We ran the model with different constants of proportionality for the noise and did not see a change in the results. Given that we have no available data on the amount of sensory or motor noise in the system we used values well in the middle of stable range.

In additional to the external state and the input, we also modeled the controller itself. Our controller is split into two parts, one for the VOR (subscripted V) and one for the OKR (subscripted R):

$$\begin{aligned} \hat{x}_{\mathrm{V},k+1} &= A'_{\mathrm{V}}\tilde{x}_{\mathrm{V},k} + B_{\mathrm{V}}u_{\mathrm{V},k} & \hat{x}_{\mathrm{R},k+1} &= A'_{\mathrm{R}}\tilde{x}_{\mathrm{R},k} + B_{\mathrm{R}}u_{\mathrm{R},k} \\ \tilde{x}_{\mathrm{V},k+1} &= \hat{x}_{\mathrm{V},k+1} & \tilde{x}_{\mathrm{R},k+1} &= \hat{x}_{\mathrm{R},k+1} \\ &\quad +K_{\mathrm{V}}\left(\dot{V}_{k-\delta_V} - D'_{\mathrm{V}}\hat{x}_{V,k+1}\right) & &\quad +K_{\mathrm{R}}\left(R_{k-\delta_R} - h(\tilde{R}_k)\right) \end{aligned} \tag{4}$$

Both parts of the controller have the same structure: a forward model of the dynamics (first equation in each) followed by state estimation, which combines forward model prediction with sensory input (second equation in each). Note that sensory inputs, $\dot{V}_{k-\delta_V}$ and $R_{k-\delta_R}$, are the delayed versions and that internal estimates of retinal slip must be saturated [$h(\bullet)$] to allow meaningful comparison to sensed retinal slip. K_V and K_R are mixing constants that determine the relative weight of forward model output and sensory input. The vestibular system weights sensory input very heavily while the retinal system weights prediction more heavily.

We use hat notation, $\hat{x}$, for estimates produced by the forward model and tilde notation, $\tilde{x}$, for the combined state estimate. The internal state of the controller, represented by $\hat{x}$ and $\tilde{x}$, represents internal estimates of the system state (Equation 3) described above with some additions. First, it contains two different estimates of eye state, separately represented by the VOR and OKR controllers. This allows the controller to make different calculations. Second, it contains two different estimates of retinal slip. The first is called the uncompensated retinal slip. It reflects an estimate of the retinal slip that remains after both the VOR and OKR contributions. This is the $\tilde{R}$ that appears in the equation above (with the tilde indicating that it is a state estimate resulting from a Kalman filter calculation and forward modeling). It is compared to the actual retinal slip to produce retinal slip prediction error.

The other estimate of retinal slip in the internal state is called the Post-VOR slip, $\tilde{R}^*$. It reflects an estimate of the amount of retinal slip that will remain after the VOR contribution. It is used to determine the OKR controller output. This estimate exists because the OKR controller assumes that that some head movement remains uncompensated by the VOR. The forward model estimate of uncompensated post-VOR retinal is thus updated by a factor proportional to head acceleration:

$$\hat{R}^*_{k+1} = \tilde{R}^*_k + \zeta\left(\hat{\dot{H}}_k - \hat{\dot{H}}_{k-1}\right) \tag{5}$$

The constant of proportionality, ζ, is the quantity that is actually being estimated by VOR adaptation. Our data was best fit by using $\zeta = -0.6$ which means that OKR assumes VOR tends to overcompensate for head rotation.

Finally, the motor command for both OKR and VOR is generated by using the equations: $u_R = -L_R \cdot \tilde{x}_R$ and $u_V = -L_V \cdot \tilde{x}_V$ and $u = u_R + u_V$ where L_R and L_V are called the command policy. These are linear functions of the internal estimate of state and the command policy was calculated using an approximation of the equations in optimal control theory (The Riccati equations for a linear-quadratic-regulator, please see **Supplementary Material** for more details). Other approaches to finding a reasonable control policy are also possible (Harris and Waddington, 2013). The controller must, in any case, compensate for the estimated error while correcting for known dynamics of the motor plant and different ways of reaching similar solutions exist.

Parameters

In the model only a few parameters were set to match the data. They were set to match data in the vVOR condition and then the same parameters were used for all conditions. Most variables were either taken from literature, or experimentally derived by us in separate experiments. Interestingly, it turned out that the model produced very similar behavior across a wide range of values for most parameters although it was sensitive to a few parameters (see **Table 1**). As much as possible, parameters were determined from the literature or from our own data. For example, we determined the maximum VOR and OKR gains from our own data. We used the response to high frequency stimulation to set the maximum gain of the VOR in the model and the response to low velocity stimulation to set the maximum gain of the OKR in the model. The response of the retina to retinal slip saturates at high velocities leading to non-linearity in the response, the value of the parameter representing the saturation point ($R_{\max}$) was fit to published results (Oyster et al., 1972; Soodak and Simpson, 1988). On the other hand, the filter of the vestibular afferents was shaped to achieve the best fit to the data. Ultimately, the filter that fit our data best was also compatible with the literature. We used a first order high pass filter with a time constant of 4 s (Yang and Hullar, 2007). Similarly, drift velocity and VOR adaptation speed were fit to data and later

TABLE 1 | Overview of all parameters used in the model, their values, the equations they are used (described in **Supplementary Material**), and a short description of their meaning.

	Value	Equations	Meaning	Is it critical?	How was it set?
dt	1 ms		Time step		
T_p	0.5 s	(1, 2, 15, 17, 24, 33, 38)	Leaky integrator time constant for motor nuclei	No	Stahl and Simpson, 1995; Stahl et al., 2015
T_v	4 s	(3, 15)	High pass filter constant for the vestibular inputs	Yes	Fit to data. Close to value found for actual vestibular afferents by Yang and Hullar (2007) (3 s)
δ_V	2 ms	(5, 20)	Vestibular sensory delay	No	
a_V	0.1	(6, 16)	Vestibular sensory noise proportionality constant	No	Middle of the stable range
R_{max}	0.65 deg/s	(8)	Retinal saturation	Yes	Oyster et al., 1972
δ_R	70 ms	(9, 20, 31)	Visual processing delay	Yes	van Alphen et al., 2001
a_R	0.1	(10, 16)	Visual sensory noise proportionality constant	No	Middle of the stable range
a_u	0.1	(15, 16)	Motor noise	No	Middle of the stable range
ζ	−0.6	(29, 33, 38, 48)	Assumed VOR inaccuracy	No	Fit to match VOR performance in the dark.
κ_V	1	(22, 42)	Kalman gain of vestibular input	No	Set so VOR is not eliminated by floccular lesion
κ_T	0.05	(30, 42)	Kalman gain for the effect of retinal slip prediction error on assumed external motion (post-VOR retinal slip)	No	Fit to data
$\kappa_{R,k}$	0.05	(31, 35, 42)	Kalman gain for the effect of retinal slip prediction error on estimate of uncompensated retinal slip	No	Fit to data
γ	$e^{\frac{1}{150}}$	(44)	Discount parameter for cost function	No	Fit to produce credible drift in the dark
θ	2	(44)	Weight of position factor in cost function	No	Fit to produce credible drift in the dark
	100,000		Number of terms kept in infinite cost function sum	No	Arbitrary

The last two columns describe whether they are critical, and how they were set. We determined how critical the parameters were, by varying them over an order of magnitude, and observing the changes in results.

found to be compatible with the literature (Stahl et al., 2006; Schonewille et al., 2010).

Animals

In order to test the model we recorded CEM in 13 C57Bl/6J mice (Charles River, Wilmington, MA, USA). C57Bl/6J mice are commonly used in oculomotor research enabling comparison of our results to previously published data. We employed four different paradigms i.e., OKR, VOR, sVOR, and vVOR and in each condition we tested a wide range of frequency and amplitude combinations. Details on the experiments are described in the **Supplementary Material**. Additionally, we measured the drift of the eye back to a central position in the dark ($N = 6$) and the rate of adaptation of the VOR ($N = 7$), full details of the methods are described in the **Supplementary Material**. All experiments were performed with approval of the local ethics committee and were in accordance with the European Communities Council Directive (86/609/EEC).

Prior to all eye movement recordings, mice underwent surgery to prepare them for head fixation and were allowed sufficient time to recover, details are provided in the **Supplementary Material** and the full procedure is described in van Alphen et al. (2009).

During an experimental session, mice were immobilized by placing them in a plastic tube with the head protruding and the head fixation attached to the turntable with the eye in the central position. Eye movements were recorded via an infra-red video system (Iscan ETL-200, Iscan, Burlington, MA, USA) at a frequency of 120 Hz. Visual stimuli were presented using a modified projector (Christie Digital Systems, Cypress, CA, USA) displaying a panoramic field of 1,592 green dots on virtual sphere fully surrounding the animal. Rotation of the sphere around the vertical axis provided the moving stimuli. Vestibular stimulation was provided via a motorized turntable Mavilor-DC motor 80 (Mavilor Motors S.A., Barcelona, Spain) on which the mouse and eye movement recording system were mounted. Further details are provided in the **Supplementary Material** and a schematic representation of the stimulus and eye movement recording apparatus in **Figure 2**.

The VOR adaptation experimental paradigm consisted of an identical stimulus setup with the animal undergoing 6 VOR trials (1 min duration, 1 Hz, 5°) to measure the gain alternating with 5 sVOR trials (5 min duration, 1 Hz, 5°) to induce adaptation.

In the Sum-of-sines (SoS) conditions, the two constituent frequencies were chosen that had no harmonic relation. Four SoS frequency combinations were used in this study: 0.6/0.8, 0.6/1.0, 0.8/1.0, and 1.0/1.9 Hz. Amplitude was either one or two degrees for each frequency component. Either both frequencies had the same amplitude (both 1° or both 2°) or they had different amplitude (one at 1° and the other at 2°). This led to a total of 24 types of stimuli in each of the OKR, VOR, vVOR, and sVOR SoS conditions. Eight mice were used in this paradigm and they all performed all conditions.

Data Analysis

Every mouse was tested once in each condition, and each stimulus consisted of at least five cycles. Only cycles after the

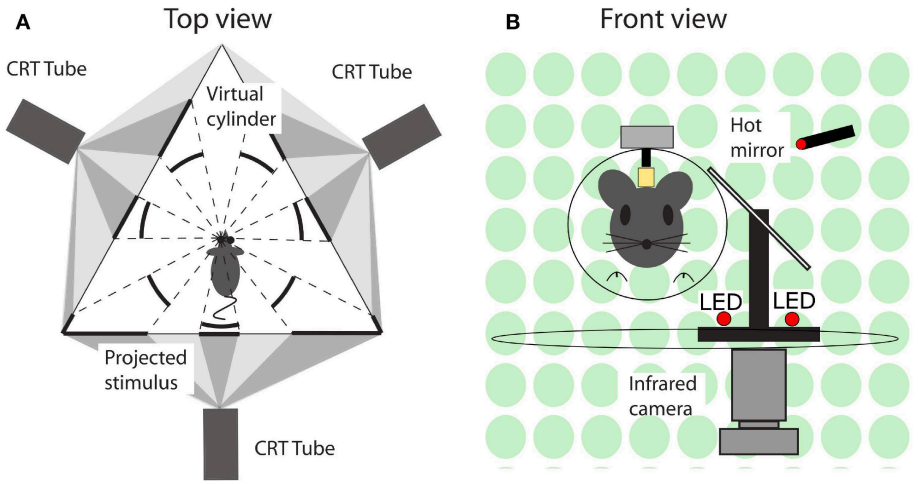

FIGURE 2 | Schematic representation of the experimental setup. **(A)** Top view. A mouse in the setup, with its left eye in the center and surrounded by three screens on which the visual stimuli are projected. The visual stimuli were programmed and displayed in such a way that from the point of view of mouse it appeared as a virtual sphere. **(B)** Front view. A mouse placed in front of a hot mirror, which enabled the infrared camera underneath the table to record the eye movements.

initial transients of the response had decayed were included in analysis. Full details of the analysis details are provided in the **Supplementary Material**. Briefly, following filtering and removal of fast phase eye movements gain and phase data was calculated by a Bayesian fitting procedure in OpenBugs (Version 3.2.3, http://www.openbugs.net, Lunn et al., 2009) and Matlab curve fitting routines, for single sinusoid stimuli and for SoS stimuli, respectively. The Matlab code and data required for replication of the analysis presented in this paper is available on the Open Science Framework website (https://osf.io/feq7c/).

RESULTS

Responses to Sinusoidal Stimulation

The behavioral data that we present are in agreement with the values that have been previously published for the C57BL/6 mouse strain (Stahl et al., 2000; Faulstich et al., 2004; van Alphen et al., 2010; Schonewille et al., 2011). The VOR (**Figure 3**) in the dark responded to high frequency stimulation, and the OKR (**Figure 4**) was mainly active in response to low velocity stimuli (van Alphen et al., 2001). The vVOR (**Figure 5**) was more or less veridical over the whole stimulus range while suppression in the sVOR (**Figure 6**) paradigm mainly happened at low frequency/velocity conditions.

In **Figure 3** we show a comparison of experimental and simulated VOR. **Figure 3A** displays examples of a single cycle of the model output for four examples of specific stimuli. We can see that the model response falls mainly within the red shaded region which represents variance of the population of mice responding to the same stimulus. The high frequency noise in the model response are due to the addition of motor and sensory noise. The high frequency noise is not seen in the mouse response as it is an estimate of mean mouse behavior. A comparable estimated mean model response is shown in **Supplement Figure 2**. Bode plots of mouse and model response across multiple frequencies and amplitudes is shown in **Figure 3B**. The figure demonstrates that model output falls within the region of typical mouse behavior across a range of frequencies of stimulation, both in terms of response gain and phase. We see that there is a good match between simulation and average experimental response over the whole stimulus range. First, a high gain at high frequencies and lower gain at low frequencies is clearly observable. Furthermore, we see a phase lead at low frequencies which diminishes with increasing stimulus frequency. Whilst the model fit well with the average of the population of mice tested, there is considerable variation between individual mice's responses to the various stimulations. In **Figures 3–6B** we present the confidence limits of estimates of each individual mouse and display any mice outside the limits of the plot as cross symbols on the limits of the y-axis.

Figure 4 follows the same format as **Figure 3** but compares simulation to experimental results for the OKR response. The simulation nicely predicts the main features of the OKR response. The gain decreases and the phase lag increases with increasing stimulus velocity.

Figure 5 shows how well simulations predict experimental data for combined visual and vestibular stimulation (vVOR). In both the simulation and experimental data, we observe high gain and almost no phase lead or lag between response and stimulus. These results show that VOR and OKR have complementary results, which allows the combined system to produce excellent compensation of the retinal slip.

Figure 6 depicts how the model fits experimental data generated during sVOR—suppression of the VOR response with visual input. The response in high frequencies looks very similar to that in VOR because OKR is not responsive in high frequencies (see **Figure 4**), and hence cannot suppress vestibular triggered response. At low frequencies, there is a very small response, because VOR has low gain and is further suppressed by OKR. At these low frequencies, where the gain is low and variable, the model systematically misrepresents the phase of the eye movement.

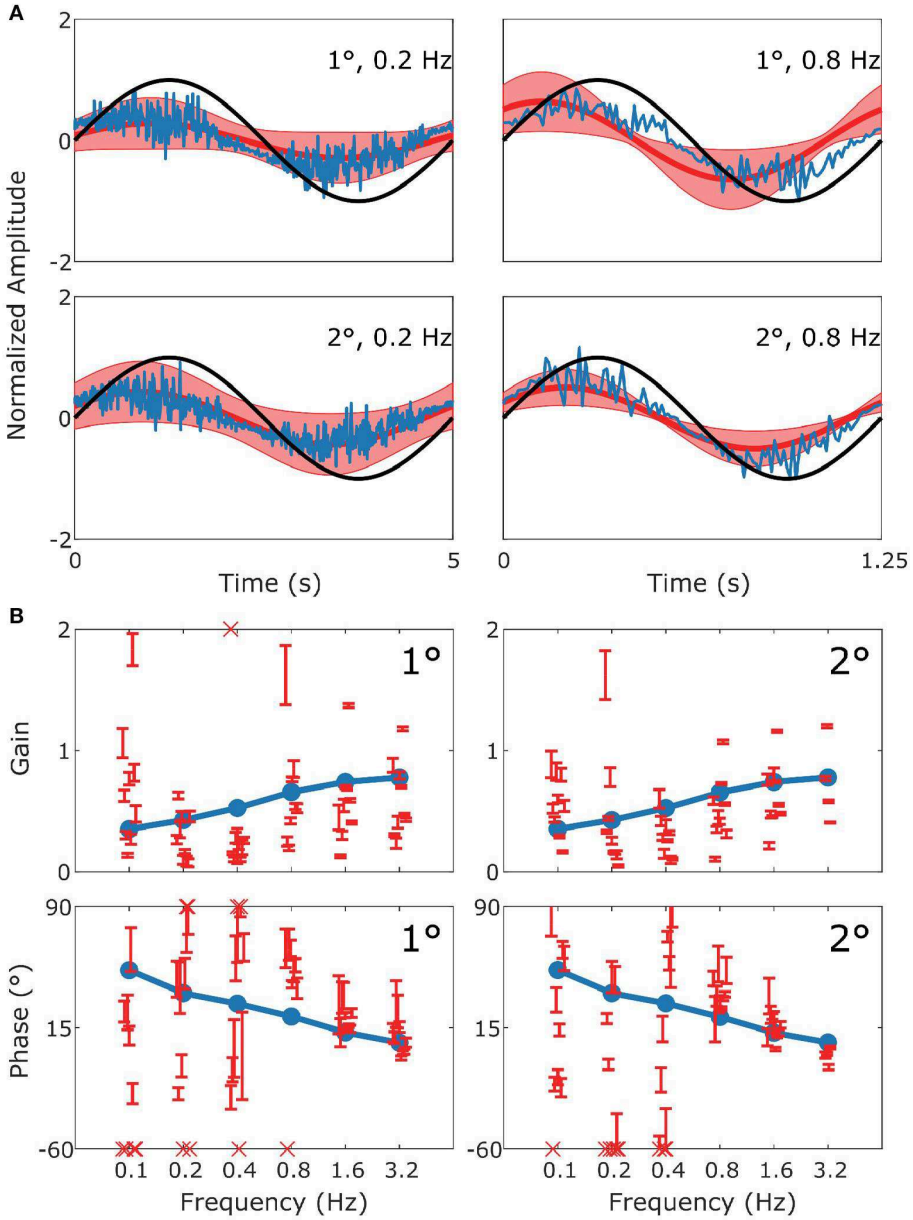

FIGURE 3 | Summary of VOR data and simulation. In **(A)** the upper row displays results for 1° stimuli, the lower row for 2° stimuli. The panels show the stimulus in black (left: 0.2 Hz; right 0.8 Hz), with the simulated response (blue) and the mean measured responses (red). Shaded red regions represent the standard deviation (SD) of the sample of mice showing that the model performance is credible given population variability. **(B)** Are Bode plots for Gain (top panels) and Phase (bottom panels) for the simulated response (blue), individual mice with SD (red error bars). Crosses in the Bode plots indicate data that extend beyond the visible axes. The left and right sides of **(B)** represent bode plots for 1° and 2° stimuli, respectively. Other stimulus conditions fit equally well.

In order to examine the overall quality of fit in each of the four experimental conditions above, we calculated the Z-scores of the overall fitting quality, these are displayed in **Figure 7**. Z-scores were calculated by subtracting the model response at each time point from the center of the region of typical mouse behavior and dividing by the standard deviation. Subsequently, we take the mean of these values across all timepoints. Therefore, the Z-score represents the number of standard deviations the model response is away from the mean mouse response. Note how the overall fit quality is good ("cool" colors in the heat map), with some poorer fits in the low frequency/high amplitude range of the sVOR condition. Because of the low amplitudes and high variability, the phase offset of the model at the lower frequencies does not lead to large Z-scores.

In addition to the comparison of model and data in terms of Z-scores (**Figure 7**), we also used the Bayesian estimates to generate

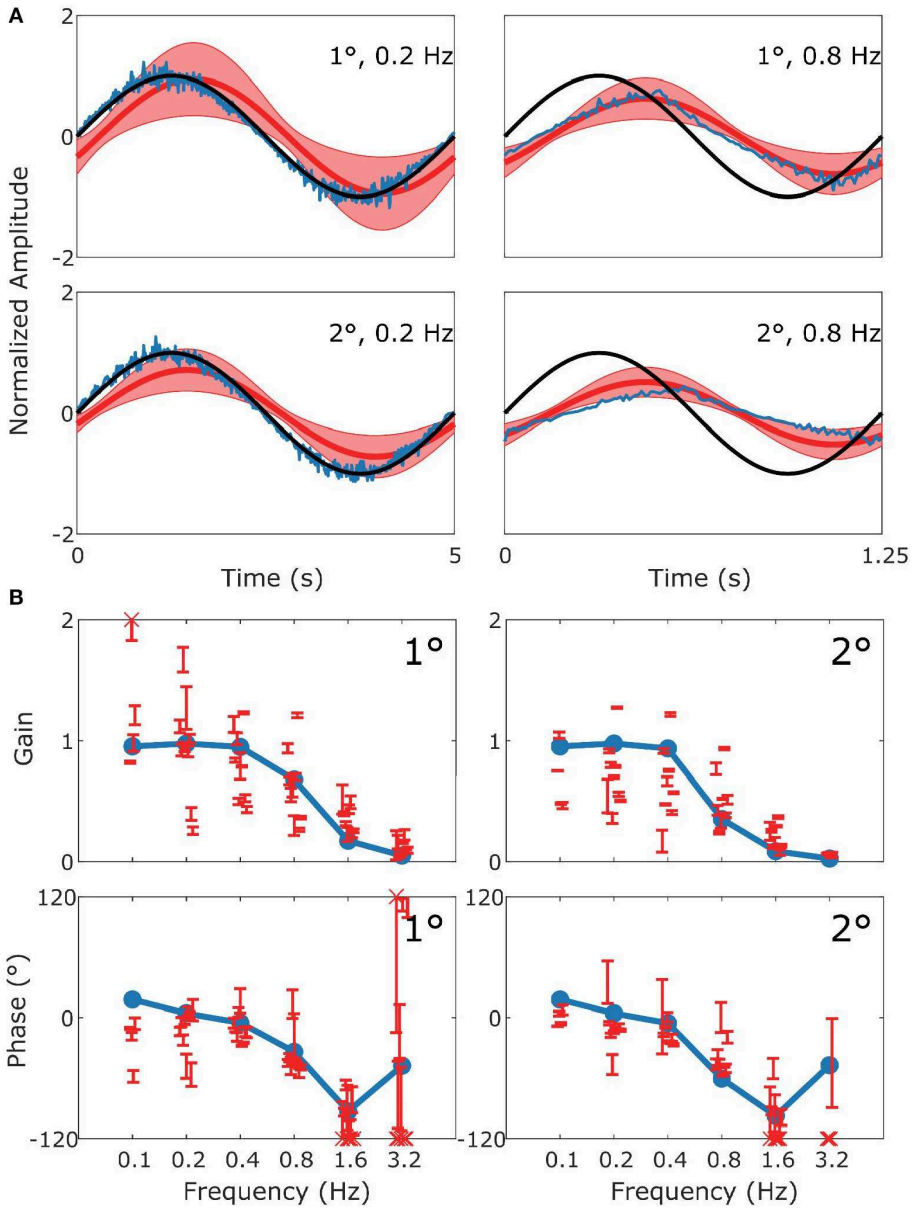

FIGURE 4 | Summary of OKR data and simulation. This figure follows the format of **Figure 3**, with panel **(A)** displaying the stimulus (black), model response (blue) and measured response (red). **(B)** Are Bode plots for Gain (top panels) and Phase (bottom panels). Note that the phase response of stimuli with Gains < 0.25 could often not reliably be determined.

probabilities for the model response falling outside the range of the behavior of a "typical mouse." These tests were carried out for every frequency and amplitude combination and assessed the similarity of gain and phase separately, a combined probability was then generated from the product of these. The results of these tests are presented in the **Supplementary Material**. Overall the model responds within the range of a typical mouse for both gain and phase individually and when combined.

Model Dynamics

The interaction of the different parts of the model in one of the conditions (vVOR, amplitude 2, frequency 0.2 Hz) are shown in **Figure 8**. The figure shows one cycle of the activity in each of the different areas being modeled during the steady state response to this stimulus. The top two boxes show that in this condition, the head is being rotated but the eyes are moving to keep the retinal slip at 0. The head rotation passes through the system in a feedforward manner to drive the vestibular controller. Additionally, this controller is modulated by knowledge of the eye position and velocity, driven by the forward model integration of the vestibular command. The figure also shows how the head rotation drives an estimate of the retinal slip that would remain uncompensated by the VOR controller. This is labeled post-VOR slip. Post-VOR slip

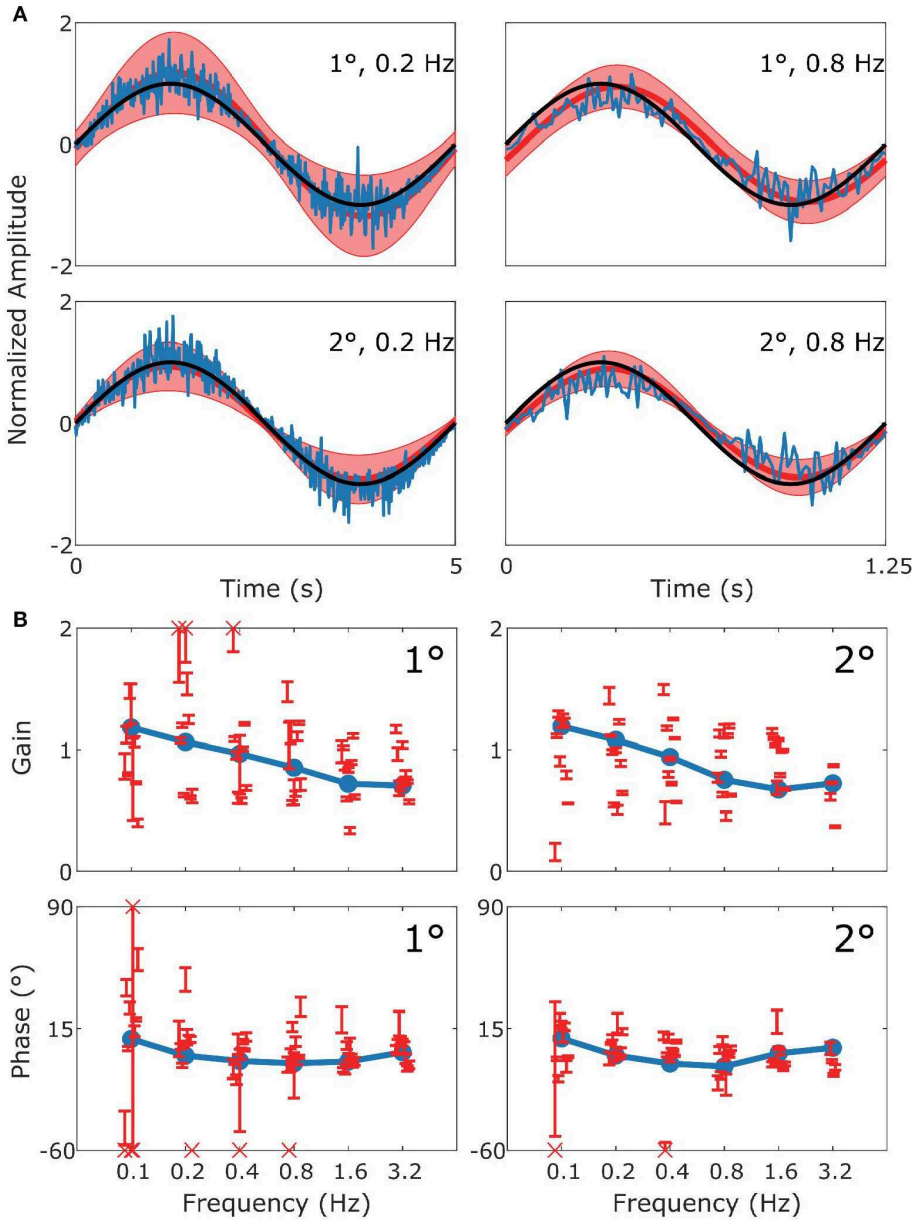

FIGURE 5 | Summary of vVOR data and simulation. This figure follows the format of **Figure 3**, with panel **(A)** displaying the stimulus (black), model response (blue) and measured response (red). **(B)** Are Bode plots for Gain (top panels) and Phase (bottom panels). Across the whole frequency range tested in both amplitudes there was a very good match of model to experimental data.

in turn drives the activity of the OKR controller. Note that in this condition, the system estimates that the VOR will over-compensate for the head rotation and the OKR controller generator actually generates a command that is roughly in counter-phase with that of the VOR controller. The success of the vVOR in generating eye movements that fully compensate for the head movement are the result of a balance between the VOR signal and the OKR signal. Without the balancing OKR signal, the gain of the VOR would need to be lowered to achieve veridical tracking, which would compromise the quality of the VOR.

Figure 8 also shows that in this situation the OKR system has stabilized, such that retinal slip prediction error is 0. If there were prediction error, generated by either a transient visual or vestibular perturbation, this would drive an increase in the post-VOR slip which would then cause a transient increase in the OKR command to correct for the extra slip. The OKR system thus serves in two complementary roles: it generates a feedforward correction for the inaccuracies of the VOR system (the size of which is learned through adaptation, as described below) and it generates an error driven correction for unexpected retinal slip. The figure thus demonstrates the balance between the VOR

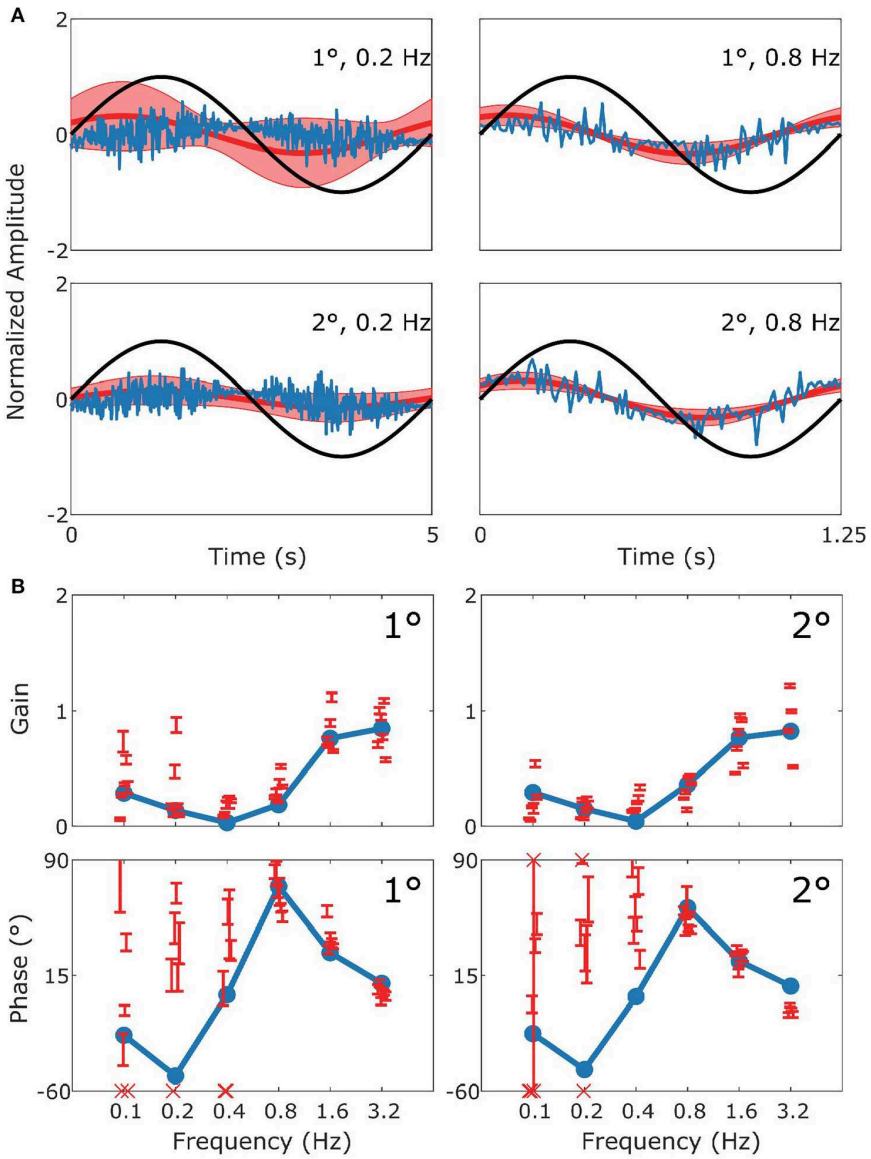

FIGURE 6 | Summary of sVOR data and simulation. This figure follows the format of **Figure 3**, with panel **(A)** displaying the stimulus (black), model response (blue) and measured response (red). **(B)** Are Bode plots for Gain (top panels) and Phase (bottom panels). Note that the phase response of stimuli with Gains < 0.25 could often not reliably be determined. The pattern of the response in the behavioral data is clearly captured by the simulation.

command, post-VOR slip and OKR command that are necessary to achieve veridical tracking in the vVOR condition. Figures in the supplementary results show dynamic plots for the VOR and OKR simulations at the same frequency and amplitude, but it is their interaction which is the key innovation of our model.

Sum of Sines

When the mouse OKR responds to sum-of-sines (SoS) stimuli, we have previously reported relative gain suppression of the lower of two frequencies in the stimulus. Conversely, in sVOR, results showed gain enhancement in the lower frequency component. In both sVOR and VOR, an overall decrease in phase lead was observed. For more details see Sibindi et al. (2016). When applying these stimuli to the model, the main pattern of effects is reproduced. Thus, we find qualitatively similar changes in both the relative gain and delay of the constituting frequencies (**Figure 9A**). Importantly, removal of retinal saturation ($R_{\max} = \infty$) eliminates the non-linearities expressed in the gain of the response (**Figure 9B**).

VOR Adaptation

Perhaps counterintuitively, VOR adaptation occurs as a result of changes in the OKR's model of VOR. Adaptation modifies the OKR's prediction of post-VOR slip. Thus, adaptation in our model involved allowing the parameter ζ to vary in response to retinal slip prediction error using gradient descent. As derived

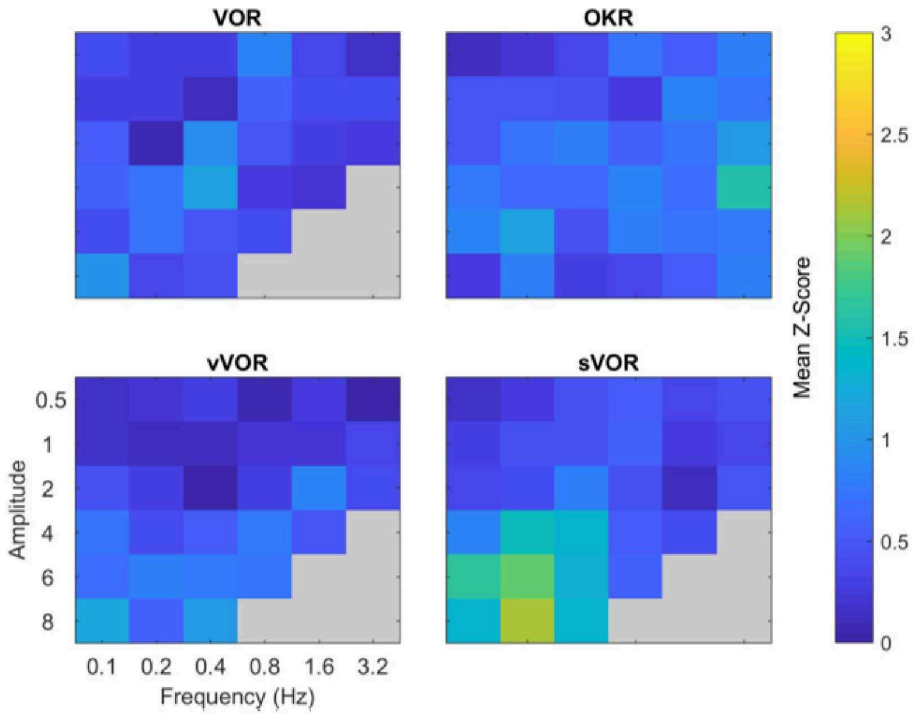

FIGURE 7 | Summary of comparison of model and data for all amplitude and frequency combinations. The four panels depict the degree to which the model response matched the experimental data for the four conditions. The degree of similarity is expressed in terms of the number of standard deviations the model response was away from the mean behavioral response, cooler colors indicate a closer match. Across all amplitude and frequencies tested the model reproduces the experimental data well, with the possible exception of high amplitude, low frequency sVOR. Gray regions indicate conditions not measured in the experimental data.

in the **Supplementary Material**, the gradient is in the direction that decorrelates head acceleration and retinal slip prediction error. The minimum error had a broad basin of attraction. Thus, regardless of the starting value of ζ, it always converged to the same value of -0.6, if the stimulation frequency was kept constant at 1 Hz. The value to which ζ converged depended on stimulus frequency but not amplitude. Nevertheless, for a broad range of frequencies ζ assumed a value around -0.6.

The adaptation protocol reduced the gain of the VOR in mice to around 50% of its original value (Visible as a normalized gain of close to 0.5 after 25 min of training, **Figure 10**), comparable to that which has been previously described in literature (Schonewille et al., 2011).

Effects of Lesions

In the model we simulated a lesion of the flocculus and a lesion of the NPH. The way in which this should be done in the model depends on the role that is ascribed to either structure (see section Discussion).

Flocculus Lesions

We modeled a lesion of the flocculus by removing all the Forward Model boxes (Hexagon boxes in **Figure 1**). **Figure 11A** shows the result. The OKR is virtually absent. Meanwhile VOR gain is increased, and VOR phase increases at low frequencies. Following a model floccular lesion, the VOR did not adapt (**Figure 10**).

NPH Lesions

If one believes the NPH to be part of the controller (Green et al., 2007), a lesion of the NPH would mean removing the inputs of the two outer hexagonal Forward Model boxes of **Figure 1**. A lesion of the flocculus would then be setting the values of all Forward Model boxes to a constant value of 0.

Alternatively, if one believes the NPH is the oculomotor integrator (Cannon and Robinson, 1987), an NPH lesion means setting the output of [outer, hexagonal (**Figure 1**)] integration boxes to 0. A flocculus lesion then only affects the two inner FM boxes of **Figure 1** ("post-VOR slip" and "uncompensated slip"). We tested both manipulations.

Both types of lesion of the NPH resulted in exactly the same result. This is not surprising, since they are equivalent to setting the input to the integration step to 0, or setting the output to 0. Both produced a small effect on the VOR with a decrease in gain at low frequencies, reflecting the mainly feed forward nature of response. OKR in contrast was greatly affected with a large decrease in gain (**Figure 11B**). As expected (see section Discussion), the lesion also had an effect on the drift of the eyes back to the center in the dark, decreasing the time constant from 2.83 to 0.31s. Stahl et al. (2006) report a time constant on the order of 5 s for the neural integrator in C57BL/6 mice, although there was considerable variation between mice and over time.

Cheron et al. (1986a,b) made lesions in the NPH of cats. They show that such a lesion reduces low frequency VOR responses

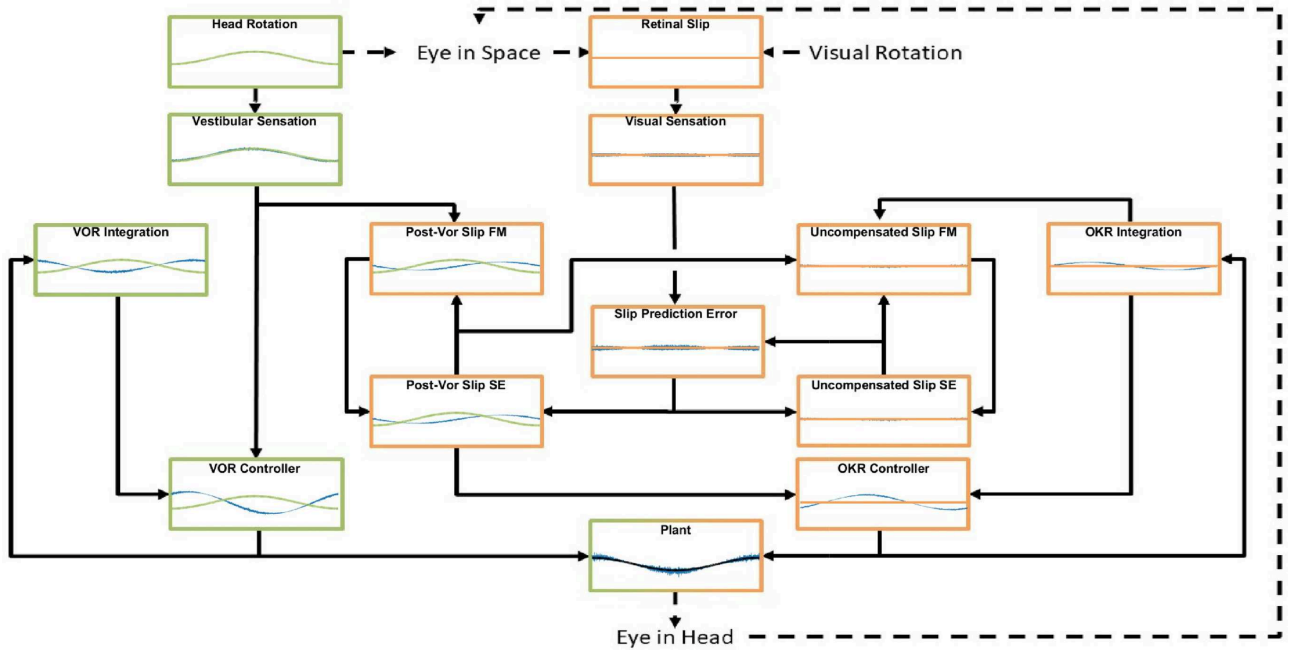

FIGURE 8 | An example of the model dynamics for one cycle of the simulation in the vVOR condition (Stimulation amplitude of 2 degrees at a frequency of 0.2 Hz) at a time by which the system has reached a steady state. The layout matches the model schematic presented in **Figure 1**, Forward Models are labeled FM and State Estimators are labeled SE. In each box the blue line represents the output of the computation performed, the green or orange line represents the appropriate stimulus, vestibular and visual, respectively. In the supplement, we display the full model dynamics for the VOR and OKR conditions in isolation, respectively, for the same frequency and amplitude of stimulation.

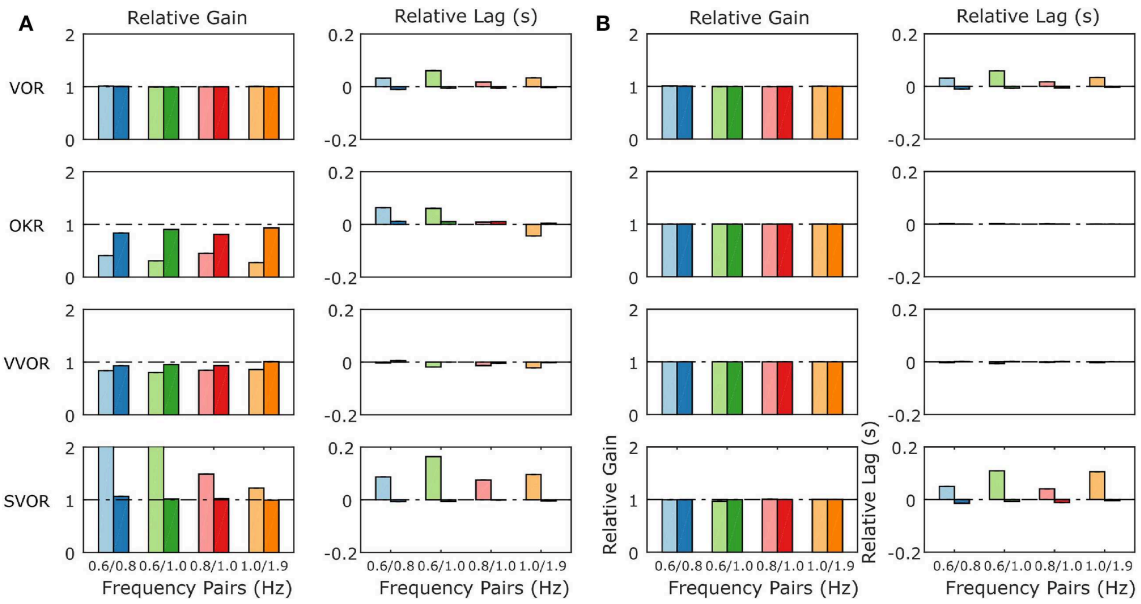

FIGURE 9 | Summary of the model response to Sum of Sines stimulation for the model with normal retinal saturation **(A)** and with the saturation of retinal input removed **(B).** The response is described in terms of gains and lags relative to the gain and lag recorded in response to the single frequency component presented in isolation. A linear system will produce only relative gains of 1 and relative delays of 0, indicated by dashed horizontal lines on each plot. The pattern of non-linearities produced by the full model **(A)** matches closely the non-linearities found in behavioral data in response to the same stimuli (Sibindi et al., 2016). Figure 6 of Sibindi et al. (2016) is reproduced with consent as a supplement to this figure, **Supplement Figure 1**. The removal of retinal saturation eliminates the non-linearities expressed in the relative gains of the OKR and sVOR but those expressed in the relative lags of VOR and sVOR remain intact. Please note that the values for relative gain for the 0.6 Hz component of the 0.6/0.8 and 0.6/1.0 Hz Sum of Sines in sVOR **(A)** are >2.

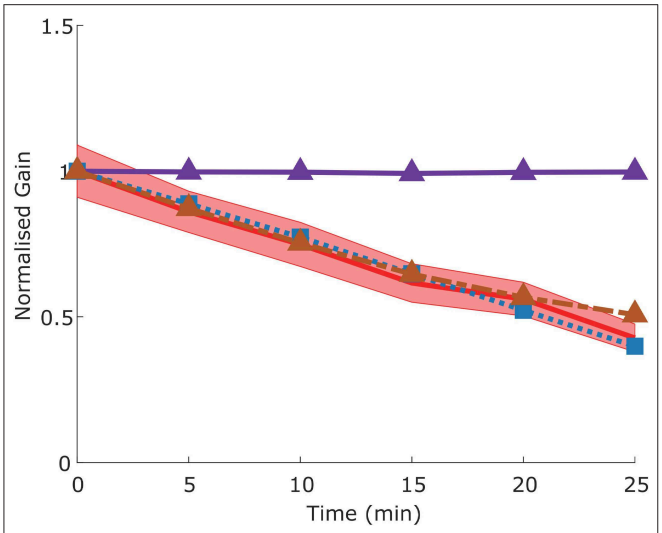

FIGURE 10 | Time course of gain decrease adaptation of the VOR in response to repeated sVOR stimulation. The decrease in gain measured experimentally (red) with confidence limits representing SEM (shaded region) matches that produced by the model (blue line) in response to the same paradigm. Simulating a flocculus lesion in the model (purple line) by removing the four forward models produces a complete abolishment of adaptation, whereas an NPH lesion (orange line) left the adaptation intact.

and completely abolishes OKR. However, the gain and phase measurements do not depict the full nature of the changes in the response to OKR. When applying low velocity stimuli, the OKR in our model becomes noisy and dominated by oscillations at the time points in which stimulus velocity is highest (**Figure 12**).

In our model, NPH lesions do not affect adaptation to the sVOR stimulation at 1 Hz (**Figure 10**), because the individual reflexes at that frequency are relatively unaffected, and the site of plasticity is not lesioned.

Effect of Lesions on Dynamics

To better understand how the different lesions affect the internal dynamics of the model, **Figure 12** presents the post-VOR slip and the activity of the visual, vestibular and combined controllers in each of the lesion conditions for each of the four different stimulus conditions. There are a number of key findings. First, both the floccular and NPH lesion have the same effect on the vestibular command. This is because both lesions impact the vestibular command by eliminating forward model estimation of eye eccentricity. This leads to a decreased amplitude and increased phase lag in the vestibular command. Meanwhile, it can be clearly seen that the NPH lesion primarily affects the magnitude of the OKR.

DISCUSSION

Brief Summary of Results

Frens and Donchin (2009) proposed that CEM can be modeled by an SPFC framework where specific functional roles can be ascribed to specific nuclei in the CEM circuitry. Here, we measured—for the first time- VOR, OKR, vVOR, and sVOR over a large range of frequencies and amplitudes in the same animals. We then implement the SPFC framework in a detailed computational model which can, with a single set of parameters, mimic the behavior of OKR and VOR (**Figures 3**, **4**, **7**). With the same set of parameters, the model also reproduces vVOR, sVOR (**Figures 5**–**7**) and non-periodic SoS-stimuli (**Figure 9**). Furthermore, it successfully predicts the effects of lesions (**Figures 11**, **12**) and has adaptive behavior, similar to VOR learning (**Figure 10**).

The strength of this model is that it has relatively few critical parameters (see **Table 1**) and that the critical parameters can be straightforwardly experimentally derived. This is an advantage over other SPFC-like models that address other motor systems (Shadmehr and Krakauer, 2008). However, it is important to recognize that although our model is in a tradition of modeling the motor system called optimal feedback models (Todorov, 2004; Shadmehr and Krakauer, 2008), this modeling approach does not assume that the motor system is actually optimal. Firstly, in biological motor control the correct cost function is unknown. Even if it were known, the biological motor system does not meet the criteria required for the optimization problem to be solved with available methods. Finally, optimal theories are difficult to falsify, as noted by the seminal paper of Shadmehr and Krakauer (2008). What the optimal control models in the neural control of movement share with true optimal feedback controllers is the basic structure of a feedback controller using forward modeling and a Kalman-like filter to produce state estimates that can be used to generate sensory prediction error. They also generally rely on an explicit or implicit cost function that balances control costs with target costs (Todorov, 2004). In the development of this model, we used a plausible cost function that could match the experimental behavior. We include both eye velocity and eye eccentricity. In combination with the signal dependent noise, the cost function penalizes larger movements. It is almost certainly not an accurate description of the real underlying cost function (see Harris and Waddington, 2013 for a more detailed approach at producing an accurate form), if indeed such a cost function exists. Our cost function follows Robinson (1981) in making the assumption that the system minimizes retinal slip. This assumption, reasonable in the afoveate, lateral eyed mouse, may not be appropriate for foveate species with saccadic systems or binocular vision. The expansion of the current model into other species is a worthy goal for future work but our aim in the current paper was to match the model to wealth of available data on the neuroanatomy and behavior for the mouse.

Another area in which we a priori limited our model was the investigation of only the steady state horizontal component of the CEM system. Other models have been developed to simulate the interaction of multi-dimensional stimuli (Laurens and Droulez, 2007; Laurens and Angelaki, 2017). The expansion of the current model to incorporate more degrees of freedom or translational stimuli is an important goal. The data presented here are all collected after the transient responses at the initialization of stimulation have abated. However, experimental data on the initialization and the termination of the CEM reflexes has previously been modeled (Raphan et al., 1979). Investigating if the current model can reproduce these effects is an important

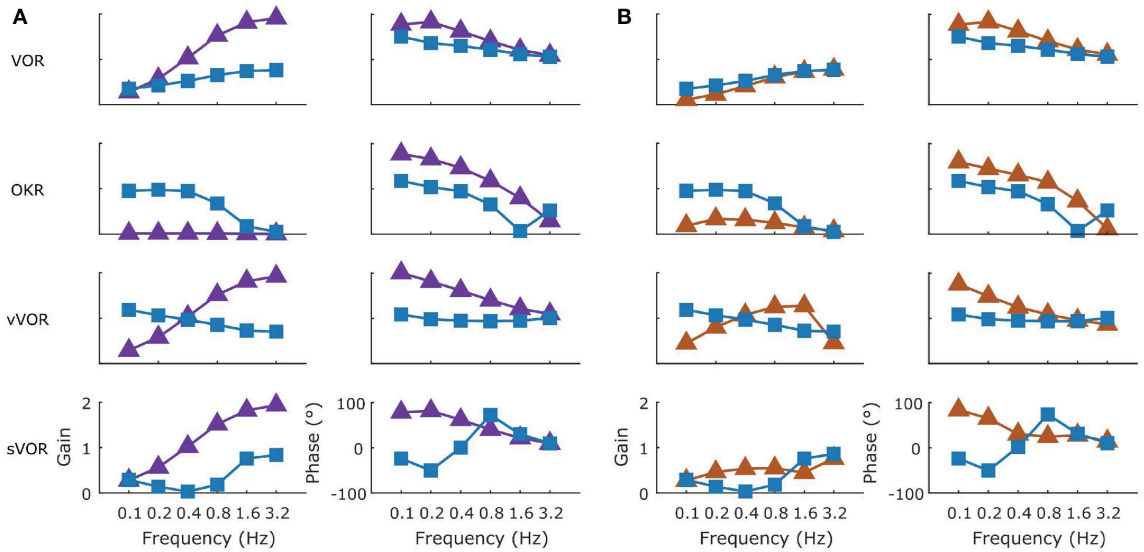

FIGURE 11 | The effect of simulated lesions of the flocculus **(A)** and NPH **(B)** in the model on compensatory eye movements. The intact (blue line) and lesioned model response are summarized in Bode plots for the four conditions with the gain and phase presented in the left and right columns, respectively. Following a simulated flocculus lesion removal of the forward model stage produces an increase in the VOR gain and phase and an almost complete loss of the OKR response. Due to the loss of the OKR component the response in the vVOR and sVOR conditions is almost identical. Similarly, the greatest effect of a lesion of the NPH was on the OKR response with a large decrease in gain and decrease in phase lag.

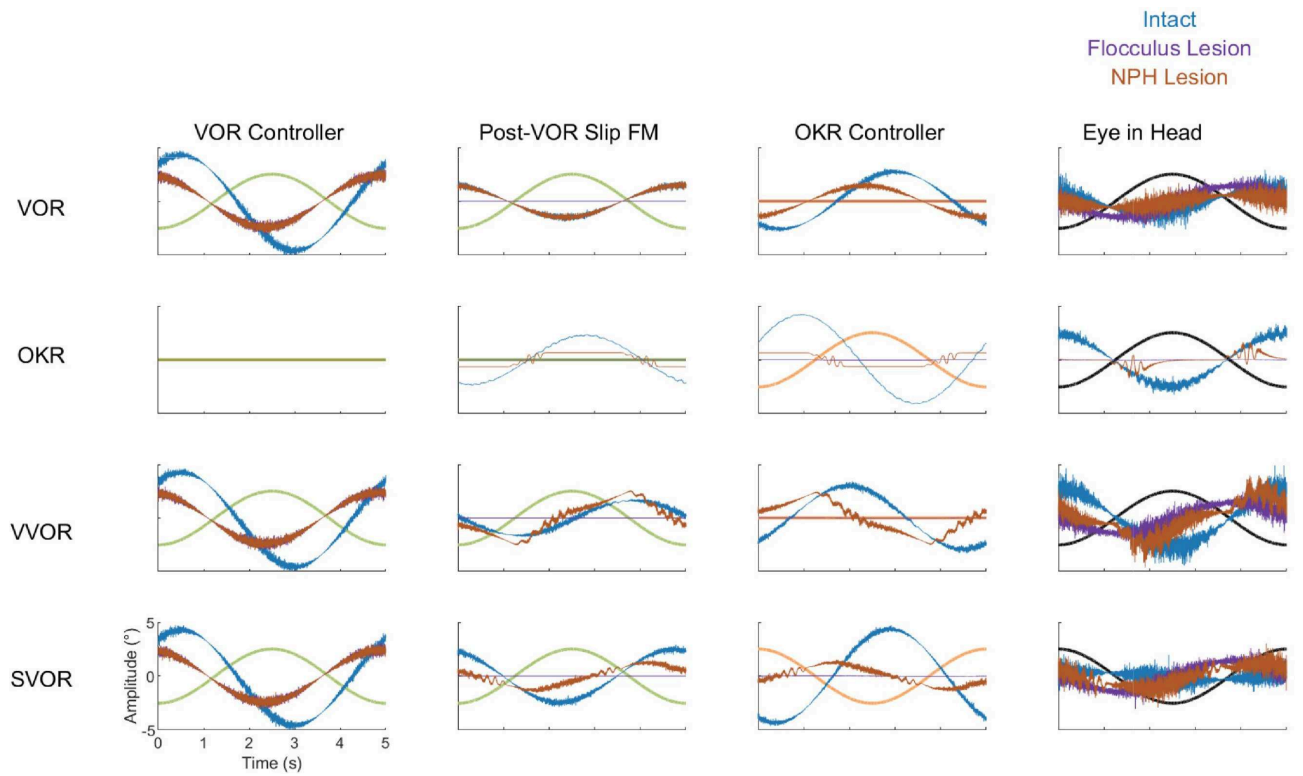

FIGURE 12 | Summary of the dynamics of key components of the model in all four stimulation conditions (VOR, OKR, vVOR, and sVOR) for the full model (blue) and the simulated Flocculus (purple) and NPH lesions (orange). The first column of plots represents the output of the VOR controller, second column displays the forward model of Post-VOR Slip, the third and fourth columns depict the commands produced by the OKR controller and the Plant, respectively. In all plots the relevant stimulus is also displayed. The high frequency content of the control signals is due to the signal dependent noise in the sensory and motor stages of the model.

area for research. Despite these limitations, the range of stimuli we have tested and the publication of all data, model, and analysis code online means that we have provided a framework that people can work with to investigate more esoteric issues and expansions.

Key to the model are two distinct circuits for VOR and OKR. The VOR loop is relatively simple, and mainly consists of an integration step. In traditional models (for review see Glasauer, 2007), the OKR responds to actual retinal slip. However, due to the relatively long delay of the visual processing, the OKR response would then typically respond late. OKR state estimation in our model resolves this by predicting retinal slip. Both the VOR and the OKR loop contribute to this internal estimate of (uncompensated) retinal slip. This combined contribution is necessary, since the OKR assumes that the vestibular system will only partially resolve the retinal slip. While the reality may be more complex, the idea that the OKR models the VOR was the only way that we could explain the relatively high gains of both the OKR and VOR systems in isolation with the veridical gain of the two systems combined.

Finally, our model implements adaptation as a recalibration of this OKR estimate of VOR slip compensation. This helps explain why floccular lesions have a stronger direct effect on OKR but also disrupt VOR adaptation.

The Non-linear Response to SoS Stimulation

In addition to reproducing the response to sinusoidal stimulation in a wide range of conditions, the model also matched responses to SoS-stimuli that are identical to those previously used by Sibindi et al. (2016). Strikingly, two non-linearities reported in the results of that study were reproduced: The first is that when confronted with a visual stimulus that consists of two non-harmonic sinusoids (e.g., the summation of 0.6 and 1.0 Hz sinusoids), the amplitude of the lower frequency is suppressed, independent of the absolute value of the constituent frequencies. This then also results in changes in the amplitudes in vVOR and sVOR conditions. The second is that the lag of the response to the lower frequency is larger, resulting in a delayed overall response. This can be seen for both VOR, OKR, and its combinations.

The model has one non-linearity specifically built in: the saturation of the visual motion sensitive neurons in the retina (see Equation 8 in the **Supplementary Material**, parameter $R_{\max}$). Explicitly removing this saturation eliminated the gain decrease and delay increase of the OKR and vVOR, but left the increased delays in the VOR and sVOR unaffected (**Figure 9**).

These modeling results support the hypothesis that Sibindi et al. used to explain their results: increased delays may be a result of the circuit properties. That is, they suggest the forward model fails to predict upcoming retinal slip in complex stimuli. Our results also support their hypothesis that the gain changes are probably the result of non-linear retinal processing.

The Role of the Flocculus

The flocculus acts as a forward model for both the VOR and the OKR loop. However, the role it plays in each reflex is completely different. The flocculus is not critical for VOR performance, as animals lacking Purkinje cells do have an intact VOR although the amplitude of the response is significantly higher (van Alphen et al., 2001). While our model does include a forward model and state estimator for head velocity, this is only a formal result of the structure of the model. In fact, our model ignores the results of the forward model and uses the sensory information exclusively to determine head velocity. Thus, the role of the forward model (green hexagon in **Figure 1**) in this system is actually only to integrate eye velocity into eye position. For the OKR loop the forward model helps to overcome the delay in the OKR feedback loop, and it is crucial to provide information about the estimated post-VOR slip.

We mimicked lesioning the flocculus by removing the output of the forward models. This removed the capability of the system to predict upcoming retinal slip. As a result, the optokinetic response was virtually abolished whereas VOR gain substantially increased (**Figure 11A**). Lurcher-mice, a mutant strain that lacks Purkinje cells, have substantially lower OKR gains than their wild type littermates (van Alphen et al., 2002). Lurcher-mice results are also similar to a floccular lesion in our model in that VOR-gain is increased. Results on VOR gain in acute, non-genetic floccular lesions are mixed (Rambold et al., 2002).

We can understand the results showing increased VOR gain in Lurcher mice using our model: the OKR generally acts to suppress the VOR and a floccular lesion releases this suppression. This interpretation leads to the further prediction that floccular lesions will reduce the effect of visual suppression of the VOR, increasing gains in the sVOR. This is true in our model as well as being compatible with the literature (Takemori and Cohen, 1974; Zee et al., 1981; Belton and McCrea, 2000).

The change in phase of VOR response that is seen in Lurcher mice (van Alphen et al., 2002) can be modeled only if we include the VOR integration stage in the flocculus. This supports the view of Green et al. (2007) that the NPH provides an efference copy that is integrated in the flocculus (see below).

The Role of the NPH

Our model provides a potential resolution to a debate about the role of the NPH in eye movement generation. In Robinson's inverse-model framework, the NPH is thought to act as the neural integrator for horizontal eye position. Such an integrator is necessary to provide the abducens nucleus with both velocity and position commands that are needed to overcome the low-pass filtering properties of the plant (Robinson, 1981). This view has been widely adopted by researchers in the oculomotor system. A critical finding supporting this view is from Cannon and Robinson (1987) showing that lesions of the NPH cause the eye to drift toward the center of the oculomotor range. This is compatible with the loss of an integrator that opposes the elastic restoring forces of the plant. However, more recently Green et al. (2007) showed that the burst tonic neurons of the NPH have activity that is nearly identical to that of the motor neurons in the abducens nucleus. Furthermore, these neurons have direct projections to the flocculus (Langer et al., 1985; McCrea and Baker, 1985; Belknap and McCrea, 1988).

On the basis of these findings, they proposed that the NPH provides efference copy input to a cerebellar forward model (Green et al., 2007; Ghasia et al., 2008). This view was also incorporated in our SPFC (Frens and Donchin, 2009). Thus, in our model, an NPH lesion removes input to the forward models. However, when we lesion the NPH projection in our simulation (by removing efferent copy to the forward model or by removing its output), we found that we had reproduced the Cannon and Robinson (1987) result: the time constant of the drift was reduced. Hence, a lesion of the efference copy projection produces the same results as those thought to support the idea that NPH is an integrator. It seems that the Cannon and Robinson (1987) results are compatible with both models while recent anatomical and physiological findings support the idea of efferent copy.

VOR Adaptation

Within our framework, VOR adaptation happens through adaptive changes in the forward model of VOR used by OKR. OKR assumes that VOR will correct a certain fraction of sensed head velocity. Determining the proportionality constant robustly led to the same value regardless of stimulus amplitude over a wide range of frequencies. When challenged with an adaptation stimulus, the model gradually changed its gain. Of course, the rate of adaptation could be set arbitrarily. Our setting led to an adaptation speed that is very similar to what we experimentally found in mice under identical experimental conditions. To our knowledge, we are the first to suggest that VOR adaptation reflects adaptation of a forward model of VOR output. However, the idea is compatible with the recent suggestion that VOR adaptation is driven by the motor consequence of retinal slip rather than the slip itself (Shin et al., 2014). Floccular lesions in our model abolish VOR adaptation, which is in line with the literature (Schonewille et al., 2010). NPH lesions do not affect adaptation at 1 Hz in our model, but to the best of our knowledge there is no literature to corroborate this finding.

Although our model is capable of adaptation, we believe that adaptation in the biological system is probably more complex than that in our model. Biological adaptation seems to reflect plasticity at multiple sites with multiple time constants (Porrill and Dean, 2007; Gao et al., 2012; Clopath et al., 2014). The introduction of more realistic adaptation and testing adaptation at higher and lower frequencies is an important future extension of the current model.

Relationship to Other Models

The CEM system is a popular candidate for computational modeling due to the known anatomical substrates and the restricted degrees of freedom. Theories of motor control are primarily based on one of two main architectures. One theory suggests that the motor system relies on generating an ideal "desired movement" or "desired trajectory" that serves as a basis for subsequent control. Such an architecture faces a number of key challenges: generating the desired trajectory, translating it into motor commands, and correcting for deviations during online control. At the heart of such a system is an "inverse model" which translates desired movement into motor commands (Jordan and Rumelhart, 1992). For the CEM system, the desired movement is always the one which will fixate the gaze in space, minimizing retinal slip. The literature in the CEM system contains a long tradition of such models (for example: Robinson, 1981; Kawato and Gomi, 1992; Glasauer, 2007; Lisberger, 2009; Clopath et al., 2014). In general, a desired motor command is fed to the brainstem, which then acts as an "inverse plant," i.e., it processes the command in order to overcome the low-pass properties of the extraocular muscles and tissues that are connected to the eye.

Our model shares the use of internal models and sensory prediction with the Merfeld Observer Model (Merfeld and Young, 1995; Karmali and Merfeld, 2012) and the models of Laurens and Angelaki (2017). However, we concern ourselves mainly with the interaction of the VOR and OKR. Raphan et al. (1979) have also modeled the interaction of these reflexes and our model shares many elements with theirs. However, we place the notion of internal models at the forefront of our approach. The key innovation in our model is the use of recurrent cerebellar-vestibular nuclei loops which enable the model to function correctly in the presence of considerable motor and sensory noise and in the presence of significant delays in sensory feedback. There exists anatomical evidence for such loops (Büttner-Ennever and Büttner, 1992) and proposals for their functional significance have been made previously (Porrill et al., 2004).

Since the optimal control framework was originally proposed as an approach to understanding vertebrate motor systems, models of this sort have been implemented in the control of various motor tasks. The implementations closest to our model are those that attempt to describe coordinated head and eye movements during gaze shifts (Todorov and Jordan, 2002; Sağlam et al., 2011, 2014). One somewhat similar model has been proposed to describe the CEM system (Haith and Vijayakumar, 2007). The Haith model is built largely to address adaptation to changing dynamics, an issue not addressed by our data or our model. Additionally, the Haith model is not confronted with actual data. In sum, our model is unique in a number of respects: (1) the extensive data with which it is challenged, including lesion data and non-sinusoidal data, (2) the idea that one of the main drivers of adaptation is compensation of the OKR system for predicted VOR error, (3) the development of a fully realized recurrent model of the CEM system in the spirit of the optimal control feedback framework.

DATA AVAILABILITY STATEMENT

The Matlab code and data required for replication of the analysis presented in this paper is available on the Open Science Framework website (https://osf.io/feq7c/).

ETHICS STATEMENT

The animal study was reviewed and approved by Erasmus MC Animal Ethics Board.

AUTHOR CONTRIBUTIONS

PH, MG, and OD wrote the code of the model as well as the analysis routines. TS, KA, and SD recorded the mouse data under the supervision of PH, OD, and MF. PH, OD, and MF wrote the manuscript. MF and OD provided the grants that sponsored the project. All authors were involved in discussions about the data, the model, and the implications.

FUNDING

This research was supported by the C7 Marie Curie ITN initiative (TS, PH, SD), TC2N Interreg Grant (OD, MF), the ABC Robotics Initiative (OD), and a Post-Doctoral Fellowship from the Kreitman School for Advanced Studies at BGU (PH).

ACKNOWLEDGMENTS

Parts are based on chapters of the theses of TS (Sibindi, 2015) and SD (Das, 2017).

SUPPLEMENTARY MATERIAL

The Supplementary Material for this article can be found online at: https://www.frontiersin.org/articles/10.3389/fnsys.2020.00013/full#supplementary-material

REFERENCES

Belknap, D. B., and McCrea, R. A. (1988). Anatomical connections of the prepositus and abducens nuclei in the squirrel monkey. *J. Comp. Neurol.* 268, 13–28. doi: 10.1002/cne.902680103

Belton, T., and McCrea, R. A. (2000). Role of the cerebellar flocculus region in cancellation of the VOR during passive whole body rotation. *J. Neurophysiol.* 84, 1599–1613. doi: 10.1152/jn.2000.84.3.1599

Blazquez, P., Hirata, Y., and Highstein, S. (2004). The vestibulo-ocular reflex as a model system for motor learning: what is the role of the cerebellum? *Cerebellum* 3, 188–192. doi: 10.1080/14734220410018120

Büttner-Ennever, J. A., and Büttner, U. (1992). Neuroanatomy of the ocular motor pathways. *Baillières Clin. Neurol.* 1, 263–287.

Cannon, S. C., and Robinson, D. A. (1987). Loss of the neural integrator of the oculomotor system from brain stem lesions in monkey. *J. Neurophysiol.* 57, 1383–1409. doi: 10.1152/jn.1987.57.5.1383

Cheron, G., Gillis, P., and Godaux, E. (1986a). Lesions in the cat prepositus complex: effects on the optokinetic system. *J. Physiol.* 372, 95–111. doi: 10.1113/jphysiol.1986.sp015999

Cheron, G., Godaux, E., Laune, J. M., and Vanderkelen, B. (1986b). Lesions in the cat prepositus complex: effects on the vestibulo-ocular reflex and saccades. *J. Physiol.* 372, 75–94. doi: 10.1113/jphysiol.1986.sp015998

Clopath, C., Badura, A., Zeeuw, C. I. D., and Brunel, N. (2014). A cerebellar learning model of vestibulo-ocular reflex adaptation in wild-type and mutant mice. *J. Neurosci.* 34, 7203–7215. doi: 10.1523/JNEUROSCI.2791-13.2014

Collewijn, H. (1969). Optokinetic eye movements in the rabbit: input-output relations. *Vision Res.* 9, 117–132. doi: 10.1016/0042-6989(69)90035-2

Das, S. (2017). *The mechanistic pathways of transcranial direct current stimulation (tDCS) in cerebellar adaptation* (Doctoral Thesis). Erasmus University Rotterdam, Rotterdam, The Netherlands.

Delgado-García, J. M. (2000). Why move the eyes if we can move the head? *Brain Res. Bull.* 52, 475–482. doi: 10.1016/S0361-9230(00)00281-1

Faulstich, B. M., Onori, K. A., and du Lac, S. (2004). Comparison of plasticity and development of mouse optokinetic and vestibulo-ocular reflexes suggests differential gain control mechanisms. *Vision Res.* 44, 3419–3427. doi: 10.1016/j.visres.2004.09.006

Frens, M. A., and Donchin, O. (2009). Forward models and state estimation in compensatory eye movements. *Front. Cell. Neurosci.* 3:13. doi: 10.3389/neuro.03.013.2009

Gao, Z., van Beugen, B. J., and De Zeeuw, C. I. (2012). Distributed synergistic plasticity and cerebellar learning. *Nat. Rev. Neurosci.* 13, 619–635. doi: 10.1038/nrn3312

Gerrits, N. M., Epema, A. H., and Voogd, J. (1984). The mossy fiber projection of the nucleus reticularis tegmenti pontis to the flocculus and adjacent ventral paraflocculus in the cat. *Neuroscience* 11, 627–644. doi: 10.1016/0306-4522(84)90049-6

Ghasia, F. F., Meng, H., and Angelaki, D. E. (2008). Neural correlates of forward and inverse models for eye movements: evidence from three-dimensional kinematics. *J. Neurosci.* 28, 5082–5087. doi: 10.1523/JNEUROSCI.0513-08.2008

Glasauer, S. (2007). Current models of the ocular motor system. *Dev. Ophthalmol.* 40, 158–174. doi: 10.1159/000100485

Glickstein, M., Gerrits, N., Kralj-Hans, I., Mercier, B., Stein, J., and Voogd, J. (1994). Visual pontocerebellar projections in the macaque. *J. Comp. Neurol.* 349, 51–72. doi: 10.1002/cne.903490105

Graf, W., Simpson, J. I., and Leonard, C. S. (1988). Spatial organization of visual messages of the rabbit's cerebellar flocculus. *II. complex and simple spike responses of purkinje cells. J. Neurophysiol.* 60, 2091–2121. doi: 10.1152/jn.1988.60.6.2091

Green, A. M., Meng, H., and Angelaki, D. E. (2007). A reevaluation of the inverse dynamic model for eye movements. *J. Neurosci.* 27, 1346–1355. doi: 10.1523/JNEUROSCI.3822-06.2007

Haar, S., and Donchin, O. (2019). A *Revised Computational Neuroanatomy* for *Motor Control.* OSF Preprints. (Charlottesville, VA: Center for Open Science) doi: 10.31219/osf.io/t6prj

Haith, A., and Vijayakumar, S. (2007). "Robustness of VOR and OKR adaptation under kinematics and dynamics transformations," in *2007 IEEE 6th International Conference on Development and Learning* (London), 37–42. doi: 10.1109/DEVLRN.2007.4354055

Harris, C. M., and Waddington, J. (2013). Optimal control theory of normal and pathological slow eye movements. *J. Control. Eng. Technol.* 3, 181–188.

Harris, C. M., and Wolpert, D. M. (1998). Signal-dependent noise determines motor planning. *Nature* 394, 780–784. doi: 10.1038/29528

Jordan, M. I., and Rumelhart, D. E. (1992). Forward models: supervised learning with a distal teacher. *Cogn. Sci.* 16, 307–354. doi: 10.1207/s15516709cog1603_1

Karmali, F., and Merfeld, D. M. (2012). A distributed, dynamic, parallel computational model: the role of noise in velocity storage. *J. Neurophysiol.* 108, 390–405. doi: 10.1152/jn.00883.2011

Kawato, M., and Gomi, H. (1992). The cerebellum and VOR/OKR learning models. *Trends Neurosci.* 15, 445–453. doi: 10.1016/0166-2236(92)90008-V

Langer, T., Fuchs, A. F., Scudder, C. A., and Chubb, M. C. (1985). Afferents to the flocculus of the cerebellum in the rhesus macaque as revealed by retrograde transport of horseradish peroxidase. *J. Comp. Neurol.* 235, 1–25. doi: 10.1002/cne.902350102

Laurens, J., and Angelaki, D. E. (2017). A unified internal model theory to resolve the paradox of active versus passive self-motion sensation. *Elife* 6:e28074. doi: 10.7554/eLife.28074.037

Laurens, J., and Droulez, J. (2007). Bayesian processing of vestibular information. *Biol. Cybern.* 96, 405–405. doi: 10.1007/s00422-007-0141-9

Lisberger, S. G. (2009). Internal models of eye movement in the floccular complex of the monkey cerebellum. *Neuroscience* 162, 763–776. doi: 10.1016/j.neuroscience.2009.03.059

Lunn, D., Spiegelhalter, D., Thomas, A., and Best, N. (2009). The BUGS project: evolution, critique and future directions. *Stat. Med*. 28, 3049–3067. doi: 10.1002/sim.3680

McCrea, R. A., and Baker, R. (1985). Anatomical connections of the nucleus prepositus of the cat. *J. Comp. Neurol.* 237, 377–407. doi: 10.1002/cne.902370308

Merfeld, D. M., and Young, L. R. (1995). The vestibulo-ocular reflex of the squirrel monkey during eccentric rotation and roll tilt. *Exp. Brain Res*. 106, 111–122. doi: 10.1007/BF00241361

Oyster, C. W., Takahashi, E., and Collewijn, H. (1972). Direction-selective retinal ganglion cells and control of optokinetic nystagmus in the rabbit. *Vision Res*. 12, 183–193. doi: 10.1016/0042-6989(72)90110-1

Porrill, J., and Dean, P. (2007). Cerebellar motor learning: when is cortical plasticity not enough? *PLoS Comput. Biol.* 3, 1935–1950. doi: 10.1371/journal.pcbi.0030197

Porrill, J., Dean, P., and Anderson, S. R. (2013). Adaptive filters and internal models: multilevel description of cerebellar function. *Neural Netw*. 47, 134–149. doi: 10.1016/j.neunet.2012.12.005

Porrill, J., Dean, P., and Stone, J. V. (2004). Recurrent cerebellar architecture solves the motor-error problem. *Proc. Biol. Sci*. 271, 789–796. doi: 10.1098/rspb.2003.2658

Rambold, H., Churchland, A., Selig, Y., Jasmin, L., and Lisberger, S. G. (2002). Partial ablations of the flocculus and ventral paraflocculus in monkeys cause linked deficits in smooth pursuit eye movements and adaptive modification of the VOR. *J. Neurophysiol*. 87, 912–924. doi: 10.1152/jn.00768.2000

Raphan, T., Matsuo, V., and Cohen, B. (1979). Velocity storage in the vestibulo-ocular reflex arc (VOR). *Exp. Brain Res*. 35, 229–248. doi: 10.1007/BF00236613

Robinson, D. A. (1981). The use of control systems analysis in the neurophysiology of eye movements. *Annu. Rev. Neurosci*. 4, 463–503. doi: 10.1146/annurev.ne.04.030181.002335

Sağlam, M., Glasauer, S., and Lehnen, N. (2014). Vestibular and cerebellar contribution to gaze optimality. *Brain* 137, 1080–1094. doi: 10.1093/brain/awu006

Sağlam, M., Lehnen, N., and Glasauer, S. (2011). Optimal control of natural eye-head movements minimizes the impact of noise. *J. Neurosci*. 31, 16185–16193. doi: 10.1523/JNEUROSCI.3721-11.2011

Schonewille, M., Belmeguenai, A., Koekkoek, S. K., Houtman, S. H., Boele, H. J., van Beugen, B. J., et al. (2010). Purkinje cell-specific knockout of the protein phosphatase PP2B impairs potentiation and cerebellar motor learning. *Neuron* 67, 618–628. doi: 10.1016/j.neuron.2010.07.009

Schonewille, M., Gao, Z., Boele, H.-J., Vinueza Veloz, M. F., Amerika, W. E., Šimek, A. A. M., et al. (2011). Reevaluating the role of LTD in cerebellar motor learning. *Neuron* 70, 43–50. doi: 10.1016/j.neuron.2011.02.044

Shadmehr, R., and Krakauer, J. W. (2008). A computational neuroanatomy for motor control. *Exp. Brain Res*. 185, 359–381. doi: 10.1007/s00221-008-1280-5

Shin, S.-L., Zhao, G. Q., and Raymond, J. L. (2014). Signals and learning rules guiding oculomotor plasticity. *J. Neurosci*. 34, 10635–10644. doi: 10.1523/JNEUROSCI.4510-12.2014

Sibindi, T. M. (2015). *Optimal control of the compensatory eye movement system* (Doctoral Thesis). Erasmus University Rotterdam, Rotterdam, The Netherlands.

Sibindi, T. M., Holland, P. J., van der Geest, J. N., Donchin, O., and Frens, M. A. (2016). Superposition violations in the compensatory eye movement system. *Invest. Opthalmol. Vis. Sci*. 57, 3554–3566. doi: 10.1167/iovs.15-18605

Sohmer, H., Elidan, J., Plotnik, M., Freeman, S., Sockalingam, R., Berkowitz, Z., et al. (1999). Effect of noise on the vestibular system–vestibular evoked potential studies in rats. *Noise Health* 2, 41–52.

Soodak, R. E., and Simpson, J. I. (1988). The accessory optic system of rabbit. I. basic visual response properties. *J. Neurophysiol*. 60, 2037–2054. doi: 10.1152/jn.1988.60.6.2037

Stahl, J. S., James, R. A., Oommen, B. S., Hoebeek, F. E., and Zeeuw, C. I. D. (2006). Eye movements of the murine P/Q calcium channel mutant tottering, and the impact of aging. *J. Neurophysiol*. 95, 1588–1607. doi: 10.1152/jn.00318.2005

Stahl, J. S., and Simpson, J. I. (1995). Dynamics of abducens nucleus neurons in the awake rabbit. *J Neurophysiol* 73, 1383–1395. doi: 10.1152/jn.1995.73.4.1383

Stahl, J. S., Thumser, Z. C., May, P. J., Andrade, F. H., Anderson, S. R., and Dean, P. (2015). Mechanics of mouse ocular motor plant quantified by optogenetic techniques. *J. Neurophysiol*. 114, 1455–1467. doi: 10.1152/jn.00328.2015

Stahl, J. S., van Alphen, A. M., and De Zeeuw, C. I. (2000). A comparison of video and magnetic search coil recordings of mouse eye movements. *J. Neurosci. Methods* 99, 101–110. doi: 10.1016/S0165-0270(00)00218-1

Takemori, S., and Cohen, B. (1974). Loss of visual suppression of vestibular nystagmus after flocculus lesions. *Brain Res*. 72, 213–224. doi: 10.1016/0006-8993(74)90860-9

Todorov, E. (2004). Optimality principles in sensorimotor control (review). *Nat. Neurosci*. 7, 907–915. doi: 10.1038/nn1309

Todorov, E., and Jordan, M. I. (2002). Optimal feedback control as a theory of motor coordination. *Nat. Neurosci*. 5, 1226–1235. doi: 10.1038/nn963

van Alphen, A. M., Schepers, T., Luo, C., and De Zeeuw, C. I. (2002). Motor performance and motor learning in lurcher mice. *Ann. N. Y. Acad. Sci*. 978, 413–424. doi: 10.1111/j.1749-6632.2002.tb07584.x

van Alphen, A. M., Stahl, J. S., and De Zeeuw, C. I. (2001). The dynamic characteristics of the mouse horizontal vestibulo-ocular and optokinetic response. *Brain Res.* 890, 296–305. doi: 10.1016/S0006-8993(00)03180-2

van Alphen, B., Winkelman, B. H. J., and Frens, M. A. (2009). Age- and sex-related differences in contrast sensitivity in C57Bl/6 Mice. *Invest. Opthalmol. Vis. Sci*. 50, 2451–2458. doi: 10.1167/iovs.08-2594

van Alphen, B., Winkelman, B. H. J., and Frens, M. A. (2010). Three-dimensional optokinetic eye movements in the C57BL/6J mouse. *Invest. Opthalmol. Vis. Sci*. 51, 623–630. doi: 10.1167/iovs.09-4072

Wakita, R., Tanabe, S., Tabei, K., Funaki, A., Inoshita, T., and Hirano, T. (2017). Differential regulations of vestibulo-ocular reflex and optokinetic response by β- and α2-adrenergic receptors in the cerebellar flocculus. *Sci. Rep*. 7:3944. doi: 10.1038/s41598-017-04273-9

Winkelman, B., and Frens, M. (2006). Motor coding in floccular climbing fibers. *J. Neurophysiol*. 95, 2342–2351. doi: 10.1152/jn.01191.2005

Yang, A., and Hullar, T. E. (2007). Relationship of semicircular canal size to vestibular-nerve afferent sensitivity in mammals. *J. Neurophysiol*. 98, 3197–3205. doi: 10.1152/jn.00798.2007

Zee, D. S., Yamazaki, A., Butler, P. H., and Gucer, G. (1981). Effects of ablation of flocculus and paraflocculus of eye movements in primate. *J. Neurophysiol*. 46, 878–899. doi: 10.1152/jn.1981.46.4.878

Conflict of Interest: The authors declare that the research was conducted in the absence of any commercial or financial relationships that could be construed as a potential conflict of interest.

frontiers in Systems Neuroscience

ORIGINAL RESEARCH
published: 25 March 2020
doi: 10.3389/fnsys.2020.00011

World Statistics Drive Learning of Cerebellar Internal Models in Adaptive Feedback Control: A Case Study Using the Optokinetic Reflex

Sean R. Anderson[1]*, *John Porrill*[2] *and Paul Dean*[2]

[1] *Department of Automatic Control and Systems Engineering, University of Sheffield, Sheffield, United Kingdom,*
[2] *Department of Psychology, University of Sheffield, Sheffield, United Kingdom*

The cerebellum is widely implicated in having an important role in adaptive motor control. Many of the computational studies on cerebellar motor control to date have focused on the associated architecture and learning algorithms in an effort to further understand cerebellar function. In this paper we switch focus to the signals driving cerebellar adaptation that arise through different motor behavior. To do this, we investigate computationally the contribution of the cerebellum to the optokinetic reflex (OKR), a visual feedback control scheme for image stabilization. We develop a computational model of the adaptation of the cerebellar response to the world velocity signals that excite the OKR (where world velocity signals are used to emulate head velocity signals when studying the OKR in head-fixed experimental laboratory conditions). The results show that the filter learnt by the cerebellar model is highly dependent on the power spectrum of the colored noise world velocity excitation signal. Thus, the key finding here is that the cerebellar filter is determined by the statistics of the OKR excitation signal.

Keywords: cerebellar, computational model, optokinetic (OKN) system, world statistics, adaptive filter

OPEN ACCESS

Edited by:
Conor J. Houghton,
University of Bristol, United Kingdom

Reviewed by:
Fahad Sultan,
University of Tübingen, Germany
Huo Lu,
Philadelphia College of Osteopathic Medicine, United States

***Correspondence:**
Sean R. Anderson
s.anderson@sheffield.ac.uk

Received: *30 August 2019*
Accepted: *07 February 2020*
Published: *25 March 2020*

Citation:
Anderson SR, Porrill J and Dean P (2020) World Statistics Drive Learning of Cerebellar Internal Models in Adaptive Feedback Control: A Case Study Using the Optokinetic Reflex. Front. Syst. Neurosci. 14:11. doi: 10.3389/fnsys.2020.00011

INTRODUCTION

Eye movements have been used extensively to investigate the functions of the cerebellum in motor control (Carpenter, 1988; Büttner-ennever, 2006). They are mechanically much simpler than movements of multi-joint limbs, and the neural circuitry underlying their control is corresponding less complicated (Robinson, 1986). Historically one type of eye movement has been of particular interest, namely that made in response to unexpected rotations of the head. The eyes rotate in the opposite direction to the head so as to stabilize the direction of gaze in space, thus minimizing the extent of whole image movement over the retina (retinal slip) and consequent loss of visual information. Since the reflex is driven by information regarding head movement provided by the vestibular system it is termed the vestibulo-ocular reflex (VOR). One of its key features is that its gain can be altered (VOR adaptation), and Ito (1970) first appreciated the importance of the cerebellum on mediating this adaptation, proposing the flocculus as the region of the cerebellum involved. Subsequent experimental and modeling work on the role of the cerebellum in VOR adaptation continues to the present (e.g., Inagaki and Hirata, 2017; Voges et al., 2017; Luque et al., 2019).

Since movements of the eyes have no effect on head position, the VOR is functionally a *feedforward* control scheme, and VOR adaptation provides a mechanism that enables the scheme

to be calibrated. But there is also a *feedback* control scheme for stabilizing gaze, which uses retinal slip itself to drive counter-rotatory eye movements, and is termed the optokinetic reflex (OKR): the neural substrate of the horizontal OKR is shown in **Figure 1**. This reflex works cooperatively with the VOR to stabilize gaze (Carpenter, 1988). The need for two control schemes (VOR and OKR) to perform one task (image stabilization) is explained by the respective operational range of the VOR and OKR: the VOR does not work effectively at low frequencies of head movement, due to poor sensing of the head velocity at those frequencies by the semicircular canals of the vestibular system. In contrast, the OKR does not function well at high frequencies of head movement because the retinal slip is delayed (by ∼100 ms) due to visual processing time (Robinson, 1987). Hence, the VOR and OKR combine to stabilize the full field visual image across a wider frequency spectrum than might be accomplished individually (Paige, 1983; Godaux and Vanderkelen, 1984; Boyle et al., 1985; Schweigart et al., 1997).

Here we model how OKR performance is improved by the contribution of the cerebellar flocculus, using an architecture based on the detailed descriptions available of the relevant neural circuitry (Fuchs and Mustari, 1993; Mustari et al., 1994). The flocculus itself is represented by the adaptive-filter model of the cerebellar cortical microcircuitry, proposed by Fujita (1982) as a development of the original Marr-Albus framework to allow direct processing of temporally varying inputs, and consequent representation of systems in which current output depends on input history. Adaptive-filter models have subsequently used extensively in system-level modeling of cerebellar function (Dean and Porrill, 2010).

We focus our analysis of the adaptive OKR model on the retinal slip signal which is used to excite the feedback control loop. The term "excite" is used in the systems engineering sense of an *excitation signal*, which refers to the input signal that causes the system to generate an output. Excitation signals can be divided into two classes: predictable and non-predictable. An example of a predictable signal is a single frequency sine wave, whilst a non-predictable signal is colored noise. Our analysis on these two classes of signal reveals the extreme dependence of cerebellar learning on the predictability of the excitation signal, in other words on the statistics of the visual world.

The OKR is an exemplar problem of adaptive feedback control. Hence, understanding how the cerebellum adapts to optimize eye movements in the OKR is potentially of great importance for understanding cerebellar involvement in feedback control throughout the nervous system.

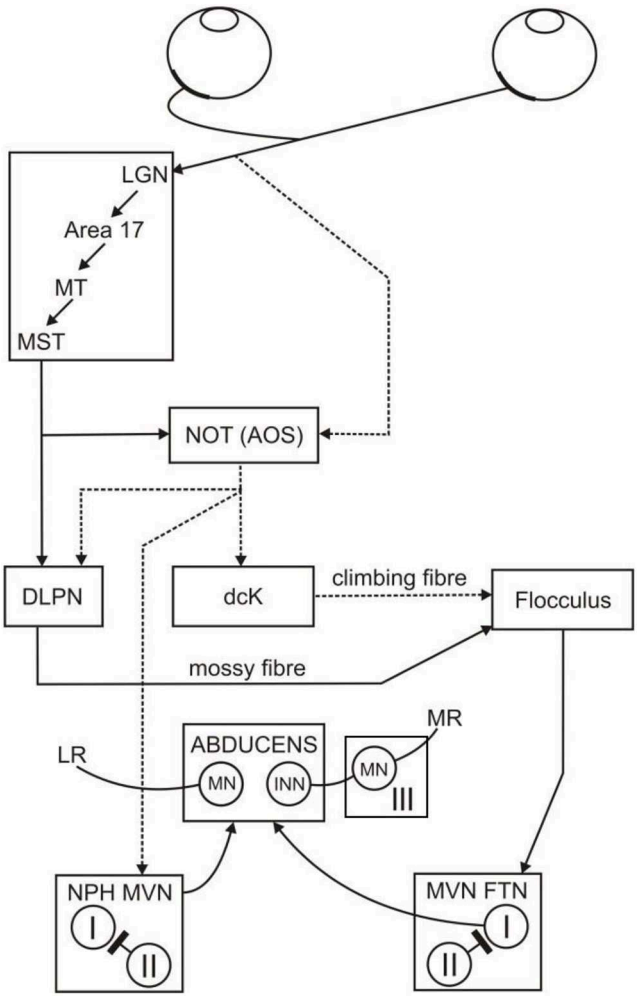

FIGURE 1 | Neural substrate of the horizontal OKR. The retinal slip signal that drives the OKR arrives at the flocculus via climbing fibers (NOT, dcK) and mossy fibers (MST, NOT, DLPN, the direct pathway). The retinal slip signal is also transmitted to the brainstem (NPH, MVN, the indirect pathway). The direct and indirect pathways both project to the abducens nucleus and from there combine to drive movements of the eye in order to stabilize the visual image. From Figure 12 of Mustari et al. (1994). I and II, type 1 and 2 neurons in the vestibular nucleus; III, oculomotor nucleus; AOS, accessory optic system; dcK, dorsal cap of Kooy of the inferior olive; DLPN, dorsolateral pontine nucleus; FTN, floccular target neurons; INN, internuclear neurons; LR, lateral rectus; LGN, lateral geniculate nucleus; MN, motor neurons; MR, medial rectus; MST, middle superior temporal gyrus of cerebral cortex; MT, middle temporal cortex; MVN, medial vestibular nucleus; NPH, nucleus prepositus hypoglossi; NOT, nucleus of the optic tract.

METHODS

The basic circuitry underlying the primate OKR has been described by Mustari et al. (1994). The box labeled flocculus in this figure refers to those microzones in the flocculus and ventral paraflocculus that are concerned with conjugate horizontal eye movements (i.e., rotations around a vertical axis). These microzones, and their connectivity, are described in detail by Voogd and Barmack (2006).

Here we model this connectivity using the simplified architecture illustrated in **Figure 2**, which is based on the previous model of Waespe et al. (1983) (subsequently referred to as WRC83), with the vestibular pathways of that model omitted because in the experimental conditions modeled here the head is fixed so no vestibular signals are involved. This architecture is also consistent with other models of the OKR, for instance that of Buizza and Schmid (1982). We focused on linear analysis of

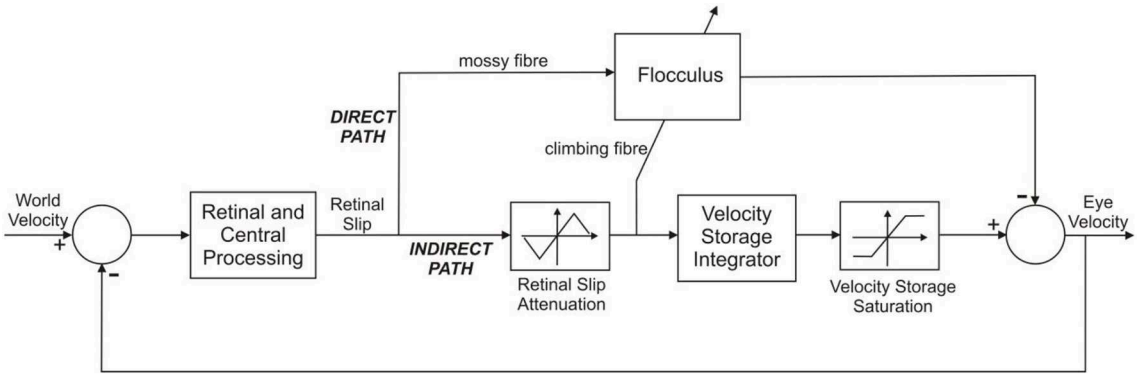

FIGURE 2 | Systems level model of the OKR. The OKR functions as an adaptive feedback control loop. World velocity excites the control scheme; error between world velocity and eye velocity drives the controllers of which there are two: (i) In the indirect pathway there is a fixed controller (located in the brainstem), known as the velocity storage integrator. (ii) The floccular region of the cerebellum is in the direct pathway of the OKR. The flocculus provides adaptive compensation of the OKR. The indirect pathway has static non-linearities that affect performance at velocities higher than ∼50 deg/s. The other important feature relating to feedback control is that the error signal, retinal slip, is delayed in visual processing by about 100 ms. Adapted from Figure 10 of WRC83.

the system, and therefore ignored the effects of the static non-linearities in the indirect pathway, activated at velocities >50 deg/s in primate WRC83.

The input to the feedback loop shown in **Figure 2** is "world velocity," appropriate for experimental studies that investigate the OKR under head fixed conditions. Here the subject is typically sat, head fixed, inside a rotating drum, so that it appears as if the world itself were moving. In non-experimental conditions the OKR would be excited by head velocity. However, head velocity is fixed to zero in experimental conditions when studying the OKR, in order to keep the eye movement response independent of the VOR. The world velocity signal is transformed by retinal and central processing into a retinal slip signal that is utilized by two main neural pathways, one the "direct" pathway through the cerebellum, the other the "indirect" pathway through the brainstem. The indirect pathway incorporates a velocity storage unit which integrates the retinal slip signal and provides a slow response component to the OKR, revealed when the flocculus is inactivated WRC83. The cerebellar contribution to the OKR is a rapid rise in eye velocity early in the response, modeled by a filter with a fast time constant, which is the case here.

The flocculus itself is modeled as an adaptive filter, which represents plasticity at the parallel fiber/Purkinje cell (PF/PC) synapse by an anti-Hebbian learning rule (Sejnowski, 1977; Fujita, 1982): synaptic efficacy changes in response to correlation in PF and CF firing. Positive correlation in PF/CF firing results in positive weight change and negative correlation results in negative weight change. Hence, LTP and LTD are modeled using this learning rule, both of which occur at the PF/PC synapse (Ito, 1989; Coesmans et al., 2004) (further details below).

The architecture in **Figure 3** can be described in terms of three distinct functional elements using Laplace transforms: (i) a time-delay operator $D(s) = e^{-ds}$, of delay d seconds, (ii) the floccular region of the cerebellum $C(s)$ and (iii) the velocity storage unit $V(s)$. We can form the closed loop description of the OKR model in **Figure 3**, which is

$$Y(s) = \frac{D(s)[C(s)+V(s)]}{1+D(s)[C(s)+V(s)]}R(s) \quad (1)$$

where $Y(s)$ is the Laplace transform of the eye velocity $y(t)$ and $R(s)$ is the Laplace transform of the world, or head, velocity $r(t)$ (note that world velocity excites the OKR in experimental setups where the head is fixed and the world rotates, whilst head velocity excites the OKR in natural conditions where the head is free to move and the world is fixed).

Model of the Velocity Storage Unit

The velocity storage unit in **Figure 3** was modeled as a first order transfer function $V(s)$, of the form

$$V(s) = \frac{K_v}{T_v s+1} \quad (2)$$

where K_v is a gain term and T_v is a time constant.

The gain and time constant of $V(s)$ were estimated by grid search, minimizing the sum-of-squared error (SSE) fit to step response data obtained after floccular removal in primate (flocculectomy) from WRC83, Figure 11D. Note that the closed loop OKR system given in (1), for the flocculectomy condition where $C(s) = 0$, reduces to

$$Y(s) = \frac{D(s)V(s)}{1+D(s)V(s)}R(s) = \frac{e^{-ds}K_v}{T_v s+e^{-ds}K_v+1}R(s) \quad (3)$$

where the closed loop transfer function has the steady-state gain $K_{ss} = K_v/(K_v + 1)$. This means that for a plausible steady-state OKR flocculectomy gain $0.9 \leq K_{ss} \leq 0.95$, the velocity storage gain is approximately $9 \leq K_v \leq 20$. Therefore, the value of K_v was estimated by performing a grid search over this range, $9 \leq K_v \leq 20$, in steps of 0.5. The time constant value T_v, was estimated by searching across the range $100 \leq T_v \leq 300$ s, in steps of 10 s.

Adaptive Filter Model of the Cerebellum

The adaptive filter model of the cerebellum used here is equivalent to the original implementation by Fujita (1982).

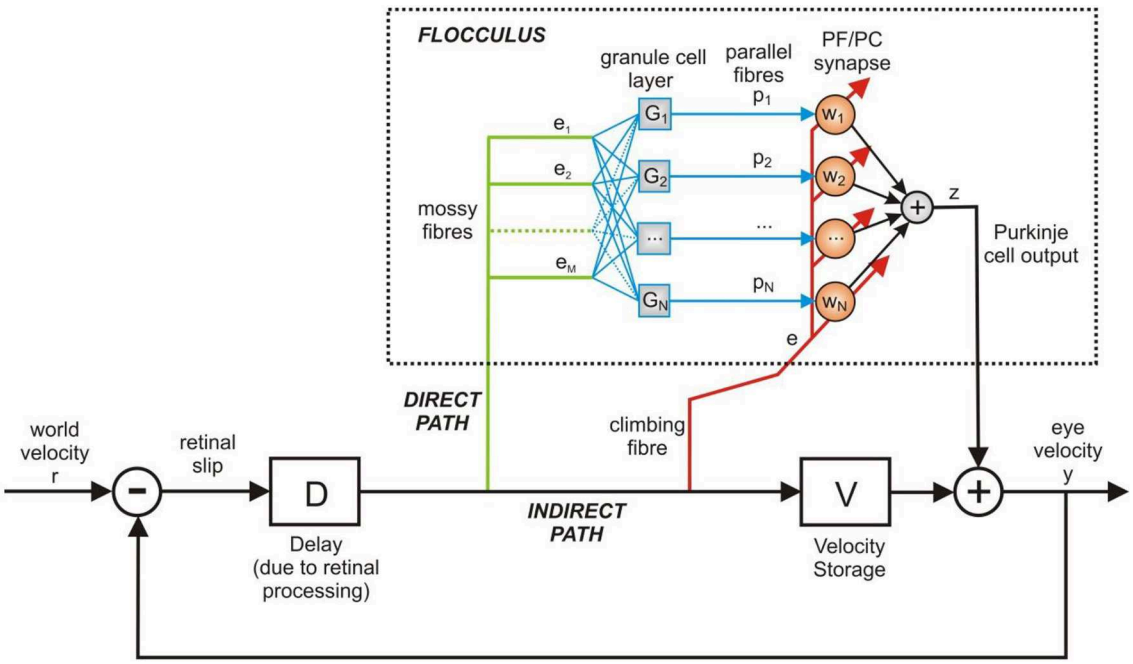

FIGURE 3 | Adaptive filter model of the cerebellum in the OKR control loop. The adaptive filter models the signal processing in the floccular region of the cerebellum. Here the adaptive filter model is inserted in the OKR model shown in **Figure 2**. The velocity storage is modeled here by a linear 1st order transfer function. The output of cerebellum and brainstem are assumed to sum together to produce the motor command, which here is equivalent to eye velocity.

Hence, for computational expedience we represent a single Purkinje cell, but mathematically this is equivalent to an arbitrary number of Purkinje cells, under the assumption that their outputs sum linearly.

The mossy fiber input to the cerebellum is processed by the granule cell layer, which is represented by a bank of N linear filters $G_i(s)$, for $i = 1, \ldots, N$ (see **Figure 3**). The exact nature of the filters $G_i(s)$ is not critical: the function of $G_i(s)$ is to act analogously to a tap-delay line, which can be achieved by using alpha-functions that have well-spaced time constants, so that

$$G_i(s) = \frac{K_G^{(i)}}{\left(T_G^{(i)} s + 1\right)^2} \quad \text{for} \quad i = 1, \ldots, N \tag{4}$$

Where $T_G^{(i)}$ is the alpha-function time constant and $K_G = 1/\left(T_G^{(i)}\right)^2$.

We assume that mossy fibers transmit the OKR error signal $e(t)$, with Laplace transform $E(s)$, which is processed by the granule cell layer represented by the filter bank $G_i(s)$, to produce the PF signal $P_i(s)$, that is

$$P_i(s) = G_i(s)E(s) \quad \text{for} \quad i = 1, \ldots, N \tag{5}$$

The PF signals, in the context of the OKR, can therefore be interpreted as a set of retinal slip signals, delayed by varying amounts by the granule cell layer.

The cerebellar model output, $Z(s)$, is the sum of weighted PF signals,

$$Z(s) = \sum_{i=1}^{N} w_i P_i(s) \quad \text{for} \quad i = 1, \ldots, N \tag{6}$$

where the plasticity of the PF/PC weights w_i is modeled by an anti-Hebbian learning rule discussed below. The cerebellar filter $C(s)$ is now conveniently described from mossy fiber input to PC output by the expression

$$C(s) = \sum_{i=1}^{N} w_i G_i(s) \quad \text{for} \quad i = 1, \ldots, N \tag{7}$$

The expression for $C(s)$ in Equation (7) is a more functionally realistic representation of the cerebellum in comparison to the proportional gain model in WRC83 because (i) it can represent varying gain across the frequency spectrum and (ii) it facilitates modeling and analyzing plasticity at the PF/PC synapse.

Learning Rule at the PF/PC Synapse

The adaptation at the PF/PC synapse is modeled by the correlation of delayed PF signal and CF signal,

$$\Delta w_i = -\beta \left\langle e(t) p_i^{(d)}(t) \right\rangle \tag{8}$$

where w_i is the i$^{\text{th}}$ weight in the cerebellar filter, β is a constant term that adjusts the learning rate, $e(t)$ is the error signal on the CF and $p_i^{(d)}(t)$ is the i$^{\text{th}}$ PF signal, whilst the superscript d

indicates that the PF signal is delayed by d seconds in the learning rule. It has been found in a modeling study of the ocular following response that a delay was required for stable adaptation in the PF/PC synapse learning rule (Yamamoto et al., 2002) and that is also the case here as using an un-delayed PF signal in the learning rule led to unstable adaptation.

We implemented the delay in the learning rule by an eligibility trace. The eligibility trace is a biologically plausible representation of a delay mechanism occurring in synaptic plasticity (Kettner et al., 1997; Wang et al., 2000). The eligibility trace was dynamically represented here by an α-function $L(s)$, where the time constant was set to the delay in retinal slip visual processing,

$$L(s) = \frac{1}{(1+ds)^2} \tag{9}$$

The input to the eligibility trace is the parallel fiber signal $p_i(t)$ and the output is a filtered version of $p_i(t)$ which peaks at d seconds,

$$P_i^{(d)}(s) = L(s)P_i(s) \tag{10}$$

where $P_i^{(d)}(s)$ and $P_i(s)$ are the Laplace transforms of $p_i^{(d)}(t)$ and $p_i(t)$, respectively.

OKR Excitation by Predictable and Non-predictable Signals

The world velocity signal $r(t)$ was used to excite the OKR model. The signal $r(t)$ can be defined as either a predictable signal such as a sine wave, or non-predictable signal such as colored noise **or white noise.** We suggest that during the natural operation of the OKR the excitation signal is well-represented by colored noise, consistent with head velocity being stochastic and hence unpredictable at any point in time, but characterized by fixed statistical properties and structured as suggested by the data in Carriot et al. (2017). Sine waves are often used in experimental investigations of the OKR, as well as computational studies and were therefore also investigated here.

For the colored noise world velocity signal $r(t)$, the power spectral density was set to

$$S_{RR}(f) = \frac{b}{f^a} \tag{11}$$

where f is frequency in Hertz, a is the spectral exponent and b is the constant of proportionality. Note that spectral exponent $a = 0$ corresponds to white noise, $a = 1$ corresponds to pink noise, and $a = 2$ corresponds to red noise. Here we only considered a value of $a = 1.2$, which has been shown to plausibly represent power in head yaw movements (Carriot et al., 2017). The scaling parameter b was adjusted by numerical simulation to fit behavioral data (see Results).

Simulation Details

To simulate the computational model of the OKR depicted in **Figure 3**, each of the transfer functions defined above in the Laplace-domain, time-delay $D(s)$, velocity storage $V(s)$, granule layer basis functions $G_j(s)$ and eligibility trace $L(s)$, were parametrised using the values in **Table 1** and defined in Matlab for simulation. The transfer functions were discretised using a zero-order hold at a sample time of 0.1 s to produce the Z-transform equivalents for simulation in discrete-time: $V(z) = \sum_{n=0}^{\infty} v(n)\, z^{-n}$, $G_j(z) = \sum_{n=0}^{\infty} g_j(n)\, z^{-n}$, $L(z) = \sum_{n=0}^{\infty} l(n)\, z^{-n}$ and $D(z) = z^{-n_d}$ (i.e., a pure delay of n_d time-steps).

TABLE 1 | Parameter values used in the computational simulations.

Parameter	Symbol	Value
Velocity storage time constant	T_V	230 s
Velocity storage gain	K_V	13.5
Number of cerebellar filter weights	N	5
Cerebellar filter alpha function time constants	$T_G^{(1,\ldots,5)}$	0.01, 0.02, 0.1, 0.2, 0.5 s
Cerebellar filter learning rate	β	0.001
Initial cerebellar filter weight values	$w_{1,\ldots,5}(0)$	0
Retinal slip delay	d	0.1 s

The colored noise world velocity signal $r(t)$ was created for the discrete-time simulations by generating samples of a white noise signal, then taking the discrete Fourier transform of this signal, applying the b/f^a transformation in the frequency-domain, then taking the inverse discrete Fourier transform to finally obtain the sampled colored noise world velocity signal $r(k)$.

The algorithm for evaluating the OKR model output is as follows: at a sample instant denoted by k sequentially evaluate

$$\begin{aligned}
e_d(k) &= e(k - n_d) && \text{(delayed retinal slip)}\\
x(k) &= \sum_{n=0}^{\infty} v(n) e_d(k-n) && \text{(velocity storage output)}\\
z(k) &= \sum_{n=0}^{\infty} c(n,k) e_d(k-n) && \text{(cerebellar output)}\\
y(k) &= z(k) + x(k) && \text{(eye velocity output)}\\
e(k) &= r(k) - y(k) && \text{(retinal slip)}
\end{aligned}$$

where the cerebellar filter $C(z,k) = \sum_{n=0}^{\infty} c(n,k) z^{-n}$ is defined by the adaptation of the filter weights, using the learning rule in (7), where

$$\begin{aligned}
p_j(k) &= \sum_{n=0}^{\infty} g_j(n) e_d(k-n) && \text{(PF signal)}\\
p_j^{(d)}(k) &= \sum_{n=0}^{\infty} l(n) p_j(k-n) && \text{(PF signal delayed by eligibility trace)}\\
\Delta w_j(k) &= -\beta e_d(k) p_j^{(d)}(k) && \text{(PF/PCcerebellar weight adaptation)}\\
w_j(k+1) &= w_j(k) + \Delta w_j(k) && \text{(updated cerebellar filter weights)}\\
C(z,k+1) &= \sum_{j=1}^{N} w_j(k+1) G_j(z) && \text{(updated cerebellar filter)}
\end{aligned}$$

To improve stability of the weight adaptation rule the cerebellar weights were updated in a batch mode of 10,000 samples (corresponding to 1,000 s of data), over 2,000 batch iterations. The weight change across batches was monitored to ensure convergence.

RESULTS

Adaptive Model Describes the OKR Step Response in Primate

In previous non-adaptive models of the OKR their parameters were specifically tuned to produce the eye movements observed experimentally. Here such tuning was used only for the time constant and gain of the velocity-storage component (Equation 2) and to illustrate the contribution of the cerebellum, in the time-domain and the frequency-domain (**Figure 4**). The experimental setup that the model simulations emulate is shown in **Figure 4A**, with the corresponding feedback control loop in **Figure 4B**. The response of the OKR model without cerebellar contribution (flocculectomy condition) to a velocity step input of 60 deg/s, compared with experimental observations from WRC83 of OKR performance after floccular removal is shown in **Figure 4C**. A reasonable fit has been obtained with a time constant of 230 s and gain of 13.5, producing a rise time of ∼20 s. The fit shown in **Figure 4C** suggests that the first order filter characterization of the velocity-storage element is a reasonable approximation. The contribution of the cerebellum is illustrated in **Figure 4D** using a fixed first order filter. This linear modeling of the OKR using transfer functions enables the computation of a Bode plot to compare the flocculectomy and intact characteristics of the OKR in the frequency-domain (**Figure 4E**).

To explore the contribution of the flocculus to OKR performance under learning conditions, the adaptive-filter model of the cerebellum was initialized to zero, then learning was driven by exciting the OKR system with a colored noise world-velocity signal, which indirectly caused parameter adaptation as a result of the learning rule describing plasticity at the PF/PC synapse. We found that when the colored noise world velocity signal spectral exponent was set to $a = 1.2$, and the scaling parameter of the noise set to $b = 0.017$, the adaptive OKR model converged to a feedback control scheme that produced an OKR step response closely resembling behavioral data (**Figure 5**). The adaptive filter model of the flocculus modified the OKR dynamics by causing a rapid increase in velocity early in the step response compared to the flocculectomy condition (**Figure 5C**) and correspondingly raising the closed loop OKR gain in the region of 0.1 Hz (**Figure 5E**).

The Learned Cerebellar Filter Depends on the Statistics of the Excitation Signal

The adaptation of the OKR is caused by the retinal slip error. The characteristics of this error signal are directly dependent on the statistics of the world velocity excitation signal. For instance, we have shown in **Figure 5** that when the scaling parameter and spectral exponent of the colored noise excitation signal are appropriately tuned, the excitation signal produces learning that converges to a system that reproduces behavioral OKR data. The implication of this result is that the excitation signal can be manipulated to cause a variety of different OKR responses. Here we simulated the adaptive OKR model with colored noise signal in a number of experimental trials, altering both the scaling parameter, b (**Figure 6**), and the spectral exponent, a (results not shown), to observe the effect on the OKR dynamics.

We systematically varied the scaling parameter, b, of the colored noise world velocity signal to produce varying power levels of excitation of the OKR model (**Figures 6A,B**). The resulting step responses of the OKR model are shown in **Figures 6C,D**. The early rapid rise in velocity, due to the cerebellar filter, increases in amplitude as the scaling parameter b increases, even leading to overshoot and oscillation in the eye velocity response (**Figures 6C,D**). The step responses and Bode plots of the OKR shown in **Figures 6C–E** are significantly different from each other: the implication of this result is that world velocity statistics have a strong influence on the resultant learned characteristics of the OKR.

The OKR Performance Improves When Excited by Simple Predictable Signals

The control of eye movements is often studied by exciting the oculomotor system with a single frequency sine wave. This would correspond to causing the full field image to oscillate at a single frequency in the case of the OKR (Paige, 1983; Boyle et al., 1985) or a target in the case of smooth pursuit (Deno et al., 1989). Studies of the OKR and smooth pursuit systems have revealed that the control performance in terms of gain and phase improve when excited by predictable signals (Wyatt and Pola, 1988; Deno et al., 1989). Here we investigated this phenomenon by exciting the adaptive OKR model with both predictable and non-predictable signals.

The predictable excitation signals in the simulation model were designed to emulate single frequency sine wave excitation of the OKR often used in experimental setups (Paige, 1983; Boyle et al., 1985). The OKR model was initialized to a "natural" state before each trial: rather than setting the adaptive filter weights to zero, we initialized the weights using the trained the OKR model after adaptation driven by the colored noise excitation signal with scaling parameter $b = 0.017$ and spectral exponent $a = 1.2$, which reproduced behavioral data shown in **Figure 5**. The OKR model was then excited in each sine wave trial for just 600 s (sequential adaptation was used in the cerebellar filter not batch adaptation). To a certain extent this setup emulates the somewhat artificial experimental conditions where a normal subject undergoes excitation of the OKR using single frequency sine waves.

The closed loop performance of the OKR model greatly improved, in terms of closed loop gain and phase, when exciting the system with single frequency sine waves (a predictable signal) rather than colored noise (an unpredictable signal) (**Figures 7A,B**). The implication of this result is that cerebellar model is able to rapidly learn to compensate for the specific and fixed characteristics of the predictable sine wave signal. It is also apparent that the modeling results are qualitatively similar to the

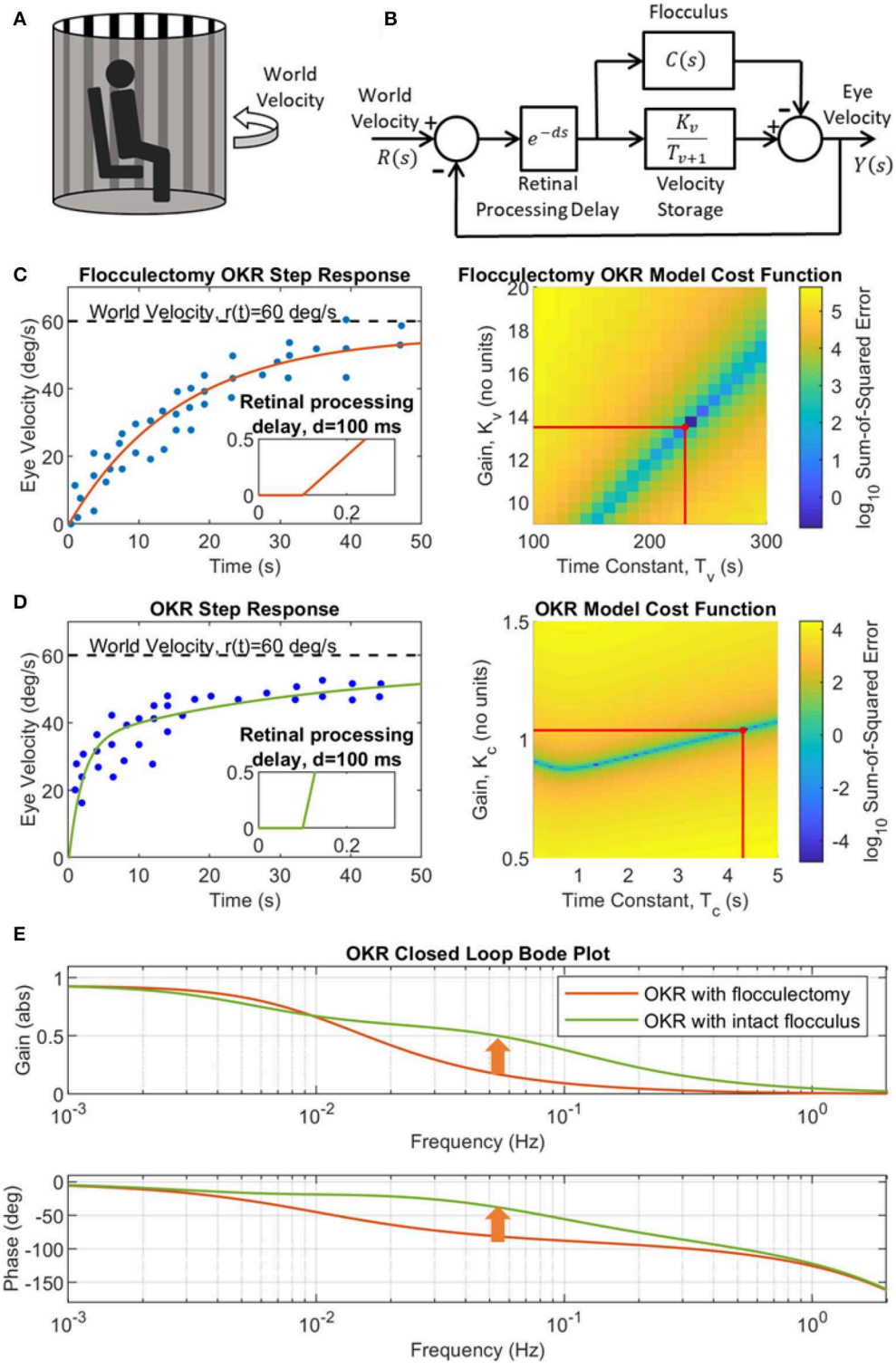

FIGURE 4 | A simple linear model of the OKR for flocculectomy and intact flocculus conditions. **(A)** Illustration of a typical OKR experimental setup, where the subject sits, head-fixed, in a rotating drum that has alternating vertical black and white stripes on the interior. **(B)** Simplified linear OKR feedback control loop with floccular region of the cerebellum modeled by a fixed transfer function $\mathbf{C}(\mathbf{s}) = \mathbf{K_C}/(\mathbf{T_C s}+\mathbf{1})$. **(C)** Identification of the velocity storage transfer function. Left panel: OKR flocculectomy step response ($C(s) = 0$) to a step of 60 deg/s where the data (dots) were extracted from Waespe et al. (1983), Figure 11D, with simulation of the estimated best model fit (solid line) in closed loop, where $T_v = 230$ s and $K_v = 13.5$. Right panel: Grid search cost function (color map) for the optimal velocity storage

(Continued)

FIGURE 4 | parameters (red lines), K_v and T_v. **(D)** Identification of the fixed cerebellar filter modeled as a first order transfer function, $C(s) = K_C/(T_C s + 1)$. Left panel: OKR step response with intact cerebellum where the data (dots) were extracted from WRC83, Figure 11B, with simulation of the feeback loop in **(B)** with best cerebellar model fit (solid line) where $T_C = 4.3$ s and gain $K_C = 1.04$. Right panel: Grid search cost function (color map) for the optimal cerebellar filter parameters (red lines), K_C and T_C. **(E)** OKR closed loop Bode plot for both flocculectomy and intact flocculus conditions derived from the model in panel B, using the transfer functions identified in **(C,D)**. The cerebellum contributes a rise in gain toward one, and phase toward zero, in the region of 0.1 Hz (indicated by the arrows), which improves control performance.

experimental results from Paige (1983) and Boyle et al. (1985) (**Figure 7B**), which suggests that experimental results reporting OKR characteristics using single frequency sine waves do not reflect "normal" operation.

DISCUSSION

Consistency With Experimental Data

Predictability and the OKR

Improvements in OKR performance related to stimulus predictability were initially described by Yasui and Young (1984) and Wyatt and Pola (1988) in humans, and subsequently in a wide range of species (Miki et al., 2018). Optokinetic adaptation, in which simple exposure to a sinusoidally moving wide-field stimulus increases OKR gain, is a well-studied example (e.g., Inoshita and Hirano, 2018).

Delay: Stable and Convergent Adaptation Requires a Delayed PF Signal in the Learning Rule

The PF signal requires a delay in the learning rule to ensure that learning is stable and convergent. It is well-known from the systems engineering literature that stability in correlation based learning rules is dependent on the correlating signals being within +/−90 degrees of the correct phase with each other (Vaudrey et al., 2003). We observed instability in the learning rule when the PF signal was not delayed, similarly to Yamamoto et al. (2002). Evidence for a delayed error signal (∼120 ms) has come from studies of cerebellar long-term depression (Suvrathan et al., 2016; Suvrathan and Raymond, 2018), which show that this delay occurs in the flocculus that deals with the OKR, while other delays are found elsewhere in the cerebellum.

Computational Framework

It has long been recognized that while the structure of cerebellar cortex is relatively uniform, different regions of cortex have different connections to external structures such as the deep cerebellar nuclei and inferior olive. This has given rise to the "chip" metaphor (e.g., Ito, 1997; Porrill et al., 2013), in which the cerebellar cortex is cast as a set of identical chips that can be used for a wide variety of purposes. In this context there are two aspects to a cerebellar model, one its representation of the microcircuit, and the second its external connectivity.

Microcircuit Model

Early modeling studies of the OKR in rabbit (Collewijn, 1969, 1972), cat (Buizza and Schmid, 1982; Gillis et al., 1984) and primate (Buizza and Schmid, 1982; Waespe et al., 1983) have represented the cerebellar OKR function as a single fixed gain. Here we use the much more powerful adaptive-filter model of the cerebellar microcircuit. First proposed by Fujita (1982), this model extends the original Marr-Albus framework to cope with dynamic time-varying signals, and is thus very well-suited to the construction of internal models of dynamic processes (Dean et al., 2010; Porrill et al., 2013).

Connectivity

The floccular connectivity illustrated in **Figure 1** is simplified in two main ways. First, as described in Methods, the box labeled flocculus in this figure refers to those microzones in the flocculus and ventral paraflocculus that are concerned with conjugate horizontal eye movements (i.e., rotations around a vertical axis). These microzones, and their connectivity, are described in detail by Voogd and Barmack (2006). Secondly, only those connections relevant to the OKR are shown: thus, vestibular inputs are omitted. These simplifications are the ones usually made in linear-system modeling of the OKR (e.g., Carpenter, 1988).

In the circuit shown in **Figure 3**, the flocculus is placed to learn an internal model incorporating any structure that may be present in the world velocity input. This structure may be present either in the external world itself (exafference), for example water currents, or derive from the organism's own movements (reafference). Successful learning enables the floccular output to alter eye-movement commands, making them more effective in reducing retinal slip. This procedure has similarities with predictive noise cancellation, which acts to remove interference (noise) from sensory signals (e.g., Anderson et al., 2010, 2012; Porrill et al., 2013).

Time Delay, the Smith Predictor, and Internal Models

Time delay in feedback control loops creates a significant problem regarding stability (aside from the adaptation problem described above). The OKR is no exception to this due to the delay in visual processing of the retinal slip signal (St.-Cyr and Fender, 1969; Waespe and Henn, 1987). Therefore it is reasonable to question whether speculation on the action of the cerebellum as a Smith predictor is relevant to this study (Miall et al., 1993). Young and Robinson have separately proposed control schemes where the cerebellum acts as a forward model of oculomotor plant dynamics in smooth pursuit and OKR, implicitly constructing a control architecture that was closely related to the Smith predictor (Young, 1971; Robinson, 1977; Robinson et al., 1986). The approach we have taken here is to construct the adaptive model with no assumptions regarding the functional role of the cerebellum. On completion of learning we examined the dynamic behavior of the cerebellar model, investigating the internal model hypothesis (Wolpert et al., 1998) in the context of the OKR. We found that the cerebellar

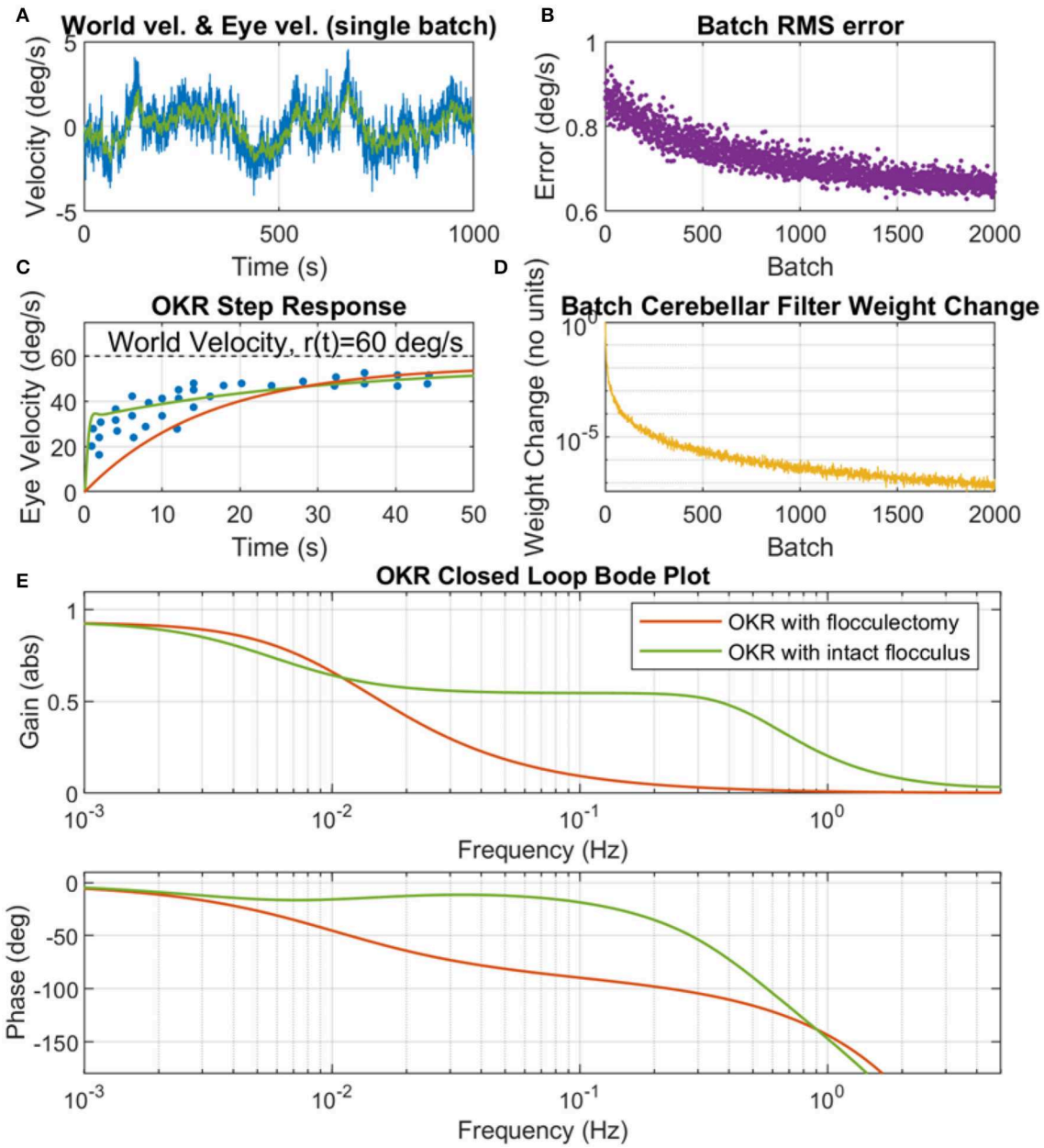

FIGURE 5 | Cerebellar adaptation in the OKR driven by a colored noise world velocity signal. **(A)** Example of a single batch of world velocity (blue line) and eye velocity (green line) simulation data, where world velocity has a spectral exponent of $a = 1.2$ and scaling parameter b = 0.017. **(B)** Batch root mean square (RMS) error (where error is the difference between world velocity and eye velocity). **(C)** OKR step response where experimental data (dots) is from WRC83, Figure 11B, OKR model step response with intact flocculus (solid green line) is from training on 2,000 batches of simulation data with colored noise world velocity signal, and OKR flocculectomy model response (solid red line) is without a cerebellar contribution. **(D)** Batch cerebellar filter weight change demonstrating convergence of the adaptive cerebellar filter in the OKR control loop. The adaptation rule is stochastic hence does not go to zero but note the log scale, which shows very small numerical change in the weights by batch 2,000. **(E)** OKR closed loop Bode plot for both flocculectomy and intact flocculus conditions, where the Bode plots are obtained from the same models as the step responses in **(C)**.

filter model did not resemble oculomotor plant dynamics so much as a generic lag compensator and that functionally such an internal oculomotor plant model did not logically fit into the control scheme (however, this is a simplified model so no definitive conclusions can be drawn). Instead we observed that the cerebellar filter acted to directly raise the gain of the closed loop system in the frequency region around 0.1 Hz and improve the phase response in the same region.

Future Work

Ahrens et al. (2012) investigated the neural substrates of an optomotor behavior related to the OKR in larval zebrafish. The

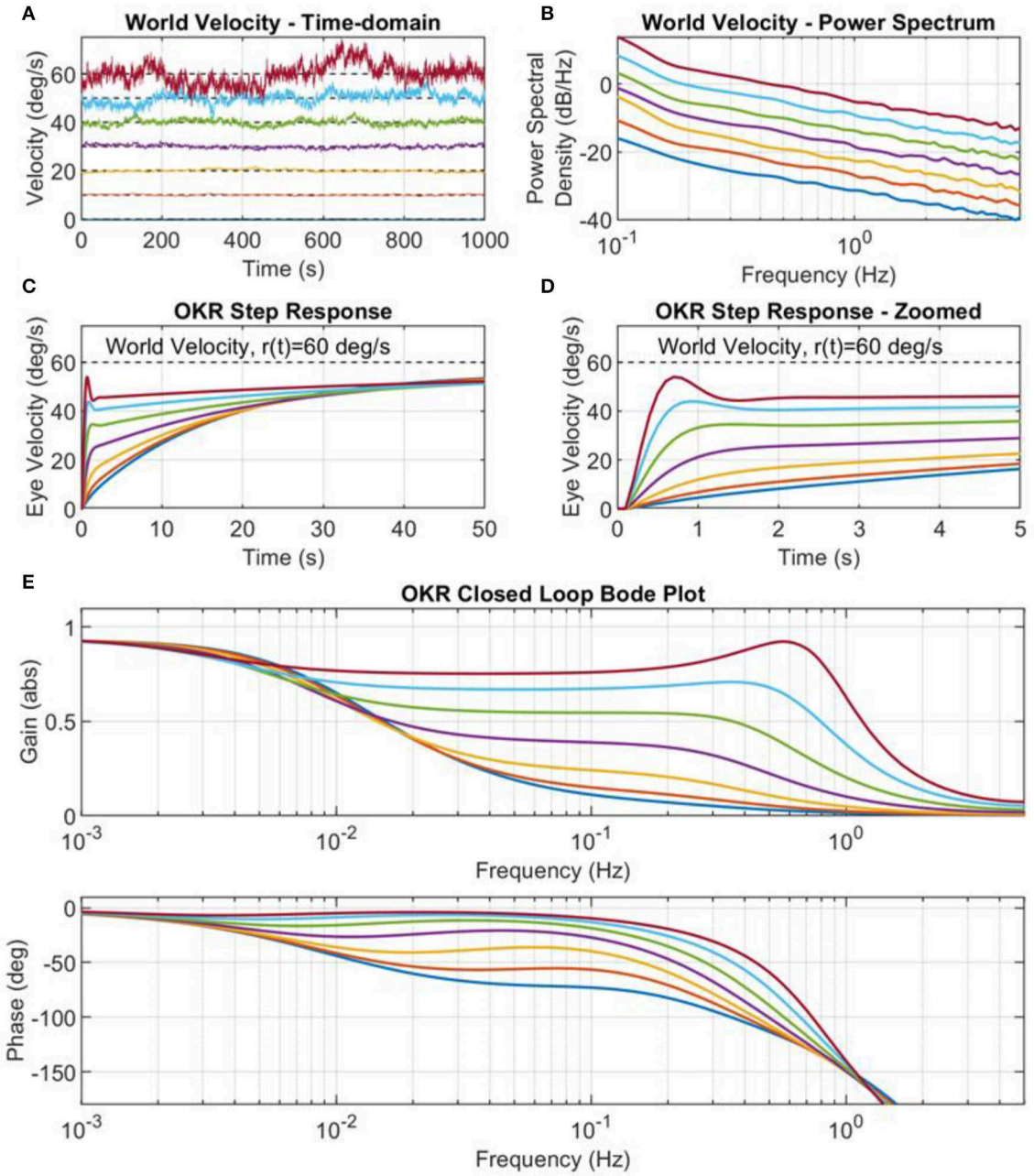

FIGURE 6 | World velocity colored noise statistics drives adaptation of the cerebellar filter. **(A)** Examples of world velocity colored noise signals used to drive adaptation of the cerebellar filter in the OKR control loop (note that each signal is successively offset for plotting by 10 deg/s for clarity, and that each signal had zero mean). Each signal has the same spectral exponent $a = 1.2$, but different scaling parameters b. The power spectrum scaling parameters, b, were obtained from testing 10 values log-spaced in the amplitude range $k_b \in [0.01, 0.1]$, where $b = k_b^2$, but only the results from values two to eight are shown here, i.e., where b values were set to 0.0003, 0.0008, 0.0022, 0.0060, 0.0167, 0.0464, 0.1292. **(B)** Power spectrum of the world velocity signals shown in **(A)**. **(C)** Step response of the closed loop OKR system after 2,000 batches of cerebellar training updates. **(D)** Step response of the closed loop OKR system after 2,000 batches of cerebellar training updates, zoomed on the time axis. **(E)** OKR closed loop Bode plots corresponding to the OKR step responses in **(C,D)**.

behavior involved swimming in the direction of translational optic flow, thereby stabilizing the fish's position in the presence of water currents. Motor output rapidly adapted to changes in visual input. This behavior was accompanied by neural activity in multiple brain regions including the cerebellum and inferior olive, and its adaptation prevented by lesions of the inferior olive. Portugues et al. (2014) subsequently extended this investigation to whole-brain mapping of the networks involved

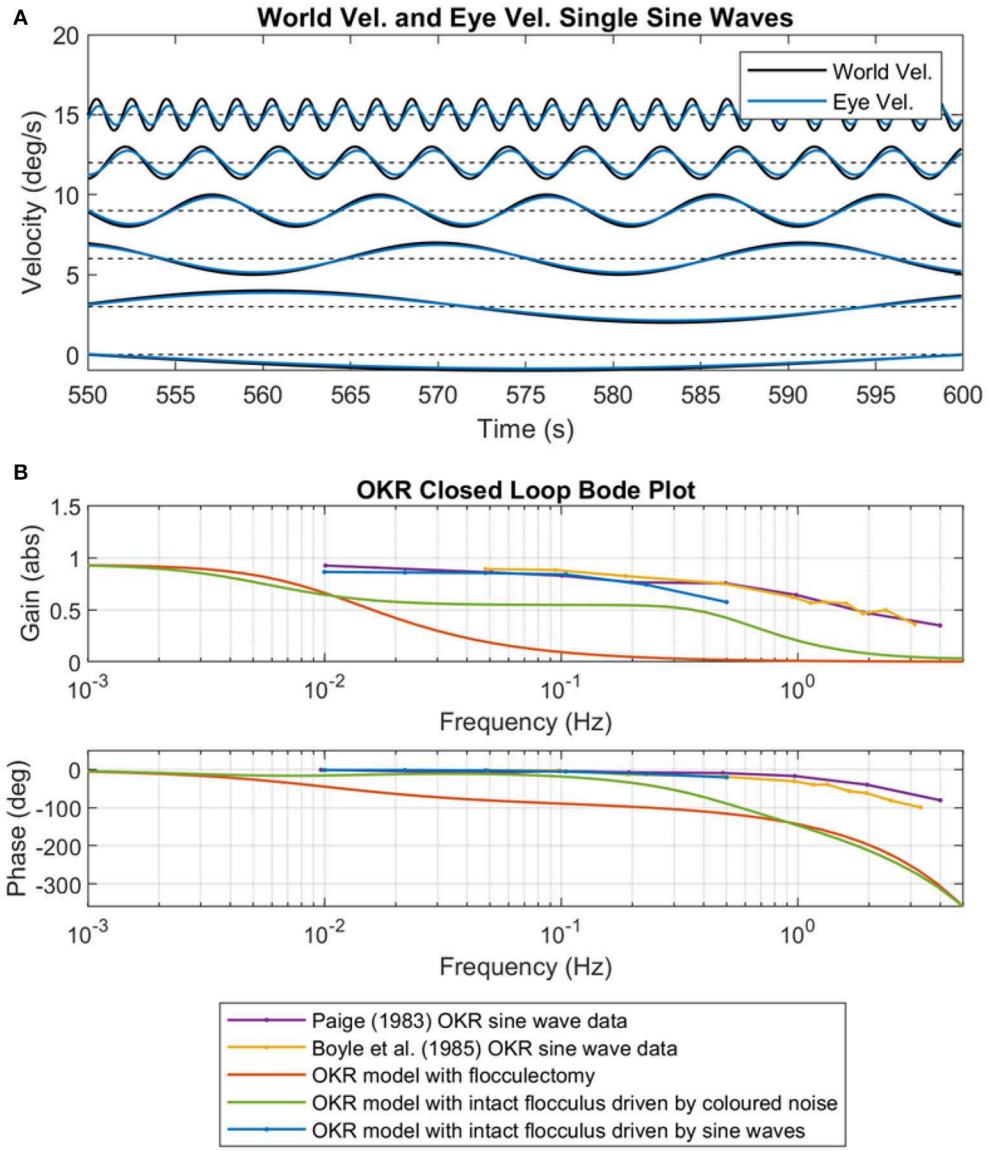

FIGURE 7 | OKR performance after training on predictable and non-predictable signals. **(A)** Predictable sine waves signals (frequencies were six log-spaced values from 0.01 to 0.5 Hz) used as the world velocity signal to excite the OKR control loop. Also shown are the corresponding eye velocity output signals after cerebellar adaptation, from 600 s of online training (non-batch), zoomed to the final 50 s of adaptation. **(B)** OKR closed loop Bode plots from OKR sinusoidal experimental data (Paige, 1983; Boyle et al., 1985), the original OKR flocculectomy model from this paper, the OKR model with intact cerebellum, and the Bode plot reconstructed from the individual sinusoidal excitations shown in **(A)**.

in rotational OKR, as modeled here. The circuits discovered resemble those described in mammals, include the cerebellum, and show little variation between individual fish. These studies suggest that the larval zebrafish's small and transparent brain offers the opportunity of further investigating the basic circuitry underlying OKR adaptation, and of exploring the neural mechanisms underlying the effects of stimulus predictability and the formation of internal models.

Summary

We have developed an adaptive model of the OKR based on the adaptive filter representation of cerebellar cortex proposed by Fujita (1982). The model demonstrates how the cerebellum improves the disturbance rejection characteristics in this exemplar problem of an adaptive feedback control task. The model describes behavioral data, specifically the step response of the OKR in primate. Our results have shown that the adaptation of the OKR is extremely sensitive to the world velocity signal used to excite the OKR feedback control loop. When the world velocity signal is a predictable single frequency sine wave the feedback control performance is much improved compared to an unpredictable colored noise signal. Finally, the nature of the world statistics were shown to be crucial in driving adaptation of the cerebellar

model to an OKR loop that described experimental step response data.

DATA AVAILABILITY STATEMENT

The datasets generated for this study are available on request to the corresponding author.

AUTHOR CONTRIBUTIONS

SA implemented the computational simulations, analyzed the results, and co-wrote the manuscript. JP conceived the work and helped implement the computational simulations. PD conceived the work and co-wrote the manuscript.

REFERENCES

Ahrens, M. B., Li, J. M., Orger, M. B., Robson, D. N., Schier, A. F., Engert, F., et al. (2012). Brain-wide neuronal dynamics during motor adaptation in zebrafish. *Nature* 485, 471–477. doi: 10.1038/nature11057

Anderson, S. R., Lepora, N. F., Porrill, J., and Dean, P. (2010). Nonlinear dynamic modelling of isometric force production in primate eye muscle. *IEEE Trans. Biomed. Eng.* 57, 1554–1567. doi: 10.1109/TBME.2010.2044574

Anderson, S. R., Porrill, J., Pearson, M. J., Pipe, A. G., Prescott, T. J., and Dean, P. (2012). An internal model architecture for novelty detection: implications for cerebellar and collicular roles in sensory processing. *PLoS ONE* 7:e44560. doi: 10.1371/journal.pone.0044560

Boyle, R., Büttner, U., and Markert, G. (1985). Vestibular nuclei activity and eye movements in the alert monkey during sinusoidal optokinetic stimulation. *Exp. Brain Res.* 57, 362–369. doi: 10.1007/bf00236542

Buizza, A., and Schmid, R. (1982). Visual-vestibular interaction in the control of eye movement: mathematical modelling and computer simulation. *Biol. Cybern.* 43, 209–223. doi: 10.1007/bf00319980

Büttner-ennever, J. A. (2006). The extraocular motor nuclei: organization and functional neuroanatomy. *Prog. Brain Res.* 151, 95–125. doi: 10.1016/S0079-6123(05)51004-5

Carpenter, R. H. S. (1988). *Movements of the Eyes,* London: Pion.

Carriot, J., Jamali, M., Chacron, M. J., and Cullen, K. E. (2017). The statistics of the vestibular input experienced during natural self-motion differ between rodents and primates. *J. Physiol.* 595, 2751–2766. doi: 10.1113/JP273734

Coesmans, M., Weber, J. T., de Zeeuw, C. I., and Hansel, C. (2004). Bidirectional parallel fiber plasticity in the cerebellum under climbing fiber control. *Neuron* 44, 691–700. doi: 10.1016/j.neuron.2004.10.031

Collewijn, H. (1969). Optokinetic eye movements in the rabbit: input-output relations. *Vis. Res.* 9, 117–132. doi: 10.1016/0042-6989(69)90035-2

Collewijn, H. (1972). An analog model of the rabbit's optokinetic system. *Brain Res.* 36, 71–88. doi: 10.1016/0006-8993(72)90767-6

Dean, P., and Porrill, J. (2010). The cerebellum as an adaptive filter: a general model? *Funct. Neurol.* 25, 173–1180.

Dean, P., Porrill, J., Ekerot, C. F., and Jörntell, H. (2010). The cerebellar microcircuit as an adaptive filter: experimental and computational evidence. *Nat. Rev. Neurosci.* 11, 30–43. doi: 10.1038/nrn2756

Deno, D. C., Keller, E. L., and Crandall, W. F. (1989). Dynamical neural network organization of the visual pursuit system. *IEEE Trans. Biomed. Eng.* 36, 85–92. doi: 10.1109/10.16451

Fuchs, A. F., and Mustari, M. J. (1993). "The optokinetic response in primates and its possible neuronal substrate," in *Visual Motion and Its Role in the Stabilization of Gaze,* eds F. A. Miles and J. Wallmann (Amsterdam: Elsevier), 343–369.

Fujita, M. (1982). Adaptive filter model of the cerebellum. *Biol. Cybern.* 45, 195–206. doi: 10.1007/BF00336192

Gillis, P., Godaux, E., Beaufays, J., and Henri, V. P. (1984). The optokinetic reflex in the cat: modeling and computer simulation. *Biol. Cybern.* 50, 135–141. doi: 10.1007/bf00337160

Godaux, E., and Vanderkelen, B. (1984). Vestibulo-ocular reflex, optokinetic response and their interactions in the cerebellectomized cat. *J. Physiol.* 346, 155–170. doi: 10.1113/jphysiol.1984.sp015013

Inagaki, K., and Hirata, Y. (2017). Computational theory underlying acute vestibulo-ocular reflex motor learning with cerebellar long-term depression and long-term potentiation. *Cerebellum* 16, 827–839. doi: 10.1007/s12311-017-0857-6

Inoshita, T., and Hirano, T. (2018). Occurrence of long-term depression in the cerebellar flocculus during adaptation of optokinetic response. *Elife* 7:e36209. doi: 10.7554/eLife.36209

Ito, M. (1970). Neurophysiological aspects of the cerebellar motor control system. *Int J Neurol.* 7, 162–176.

Ito, M. (1989). Long-term depression. *Annu. Rev. Neurosci.* 12, 85–102. doi: 10.1146/annurev.ne.12.030189.000505

Ito, M. (1997). Cerebellar microcomplexes. *Int. Rev. Neurobiol.* 41, 475–487. doi: 10.1016/S0074-7742(08)60366-9

Kettner, R. E., Mahamud, S., Leung, H. C., Sitkoff, N., Houk, J. C., Peterson, B. W., et al. (1997). Prediction of complex two-dimensional trajectories by a cerebellar model of smooth pursuit eye movement. *J. Neurophysiol.* 77, 2115–2130. doi: 10.1152/jn.1997.77.4.2115

Luque, N. R., Naveros, F., Carrillo, R. R., Ros, E., and Arleo, A. (2019). Spike burst-pause dynamics of Purkinje cells regulate sensorimotor adaptation. *PLoS Comput. Biol.* 15:e1006298. doi: 10.1371/journal.pcbi.1006298

Miall, R. C., Weir, D. J., Wolpert, D. M., and Stein, J. F. (1993). Is the cerebellum a Smith predictor? *J. Mot. Behav.* 25, 203–216. doi: 10.1080/00222895.1993.9942050

Miki, S., Baker, R., and Hirata, Y. (2018). Cerebellar role in predictive control of eye velocity initiation and termination. *J. Neurosci.* 38, 10371–10383. doi: 10.1523/JNEUROSCI.1375-18.2018

Mustari, M. J., Fuchs, A. F., Kaneko, C. R., and Robinson, F. R. (1994). Anatomical connections of the primate pretectal nucleus of the optic tract. *J. Comp. Neurol.* 349, 111–128. doi: 10.1002/cne.903490108

Paige, G. D. (1983). Vestibulo-ocular reflex and its interaction with visual following mechanisms in the squirrel monkey. I. response characteristics in normal animals. *J. Neurophysiol.* 49, 134–151. doi: 10.1152/jn.1983.49.1.134

Porrill, J., Dean, P., and Anderson, S. R. (2013). Adaptive filters and internal models: multilevel description of cerebellar function. *Neural Netw.* 47, 134–149. doi: 10.1016/j.neunet.2012.12.005

Portugues, R., Feierstein, C. E., Engert, F., and Orger, M. B. (2014). Whole-brain activity maps reveal stereotyped, distributed networks for visuomotor behavior. *Neuron* 81, 1328–1343. doi: 10.1016/j.neuron.2014.01.019

Robinson, D. A. (1977). "Vestibular and optokinetic symbiosis: an example of explaining by modelling," in *Control of Gaze by Brain Stem Neurons,* eds A. Baker and R. Berthoz (Amsterdam: Elsevier/North Holland), 49–58.

Robinson, D. A. (1986). Is the oculomotor system a cartoon of motor control. *Prog. Brain Res.* 64, 411–417. doi: 10.1016/S0079-6123(08)63435-4

Robinson, D. A. (1987). "Why visuomotor systems don't like negative feedback and how they avoid it," in *Vision, Brain and Cooperative Computation,* ed M. A. H. A. Arbib (Cambridge, MA: MIT Press), 89–107.

Robinson, D. A., Gordon, J. L., and Gordon, S. E. (1986). A model of the smooth pursuit eye movement system. *Biol. Cybern.* 55, 43–57. doi: 10.1007/bf00363977

Schweigart, G., Mergner, T., Evdokimidis, I., Morand, S., and Becker, W. (1997). Gaze stabilization by optokinetic reflex (OKR) and vestibulo- ocular reflex (VOR) during active head rotation in man. *Vis. Res.* 37, 1643–1652. doi: 10.1016/s0042-6989(96)00315-x

Sejnowski, T. J. (1977). Storing covariance with nonlinearly interacting neurons. *J. Math. Biol.* 4, 303–321. doi: 10.1007/BF00275079

St.-Cyr, G. J., and Fender, D. H. (1969). Nonlinearities of the human oculomotor system: time delays. *Vis. Res.* 9, 1491–1503. doi: 10.1016/0042-6989(69)90065-0

Suvrathan, A., Payne, H. L., and Raymond, J. L. (2016). Timing rules for synaptic plasticity matched to behavioral function. *Neuron* 92, 959–967. doi: 10.1016/j.neuron.2016.10.022

Suvrathan, A., and Raymond, J. L. (2018). Depressed by learning - heterogeneity of the plasticity rules at parallel fiber synapses onto Purkinje cells. *Cerebellum* 17, 747–755. doi: 10.1007/s12311-018-0968-8

Vaudrey, M. A., Baumann, W. T., and Saunders, W. R. (2003). Stability and operating constraints of adaptive LMS-based feedback control. *Automatica* 39, 595–605. doi: 10.1016/S0005-1098(02)00288-1

Voges, K., Wu, B., Post, L., Schonewille, M., and de Zeeuw, C. I. (2017). Mechanisms underlying vestibulo-cerebellar motor learning in mice depend on movement direction. *J. Physiol.* 595, 5301–5326. doi: 10.1113/JP274346

Voogd, J., and Barmack, N. H. (2006). Oculomotor cerebellum. *Prog. Brain Res.* 151, 231–268. doi: 10.1016/S0079-6123(05)51008-2

Waespe, W., Cohen, B., and Raphan, T. (1983). Role of the flocculus and paraflocculus in optokinetic nystagmus and visual-vestibular interactions: effects of lesions. *Exp. Brain Res.* 50, 9–33. doi: 10.1007/BF00238229

Waespe, W., and Henn, V. (1987). Gaze stabilization in the primate: the interaction of the vestibulo-ocular reflex, optokinetic nystagmus, and smooth pursuit. *Rev. Physiol. Biochem. Pharmacol.* 106, 37–125. doi: 10.1007/BFb0027575

Wang, S. S., Denk, W., and Häusser, M. (2000). Coincidence detection in single dendritic spines mediated by calcium release. *Nat. Neurosci.* 3, 1266–1273. doi: 10.1038/81792

Wolpert, D. M., Miall, R. C., and Kawato, M. (1998). Internal models in the cerebellum. *Trends Cogn. Sci.* 2, 338–347. doi: 10.1016/S1364-6613(98)01221-2

Wyatt, H. J., and Pola, J. (1988). Predictive behavior of optokinetic eye movements. *Exp. Brain Res.* 73, 615–626. doi: 10.1007/BF00406621

Yamamoto, K., Kobayashi, Y., Takemura, A., Kawano, K., and Kawato, M. (2002). Computational studies on acquisition and adaptation of ocular following responses based on cerebellar synaptic plasticity. *J. Neurophysiol.* 87, 1554–1571. doi: 10.1152/jn.00166.2001

Yasui, S., and Young, L. R. (1984). On the predictive control of foveal eye tracking and slow phases of optokinetic and vestibular-nystagmus. *J. Physiol.* 347, 17–33. doi: 10.1113/jphysiol.1984.sp015050

Young, L. R. (1971). "Pursuit eye tracking movements," in *Control of Eye Movements,* eds P. Bach-y-Rita, C. C. Collins, and J. E. Hyde (New York, NY: Academic Press), 429–443.

Conflict of Interest: The authors declare that the research was conducted in the absence of any commercial or financial relationships that could be construed as a potential conflict of interest.

frontiers in Systems Neuroscience

REVIEW
published: 09 April 2020
doi: 10.3389/fnsys.2020.00019

The Cerebro-Cerebellum as a Locus of Forward Model: A Review

Hirokazu Tanaka[1], *Takahiro Ishikawa*[2], *Jongho Lee*[3] *and Shinji Kakei*[2]*

[1]Japan Advanced Institute of Science and Technology, Nomi, Japan, [2]Tokyo Metropolitan Institute of Medical Science, Tokyo, Japan, [3]Komatsu University, Komatsu, Japan

This review surveys physiological, behavioral, and morphological evidence converging to the view of the cerebro-cerebellum as loci of internal forward models. The cerebro-cerebellum, the phylogenetically newest expansion in the cerebellum, receives convergent inputs from cortical, subcortical, and spinal sources, and is thought to perform the predictive computation for both motor control, motor learning, and cognitive functions. This predictive computation is known as an internal forward model. First, we elucidate the theoretical foundations of an internal forward model and its role in motor control and motor learning within the framework of the optimal feedback control model. Then, we discuss a neural mechanism that generates various patterns of outputs from the cerebro-cerebellum. Three lines of supporting evidence for the internal-forward-model hypothesis are presented in detail. First, we provide physiological evidence that the cerebellar outputs (activities of dentate nucleus cells) are predictive for the cerebellar inputs [activities of mossy fibers (MFs)]. Second, we provide behavioral evidence that a component of movement kinematics is predictive for target motion in control subjects but lags behind a target motion in patients with cerebellar ataxia. Third, we provide morphological evidence that the cerebellar cortex and the dentate nucleus receive separate MF projections, a prerequisite for optimal estimation. Finally, we speculate that the predictive computation in the cerebro-cerebellum could be deployed to not only motor control but also to non-motor, cognitive functions. This review concludes that the predictive computation of the internal forward model is the unifying algorithmic principle for understanding diverse functions played by the cerebro-cerebellum.

Keywords: cerebral cortex, cerebellar circuitry, forward model, motor function, higher brain function, neural networks

OPEN ACCESS

Edited by:
Richard Apps,
University of Bristol, United Kingdom

Reviewed by:
R. Chris Miall,
University of Birmingham, United Kingdom
Jeffery Allen Boychuk,
The University of Texas Health Science Center at San Antonio, United States

***Correspondence:**
Shinji Kakei
kakei-sj@igakuken.or.jp

Received: *11 November 2019*
Accepted: *20 March 2020*
Published: *09 April 2020*

Citation:
Tanaka H, Ishikawa T, Lee J and Kakei S (2020) The Cerebro-Cerebellum as a Locus of Forward Model: A Review. Front. Syst. Neurosci. 14:19. doi: 10.3389/fnsys.2020.00019

INTRODUCTION

The cerebellum has developed in the sensory domain of the central nervous system (CNS) as evidenced by the fact that it has emerged in the alar plate (i.e., the sensory part (dorsal half) of the neural tube of the rhombencephalon of primitive jawless vertebrate such as myxinoids (hagfish) or petromyzonts (lampreys; Larsell, 1967; Sugahara et al., 2016). The cerebellum is hence ideally located to accommodate multimodal sensory inputs (Larsell, 1967) including both exteroceptive (lateral-line, vestibular, acoustic, visual) and interoceptive (somatosensory) inputs, thereby functioning as the hub of sensory integration. In addition to sensory inputs, the mammalian cerebellum receives inputs from cortical areas including sensory, motor, and association areas

through the pontine nuclei (PN). In humans, the cerebellum is estimated to share no less than 80% of the CNS neurons in no more than 10% of the brain volume (Herculano-Houzel, 2009). To summarize, the cerebellum has been, throughout its long phylogenetic history, the unique hub in the CNS to accommodate and integrate both afferent and efferent inputs from almost the entire brain, a prerequisite for a neural substrate for adaptive and flexible behaviors.

The cerebellum is homogenous in its local neural circuity and heterogeneous in its input-output organization (Ito, 1984). The local neural circuitry of the cerebellar cortex is characterized by its superb homogeneity, sometimes expressed as being "crystal-like," whereas the inputs to and the outputs from the cerebellum are heterogeneous from one region to another. Therefore, it is commonly postulated that the functional diversity of the cerebellum originates from heterogeneous input-output connectivity and is processed through a common algorithm that is implemented in the homogenous neural circuitry in the cerebellar cortex. In light of Marr's three levels of analysis, the cerebellum may perform common computation on diversified representations of cerebellar inputs and outputs. Therefore, the cerebellum may be better understood if we ask "how the cerebellum computes" than "what the cerebellum computes." In contrast to previous studies that have focused on neural representations of an internal forward model, we explored how the cerebellum transforms its inputs [mossy fibers (MFs)] to its outputs [dentate nucleus cells (DNCs); Tanaka et al., 2019]. Given the postulate that the cerebellum may process a common algorithm, the main goal of this review is to comprehend the physiology and pathology of different regions of the cerebellum on a common ground of the algorithm (Diedrichsen et al., 2019).

Among a range of proposals for the cerebellar algorithm including timing processing (Ivry et al., 2002; Ivry and Spencer, 2004) and temporal pattern generator (Fujita, 1982; Dean et al., 2010), one plausible candidate is the prediction of sensory outcomes as a consequence of motor action, referred to as the computation of an internal forward model (Jordan and Rumelhart, 1992; Wolpert and Miall, 1996; Bastian, 2006; Ishikawa et al., 2016). The predictive computation of the internal forward model plays a key role in predicting outcomes of self-action, fast and stable motor control, integrating the prediction with sensory feedback, and adaptation to a novel environment. This review article provides physiological, behavioral, and morphological evidence that converges to the cerebro-cerebellum as a neural substrate of the internal forward model. In particular, we introduce neural evidence that current outputs from the cerebellum [i.e., outputs from the dentate nucleus (DN)] can predict future inputs to the cerebellum (i.e., cortical outputs relayed by MFs originated from PN), a hallmark of an internal forward model. We will also discuss how the input-output organization of the cerebro-cerebellum may contribute to forward models for higher (i.e., non-motor) brain functions.

This article is organized as follows. Section "Predictive Computation of Internal Forward Model" begins by defining the computation of the internal forward model, discusses its multiple functions in a computation model of motor control and motor adaptation, and reviews experimental evidence for the cerebellum as a locus of an internal forward model. Whereas the topic of internal models has been reviewed previously in the existing literature, this section emphasizes background information for facilitating the following discussions. In particular, we emphasize multiple computational roles that an internal forward model can play. Section "Generation of Outputs From the Cerebro-Cerebellum" delves into a physiological mechanism to generate a wide range of output from DN by modulating the inhibitory inputs from Purkinje cells (PCs). Section "Functional Evidence for Cerebellar Forward Model" summarizes neural and behavioral evidence that the cerebellum performs predictive computation. Section "Anatomical Structure Supporting for Cerebellar Forward Models" surveys anatomical structures of the cerebro-cerebellum that potentially scaffold the forward-model computation. Section "Cognitive Functions and Cerebellar Forward Models" branches out to speculate a possible role of the cerebro-cerebellum in higher cognitive functions from the viewpoint of the internal forward model. Finally, Section "Remaining Issues About Cerebellar Internal Models" concludes the internal-model hypothesis of the cerebellum and enumerates unresolved issues toward the goal of understanding the cerebro-cerebellum.

PREDICTIVE COMPUTATION OF INTERNAL FORWARD MODEL

Internal Forward Model and its Computational Roles

One critical problem in biological motor control is that afferent sensory signals have inevitable temporal delays in reaching the central nervous system. In other words, the brain always observes "the past" of its own body and environments. Visual signals, for example, arrive at the primary visual cortex about 30 ms later and at the parietal cortex about 80 ms later than an onset of a visual stimulus (Schmolesky et al., 1998). Delays in sensory feedback originate from several factors, as quantified in locomotor reflex movements in terrestrial animals of various sizes (More et al., 2010; More and Donelan, 2018). Among factors contributing to the feedback delay such as a synaptic delay or an electro-mechanical delay, the dominant factor is the nerve conduction delay, ranging about 10 ms for a shrew to about 100 ms for an elephant. Larger animals experience a longer feedback delay yet move more slowly, whereas smaller animals experience a shorter feedback delay but move more quickly. In sum, sensory delays are comparable to typical time scales of rapid movements and hence not negligible both in small and large animals.

The delay in sensory feedback is problematic not only in sensing the body and the environments but also in controlling the body. It is well known in control engineering that feedback control based on a previous state causes oscillatory and unstable movements if the delay in feedback control is of the order of or larger than a time constant of a controlled plant (Wolpert and Miall, 1996). The delays in visual feedback are comparable to the

movement time of rapid reaching movement of the upper limb (about a few hundred milliseconds) and saccadic eye movements (typically less than fifty milliseconds). Therefore, in biological motor control, feedback control based on delayed sensory signals would result in unstable movements. Nonetheless, animals can perform a fast movement without losing its stability. Biological motor control must be equipped with a mechanism to compensate for the sensory delay for a fast and stable movement.

One mechanism proposed to cope with the delay in sensory feedback is to compute a future state of the body based on a current estimate of the body and an efferent signal of motor control (**Figure 1A**). This predictive computation internally emulates or models an actual movement of the body by essentially solving an equation of motion of the body forward in time, thereby known as an internal forward model (Wolpert et al., 1998; McNamee and Wolpert, 2019). An internal forward model predicts the state of the body time by time that is then used by a feedback controller, thereby allowing fast and stable movements. The feedback control based on the prediction of the internal forward model is called internal feedback. There are lines of evidence supporting the hypothesis of predictive forward model and internal feedback from neuroimaging studies (Heinks-Maldonado et al., 2006; Bäss et al., 2008), non-invasive stimulation studies (Miall et al., 2007; Lesage et al., 2012), and psychophysics studies (Lang and Bastian, 1999; Nowak et al., 2004, 2007) in human.

An internal forward model plays a role not only in online control but also in motor learning (Sokolov et al., 2017). In addition to delay compensation, the computation of state prediction has been proposed to serve motor control for cancellation of sensory effects of movements (Blakemore et al., 1998), the transformation between sensory errors and motor errors (Jordan and Rumelhart, 1992), and mental practice for a selection among possible actions (Gentili et al., 2006). A predicted consequence of a movement is to be compared with the actual consequence of that movement, referred to as a prediction error. Note that the prediction error differs from a target error, which is a difference between the target and the actual reaching point. A clever experiment revealed that the prediction error, but not the target error, drives motor adaptation in a visuomotor rotation experiment by dissociating a prediction error from a target error (Mazzoni and Krakauer, 2006). In this experiment, subjects were instructed that a movement of the cursor on the display was rotated counter-clockwise from movement directions of the hand and that they should aim an adjacent target (or intended target) located clockwise from a target of the task (or task target) to intentionally cancel the imposed counter-clockwise rotation. In this design, the predicted outcome of movement was the adjacent target. Therefore, the target error was the difference between the task target and actual movement, while the prediction error was the difference between the intended target and actual movement. By strategically aiming at the adjacent target, the target error was null. A surprising finding was that the target error increased in subsequent trials even when the target error was almost null, indicating that the prediction error, not the target error, drove the adaptation to visuomotor rotation. Intriguingly, similar prediction-based learning algorithms have been also proposed in reinforcement learning where a reward drives a learning process (Barto et al., 1983). There, a reward prediction error (i.e., an actual reward minus an expected reward) but not a reward itself plays a critical role in driving learning processes. In sum, the brain predicts a consequence of its action, compares the prediction with an actual consequence, and improves the next action both in error-based motor learning and reward-based reinforcement learning (Shadmehr et al., 2010).

A less well-known but equally important function of an internal forward model is its role in the computation of gains in feedback control and Kalman filtering. In addition to the predictive computation reviewed above, the forward model is required for the computation of gain matrices both for the feedback controller and Kalman filtering. The optimal feedback control (OFC) model provides a unified framework that integrates diverse computational processes in motor control and motor learning such as the internal forward model, Kalman filter, and feedback control (Todorov and Jordan, 2002; Todorov, 2004). In the OFC model, the cost function (typically expected movement error plus control cost) is optimized so that a task goal is achieved with a minimum energy. There, the state of the body is not directly observable but must be estimated from sensory feedback signals, and the feedback controller is driven by the estimated state. Therefore, the OFC model naturally incorporates the predictive computation of the internal forward model.

The core element in the OFC model is the computation of two gain matrices (Kalman gain and feedback gain matrices). First, the Kalman filter is a recursive method to estimate the current state that integrates a predicted state from an internal forward model and sensory afferents. An optimal estimator is a weighted sum of a predicted state and sensory afferents determined by Kalman gain according to their relative accuracies (or variances). The computation of Kalman gain requires the accuracy of a predicted state from an internal forward model for the optimal tradeoff. Second, the optimally estimated state propels the feedback controller to generate appropriate motor commands, which is a product of the estimated state and the feedback gain matrix. Here, the computation of the feedback gain matrix requires information about the body dynamics and the control cost so that the body is guided to achieve the task goal with a minimum amount of energy. Again, the internal forward model contributes to the computation of feedback gain. Accordingly, the computation of gain matrices in the OFC model necessitates the knowledge of dynamics implemented in an internal forward model.

To summarize, an internal forward model plays at least the three key roles in motor control and motor learning: (1) state prediction for compensating the delay in sensory feedback in online motor control; (2) state prediction for computing a prediction error between a predicted outcome and an actual outcome in motor learning; and (3) computation of Kalman gain and feedback gain. Theoretically speaking, it is possible that these roles are solved collectively by a single, unified forward model or separately by multiple, distributed forward models. Convergent

lines of evidence suggest that the cerebellum is a neural correlate of an internal forward model, as discussed below.

Previous Evidence for Cerebellar Forward Model in the Cerebellum

An internal forward model contributes not only to state prediction for a fast movement but also to the computation of prediction error for motor learning and of gain matrices for the OFC model. A wide range of previous studies converge to the cerebellum processes as the loci of internal forward models (Nowak et al., 2004; Bastian, 2006; Morton and Bastian, 2006; Nowak et al., 2007; Tseng et al., 2007; Lesage et al., 2012). The internal-forward-model hypothesis of the cerebellum indicates that the delayed state and control signal in **Figure 1A** corresponds to the MFs in **Figure 1B** and that the predicted state in **Figure 1A** corresponds to the DNCs in **Figure 1B**. The cerebellar circuit is characterized by two specific features (**Figure 1B**): (1) the mostly feedforward connectivity from MFs as an input to DN as an output; and (2) the expansion from MFs (input to the cerebellum) to granule cells (GCs; input to the cerebellar cortex) and the compression from MFs to DNCs (output from the cerebellum). A possible computational role of the expansion coding in GCs is reviewed in Sanger et al. (2020). Given the multitude of computational functions of the internal forward model, it is not surprising that an impairment of the cerebellum leads to a plethora of motor deficiencies collectively known as cerebellar ataxia (Holmes, 1917). Also, cerebellar patients suffer from an inability in motor adaptation and motor learning (Martin et al., 1996; Smith and Shadmehr, 2005; Morton and Bastian, 2006; Tseng et al., 2007). Therefore, the proper functioning of the cerebellum is required for well-coordinated movements and adaptive motor learning.

Most supporting evidence for the internal-forward-model hypothesis of the cerebellum comes from clinical studies, human neuroimaging and non-invasive stimulation studies (Imamizu et al., 2000; Miall et al., 2007; Ishikawa et al., 2016). These studies are broadly categorized into two aspects of the hypothesis: predictive activities and motor learning. First, predictive activities are diminished or altered when the cerebellum is impaired or suppressed. Nowak et al. (2004, 2007), for example, reported that patients of cerebellar agenesis did not show predictive muscle activities in one hand when catching a ball released by the other hand. Miall et al. (2007) applied transcranial magnetic stimulation to the cerebellum during hand movements and found that the hand trajectories deviated from a target. This deviation of trajectories was interpreted as a temporary disruption of forward-model prediction by the stimulation. Second, motor leaning is deteriorated in cerebellar patients. Martin et al. (1996) reported that motor adaptation to displacement prism was severely diminished in cerebellar patients. More recently, Tseng et al. (2007) reported that cerebellar patients had selective impairment in a rapid adaptive process but retained a slow adaptive process. These deficits in motor prediction and motor leaning are supportive of the internal-forward-model hypothesis of the cerebellum.

GENERATION OF OUTPUTS FROM THE CEREBRO-CEREBELLUM

The DN is the final output station from the cerebro-cerebellum. To contribute to the three roles of an internal forward model mentioned above, DNCs should be able to generate dynamic patterns of output. Our previous study unveiled a simple mechanism to explain a wide range of modulation (i.e., facilitation and suppression) of DNC activity (Ishikawa et al., 2014) and solved the controversy over the generation of burst activity of DNCs before limb movement (Thach, 1970; Strick, 1983; Wetts et al., 1985; Chapman et al., 1986; Fortier et al., 1989; van Kan et al., 1993; Goodkin and Thach, 2003) without a major excitatory drive.

To explain the excitation of DNCs [specifically, deep cerebellar nuclei (dCN) cells], two physiological mechanisms have been proposed. One mechanism is the recruitment of a post-inhibitory rebound excitation (Aizenman and Linden, 1999; Hoebeek et al., 2010; Tadayonnejad et al., 2010; Witter et al., 2013). Another mechanism is the suppression of PCs that facilitates dCN cells by a release from tonic inhibition from PCs, a mechanism known as disinhibition (Albus, 1971; Miyashita and Nagao, 1984; Nagao, 1992; Shinoda et al., 1992; Medina and Mauk, 2000). To address how DNCs become excited or inhibited during voluntary limb movements, we compared the temporal patterns of activity for PCs and DNCs recorded from the same monkeys during step-tracking movements of the wrist (Ishikawa et al., 2014). If the post-inhibitory rebound excitation serves for the facilitation, phasic excitation of PCs and a concomitant inhibition of DNCs should precede the main excitation of DNCs. On the other hand, if the disinhibition serves for the facilitation, we should observe the suppression of PCs and the activation of DNCs at the same timing. We found that (Ishikawa et al., 2014) the majority of PCs in the Cerebro-cerebellum demonstrated suppression before the onset of wrist movements. At the same time, the majority of DNCs were activated without prior suppression. This finding supports the disinhibition mechanism that the movement-related activation of DNCs occurs when they are released from tonic inhibition from PCs.

The proposed mechanism in generating burst activities of DNCs is summarized in **Figure 2**. MF inputs to the cerebellar cortex are relayed by GCs and activate one or both of parallel pathways to PCs. The indirect pathway suppresses PCs *via* inhibitory interneurons (INs; **Figure 2A**) whereas the direct pathway activates PCs directly through parallel fibers (PFs; **Figure 2B**). In this way, the activity of individual DNC is regulated by the summation of inputs through the parallel pathways. In line with our proposal, Dean and Porrill (2010) proposed that the parallel pathways perform in a competitive way to suppress or facilitate the activity of PCs in the cerebellar cortex. Our finding extends their idea to explain the role of the parallel pathways for the generation of dynamic output from DN (Ishikawa et al., 2014). Overall, in our population of PCs, movement-related suppression of simple spike (SS) activity dominates before movement onset and contributes to the initiation of movement, while movement-related facilitation

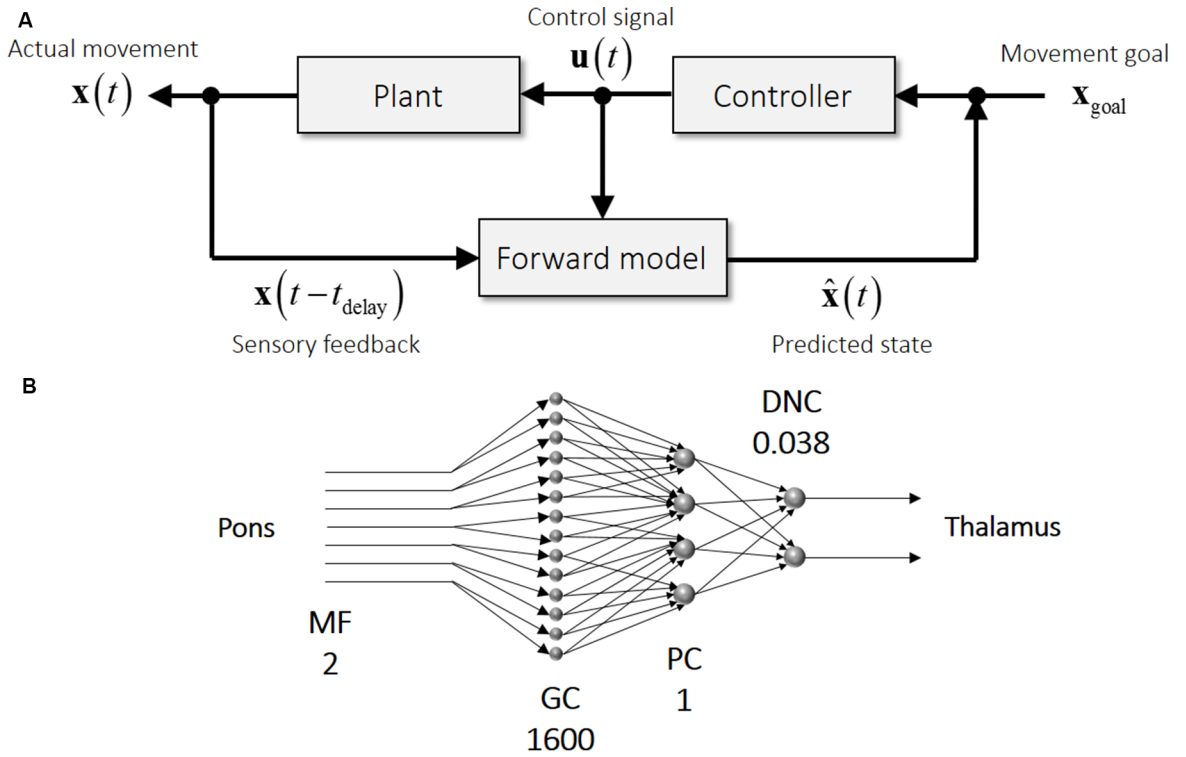

FIGURE 1 | Schematics of motor control and the cerebellar circuit. **(A)** An internal forward model receives time-delayed sensory feedback ($\mathbf{x}_{(t\ -\ t\ delay)}$) and efference copy (**u** (t)) and predicts a current state ($\hat{\mathbf{x}}$ (t)) (bottom row). Difference between movement goal ($\mathbf{x}_{goal}$) and predicted state ($\hat{\mathbf{x}}$ (t)) drives a feedback controller to generate a control signal (**u** (t)), which in turn steers the controlled plant (top row). **(B)** Schematics of the neural circuit in the cerebellum from mossy fibers (MFs) to dentate nucleus cells (DNCs). Note that this feedforward circuitry resembles that of an internal forward model, indicating that the cerebellar input representing a time-delayed state is converted into the cerebellar output representing a current state. The numbers accompanied by the cell labels denote the relative numbers of cells in comparison with Purkinje cells (PCs), illustrating the expansion from MFs to granule cells (GCs) and the compression from MFs to DNCs. These numbers were calculated from corresponding numbers listed in Ito (1984).

dominates after movement onset and contributes to termination of movement (see Figures 8A, 9A in Ishikawa et al., 2014).

The differential recruitment of the two pathways is also organized in a spatially congruent manner; activities of DNCs were modulated by activities of PCs with overlapping receptive fields (RFs; Ishikawa et al., 2014). A large proportion of PCs whose somatosensory RFs were found in the distal arm (i.e., around the wrist joint) showed strong suppression before movement onset, whereas the majority of DNCs with the same RFs showed a concurrent burst of activity. In contrast, PCs with RFs in the proximal arm demonstrated a marked and simultaneous increase in activity, while DNCs with the same RFs were strongly suppressed. Our observation suggests that activation of DNCs by disinhibition from PCs facilitates the execution of wrist movement, whereas suppression of the DNCs due to increased PC activity contributes to the stabilization of proximal muscles and improves task performance.

The organization of the parallel pathways of the cerebellar outputs and its spatially congruent recruitment reminds us of two often overlooked clinical signs described by Holmes (i.e., *asthenia* and *adventitiousness*). We proposed that these signs may be caused by malfunctions of the two output modes (Ishikawa et al., 2015). Asthenia represents a failure of the recruitment of muscle activities resulting in delayed initiation and the slow build-up of movement, whereas adventitious movement is sporadic or erratic activation of muscles to be suppressed resulting in instability. Namely, the asthenia and adventitiousness may reflect deficits in the control of the disinhibition and inhibition, and they could be essential building blocks of various ataxic movements (Ishikawa et al., 2015). Overall, the malfunction of the parallel pathways disturbs whatever contribution of the cerebellum by altering the proper input-output organization.

FUNCTIONAL EVIDENCE FOR CEREBELLAR FORWARD MODEL

Neural Evidence for Cerebellar Internal Model

In contrast to the wealth of evidence, it is intriguing that few previous studies hitherto examined the internal-forward-model hypothesis of the cerebellum from electrophysiological data. Of particularly notable is a series of electrophysiological studies recorded from monkeys performing a manual pursuit

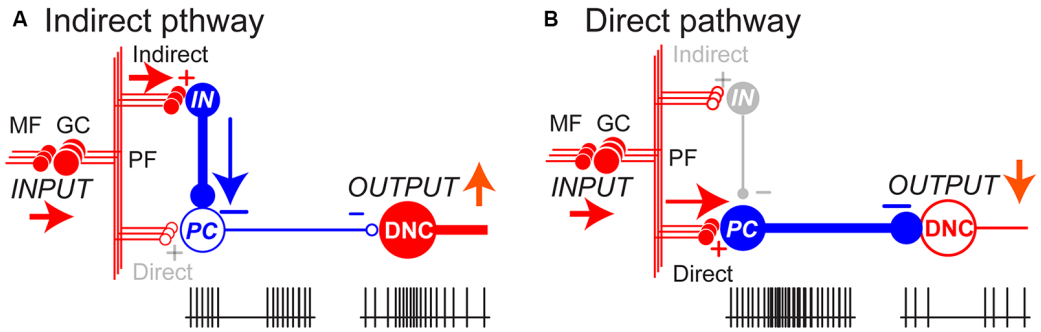

FIGURE 2 | The balance between parallel pathways in the cerebellar cortex determine DNC output. **(A)** In the indirect pathway, the PC activity is suppressed through inhibitory interneurons (IN), which in turn enhances the DNC activity with disinhibition. **(B)** In the direct pathway, PC is activated through excitatory parallel fiber (PF) inputs, which in turn suppresses the DNC activity. The balance between the two pathways determines the final output patterns of individual DNCs. In this way, inhibitory PCs can exert bidirectional effects on DNCs and generate a variety of output patterns. Pluses (+) and minuses (–) represent excitatory and inhibitory synapses, respectively. Adapted from Ishikawa et al. (2014) under CC-BY license.

tracking task (Roitman et al., 2005; Pasalar et al., 2006; Ebner and Pasalar, 2008). Firing rates of SSs of PCs reflected and preceded movement kinematics (hand position and velocity) irrespective of assistive/resistive forces imposed on the hand, supporting that the PCs implement the forward-model computation in the kinematic space. On the other hand, there is another electrophysiological study that contradicts with the internal-forward-model hypothesis. Firing rates of PCs recorded from monkeys performing an elbow flexion/extension task consistently covaried with the level of imposed force, indicating that the PCs represent movement dynamics but not movement kinematics, the findings more consistent with the internal-inverse-model computation (Yamamoto et al., 2007). Therefore, it is yet an open question whether the cerebellum performs the forward-model computation in kinematic space or the inverse-model computation in dynamic space. These studies posit that kinematic and dynamic representations in PCs correspond to a forward model or an inverse model, respectively. But both internal models contain kinematic and dynamic representations, and PCs are not final outputs of the cerebellum. We hence think that examining the coding representation of PCs does not directly address the question about the internal-model hypotheses of the entire cerebellum.

Instead of focusing on a neural representation in single population as in the previous studies, our recent study tackled this problem by examining how neural representations are transformed from one population to another through the cerebellar circuit (Tanaka et al., 2019). The cerebellum has the unique anatomical structure composed of feedforward connectivity particularly suited for the internal-forward-model computation (**Figure 1B**). One natural prediction derived from the hypothesis is that a current output of an internal forward model should contain predictive information about a future input to that internal forward model. If the internal-forward-model hypothesis of the cerebellum holds, current activities of the cerebellar outputs should be able to predict future activities of the cerebellar inputs. Our previous studies reported movement-related modulation of firing rates of MFs, Golgi cells, PCs and DNCs recorded from monkeys performing step-track wrist movements (Ishikawa et al., 2014; Tomatsu et al., 2016). Specifically, we analyzed the firing rates of 94 MFs, 83 PCs, and 73 DNCs (Tanaka et al., 2019).

We first addressed how the firing cells of PCs were driven by the firing rates of MFs. A linear weighted sum of MF firing rates reconstructed PC firing rates most parsimoniously, in comparison with a thresholding model, a quadratic model or an FIR model. The successful reconstruction by the linear model was unanticipated given the fact that a PC receives an estimated 10^5 PF inputs whereas our linear reconstruction included only 94 MF inputs per PC. This was probably because all recorded cells were task-related whose activities were modulated by the movement task, and we surmise that only a few dozens of MFs contributed significantly to the task-related firing rates of PCs. Similarly, we found that the firing rates of DNCs were also well reconstructed as a weighted linear sum of MFs and PCs. Dominant computational models of the cerebellar cortex posit more complex processes; the perceptron model assumes nonlinear thresholding at PCs (Marr, 1969; Albus, 1971), and the adaptive filter model assumes a dependence of PC firing rates on current and previous MF firing rates (Fujita, 1982; Dean et al., 2010). Our analysis, on the other hand, implies that the cerebellar computation is rather linear, markedly simpler than previously thought.

We then proceeded to directly test the internal-forward-model hypothesis by examining whether the cerebellar output could predict the cerebellar input in the future. Following the linear reconstructions of PC and DNC firing rates, the MF firing rates at time $t+t_1$ were predicted as a linear weighted sum of the DNC firing rates at time t. We found that the linear prediction of MF firing rates was statistically significant when compared to directionally randomized surrogate data. This analysis suggests that the current output from the cerebellum (DNC firing rates at time t) contained predictive information about the future input to the cerebellum (MF firing rates at time $t+t_1$), which in turn supports the internal-forward-model hypothesis of the

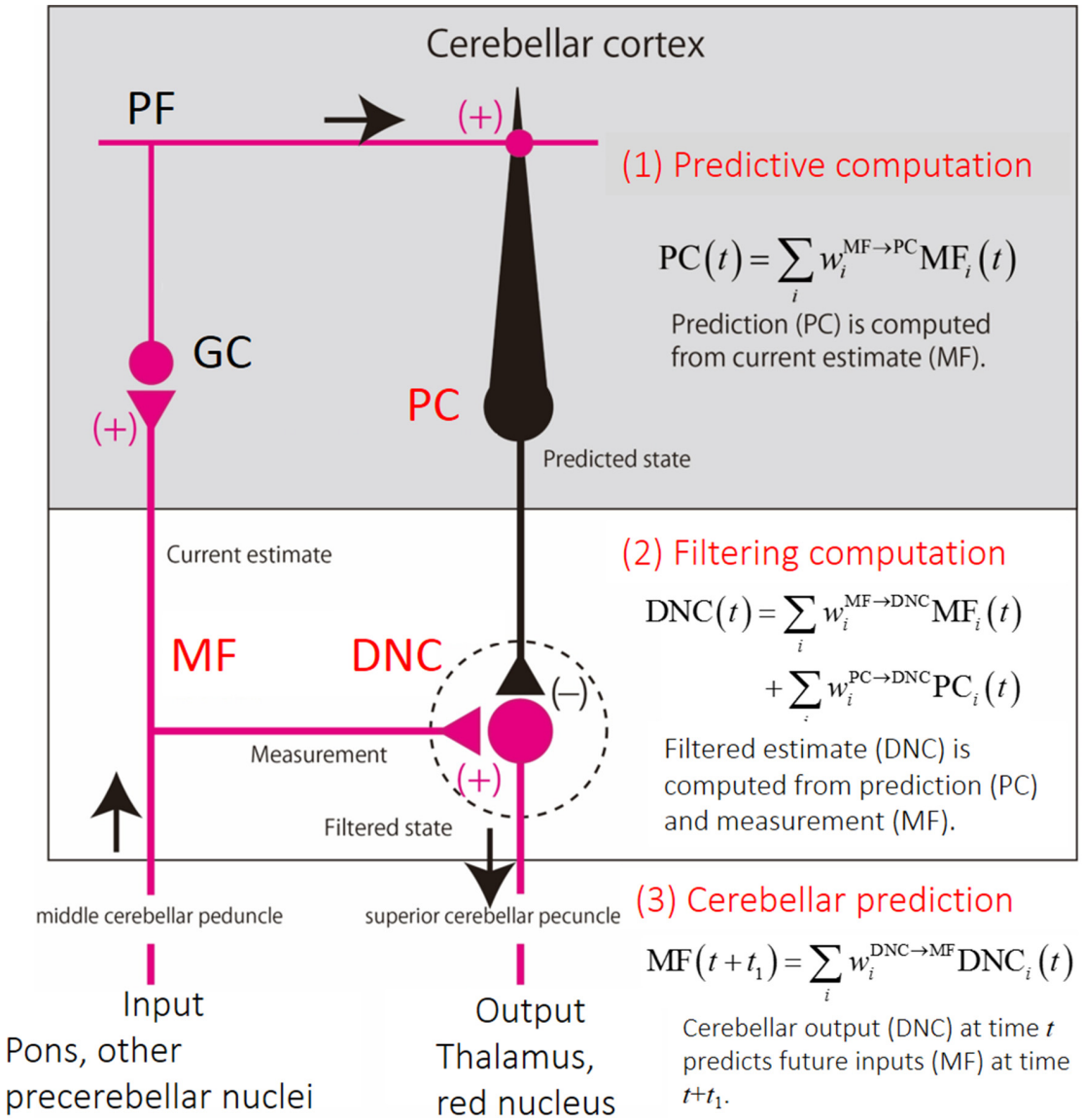

FIGURE 3 | Schematics of the cerebellar circuit and corresponding computational steps. (1) Prediction computation. The PCs computes a predicted state from a current estimate conveyed by the MFs. (2) Filtering computation. The predictive state computed by the PCs are integrated with an observation signal conveyed by other MFs for optimal estimation in DNCs. (3) Cerebellar prediction. The current output from the cerebellar circuit (DNCs) can predict future inputs to the cerebellum (MFs).

cerebellum. Since the MF activities analyzed here originate from the motor cortex, the cerebellar output predicts the future state of the motor cortex, which in turn returns to the motor cortex through the thalamus.

We note that the linear equations derived from the experimental firing rates resemble those of optimal estimation known as Kalman filter. Based on formal correspondence between the experimentally derived linear equations and the Kalman-filter equations, we speculate the following computational steps in the cerebellar circuits (**Figure 3**): (1) the PCs compute a predictive state from a current estimate conveyed by the MFs (Predictive computation); (2) the DNC activities combine the predicted state from the PC activities and sensory feedback from the MF activities (Filtering computation); and (3) the DNC activities predicts a future input to the MFs (Cerebellar prediction). Our finding indicates that the cerebellum performs not only an internal-forward-model prediction but also an optimal integration of a predicted state and sensory feedback signals.

Behavioral Evidence for Cerebellar Internal Model

Although the cerebro-cerebellum has long been suggested as a neural substrate of internal forward models (Wolpert and

Miall, 1996; Bastian, 2006; Ebner and Pasalar, 2008; Ishikawa et al., 2016), few behavioral methods are available to evaluate the contribution of forward models in patients with cerebellar ataxia (but see Bhanpuri et al., 2014). Our previous studies have developed a method to analyze the contribution of position- and velocity-dependent motor commands (i.e., muscle activities) in visually-guided pursuit movements of the wrist (termed as B_r/K_r ratio, defined below; Lee et al., 2015; Kakei et al., 2019). Here, B_r and K_r stand for viscous and elastic coefficients, respectively, estimated from wrist movements of a subject with a canonical correlation analysis, and the B_r/K_r ratio evaluates the ratio of velocity control to position control. The movement kinematics of wrist was decomposed into a slower (i.e., lower-frequency, <0.5 Hz) F1 component and a faster (i.e., higher-frequency, >0.5 Hz) F2 component, and the B_r/K_r ratio was computed for F1 component and F2 component, respectively. The F1 component belonged to the same frequency range of the target motion and encoded both velocity and position (higher B_r/K_r ratio) of the target motion. This kinematic formula of the F1 component appeared optimal to synchronize the wrist movement with the target motion in a *predictive* manner. Indeed, for the control subjects, the F1 component lagged behind the target motion for about 60 ms (15.0–107.4 ms, mean ± SD = 66.3 ± 29.4 ms, 13 subjects; **Figure 4A**, Controls). The short delay excludes a possibility that the F1 component of the wrist movement was generated with visual feedback of the target motion. The conduction time of the peripheral motor nerve (∼10 ms) and electromechanical delay (∼50 ms) alone would take that long (∼60 ms). Thus, the delay of the F1 component was too short to be a feedback delay. Rather, the generation of the F1 component in the CNS must have preceded the corresponding motion of the target, considering the average lead time of neuron activity in the primary motor cortex for the wrist movement (∼100 ms).

We next evaluated the delay of the F1 component in patients with cerebellar ataxia. The F1 component was delayed significantly more (∼100 ms) in the patient group (79.5–322.4 ms, mean ± SD = 172.1 ± 82.0 ms, 19 subjects; $p < 0.0001$) than in the control group (**Figure 4A**, Patients). The delay may be explained as poor recruitment of facilitation in DN due to a decrease in the disinhibition of DNCs, i.e., asthenia (Ishikawa et al., 2015). The prediction delayed by this amount is no longer predictive and may force the patients to rely on the pure feedback control, further destabilizing the wrist movement ataxic (Kakei et al., 2019).

We further demonstrated that the B_r/K_r ratios of the predictive (F1) component had a significant difference between the control and patient groups. Namely, the B_r/K_r ratios of the F1 component of the patient group (0.3–1.9, mean ± SD = 0.99 ± 0.42; **Figure 4B**, Patients, F1) were significantly lower than those of the control group (1.4–2.5, mean ± SD = 1.73 ± 0.36; **Figure 4B**, Controls, F1; $p < 0.001$), suggesting difficulty in recruiting velocity control in cerebellar patients. In contrast, B_r/K_r ratios of the F2 component were comparable for both groups (compare **Figure 4B**, *Cerebellar patients, F2* and *Controls, F2*). Taken together, our results support the hypothesis that cerebellar patients have an impairment in the forward-model prediction while relatively maintaining corrective control in response to sensory feedback.

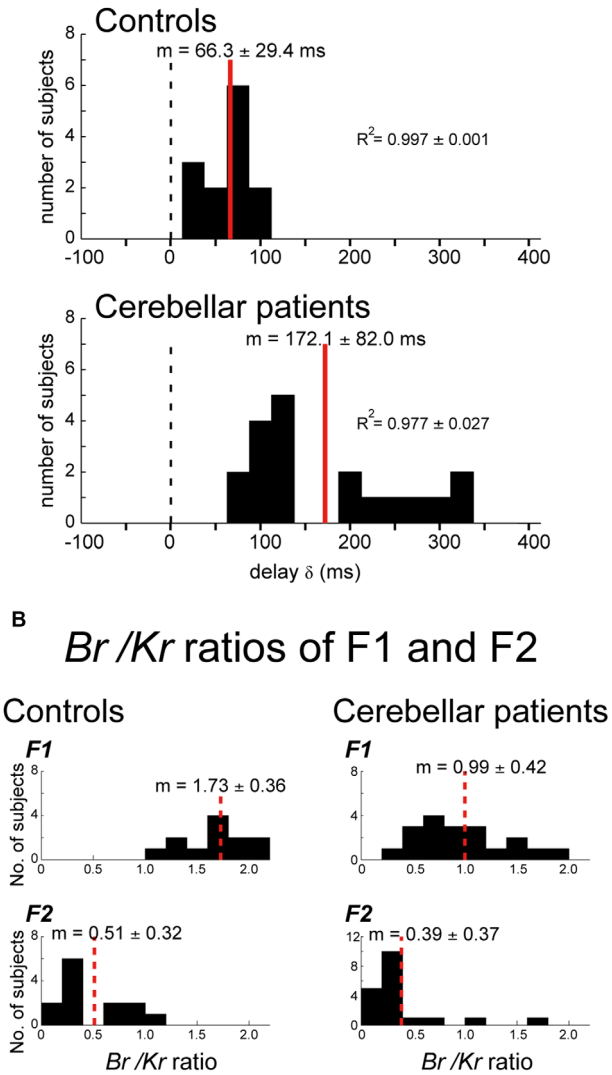

FIGURE 4 | Changes in movement kinematics of ataxic patients. **(A)** Delay of the F1 domain of the wrist movement from the target motion. Cross-correlation was calculated by changing the delay δ of the target motion relative to the wrist movement. *Controls*: Histogram of the optimal delay δ for the control subjects ($n = 13$). *Cerebellar patients*: Histogram of the optimal delay δ for the cerebellar patients ($n = 19$). **(B)** Comparison of the B_r/K_r ratios for the F1 and F2 components between the controls and the cerebellar patients. *Controls*: B_r/K_r ratios of the control subjects for the F1 component (top) and the F2 component (bottom; $n = 13$). Note the highly significant difference between the two components. *Cerebellar patients*: B_r/K_r ratios of the patients for the F1 (top) and the F2 (bottom) components ($n = 19$). Note the selective decrease of B_r/K_r ratios for the F1 component in the patients. Adapted from Kakei et al. (2019) under CC-BY license.

We then proceeded to examine the relationship between B_r/K_r ratios of the F1 component and performance/accuracy of pursuit movement in the cerebellar patients and the control subjects (**Figure 5**), because the characteristic decrease in B_r/K_r ratio

of the F1 component might have reflected impaired predictive control in the patient group. To test this hypothesis, we examined the relationship between the B_r/K_r ratios of the F1 component and the accuracy of the pursuit movement (i.e., F1 error, Kakei et al., 2019). The B_r/K_r ratio of the F1 component and the F1 error were negatively correlated (**Figure 5A**). Next, we examined the relationship between the F1 error and the tracking score. The tracking score was defined as a percentage of time when the cursor was kept within the target circle. The F1 error and the tracking score demonstrated a strikingly linear, negative correlation (**Figure 5B**). Overall, the B_r/K_r ratio of the F1 component is a useful measure to assess the accuracy of predictive control, which could be quantified noninvasively in a clinical setting.

ANATOMICAL STRUCTURE SUPPORTING FOR CEREBELLAR FORWARD MODELS

Morphologic Substrata of the cerebro-Cerebellum for Kalman Filter

Here we argue morphological substrata supporting our findings of predictive computation presented in Section "Behavioral Evidence for Cerebellar Internal Model". The conventional circuit diagram of the cerebro-cerebellum (**Figure 6A**) depicts the MFs projecting both to the cerebellar cortex and DN as collaterals, implying that the cerebellar cortex and DN share the same source of input. On the other hand, the prerequisite of the Kalman filter is the two distinct inputs: current estimate and current measurement; One MF input comes from the cerebral cortex to the cerebellar cortex (*via* PN) and plays an essential role in the prediction step, and another MF input to DN conveys sensory feedback information and plays a critical role in the filtering step. Therefore, the conventional diagram of the cerebro-cerebellum in which the same MF projecting to the cerebellar cortex and DN is not compatible with our proposal of Kalman-filter computation in the cerebellum.

Discordant to the conventional diagram, extant anatomical studies rather suggest that the cerebro-cerebellum receives respective projections to the cerebellar cortex and DN (**Figure 6B**). The first requirement of the Kalman-filter model is that MFs originated from the PN project to the cerebro-cerebellum *without* collaterals to DN. Indeed, Kelly and Strick (2003) demonstrated a strong projection from the primary motor cortex (M1) to the cerebro-cerebellum, which was assumed to carry efference copy signals. Also, Na et al. (2019) demonstrated that MFs originated from PN have virtually no collateral projection to DN on their way to the cerebro-cerebellum. Taken together, it is most likely that the first requirement is satisfied for the input from M1 to the cerebro-cerebellum. The second requirement of the Kalman-filter model is that MFs conveying feedback input provide collaterals to DN. Wu et al. (1999) demonstrated that MFs originated from the lateral reticular nucleus (LRN), which receives strong somatosensory inputs from the spinal cord, have abundant collateral projection to DN and other cerebellar nuclei on their way to the vermis and the intermediate zone (see Figures 8–10 in Wu et al., 1999). Also, these MFs from PN and LRN have only minor overlap in their projection to the cerebellar cortex (Wu et al., 1999; Na et al., 2019). These observations converge to the neural organization compatible with the requirement of the Kalman-filter model (**Figure 6B**).

Consistent with the anatomical observations, there were two functionally distinct populations of MFs in our data set (Tanaka et al., 2019). One population of MFs contributed to the prediction step and the other population of MFs contributed to the filtering step. We confirmed that partially distinct populations of MFs contributed to the reconstructions of PCs and DNCs, respectively; the average correlation coefficient between weights of MF–PC and MF–DNC projections was no more than 0.060. A statistical test based on resampling verified that the correlation between the two MF populations was statistically significant ($p < 10^{-5}$). Therefore, it was concluded that PCs and DNCs received the projections from distinct populations of MFs, thereby fulfilling the requirements of the Kalman-filter model.

As outlined in the "Introduction" section, an input to and an output from a specific region of the cerebellum are a key to understanding of the function played by that region. The "corticonuclear organization" depicted in **Figure 6B** appears to be specific for the cerebro-cerebellum (i.e., the *newer* part of the cerebellum), the other regions of the cerebellum could receive input projections in different ways (Ito, 1984). For instance, in the vestibular nucleus, nuclear neurons may act as a relay for MF afferents, whereas PCs activated by the MF afferents may exert modulatory action on the nuclear relay cells (**Figure 6A**, see also Figure 92A in Ito, 1984). Similarly, in the fastigial nucleus, nuclear cells may serve as a relay for PC output reflecting MF inputs, while collaterals of MFs provide a background excitation on which PCs can impose efficient bidirectional modulation (i.e., inhibition and disinhibition; **Figure 6A**, see also Figure 92B in Ito, 1984). In these cerebellar regions, the corticonuclear organization is not compatible with the Kalman filter, where the cerebellar cortex and DN receive shared MF projections. Overall, even if the input-output organization is common for the entire cerebellar cortex, different regions may contribute to computationally different operations depending on the organization of MF collaterals in the cerebellar nuclei (Ito, 1984). It should be noted that Ito (1984) pointed out the possibility of this type of heterotopic combination of a direct collateral MF input and an indirect MF input *via* PCs (i.e., "sidepath") to DN (see Figure 92D in Ito, 1984), to explain spontaneous activities of DN neurons that lack collateral inputs of MFs originated from PN (Allen and Tsukahara, 1974).

Compressed Prediction of the Cerebellar Internal Model

The cerebro-cerebellar loop has more abundant projections from the cerebral cortex to the cerebellum than those from the cerebellum to the cerebral cortex (**Figure 1B**). To the best of our knowledge, little attention is paid to the asymmetry of the cerebro-cerebellar loop, in terms of the number of output neurons on each side of the loop. The number of axons in the cerebral peduncle (CP) conveying cortical outputs to PN and other precerebellar nuclei is estimated as twenty-one million in

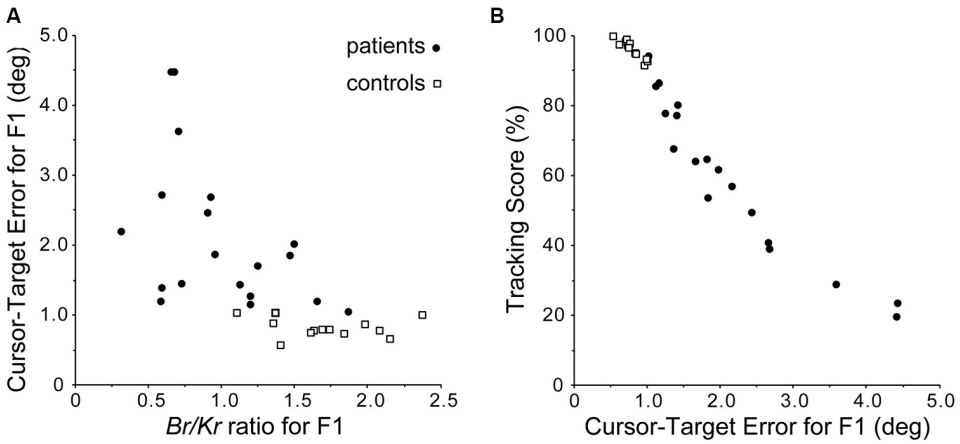

FIGURE 5 | Accuracy of predictive (F1) component. **(A)** Relationship between the B_r/K_r ratios for F1 component and Cursor-Target error for F1 (F1 error, in short). The F1 error is defined as an average error between the target motion and the F1 component of the movement during a trial. Note the negative correlation. **(B)** Relationship between F1 error and Tracking Score. Note the linear relationship. Overall, B_r/K_r ratio for the F1 component has a strong positive correlation with the accuracy of the pursuit movement. Adapted from Kakei et al. (2019) under CC-BY license.

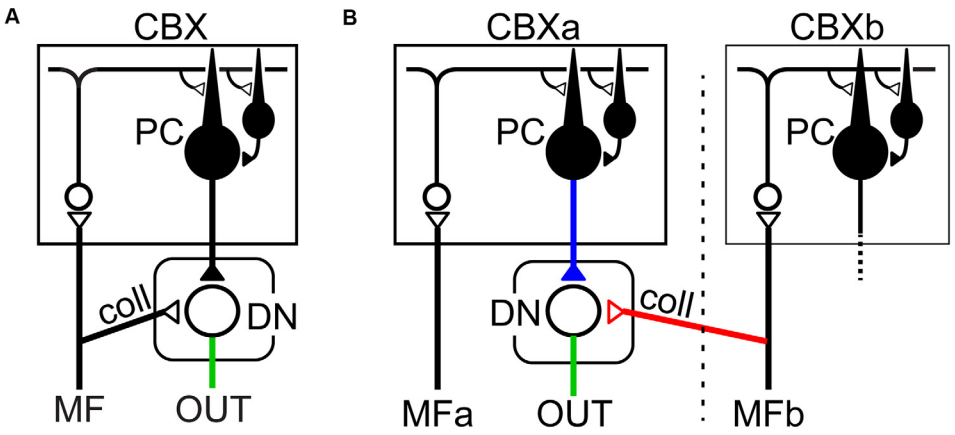

FIGURE 6 | Two schematics of cortico-nuclear organization. **(A)** The conventional scheme in which the same MF projects to the cerebellar cortex (CBX) and DN both of which belong to the same corticonuclear complex (Ito, 1984). **(B)** Proposed scheme that one MF (MFa) from pontine nuclei (PN) projects to the cerebellar cortex (i.e., cerebro-cerebellum; CBXa) without collateral projection to DN, whereas another, separate MF (MFb) projects to DN. Note that MFa and MFb have distinct projection areas in the cerebellar cortex, CBXa, and CBXb, respectively. This scheme is consistent with the requirements of the Kalman-filter model.

humans (Tomasch, 1969). On the other hand, the number of axons in the return path, i.e., the superior cerebellar peduncle (SCP) relaying the cerebellar output to the thalamus, is no more than 0.8 million in human (Heidary and Tomasch, 1969). Therefore, the output from DN can convey less than 5% of the information of the cortical output assuming comparable discharge frequencies for corticofugal neurons and DNCs (Kakei et al., 1999, 2001; Ishikawa et al., 2014; Tomatsu et al., 2016). The cerebro-cerebellum returns its output back to the cerebral cortex that is considerably compressed from the input it receives. One may then wonder what the functional advantage of the compact representation is. There appears no consensus on the functional role of the compact representation (Sanger et al., 2020). Given the fact that the cerebellum contributes to fast, trained and automated motor control with reduced effort and attention, the compressed representation may be beneficial or even necessary to extract relevant information from numerous and redundant cerebellar inputs and to assign more attention to the task currently in the focus.

COGNITIVE FUNCTIONS AND CEREBELLAR FORWARD MODELS

The cerebellum was once thought of as an organ for motor coordination. The motor cerebellum is mainly represented in the anterior lobe with a smaller, secondary representation in lobule

VIII (Kelly and Strick, 2003). Although possible involvement of the cerebellum in non-motor mental functions had been suggested occasionally in the past, it has become the subject of systematic consideration since the beginning of 1990s (Leiner et al., 1986; Schmahmann, 1991; Ito, 1993; Schmahmann, 2004; Ito, 2008). With a use of trans-neuronal transport of neurotropic viruses, Middleton and Strick (1994) provided the first evidence in the monkey that the cerebellum is connected to the non-motor area 46 of the prefrontal cortex and revised the conventional view of the cerebellar devotion to motor control. Strick and his colleagues eventually established that the hemispheric parts of the cerebellum (mainly Crus I and Crus II) are connected with various cortical association areas through DN (Middleton and Strick, 1994; Dum and Strick, 2003; Kelly and Strick, 2003).

The existence of the human non-motor cerebellum was later demonstrated repeatedly in non-invasive imaging studies (e.g., Hanakawa et al., 2003; for reviews see Stoodley and Schmahmann, 2009; Buckner, 2013). A surprisingly powerful approach capable to map the topographical organization of the cerebellar cortex in the human has recently provided insight into the functional mapping between the cerebellum and the cerebral cortex. The approach derives from the observation that brain organization can be inferred by measuring spontaneous low-frequency fluctuations in intrinsic activity (Biswal et al., 1995; Fox and Raichle, 2007). Recently, Buckner et al. (2011) and Wang et al. (2013) demonstrated base on this approach that the cerebro-cerebellum collects information from almost all the entire cortical areas, suggesting that the cerebellum still keeps the position of the CNS *hub* even in human. More recently, Guell et al. (2018) used data from the Human Connectome Project (n = 787) to analyze cerebellar fMRI task activation (motor, working memory, language, social and emotion processing) and resting-state functional connectivity. They demonstrated novel aspects of the functional topography of the human cerebellum. There were two distinct representations (lobules I-VI and lobule VIII) of motor activation that was consistent with prior studies, in particular with the above-mentioned trans-neuronal tracing study in the monkey (Kelly and Strick, 2003). Newly revealed were three distinct regions (Crus I, Crus II, lobules IX/X) in the cerebellar posterior lobe that show topographical relationship with cortical association areas (Buckner et al., 2011; Wang et al., 2013). Each region contains four domains of non-motor functions (working memory, language, social, and emotional task processing). Indeed, lesions in the posterior lobe result in the cerebellar cognitive affective syndrome (CCAS), which includes deficits in executive function, visual spatial processing, linguistic skills and regulation of affect (Schmahmann, 2019).

The critical question arises whether the Kalman-filter mechanism identified for the prediction in the *motor* part of the cerebro-cerebellum (Tanaka et al., 2019) generalizes to the *cognitive/affective* part of the cerebro-cerebellum. Our dataset of MFs, PCs, and DNCs recorded during the motor task cannot support or reject the predictive mechanism of the cerebellum for cognitive/affective functions. Nevertheless, it is possible to search for the *same* corticonuclear organization (**Figure 6B**) in the *non-motor* part of the cerebro-cerebellum. There are two requirements: (1) the main MFa input to the cerebro-cerebellum is originated from a non-motor area and relayed by PN, and (2) the filtering MFb input is originated from a distinct cortical or subcortical source and relayed by a *non-PN* nucleus that has significant collateral projection to DN (**Figure 6B**). The requirement 2 is the key because the requirement one is common for several cortical areas, including prefrontal areas (Schmahmann and Pandya, 1997), parietal association areas (Schmahmann and Pandya, 1989), superior temporal areas (Schmahmann and Pandya, 1991), occipitotemporal and parahippocampal areas (Schmahmann and Pandya, 1993). There are only a few major sources of collateral MF inputs to DN, the lateral reticular nucleus (LRN; Wu et al., 1999) and the nucleus reticularis tegmenti pontis (NRTP; Gerrits and Voogd, 1986) in the reticular formation. The LRN receives main inputs from the spinal cord (Alstermark and Ekerot, 2013) and additional inputs from the sensorimotor areas and the red nucleus (Bruckmoser et al., 1969; Matsuyama and Drew, 1997). The NRTP receives inputs mainly from the sensorimotor areas, the prefrontal areas and the parietal association areas (Schmahmann et al., 2004). Overall, the Kalman-filter model is at least compatible with the non-motor part of the cerebro-cerebellum if the two inputs to non-motor parts of DN (Dum and Strick, 2003) are proven to have different origins in future studies.

REMAINING ISSUES ABOUT CEREBELLAR INTERNAL MODELS

This review article has discussed physiological, behavioral, and morphological evidence supporting the internal-forward-model hypothesis of the cerebellum, with an emphasis on our recent studies. This final section expands our speculation on a possible computational role of the cerebro-cerebellar loops and raises remaining unsolved issues on the functioning of the cerebellum for a future study.

Possible Computational Role of Cerebro-Cerebellar Loops

The cerebral cortex and the cerebellum have evolved together as their volume has increased in a proportional manner (Rilling and Insel, 1998), and form an anatomically closed connectivity known as the cerebro-cerebellar loop (Kelly and Strick, 2003; Bostan et al., 2013). These findings indicate that the evolutionally conserved anatomical structure composed of the cerebral cortex and the cerebellum plays a functionally relevant role, but to the best of our knowledge, there appears no consensus about its specific function. We below expand our speculation on a computational role considering our findings and artificial neural networks.

The cerebral cortex and the cerebellum have contrasting anatomical structures. The cerebral cortex is characterized by hierarchical recurrent connections composed of local connections across cortical layers and lateral connections (for a review see DeFelipe and Jones, 1988), so it is appropriate to model the cerebral cortex, at least locally, as a recurrent neural network. An artificial neural network model with recurrent connections is known to be able to approximate any dynamical

systems (Funahashi and Nakamura, 1993), so it is appropriate to model a neural process that evolves over a period such as a production of a motor sequence. A recurrent neural network is also known to be difficult to train and control because it may exhibit chaotic behavior (Sompolinsky et al., 1988; Sussillo and Abbott, 2009; Laje and Buonomano, 2013; Ben-Shushan and Tsodyks, 2017). On the other hand, the cerebellum consists essentially of a feedforward connectivity from the MFs as an input to the cerebellar nuclei as an output. An artificial neural network model composed of more than two layers is known to be able to approximate any continuous mapping (Cybenko, 1989; Funahashi, 1989; Hornik et al., 1989), which is a theoretical basis of the universal cerebellar transform (Schmahmann, 2004). Also, the MF inputs are considerably expanded by the GCs by about one-thousand-fold and then converged into the DNCs (**Figure 1B**). This divergence-convergence structure resembles a shallow learning scheme in machine learning. A feedforward neural network model is straightforward to train, but its computation is limited to a static input-output function.

We here speculate a computational possibility that the cerebellum copies the dynamics of the cerebral cortex and then predicts the state of the cerebral cortex for fast and stable operations in motor control and cognitive processing (**Figure 7**). There are some advantages and disadvantages of recurrent and feedforward neural networks, and we propose that the recurrent neural networks of the cerebral cortex and the feedforward neural networks of the cerebellum complement each other. Recurrent connections in a neural network provide computational flexibility to model a dynamical system (Funahashi and Nakamura, 1993) but cause a chaotic instability due to dependence on previous activities and random noises (Sompolinsky et al., 1988). Therefore, a sequence production solely by a recurrent neural network can be unstable against small fluctuations in activities and unwanted noises (Jaeger and Haas, 2004). A feedforward neural network, on the other hand, is stable because its output depends not on previous inputs but only current inputs and a fluctuation at one point of time does not propagate over time. Our recent results demonstrated that the cerebellar circuit could perform the predictive computation of an internal forward model, so we propose that the cerebellum tames computationally flexible but chaotic dynamics of cortical recurrent neural network by predicting the expected activity of the cerebral cortex. In line with our proposal, the FORCE learning algorithm generates stable patterns of activity in a recurrent neural network by adding feedback connections from the output unit to recurrent units (Sussillo and Abbott, 2009). In our proposed scheme, the feedforward network of the cerebellum continuously monitors and predicts the activities of the recurrent network of the cerebral cortex. The recurrent network, in turn, stabilizes its activities and corrects any deviations by comparing the current activity in the recurrent network and the predicted activity from the cerebellar feedforward network. Therefore, an internal model allows fast and robust computation not only in motor control but also in recurrent neural networks in the cerebral cortex.

Whereas recurrent and feedforward neural networks differ from each other in their formulation, they are in fact equivalent because recurrent neural networks can be transformed into feedforward neural networks by a proper redefinition. A standard algorithm for training a recurrent neural network, backpropagation-through-time, exploits the fact that a recurrent neural network can be regarded as a temporally unfolded feedforward neural network (Werbos, 1990). Also, it was shown that a proper redefinition of units can transform a recurrent neural network into a feedforward neural network, known as a method of matrix decomposition (Schur decomposition) in matrix algebra (Goldman, 2009). Therefore, recurrent and feedforward neural networks possess the same ability in terms of computation.

Our computational scheme requires that a part of the cerebro-cerebellum and a part of the cerebral cortex connected by a cerebro-cerebellar loop should perform the same computation so that the cerebellum can predict activity patterns of the cerebral cortex. We, therefore, speculate that the computational role of the cerebellum is to copy the function of the cerebral cortex for predicting and stabilizing the dynamics of the cerebral cortex. Results from a recent imaging study are in line with this speculation; activities of layer 5 pyramidal cells in the neocortex and those of GCs in the cerebellar cortex share task-encoding characteristics acquired during learning, indicating that a key function of cerebro-cerebellar loop is the propagation of shared neural dynamics (Wagner et al., 2019). A tentative computational scheme posits that dynamics learned by a recurrent neural network are transferred to a feedforward neural network, and then the feedforward neural network stabilizes the dynamics of the recurrent neural network by predicting the dynamics. An additional merit of feedforward neural network is single-shot, fast computation; a recurrent neural network requires multiple, iterative steps for computing a transition from $\mathbf{x}_t$ to $\mathbf{x}_{(t+t_1)}$ (**Figure 7**, top), which could be computed in a single step in a feedforward network (**Figure 7**, bottom). Our speculation discussed here is mainly motivated by the results of artificial neural networks; however, given the recent productive interactions between deep neural networks and the primate visual system, it is not unreasonable to incorporate ideas developed in artificial neural networks to understanding the biological nervous system. We hope that this speculative function proposed here will guide the future computational study on the role of cerebro-cerebellar loops.

Future Problems

Our recent study arguably demonstrated that the cerebellar output (activities of DCs) at current time was predictive about the cerebellar input (activities of MFs) at a future time, supporting the hypothesis that the cerebellum performs the computation of an internal forward model (Tanaka et al., 2019). The dataset analyzed in this study was recorded when the monkey was over-trained for the movement task for years and there was no sign of learning in performance. Hence, our study demonstrated one aspect of forward model, namely the predictive activity, but not another aspect of forward model, namely motor learning. Electrophysiological recording of single units usually requires averages to remove trial variance, so it is not ideal for analyzing activity changes in an individual trial before, during, and after

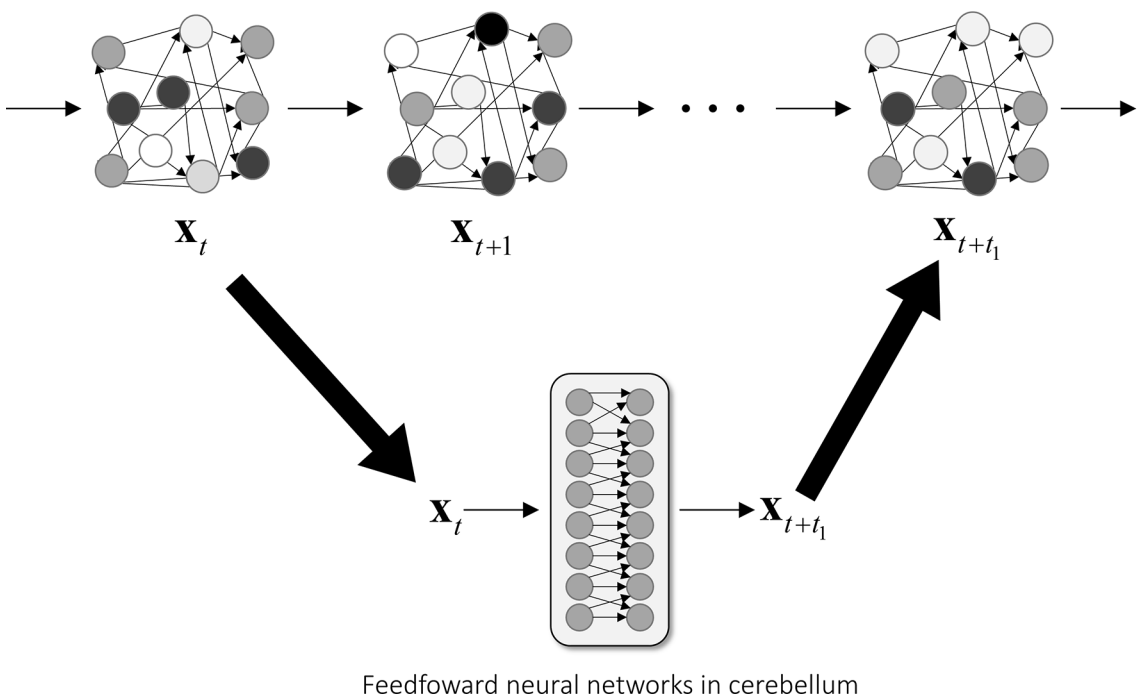

FIGURE 7 | Proposed mechanism of predictive stabilization of cortical dynamics through the cerebro-cerebellar loop. The dynamics of the cerebral cortex and the cerebellum are modeled as a recurrent neural network (top row) and a feedforward neural network (bottom row), respectively. The cerebellum receives a current cortical state at time t and projects back a future cortical state at time $t+t_1$ through the cerebro-cerebellar loop. In this proposed mechanism, the cerebellar prediction guides and stabilizes the recurrent dynamics of the cerebral cortex, thereby realizing fast and robust information processing.

learning. This is particularly problematic when we want to address the circuit-level analysis where cells from multiple populations need to be recorded simultaneously. Fortunately, new recording techniques such as calcium imaging are available to track learning-related changes in the activities of multiple neurons (Wagner et al., 2019). We hope that the new approach will reveal the contribution of the internal-forward-model to the motor-learning shortly.

We would like to conclude this review article by enlisting two unanswered questions that we think important for promoting a better understanding of the computational functions and the neural mechanisms of the cerebellum. First, how is a predictive activity computed in the cerebellum utilized in the cerebral cortex? Our previous study reported that MF activities, the input to the cerebellum, shared response properties with the activity of neurons in motor areas, implying that activities of the cortical neurons are copied into the cerebellum as an input (Tomatsu et al., 2016). On the other hand, it remains to be examined how the cerebellar output influences the activities of the cortical neurons. Second, how do linear dynamics in the cerebellar circuit approximate the nonlinear dynamics of the musculoskeletal system? Biological motor control must face with the large degrees of freedom of the body and corresponding nonlinear dynamics, and we know little about how such dynamics is solved in the brain. We hope that future studies will take a challenge in addressing these questions toward the goal of understanding the functions and the neural mechanisms of the cerebellum.

AUTHOR CONTRIBUTIONS

SK, HT, TI and JL conceived the research. HT and SK drafted the manuscript. HT, SK, TI and JL finalized the manuscript.

FUNDING

This work was supported by Grants-in-aid from the Ministry of Education, Culture, Sports, Science and Technology in Japan (MEXT; http://www.mext.go.jp/; No. 26120003, No. 14580784, No. 15016008, No. 16015212, No. 20033029, No. 21500319 to SK, No. 25430007, No. 26120005 and No. 16K12476 to HT, No. 21700229, No. 24650304 to JL, and No. 24650224 to TI), the Japan Science and Technology Agency (A-STEP) to SK, http://www.jst.go.jp/ the Japan Science and Technology Agency (PRESTO: Intelligent Cooperation and Control; SK), NBRP "Japanese Monkeys" through the National BioResource Project of MEXT, the JSPS Programs (Program for Advancing Strategic International Networks to Accelerate the Circulation of Talented Researchers, and Embodied-Brain Systems Science; HT), and the Hitachi-Kurata and the Tateishi Science Foundations (HT). This

research was also supported by AMED under Grant Number 16ek0109048h0003 to SK. The funders had no role in study design, data collection and analysis, decision to publish, or preparation of the manuscript.

ACKNOWLEDGMENTS

We thank Profs. Hiroshi Mitoma and Koji Ito for their invaluable comments and discussions.

REFERENCES

Aizenman, C. D., and Linden, D. J. (1999). Regulation of the rebound depolarization and spontaneous firing patterns of deep nuclear neurons in slices of rat cerebellum. *J. Neurophysiol.* 82, 1697–1709. doi: 10.1152/jn.1999.82.4.1697

Albus, J. S. (1971). A theory of cerebellar function. *Math. Biosci.* 10, 25–61. doi: 10.1016/0025-5564(71)90051-4

Allen, G. I., and Tsukahara, N. (1974). Cerebrocerebellar communication systems. *Physiol. Rev.* 54, 957–1006. doi: 10.1152/physrev.1974.54.4.957

Alstermark, B., and Ekerot, C. F. (2013). The lateral reticular nucleus: a precerebellar centre providing the cerebellum with overview and integration of motor functions at systems level. A new hypothesis. *J. Physiol.* 591, 5453–5458. doi: 10.1113/jphysiol.2013.256669

Barto, A. G., Sutton, R. S., and Anderson, C. W. (1983). Neuronlike adaptive elements that can solve difficult learning control problems. *IEEE Trans. Syst. Man Cybern.* 13, 834–846. doi: 10.1109/tsmc.1983.6313077

Bäss, P., Jacobsen, T., and Schröger, E. (2008). Suppression of the auditory N1 event-related potential component with unpredictable self-initiated tones: evidence for internal forward models with dynamic stimulation. *Int. J. Psychophysiol.* 70, 137–143. doi: 10.1016/j.ijpsycho.2008.06.005

Bastian, A. J. (2006). Learning to predict the future: the cerebellum adapts feedforward movement control. *Curr. Opin. Neurobiol.* 16, 645–649. doi: 10.1016/j.conb.2006.08.016

Ben-Shushan, N., and Tsodyks, M. (2017). Stabilizing patterns in time: neural network approach. *PLoS Comput. Biol.* 13:e1005861. doi: 10.1371/journal.pcbi.1005861

Bhanpuri, N. H., Okamura, A. M., and Bastian, A. J. (2014). Predicting and correcting ataxia using a model of cerebellar function. *Brain* 137, 1931–1944. doi: 10.1093/brain/awu115

Biswal, B., Yetkin, F. Z., Haughton, V. M., and Hyde, J. S. (1995). Functional connectivity in the motor cortex of resting human brain using echo-planar MRI. *Magn. Reson. Med.* 34, 537–541. doi: 10.1002/mrm.1910340409

Blakemore, S. J., Wolpert, D. M., and Frith, C. D. (1998). Central cancellation of self-produced tickle sensation. *Nat. Neurosci.* 1, 635–640. doi: 10.1038/2870

Bostan, A. C., Dum, R. P., and Strick, P. L. (2013). Cerebellar networks with the cerebral cortex and basal ganglia. *Trends Cogn. Sci.* 17, 241–254. doi: 10.1016/j.tics.2013.03.003

Bruckmoser, P., Hepp, M. C., and Wiesendanger, M. (1969). Cortical influence on the lateral reticular nucleus of the cat. *Brain Res.* 15, 556–558. doi: 10.1016/0006-8993(69)90183-8

Buckner, R. L. (2013). The cerebellum and cognitive function: 25 years of insight from anatomy and neuroimaging. *Neuron* 80, 807–815. doi: 10.1016/j.neuron.2013.10.044

Buckner, R. L., Krienen, F. M., Castellanos, A., Diaz, J. C., and Yeo, B. T. (2011). The organization of the human cerebellum estimated by intrinsic functional connectivity. *J. Neurophysiol.* 106, 2322–2345. doi: 10.1152/jn.00339.2011

Chapman, C. E., Spidalieri, G., and Lamarre, Y. (1986). Activity of dentate neurons during arm movements triggered by visual, auditory, and somesthetic stimuli in the monkey. *J. Neurophysiol.* 55, 203–226. doi: 10.1152/jn.1986.55.2.203

Cybenko, G. (1989). Approximation by superpositions of a sigmoidal function. *Math. Control Signals Syst.* 2, 303–314. doi: 10.1007/bf02551274

Dean, P., and Porrill, J. (2010). The cerebellum as an adaptive filter: a general model? *Funct. Neurol.* 25, 173–180.

Dean, P., Porrill, J., Ekerot, C. F., and Jörntell, H. (2010). The cerebellar microcircuit as an adaptive filter: experimental and computational evidence. *Nat. Rev. Neurosci.* 11, 30–43. doi: 10.1038/nrn2756

DeFelipe, J., and Jones, E. G. (1988). *Cajal on the Cerebral Cortex: An Annotated Translation of the Complete Wrings.* New York, NY: Oxford University Press.

Diedrichsen, J., King, M., Hernandez-Castillo, C., Sereno, M., and Ivry, R. B. (2019). Universal transform or multiple functionality? understanding the contribution of the human cerebellum across task domains. *Neuron* 102, 918–928. doi: 10.1016/j.neuron.2019.04.021

Dum, R. P., and Strick, P. L. (2003). An unfolded map of the cerebellar dentate nucleus and its projections to the cerebral cortex. *J. Neurophysiol.* 89, 634–639. doi: 10.1152/jn.00626.2002

Ebner, T. J., and Pasalar, S. (2008). Cerebellum predicts the future motor state. *Cerebellum* 7, 583–588. doi: 10.1007/s12311-008-0059-3

Fortier, P. A., Kalaska, J. F., and Smith, A. M. (1989). Cerebellar neuronal activity related to whole-arm reaching movements in the monkey. *J. Neurophysiol.* 62, 198–211. doi: 10.1152/jn.1989.62.1.198

Fox, M. D., and Raichle, M. E. (2007). Spontaneous fluctuations in brain activity observed with functional magnetic resonance imaging. *Nat. Rev. Neurosci.* 8, 700–711. doi: 10.1038/nrn2201

Fujita, M. (1982). Adaptive filter model of the cerebellum. *Biol. Cybern.* 45, 195–206. doi: 10.1007/bf00336192

Funahashi, K.-I. (1989). On the approximate realization of continuous mappings by neural networks. *Neural Netw.* 2, 183–192. doi: 10.1016/0893-6080(89)90003-8

Funahashi, K.-I., and Nakamura, Y. (1993). Approximation of dynamical systems by continuous time recurrent neural networks. *Neural Netw.* 6, 801–806. doi: 10.1016/s0893-6080(05)80125-x

Gentili, R., Papaxanthis, C., and Pozzo, T. (2006). Improvement and generalization of arm motor performance through motor imagery practice. *Neuroscience* 137, 761–772. doi: 10.1016/j.neuroscience.2005.10.013

Gerrits, N. M., and Voogd, J. (1986). The nucleus reticularis tegmenti pontis and the adjacent rostral paramedian reticular formation: differential projections to the cerebellum and the caudal brain stem. *Exp. Brain Res.* 62, 29–45. doi: 10.1007/bf00237401

Goldman, M. S. (2009). Memory without feedback in a neural network. *Neuron* 61, 621–634. doi: 10.1016/j.neuron.2008.12.012

Goodkin, H. P., and Thach, W. T. (2003). Cerebellar control of constrained and unconstrained movements. II. EMG and nuclear activity. *J. Neurophysiol.* 89, 896–908. doi: 10.1152/jn.00115.2002

Guell, X., Gabrieli, J. D. E., and Schmahmann, J. D. (2018). Triple representation of language, working memory, social and emotion processing in the cerebellum: convergent evidence from task and seed-based resting-state fMRI analyses in a single large cohort. *NeuroImage* 172, 437–449. doi: 10.1016/j.neuroimage.2018.01.082

Hanakawa, T., Honda, M., Okada, T., Fukuyama, H., and Shibasaki, H. (2003). Neural correlates underlying mental calculation in abacus experts: a functional magnetic resonance imaging study. *NeuroImage* 19, 296–307. doi: 10.1016/s1053-8119(03)00050-8

Heidary, H., and Tomasch, J. (1969). Neuron numbers and perikaryon areas in the human cerebellar nuclei. *Acta Anat.* 74, 290–296. doi: 10.1159/000143382

Heinks-Maldonado, T. H., Nagarajan, S. S., and Houde, J. F. (2006). Magnetoencephalographic evidence for a precise forward model in speech production. *Neuroreport* 17, 1375–1379. doi: 10.1097/01.wnr.0000233102.43526.e9

Herculano-Houzel, S. (2009). The human brain in numbers: a linearly scaled-up primate brain. *Front. Hum. Neurosci.* 3:31. doi: 10.3389/neuro.09.031.2009

Hoebeek, F. E., Witter, L., Ruigrok, T. J., and De Zeeuw, C. I. (2010). Differential olivo-cerebellar cortical control of rebound activity in the cerebellar nuclei. *Proc. Natl. Acad. Sci. U S A* 107, 8410–8415. doi: 10.1073/pnas.0907118107

Holmes, G. (1917). The symptoms of acute cerebellar injuries due to gunshot injuries. *Brain* 40, 461–535. doi: 10.1093/brain/40.4.461

Hornik, K., Stinchcombe, M., and White, H. (1989). Multilayer feedforward networks are universal approximators. *Neural Netw.* 2, 359–366. doi: 10.1016/0893-6080(89)90020-8

Imamizu, H., Miyauchi, S., Tamada, T., Sasaki, Y., Takino, R., Pütz, B., et al. (2000). Human cerebellar activity reflecting an acquired internal model of a new tool. *Nature* 403, 192–195. doi: 10.1038/35003194

Ishikawa, T., Kakei, S., and Mitoma, H. (2015). Overlooked Holmes' clinical signs: reevaluation by recent physiological findings. *Cerebellum Ataxias* 2:13. doi: 10.1186/s40673-015-0033-z

Ishikawa, T., Tomatsu, S., Izawa, J., and Kakei, S. (2016). The cerebro-cerebellum: could it be loci of forward models? *Neurosci. Res.* 104, 72–79. doi: 10.1016/j.neures.2015.12.003

Ishikawa, T., Tomatsu, S., Tsunoda, Y., Lee, J., Hoffman, D. S., and Kakei, S. (2014). Releasing dentate nucleus cells from Purkinje cell inhibition generates output from the cerebrocerebellum. *PLoS One* 9:e108774. doi: 10.1371/journal.pone.0108774

Ito, M. (1984). *The Cerebellum and Neural Control.* New York, NY: Raven Press.

Ito, M. (1993). Movement and thought: identical control mechanisms by the cerebellum. *Trends Neurosci.* 16, 448–450; discussion 453–444. doi: 10.1016/0166-2236(93)90073-u

Ito, M. (2008). Control of mental activities by internal models in the cerebellum. *Nat. Rev. Neurosci.* 9, 304–313. doi: 10.1038/nrn2332

Ivry, R. B., and Spencer, R. M. (2004). The neural representation of time. *Curr. Opin. Neurobiol.* 14, 225–232. doi: 10.1016/j.conb.2004.03.013

Ivry, R. B., Spencer, R. M., Zelaznik, H. N., and Diedrichsen, J. (2002). The cerebellum and event timing. *Ann. N Y Acad. Sci.* 978, 302–317. doi: 10.1111/j.1749-6632.2002.tb07576.x

Jaeger, H., and Haas, H. (2004). Harnessing nonlinearity: predicting chaotic systems and saving energy in wireless communication. *Science* 304, 78–80. doi: 10.1126/science.1091277

Jordan, M. I., and Rumelhart, D. E. (1992). Forward models: supervised learning with a distal teacher. *Cogn. Sci.* 16, 307–354. doi: 10.1207/s15516709cog1603_1

Kakei, S., Hoffman, D. S., and Strick, P. L. (1999). Muscle and movement representations in the primary motor cortex. *Science* 285, 2136–2139. doi: 10.1126/science.285.5436.2136

Kakei, S., Hoffman, D. S., and Strick, P. L. (2001). Direction of action is represented in the ventral premotor cortex. *Nat. Neurosci.* 4, 1020–1025. doi: 10.1038/nn726

Kakei, S., Lee, J., Mitoma, H., Tanaka, H., Manto, M., and Hampe, C. S. (2019). Contribution of the cerebellum to predictive motor control and its evaluation in ataxic patients. *Front. Hum. Neurosci.* 13:216. doi: 10.3389/fnhum.2019.00216

Kelly, R. M., and Strick, P. L. (2003). Cerebellar loops with motor cortex and prefrontal cortex of a nonhuman primate. *J. Neurosci.* 23, 8432–8444. doi: 10.1523/JNEUROSCI.23-23-08432.2003

Laje, R., and Buonomano, D. V. (2013). Robust timing and motor patterns by taming chaos in recurrent neural networks. *Nat. Neurosci.* 16, 925–933. doi: 10.1038/nn.3405

Lang, C. E., and Bastian, A. J. (1999). Cerebellar subjects show impaired adaptation of anticipatory EMG during catching. *J. Neurophysiol.* 82, 2108–2119. doi: 10.1152/jn.1999.82.5.2108

Larsell, O. (1967). *The Comparative Anatomy and Histology of the Cerebellum.* Minneapolis: University of Minnesota Press.

Lee, J., Kagamihara, Y., and Kakei, S. (2015). A new method for functional evaluation of motor commands in patients with cerebellar ataxia. *PLoS One* 10:e0132983. doi: 10.1371/journal.pone.0132983

Leiner, H. C., Leiner, A. L., and Dow, R. S. (1986). Does the cerebellum contribute to mental skills? *Behav. Neurosci.* 100, 443–454. doi: 10.1037/0735-7044.100.4.443

Lesage, E., Morgan, B. E., Olson, A. C., Meyer, A. S., and Miall, R. C. (2012). Cerebellar rTMS disrupts predictive language processing. *Curr. Biol.* 22, R794–R795. doi: 10.1016/j.cub.2012.07.006

Marr, D. (1969). A theory of cerebellar cortex. *J. Physiol.* 202, 437–470. doi: 10.1113/jphysiol.1969.sp008820

Martin, T. A., Keating, J. G., Goodkin, H. P., Bastian, A. J., and Thach, W. T. (1996). Throwing while looking through prisms. I. Focal olivocerebellar lesions impair adaptation. *Brain* 119, 1183–1198. doi: 10.1093/brain/119.4.1183

Matsuyama, K., and Drew, T. (1997). Organization of the projections from the pericruciate cortex to the pontomedullary brainstem of the cat: a study using the anterograde tracer Phaseolus vulgaris-leucoagglutinin. *J. Comp. Neurol.* 389, 617–641. doi: 10.1002/(sici)1096-9861(19971229)389:4<617::aid-cne6>3.0.co;2-3

Mazzoni, P., and Krakauer, J. W. (2006). An implicit plan overrides an explicit strategy during visuomotor adaptation. *J. Neurosci.* 26, 3642–3645. doi: 10.1523/JNEUROSCI.5317-05.2006

McNamee, D., and Wolpert, D. M. (2019). Internal models in biological control. *Annu. Rev. Control Robot. Auton. Syst.* 2, 339–364. doi: 10.1146/annurev-control-060117-105206

Medina, J. F., and Mauk, M. D. (2000). Computer simulation of cerebellar information processing. *Nat. Neurosci.* 3, 1205–1211. doi: 10.1038/81486

Miall, R. C., Christensen, L. O., Cain, O., and Stanley, J. (2007). Disruption of state estimation in the human lateral cerebellum. *PLoS Biol.* 5:e316. doi: 10.1371/journal.pbio.0050316

Middleton, F. A., and Strick, P. L. (1994). Anatomical evidence for cerebellar and basal ganglia involvement in higher cognitive function. *Science* 266, 458–461. doi: 10.1126/science.7939688

Miyashita, Y., and Nagao, S. (1984). Contribution of cerebellar intracortical inhibition to Purkinje cell response during vestibulo-ocular reflex of alert rabbits. *J. Physiol.* 351, 251–262. doi: 10.1113/jphysiol.1984.sp015243

More, H. L., and Donelan, J. M. (2018). Scaling of sensorimotor delays in terrestrial mammals. *Proc. Biol. Sci.* 285:20180613. doi: 10.1098/rspb.2018.0613

More, H. L., Hutchinson, J. R., Collins, D. F., Weber, D. J., Aung, S. K., and Donelan, J. M. (2010). Scaling of sensorimotor control in terrestrial mammals. *Proc. Biol. Sci.* 277, 3563–3568. doi: 10.1098/rspb.2010.0898

Morton, S. M., and Bastian, A. J. (2006). Cerebellar contributions to locomotor adaptations during splitbelt treadmill walking. *J. Neurosci.* 26, 9107–9116. doi: 10.1523/JNEUROSCI.2622-06.2006

Na, J., Sugihara, I., and Shinoda, Y. (2019). The entire trajectories of single pontocerebellar axons and their lobular and longitudinal terminal distribution patterns in multiple aldolase C-positive compartments of the rat cerebellar cortex. *J. Comp. Neurol.* 527, 2488–2511. doi: 10.1002/cne.24685

Nagao, S. (1992). Different roles of flocculus and ventral paraflocculus for oculomotor control in the primate. *Neuroreport* 3, 13–16. doi: 10.1097/00001756-199201000-00003

Nowak, D. A., Hermsdorfer, J., Rost, K., Timmann, D., and Topka, H. (2004). Predictive and reactive finger force control during catching in cerebellar degeneration. *Cerebellum* 3, 227–235. doi: 10.1080/14734220410019057

Nowak, D. A., Timmann, D., and Hermsdorfer, J. (2007). Dexterity in cerebellar agenesis. *Neuropsychologia* 45, 696–703. doi: 10.1016/j.neuropsychologia.2006.08.011

Pasalar, S., Roitman, A. V., Durfee, W. K., and Ebner, T. J. (2006). Force field effects on cerebellar Purkinje cell discharge with implications for internal models. *Nat. Neurosci.* 9, 1404–1411. doi: 10.1038/nn1783

Rilling, J. K., and Insel, T. R. (1998). Evolution of the cerebellum in primates: differences in relative volume among monkeys, apes and humans. *Brain Behav. Evol.* 52, 308–314. doi: 10.1159/000006575

Roitman, A. V., Pasalar, S., Johnson, M. T., and Ebner, T. J. (2005). Position, direction of movement, and speed tuning of cerebellar Purkinje cells during circular manual tracking in monkey. *J. Neurosci.* 25, 9244–9257. doi: 10.1523/jneurosci.1886-05.2005

Sanger, T. D., Yamashita, O., and Kawato, M. (2020). Expansion coding and computation in the cerebellum: 50 years after the Marr-Albus codon theory. *J. Physiol.* 598, 913–928. doi: 10.1113/JP278745

Schmahmann, J. D. (1991). An emerging concept. The cerebellar contribution to higher function. *Arch. Neurol.* 48, 1178–1187. doi: 10.1001/archneur.1991.00530230086029

Schmahmann, J. D. (2004). Disorders of the cerebellum: ataxia, dysmetria of thought, and the cerebellar cognitive affective syndrome. *J. Neuropsychiatry Clin. Neurosci.* 16, 367–378. doi: 10.1176/jnp.16.3.367

Schmahmann, J. D. (2019). The cerebellum and cognition. *Neurosci. Lett.* 688, 62–75. doi: 10.1016/j.neulet.2018.07.005

Schmahmann, J. D., and Pandya, D. N. (1989). Anatomical investigation of projections to the basis pontis from posterior parietal association cortices in rhesus monkey. *J. Comp. Neurol.* 289, 53–73. doi: 10.1002/cne.902890105

Schmahmann, J. D., and Pandya, D. N. (1991). Projections to the basis pontis from the superior temporal sulcus and superior temporal region in the rhesus monkey. *J. Comp. Neurol.* 308, 224–248. doi: 10.1002/cne.903080209

Schmahmann, J. D., and Pandya, D. N. (1993). Prelunate, occipitotemporal, and parahippocampal projections to the basis pontis in rhesus monkey. *J. Comp. Neurol.* 337, 94–112. doi: 10.1002/cne.903370107

Schmahmann, J. D., and Pandya, D. N. (1997). Anatomic organization of the basilar pontine projections from prefrontal cortices in rhesus monkey. *J. Neurosci.* 17, 438–458. doi: 10.1523/jneurosci.17-01-00438.1997

Schmahmann, J. D., Rosene, D. L., and Pandya, D. N. (2004). Motor projections to the basis pontis in rhesus monkey. *J. Comp. Neurol.* 478, 248–268. doi: 10.1002/cne.20286

Schmolesky, M. T., Wang, Y., Hanes, D. P., Thompson, K. G., Leutgeb, S., Schall, J. D., et al. (1998). Signal timing across the macaque visual system. *J. Neurophysiol.* 79, 3272–3278. doi: 10.1152/jn.1998.79.6.3272

Shadmehr, R., Smith, M. A., and Krakauer, J. W. (2010). Error correction, sensory prediction, and adaptation in motor control. *Annu. Rev. Neurosci.* 33, 89–108. doi: 10.1146/annurev-neuro-060909-153135

Shinoda, Y., Sugiuchi, Y., Futami, T., and Izawa, R. (1992). Axon collaterals of mossy fibers from the pontine nucleus in the cerebellar dentate nucleus. *J. Neurophysiol.* 67, 547–560. doi: 10.1152/jn.1992.67.3.547

Smith, M. A., and Shadmehr, R. (2005). Intact ability to learn internal models of arm dynamics in Huntington's disease but not cerebellar degeneration. *J. Neurophysiol.* 93, 2809–2821. doi: 10.1152/jn.00943.2004

Sokolov, A. A., Miall, R. C., and Ivry, R. B. (2017). The cerebellum: adaptive prediction for movement and cognition. *Trends Cogn. Sci.* 21, 313–332. doi: 10.1016/j.tics.2017.02.005

Sompolinsky, H., Crisanti, A., and Sommers, H.-J. (1988). Chaos in random neural networks. *Phys. Rev. Lett.* 61, 259–262. doi: 10.1103/PhysRevLett.61.259

Stoodley, C. J., and Schmahmann, J. D. (2009). Functional topography in the human cerebellum: a meta-analysis of neuroimaging studies. *NeuroImage* 44, 489–501. doi: 10.1016/j.neuroimage.2008.08.039

Strick, P. L. (1983). The influence of motor preparation on the response of cerebellar neurons to limb displacements. *J. Neurosci.* 3, 2007–2020. doi: 10.1523/jneurosci.03-10-02007.1983

Sugahara, F., Pascual-Anaya, J., Oisi, Y., Kuraku, S., Aota, S., Adachi, N., et al. (2016). Evidence from cyclostomes for complex regionalization of the ancestral vertebrate brain. *Nature* 531, 97–100. doi: 10.1038/nature16518

Sussillo, D., and Abbott, L. F. (2009). Generating coherent patterns of activity from chaotic neural networks. *Neuron* 63, 544–557. doi: 10.1016/j.neuron.2009.07.018

Tadayonnejad, R., Anderson, D., Molineux, M. L., Mehaffey, W. H., Jayasuriya, K., and Turner, R. W. (2010). Rebound discharge in deep cerebellar nuclear neurons *in vitro*. *Cerebellum* 9, 352–374. doi: 10.1007/s12311-010-0168-7

Tanaka, H., Ishikawa, T., and Kakei, S. (2019). Neural evidence of the cerebellum as a state predictor. *Cerebellum* 18, 349–371. doi: 10.1007/s12311-018-0996-4

Thach, W. T. (1970). Discharge of cerebellar neurons related to two maintained postures and two prompt movements. *J. Neurophysiol.* 33, 527–536. doi: 10.1152/jn.1970.33.4.527

Todorov, E. (2004). Optimality principles in sensorimotor control. *Nat. Neurosci.* 7, 907–915. doi: 10.1038/nn1309

Todorov, E., and Jordan, M. I. (2002). Optimal feedback control as a theory of motor coordination. *Nat. Neurosci.* 5, 1226–1235. doi: 10.1038/nn963

Tomasch, J. (1969). The numerical capacity of the human cortico-pontocerebellar system. *Brain Res.* 13, 476–484. doi: 10.1016/0006-8993(69)90261-3

Tomatsu, S., Ishikawa, T., Tsunoda, Y., Lee, J., Hoffman, D. S., and Kakei, S. (2016). Information processing in the hemisphere of the cerebellar cortex for control of wrist movement. *J. Neurophysiol.* 115, 255–270. doi: 10.1152/jn.00530.2015

Tseng, Y. W., Diedrichsen, J., Krakauer, J. W., Shadmehr, R., and Bastian, A. J. (2007). Sensory prediction errors drive cerebellum-dependent adaptation of reaching. *J. Neurophysiol.* 98, 54–62. doi: 10.1152/jn.00266.2007

van Kan, P. L., Houk, J. C., and Gibson, A. R. (1993). Output organization of intermediate cerebellum of the monkey. *J. Neurophysiol.* 69, 57–73. doi: 10.1152/jn.1993.69.1.57

Wagner, M. J., Kim, T. H., Kadmon, J., Nguyen, N. D., Ganguli, S., Schnitzer, M. J., et al. (2019). Shared cortex-cerebellum dynamics in the execution and learning of a motor task. *Cell* 177, 669.e24–682.e24. doi: 10.1016/j.cell.2019.02.019

Wang, D., Buckner, R. L., and Liu, H. (2013). Cerebellar asymmetry and its relation to cerebral asymmetry estimated by intrinsic functional connectivity. *J. Neurophysiol.* 109, 46–57. doi: 10.1152/jn.00598.2012

Werbos, P. J. (1990). Backpropagation through time: what it does and how to do it. *Proc. IEEE* 78, 1550–1560. doi: 10.1109/5.58337

Wetts, R., Kalaska, J. F., and Smith, A. M. (1985). Cerebellar nuclear cell activity during antagonist cocontraction and reciprocal inhibition of forearm muscles. *J. Neurophysiol.* 54, 231–244. doi: 10.1152/jn.1985.54.2.231

Witter, L., Canto, C. B., Hoogland, T. M., de Gruijl, J. R., and De Zeeuw, C. I. (2013). Strength and timing of motor responses mediated by rebound firing in the cerebellar nuclei after Purkinje cell activation. *Front. Neural Circuits* 7:133. doi: 10.3389/fncir.2013.00133

Wolpert, D. M., and Miall, R. C. (1996). Forward models for physiological motor control. *Neural Netw.* 9, 1265–1279. doi: 10.1016/s0893-6080(96)00035-4

Wolpert, D. M., Miall, R. C., and Kawato, M. (1998). Internal models in the cerebellum. *Trends Cogn. Sci.* 2, 338–347. doi: 10.1016/s1364-6613(98)01221-2

Wu, H. S., Sugihara, I., and Shinoda, Y. (1999). Projection patterns of single mossy fibers originating from the lateral reticular nucleus in the rat cerebellar cortex and nuclei. *J. Comp. Neurol.* 411, 97–118. doi: 10.1002/(sici)1096-9861(19990816)411:1<97::aid-cne8>3.0.co;2-o

Yamamoto, K., Kawato, M., Kotosaka, S., and Kitazawa, S. (2007). Encoding of movement dynamics by Purkinje cell simple spike activity during fast arm movements under resistive and assistive force fields. *J. Neurophysiol.* 97, 1588–1599. doi: 10.1152/jn.00206.2006

Conflict of Interest: The authors declare that the research was conducted in the absence of any commercial or financial relationships that could be construed as a potential conflict of interest.

frontiers in Systems Neuroscience

ORIGINAL RESEARCH
published: 10 November 2020
doi: 10.3389/fnsys.2020.475948

Cerebellar Cortex 4–12 Hz Oscillations and Unit Phase Relation in the Awake Rat

*Maxime Lévesque[1†], HongYing Gao[2†], Carla Southward[3], J. M. Pierre Langlois[4], Clément Léna[2] and Richard Courtemanche[3]**

[1]Department of Neurology and Neurosurgery, Montreal Neurological Institute, McGill University, Montréal, QC, Canada, [2]Institut de Biologie, CNRS UMR 8197–U 1024, École Normale Supérieure, Paris, France, [3]Department of Health, Kinesiology and Applied Physiology, Center for Studies in Behavioral Neurobiology, Concordia University, Montréal, QC, Canada, [4]Département de Génie Informatique et Génie Logiciel, Polytechnique Montréal, Montréal, QC, Canada

Oscillations in the granule cell layer (GCL) of the cerebellar cortex have been related to behavior and could facilitate communication with the cerebral cortex. These local field potential (LFP) oscillations, strong at 4–12 Hz in the rodent cerebellar cortex during awake immobility, should also be an indicator of an underlying influence on the patterns of the cerebellar cortex neuronal firing during rest. To address this hypothesis, cerebellar cortex LFPs and simultaneous single-neuron activity were collected during LFP oscillatory periods in the GCL of awake resting rats. During these oscillatory episodes, different types of units across the GCL and Purkinje cell layers showed variable phase-relation with the oscillatory cycles. Overall, 74% of the Golgi cell firing and 54% of the Purkinje cell simple spike (SS) firing were phase-locked with the oscillations, displaying a clear phase relationship. Despite this tendency, fewer Golgi cells (50%) and Purkinje cell's SSs (25%) showed an oscillatory firing pattern. Oscillatory phase-locked spikes for the Golgi and Purkinje cells occurred towards the peak of the LFP cycle. GCL LFP oscillations had a strong capacity to predict the timing of Golgi cell spiking activity, indicating a strong influence of this oscillatory phenomenon over the GCL. Phase-locking was not as prominent for the Purkinje cell SS firing, indicating a weaker influence over the Purkinje cell layer, yet a similar phase relation. Overall, synaptic activity underlying GCL LFP oscillations likely exert an influence on neuronal population firing patterns in the cerebellar cortex in the awake resting state and could have a preparatory neural network shaping capacity serving as a neural baseline for upcoming cerebellar operations.

Keywords: oscillation, phase-locking, cerebellum, rhythmicity, network

OPEN ACCESS

Edited by:
Richard Apps,
University of Bristol, United Kingdom

Reviewed by:
Guy Chéron,
Université libre de Bruxelles, Belgium
Kathryn Bennett,
University of Bristol, United Kingdom

****Correspondence:***
Richard Courtemanche
richard.courtemanche@concordia.ca

[†]These authors have contributed equally to this work

Received: *31 May 2019*
Accepted: *13 October 2020*
Published: *10 November 2020*

Citation:
Lévesque M, Gao H, Southward C, Langlois JMP, Léna C and Courtemanche R (2020) Cerebellar Cortex 4–12 Hz Oscillations and Unit Phase Relation in the Awake Rat. Front. Syst. Neurosci. 14:475948. doi: 10.3389/fnsys.2020.475948

INTRODUCTION

With its systematic structure, the cerebellum possesses inherent modularity supporting the flow of information (Voogd and Glickstein, 1998; Llinás et al., 2004; Ito, 2010), and its coding capacity has been the object of multiple decades of neurophysiological inquiry (Eccles et al., 1967; Ito, 2006; Heck, 2015). Some of the mechanisms uncovered focus on oscillatory activity: one way

to control the spatiotemporal flow of information across modules is through interconnected oscillating networks: these can be variably coupled to support information flow according to specific frequencies or multiple modes (Fries, 2015; Maris et al., 2016). In turn, these oscillations can act as a modulator or amplifier of information throughput across and within circuits (Akam and Kullmann, 2010).

Recent reviews highlight the capacity of cerebellar cortex circuits to harbor rhythmic activity, with potential functional roles, including modulating the timing of cerebellar neuronal firing (Isope et al., 2002; D'Angelo et al., 2009; De Zeeuw et al., 2011; Courtemanche et al., 2013). For instance, olivo-cerebellar neurons carry an intrinsic 6–10 Hz intracellular rhythm able to influence the timing of Purkinje cell complex spikes across the cerebellar cortex (Welsh et al., 1995; Lang et al., 1999; Llinás, 2009). The granule cell layer (GCL) also shows local field potential (LFP) rhythmic activity, namely at 10–25 Hz in the monkey (Pellerin and Lamarre, 1997; Courtemanche et al., 2002), and 4–12 Hz in the rodent (Hartmann and Bower, 1998; O'Connor et al., 2002; Dugué et al., 2009). High-frequency oscillations (150–300 Hz) have also been detected in the Purkinje cell and molecular layers, or cerebellar cortex surface (Chéron et al., 2004; Middleton et al., 2008; de Solages et al., 2008; Groth and Sahin, 2015). Finally, slower (<1 Hz) oscillations have been recorded in the cerebellar cortex of rodents (Ros et al., 2009) and tottering mouse (Chen et al., 2009). Overall, these LFP oscillations provide indirect evidence of rhythmic synaptic input that could serve to influence the firing patterns of cerebellar networks, and their temporal coordination, influencing neuronal coding and communication (De Zeeuw et al., 2011; Courtemanche et al., 2013).

Cerebellar cortex GCL oscillations between 4 and 25 Hz are present at rest (Hartmann and Bower, 1998; Dugué et al., 2009; D'Angelo et al., 2009; Courtemanche et al., 2013), and can enhance cerebro-cerebellar synchronization even though these rhythms are in distant structures (O'Connor et al., 2002; Courtemanche and Lamarre, 2005). Rhythms in the 5–30 Hz range have indeed shown capacity to dynamically link distant systems *via* local and long-range neuronal firing and connections (Bullock, 1997; Buzsáki and Draguhn, 2004; Buzsáki, 2006; Senkowski et al., 2008). It is well-established that LFPs are related to the synaptic activity (Buzsáki and Draguhn, 2004): single-unit activity should thus have a role in how GCL LFPs synchronize with cerebral cortex LFPs. However, GCL oscillations do not have a readily defined substrate, though granule and Golgi cells should be implicated, the latter coupled *via* gap junctions (Courtemanche et al., 2002; Maex and De Schutter, 2005; D'Angelo and de Zeeuw, 2009; Simões de Souza and De Schutter, 2011). Indeed, GCL oscillations show a strong relation to granule cell firing (Pellerin and Lamarre, 1997; Hartmann and Bower, 1998; Courtemanche et al., 2002) but the extent of the influence across the layers has not been assessed. Granule cells have rhythm-permissive cellular properties and could be part of a resonant network (D'Angelo et al., 2001, 2009). Intrinsic oscillatory capacities of the GCL local network have been modeled (Maex and De Schutter, 2005; Dugué et al., 2009; Honda et al., 2011; Simões de Souza and De Schutter, 2011; Sudhakar et al., 2017). For instance, Golgi cell-mediated feedforward and feedback loops (Forti et al., 2006; D'Angelo, 2008; Dugué et al., 2009; Galliano et al., 2010), and Golgi-Golgi electrical synapses could be implicated in the rhythm formation (Dugué et al., 2009; Vervaeke et al., 2010; Simões de Souza and De Schutter, 2011; Robinson et al., 2017). Further in the circuit, in a limited dataset, we saw that Purkinje cell simple spikes (SSs) can follow the 10–25 Hz GCL rhythm, contrary to complex spikes (Courtemanche et al., 2002). In contrast, for a slow <1 Hz rhythm, only complex spikes can follow the activity (Ros et al., 2009), and fast Purkinje cell layer oscillations can entrain SSs (Chéron et al., 2004; Middleton et al., 2008; de Solages et al., 2008). It is unclear if this oscillatory activity can influence the cerebellar nuclei, but the synchronization of SSs promotes the downstream activation of cerebellar nuclei (Person and Raman, 2012a,b).

This report focuses on the relationship between cerebellar cortex units recorded using electrodes and tetrodes with simultaneously recorded GCL LFPs in the awake rat, putting a particular focus on unit phase relation and rhythmicity. We recorded Golgi and Purkinje cell SSs and evaluated their firing patterns concerning 4–12 Hz GCL LFP oscillations. We hypothesized that the unit firing would be related to those oscillations and that Golgi firing in the GCL would be more phase-locked to the oscillations than the SSs, principally because of the diverging/converging connections between the GCL and Purkinje cells.

MATERIALS AND METHODS

Data for this study were collected at Concordia University (Montréal, QC, Canada), and École Normale Supérieure (Paris, France), using the same rat strain, along with similar recording techniques and analysis parameters.

Animals and Behavior

Seven (7) male Sprague–Dawley rats (four rats/Charles River, St-Constant, QC; three rats/Institut de Biologie vivarium, ENS, ∼400–500 g) were initially handled and habituated to the lab environment. Once implanted with electrodes, they were housed individually on an 8:00 AM to 8:00 PM reversed light/dark schedule. Recording sessions were conducted in a Lafayette Instruments (Lafayette, IN, USA) test chamber or in a custom dark Plexiglas field arena. Rats were kept in the test area for a period of 1–2 h under dim light and quiet conditions. Most rats explored the area for the first few minutes, then calmed down and stayed relatively immobile; they were kept attentive by the experimenter. All animal handling, care, and surgical procedures were following the guidelines of the respective animal national welfare councils and approved by the respective University Animal Research Ethics Committees.

Surgical Procedures

The surgery and electrophysiological methods were similar to Dugué et al. (2009) and Gao et al. (2011). Briefly, four rats were mounted with a Neuralynx 12-drive electrode holder (Bozeman, MO, USA) for recordings in the posterior

cerebellum; three animals were mounted with a custom headstage housing 1–4 quartz tetrodes (Thomas Recording GmbH, Giessen, Germany). Electrode and tetrode shapes and impedances were optimally chosen to capture both LFP and unit signals, and electrodes could be moved longitudinally with precision (described below), permitting to isolate units during the experiment.

Similar procedures were followed for surgery for both sets of animals. Body temperature was continuously monitored with a rectal probe and maintained with a heating pad. General anesthesia was induced either with (1) an i.m. injection of ketamine hydrochloride (Ketaset, 100 mg/kg) and xylazine (AnaSed, 2.2 mg/kg) and maintained by supplemental injections as required; or with (2) a ketamine-xylazine mixture, and maintained with a mixture of isoflurane (0.5–1.5%) and oxygen. All rats were then mounted on a stereotaxic instrument. To reduce bronchial secretions, rats were injected with 0.04 mg/kg s.c. of atropine sulfate before inducing anesthesia. The skull and dura over the posterior cerebellum were removed using a dental drill and precision forceps. The headstage was implanted and fixed in the skull with screws in the frontal and parietal bones above the cerebellar cortex with dental cement. At the end of the surgery, the wound was carefully sutured and covered with antibiotic cream. Animals were allowed to recover several days before recording.

Electrophysiological Setups and Recordings

Methods for LFP and unit recordings closely followed published procedures (Dugué et al., 2009; Gao et al., 2011). For the multiple single electrode implants, the implantation target was at Bregma −12, lateral 2.5–3, aiming for the crus II/paramedian lobule. One bone screw served as the ground contact and a stainless-steel needle (19 G) placed in brain tissue, providing a large cylindrical contact at the surface of the cerebellum, served as reference. Three to seven tungsten microelectrodes with shank diameters of 75 μM and impedances around 1 MΩ (0.2–1.5 MΩ–FHC Inc., Bowdoin, ME, USA) were inserted into individual drives, mounted onto the headstage. Each microelectrode could be moved independently using a small screwdriver to advance and retract the electrode. LFP data were on-line filtered between 1 and 475 Hz and sampled at 2,003 Hz. For unit activity, the signal was filtered between 600 and 6,000 Hz and sampled at 32 kHz. Spike isolation was achieved by lowering or retracting the individual microdrives (160 μm/turn precision, with usual increments of about $\frac{1}{4}$ or $\frac{1}{2}$ turn, so 40–80 μm, or even less when isolating a unit). Adjustments on spike detection were then performed on the Neuralynx DAS software 32-point digitized thresholded waveform, overlaid to verify reproducibility. Also, the analog unit signal was monitored for waveform stability on an oscilloscope and spike loudspeaker sound output, useful during microelectrode positioning. Mostly one single unit, sometimes two, could be isolated at a site.

For three animals, tetrodes were implanted in a lightweight tetrode headstage holding multiple microdrives, each with a reference and 1–4 quartz tetrodes (constructed as four platinum/tungsten-cores in a quartz rod, sculpted with a sharp tip). The microdrives were moved *via* a cubic screw mounted on a threaded rod. Tetrodes were protected by a stainless steel tube and a 30 G beveled guide tube. Drives were enveloped in a grounded conic piece of cardboard and aluminum foil. The tips of the tetrodes were cleaned and gold-plated to lower their impedance to 0.1–0.3 MΩ. Signals were acquired with a Tucker-Davis Technologies System 3 (TDT, Alachua, FL, USA), filtered at 0.1 Hz to 8 kHz with a Butterworth filter, then differentially amplified, sampled at 25 kHz, and stored to disk for off-line analysis. During tetrode adjustment and recordings, lowered in increments of 10–50 μm, the neuronal activity was continuously monitored through loudspeakers and displayed on a computer screen. To isolate spikes, continuous wide-band extracellular recordings were first filtered off-line with a two-pole Butterworth 500 Hz high-pass filter. Spikes were then discriminated by thresholding the filtered trace and extracting the main parameters of their waveform (width and amplitude on the four channels). LFPs were also extracted from one of the tetrode channels wide-band signal, with the initial signal downsampled at 2,003 Hz and low-pass filtered at 475 Hz.

Recording placement of at least one single microelectrode or tetrode in an animal would be optimized for GCL activity with oscillatory LFPs: this would be monitored on-line, often with phasic multiunit activity serving as a guide. The electrode site would be further adjusted if a putative GCL unit was nearby. The other probes could then be independently moved to seek other units, searching for Golgi unit activity in the GCL (which usually had a moderate firing rate), or sharper cell activity in the neighboring Purkinje cell layer (which usually had a much faster firing rate). The rats were brought to the laboratory for durations of up to 90 min of quiet rest, and the rat would be kept periodically attentive by providing small food pellets and water in the recording chamber. Continuous recording sessions lasted up to 20 min.

Data Analysis

LFP and unit signal processing and quantitative analyses were performed using NeuroExplorer (Nex Technologies, Littleton, MA, USA) and MATLAB (MathWorks, Natick, MA, USA), the latter with routines based on standardized functions (e.g., signal processing toolbox). LFP periods of strong oscillations, in contrast with periods when oscillations were weaker, were identified using spectrograms, calculated using the discrete short-time Fourier transform to evaluate rhythmicity. A multi-parametric algorithm was used to identify oscillatory periods in the 4–12 Hz band of the spectrogram, corresponding with rodent GCL oscillations from other *in vivo* studies (Hartmann and Bower, 1998; O'Connor et al., 2002; Dugué et al., 2009; Frederick et al., 2014; Robinson et al., 2017). This algorithm has been used previously to detect and process various rhythmic signals [gamma (Lévesque et al., 2009), and theta (Berryer et al., 2016)]. In certain cases, coherence spectrograms were also used to evaluate LFP synchronization. The first step consisted of a spectrogram analysis, where data sampled at 2,003 Hz were decimated by a factor of 15 after being low-pass filtered by a

100th order FIR filter. The spectrogram was then elaborated from the dataset, separated into one-s intervals (134 points) to which a Hamming window was applied, and the windows were overlapped by 50%. The discrete Fourier transforms were evaluated over 256 points with zero paddings. A gamma correction with a factor of 0.2 was applied to the spectrogram to improve contrast with random noise. Following, for each time window, the algorithm identified the peak frequency in the band of interest and calculated the energy within a 1 Hz band centered on this peak. To be considered a valid candidate, a peak must have met time and frequency domain criteria, with parameters adjusted to the analyzed trace. To better describe, here are some example settings for one particular session: the energy within the peak was set at least at 30% of the largest peak within a 60-s window (time-domain criterion), and containing at least 40% of the band energy at that time (frequency domain criterion). This identified an oscillatory period composed of a succession of peaks with a determinate track in time and frequency. In those, the relative peak intensities must not have varied in time by more than 100% per second, successive peak frequencies must not have varied by more than 7.5 Hz per second, and there must have been a continuous track of candidate peaks at least 5 s long, and the oscillatory period had to be longer than or equal to a 3 s duration. These parameters were adjusted for each recording location and session. This would permit detections of periods of oscillation, as shown in the example in **Figure 2**. To compare the spike-LFP oscillation over several cycles, we opted for a duration threshold that allowed to characterize a strong oscillatory influence, with salient oscillatory periods lasting long enough to potentially indicate a state-like influence on the neurophysiological signal. The parameters were selected through systematic data analysis and had the advantage of standardizing the detection of oscillation events over all data sets, eliminating bias. LFP traces were normalized using a *z*-score transform, and the power spectral density was also normalized to the maximum values in the dataset. The end result was a list of "oscillation periods" throughout the recording file and interspersed in between those, periods of weaker or no oscillation. **Figure 2** illustrates detected periods for 50 s of LFPs, delineated with a red box.

For unit data, the digitized spikes were processed for single-unit identification. For single electrode recordings, this was done in SpikeSort (Neuralynx, Bozeman, MT, USA) in manual mode, focusing on spikes corresponding to an adapted extracellular action potential shape template, estimated from the overlaid spikes (based on >100 detections). Secondary elements were also used such as the 2-D scatterplot distribution of the spike amplitude and duration values (e.g., peak height, valley depth, action potential duration). Interspike intervals (ISIs) of less than 1 ms were removed. Generally, units with fewer than 2% of the ISIs under 3 ms were kept. This methodology is based on parameters used in articles using similar recording techniques (Csicsvari et al., 1998; Stratton et al., 2012; Lévesque et al., 2016, 2018; Chen et al., 2018). For tetrode recordings, a similar process was used; data were hand-clustered by polygon-cutting in two-dimension projections of the parameter space using Xclust [(Davidson et al., 2009) and Matt Wilson, MIT]. Parameter space was centered on spike amplitude and width properties. The quality of clustering was evaluated by inspecting the autocorrelograms of the units. The unit classification was based on electrode tip localization relative to the surface and the GCL (with the characteristic dense background activity), the action potential properties (spike amplitude or presence of a rare complex spike), and the inter-spike interval properties [such as the median ISI vs. median absolute difference (MAD) ISI relation, as presented in Vos et al., 1999]. The indirect nature of this classification makes us qualify our cell types as putative (see "Limitations" section), but similar in properties to previously reported. The database of units is described in "Database of Units" section.

The relation between the timing of single-unit activity and LFPs was established by cross-correlating the spike train with events representing detected LFP peaks (FindPeaks, Tom O'Haver, U. Maryland; which was later included in the MATLAB functions) during oscillatory periods (Courtemanche et al., 2003). The cross-correlation between the LFP peak events and the spike events was calculated, with the LFP peak used as the reference point (Lamarre and Raynauld, 1965; Gerstein, 1999; Courtemanche et al., 2002, 2003). To establish the significance of the spike-LFP relationship, an index was computed based on the cross-correlogram for each unit (Destexhe et al., 1999). We computed artificial controls, using 50 or more artificial spike trains generated with randomized interspike delays (equal number of spikes as the original spike train, so isofrequency). For each artificial spike train, an LFP peak-triggered histogram with mean and SD for each 10 ms bin was processed. Within two cycles on either side (250 ms, corresponding to two cycles at 4 Hz), peaks above or valleys below 2 SD from the mean of the spike-shuffled control histogram were then identified in the LFP-triggered cross-correlogram peaks. LFP rhythmic modulation at this frequency will usually influence multiple consecutive bins; consequently, following this detection, a summation of counts from seven bins, three before the peak, the one on the peak, and three after, gave a "density" count for the detection. Seven 10-ms bins (70 ms) correspond to $\frac{1}{2}$ cycle at 14 Hz, chosen to follow faster-modulated units. This summation was divided by the median count for the overall cross-correlogram to account for the general quantity of collisions, providing values moving about around 1. Finally, a value of 7 was subtracted to resemble a general count per bin, as the sum of 7 bins would have values around 7. We termed this index the phase lock index or PLI. Units with a high PLI would thus show a strong spike-LFP relationship. The spike-LFP phase relationship, for each cell with a significant LFP-triggered histogram peak, was computed using the following equation: phase of peak (rad) = [time of peak (in ms) $\times$ 2π] /cycle time (ms; Fisher, 1995; Perez-Orive et al., 2002). This permitted to produce of a polar histogram of the spike–LFP phase relationship that could be generated for the group of units.

In the same way, an algorithm based on the 2 SD shuffling of spikes was also used for determining the significance of the spiking autocorrelation peaks: a rhythmicity index (RI),

using the height of the peaks or the depth of the valleys when located outside the 2 SD threshold, adapted from previous methods (Sugihara et al., 1995; Lang et al., 1999). The difference in amplitude between the detected peak/valley and the next valley/peak within half a cycle was calculated (Sugihara et al., 1995); for instance, if a significant peak was detected at 120 ms, we calculated the difference in amplitude between this peak and a valley between 60 and 180 ms. The summation of peak/valley distances (that were different from the shuffled values) permitted to calculate the RI; this value is above zero then permitted to define if the cell was oscillatory.

Histology

After the last recording session, electrolytic lesions (200 μA, 45 s, anodal) were made in the cerebellar cortex at selected sites where oscillations of single units were found, while rats were under ketamine-xylazine anesthesia. Two days later, rats were deeply anesthetized with ketamine-xylazine and perfused through the heart using a buffered 10% formalin–0.9% saline solution. The brains were removed and kept in 10% formalin for at least 48 h. They were then put in a 20% sucrose-formalin solution for another 48 h. The brains were frozen in pulverized dry ice and then sliced in a cryostat. The 40-μm thick sections were mounted on glass slides coated with gelatin. The slides were stained using a Cresyl Violet solution. The location of the lesions was evaluated following the denomination in the Paxinos and Watson (1998) atlas and electrode tracks were reconstructed for localization of recording sites.

RESULTS

Cerebellar Cortex GCL Oscillations in the Awake Rodent

Figure 1 presents Golgi cell spike activity and simultaneously recorded LFPs at three different sites in the posterior lobe cerebellum (three LFP traces, LFP1–3, **Figure 1A**). For each trace, the corresponding power spectral density signal was computed and is shown in **Figure 1B**. For LFP1, single-unit activity simultaneously recorded with the LFP is shown. For this experiment, the location of electrode #1, corresponding to LFP1, was marked by an electrolytic lesion (**Figure 1C**, and inset). The other recording site from a nearby electrode sharing

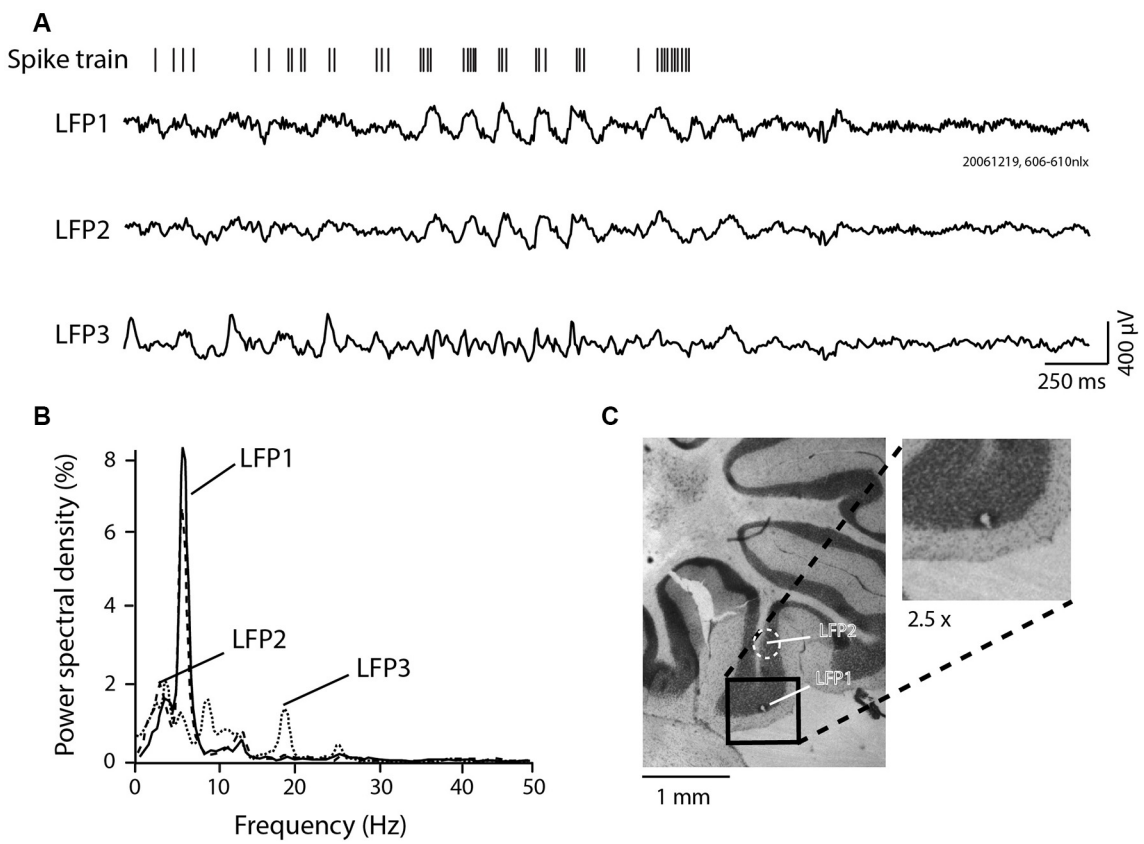

FIGURE 1 | Local field potential (LFP) 4–12 Hz granule cell layer (GCL) oscillations recorded in the posterior lobe of the awake rat. **(A)** GCL activity recorded at three different sites (three LFP traces, LFP1, 2, and 3), with corresponding single unit Golgi spike train recorded at the same site as LFP1. Notice the relative similarity between LFP1 and LFP2, with LFP3 being relatively different. Also, notice the in-phase spiking for the spike trace relative to LFP1. **(B)** Power spectral density results for each LFP shown in panel **(A)**. **(C)** Lesion made in the paramedian lobule GCL, at the site of recording for LFP1, with the relative localization of the LFP2 recording site. Inset: Magnification (2.5×) of the lesion site.

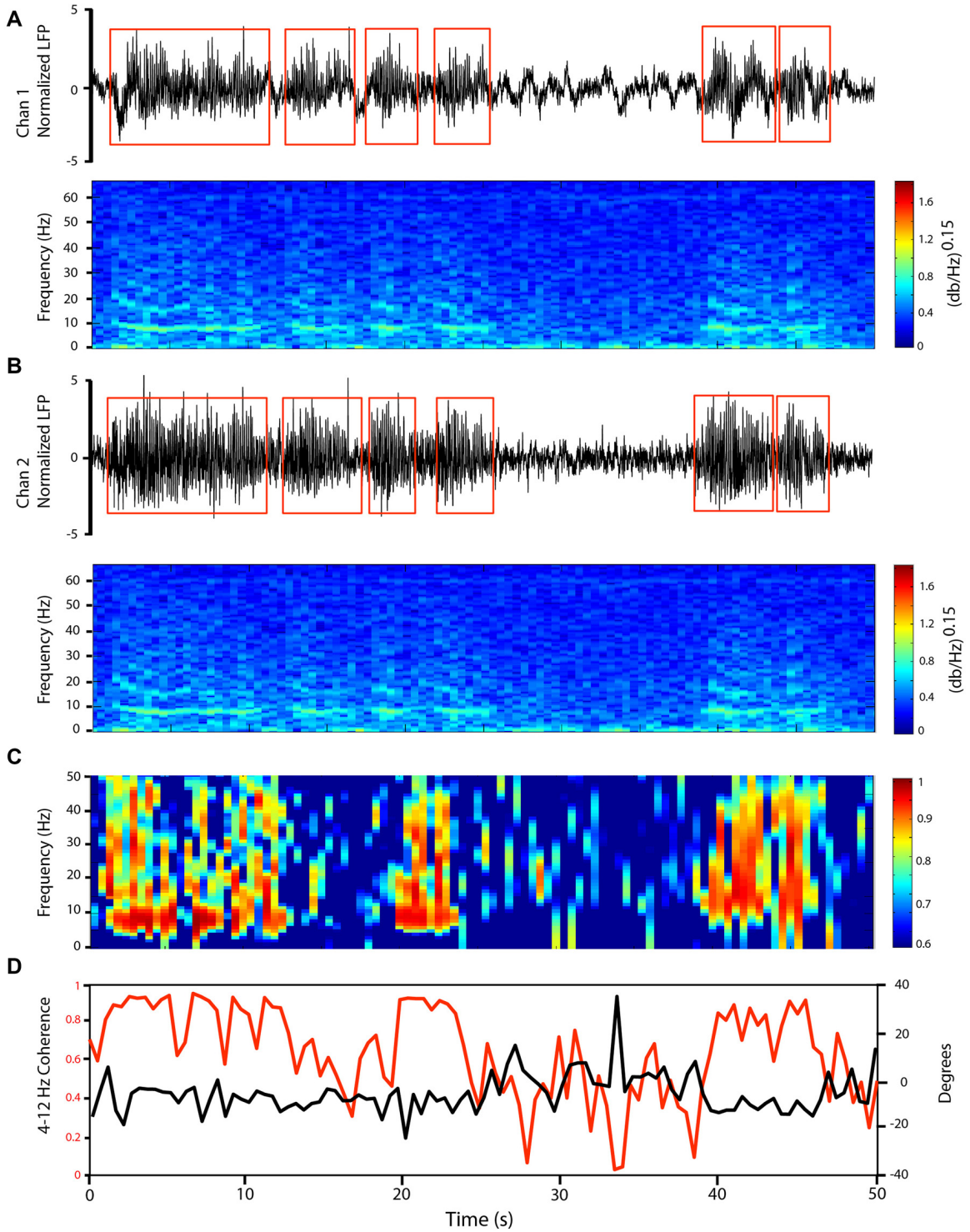

FIGURE 2 | LFP oscillations at 4–12 Hz in the cerebellar cortex GCL show variable coherence patterns across time. Simultaneous GCL LFP recordings from two microelectrodes distanced ∼3 mm (Chan 1 in paramedian lobule, Chan 2 in Crus II). **(A,B)** Simultaneously recorded GCL LFPs (top) and corresponding frequency spectrogram (bottom) showing changes in oscillatory activity through time. LFP trace amplitude *z*-score normalized, to perform oscillatory episode detection. Detected episodes of oscillation are represented by the red square box. Frequency spectrogram shown with 1-s windows. **(C)** Coherence spectrogram, 1-s windows, showing 0–50 Hz coherence patterns in time. **(D)** 4–12 Hz Coherence (red line), and corresponding phase lag (black line) between the two LFP traces.

a similar track, LFP2, is also indicated on the histological section, located 0.96 mm above the lesion, in the GCL or the GCL-white matter border. Both LFP1 and LFP2 were thus recorded in the paramedian lobule. LFP3 was recorded in a different plane, at a similar depth as the lesion, yet also in the cerebellar cortex from the neighboring multiunit activity, likely in the anterior copula of the pyramis region (not shown). As can be seen from the figure, the simultaneously recorded LFP activity differed at the three individual recording sites. LFP1 and LFP2 appear more similar: these were closer and presumably both in the GCL. A period of oscillatory activity is evident around the midpoint of the recording trace, for LFP1 and LFP2. LFP3 was not oscillatory in the 4–12 Hz range. The power spectral density analysis in **Figure 1B** confirms the similar oscillations on LFP1 and LFP2. Golgi unit activity simultaneously recorded with the LFP1 oscillations showed bursts occurring in-phase with the oscillation cycles.

As another way to approach the local nature of the LFP, we provide an example of the effect of the presence of oscillations on cerebellar inter-electrode synchrony. The GCL oscillations could synchronously affect neighboring electrodes: **Figure 2** shows recordings from two electrodes within the posterior lobe GCL, one (Chan l) in the paramedian lobule, and the second (Chan 2) in Crus II. The 4–12 Hz LFP oscillations showed waxing and waning qualities at ∼8 Hz on both channels, as seen on the power spectral density spectrogram (**Figures 2A,B**). Our detected periods (see "Materials and Methods" section) with strong 4–12 Hz oscillations are shown on the two LFP channels. In many instances, multiple channels could show simultaneous oscillations. In optimal conditions, these oscillation periods could last several seconds (**Figure 2**). Detected oscillation periods (which had to last longer than 3 s) would last on average 4.5 s, and on average would be present 20.9 ± 13.0% of the total recording time. During oscillations periods, the 4–12 Hz oscillations could be synchronized between the two traces, as can be seen on the coherence spectrogram (**Figures 2C,D**). To illustrate, we show a 50-s recording example with two electrodes in the rodent awake resting cerebellum. From the 4–12 Hz coherence spectrogram (**Figures 2C,D**), in the presence of oscillations, coherence values would reach 0.9 for long periods (e.g., 40–48 s). During these periods of stronger coherence, the phase relationship between the two traces was around −10 degrees, so close to in-phase. In out-of-oscillation periods (e.g., 25–40 s), the coherence would drop markedly, with accompanying phase variations. To further document the effect of oscillations on coherence, we analyzed the alpha/theta coherence between electrodes in three of our rats, with three sessions each, in a dataset of over 5,000 detected periods with at least one electrode with detected oscillations, and an overall pool of over 28,000 time periods (see **Supplementary Data**). We saw that when oscillations are present on at least one electrode, there would always be an increase in coherence. As this oscillatory phenomenon can serve to describe network coherence in the cerebellar cortex, we next investigated how LFPs were related to unit firing, providing an indirect but useful view of the effects of rhythmic synaptic inputs on specific neuronal groups.

TABLE 1 | The number of single units recorded and classified in the Golgi and Purkinje cell simple spike (SS) groups.

Group	*n*	Firing rate (spikes/s)	Median ISI (ms)	Units with simultaneous 4–12 Hz LFP oscillations
Golgi	46	7.1 (± 5.2)	72.7 (± 36.8)	74% (34/46)
Purkinje cell SS	126	40.6 (± 24.1)*	24.6 (± 12.7)	64.3% (81/126)

*We show the average firing rate and the average median ISI (±standard deviation). Approximately two-thirds of the unit sample recorded in each group had simultaneous 4–12 Hz LFP oscillations (*t-test, $p < 0.05$, Golgi vs. SS).*

Database of Units

A total of 207 cells were isolated with the microelectrodes and tetrodes, and recorded simultaneously with the LFPs, and were classified by neuronal type. Of these, we managed to capture 115 stable cells with the simultaneous presence of 4–12 Hz LFP oscillations. Descriptive data on our sample is given in **Table 1**, and the classification is further detailed below.

The identified single units had variable extracellular firing properties. During our recordings, these were initially classified based on: (1) the location of the isolated cell concerning the track and the background activity (i.e., the cerebellar cortex layer), with the typical GCL dense multiunit activity, or the sparser sharp fast-spiking Purkinje cell SSs; and (2) the action potential shape and duration, along with the rare co-occurrence of the occasional complex spike for Purkinje cells. Because our approach focused on GCL oscillations, it should be noted that our search for units was GCL-centric, and we did not seek out complex spike recordings. **Figure 3** displays certain typical spike firing characteristics of the units. To further refine our classification, we also used the offline identification method of Vos et al. (1999), which graphically compares the median of the inter-spike interval and the median absolute difference of the ISI (MAD ISI) to identify the groups of spikes corresponding to a given cell type. The median ISI was calculated for 20 consecutive bins of 10 spikes. For the same 20 consecutive bins, the MAD ISI representing the median difference between each ISI and the median ISI was obtained. **Figure 3A** provides the clustered distribution of a representative sample of the Golgi and Purkinje cell types. Evident are the differences between our two identified subpopulations of spikes: the two-dimensional spread of the Golgi spike values is more spread out, while the Purkinje cell SS values were all aggregated towards the graph origin (**Figure 3A**). A representative ISI histogram for a Golgi spike is shown in **Figure 3B**, while the equivalent for a Purkinje cell SS is shown in **Figure 3C**. Using those methods, out of 207 recorded isolated units, spikes were classified as coming from either putative Golgi cells (n = 46) or Purkinje cells SSs (n = 126). The remaining 35 isolated cells were classified as coming from either Purkinje cell complex spikes (n = 3, easily identified larger spikes with after-ripples coming from Purkinje cell layer or molecular layer), mossy fibers (n = 8) or were classified as isolated spikes from unidentified cells (n = 24), as their respective 2-D median ISI vs. MAD ISI distribution was different from typical Purkinje cell SSs or Golgi cell spikes. Overall, our Golgi cells had a mean firing rate around 7 Hz (see **Table 1**) and a median ISI in the range of

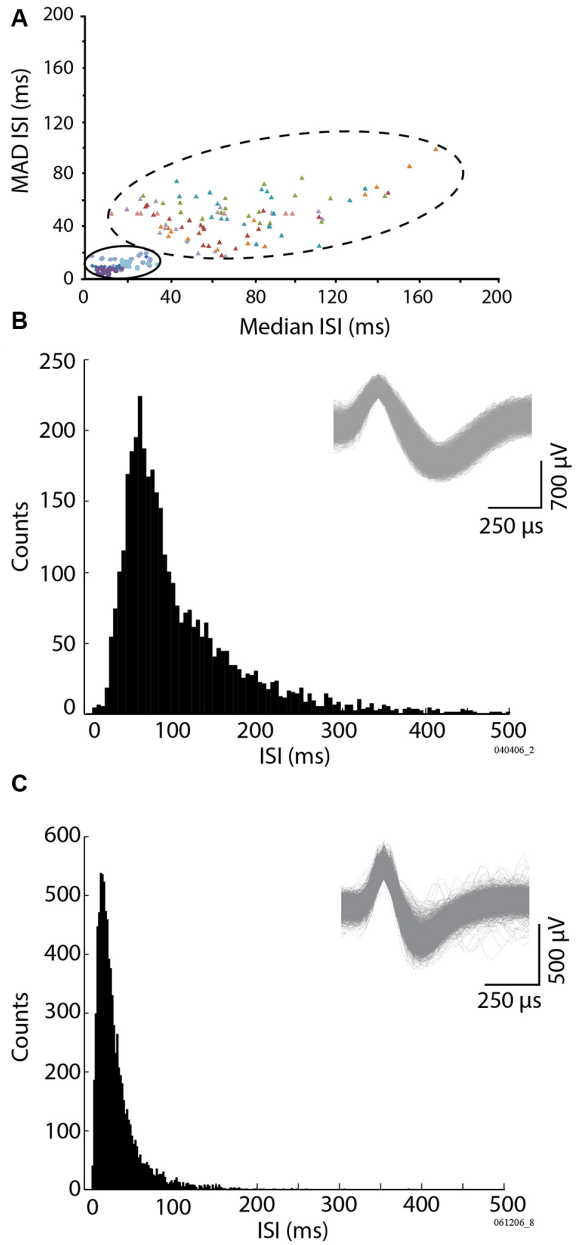

FIGURE 3 | Identification of the Golgi cells vs. Purkinje cell simple spikes (SSs), based on the firing properties. The method follows the one used by Vos et al. (1999), based on the variability of the cell firing (MAD ISI) vs. its median firing values (Median ISI). **(A)** Representation of two subpopulations of units, Golgi cell units (large ensemble, filled triangles, six cells, colors identify different units), and Purkinje cell SSs (small ensemble, filled circles, and diamonds, four cells), by the relationship between their median inter-spike interval (Median ISI), and the absolute deviation of their median firing inter-spike interval (MAD ISI). **(B)** Inter-spike interval of a representative identified Golgi cell. **(C)** Inter-spike interval of a representative Purkinje cell SS. **(B,C)** Insets: example spike waveforms for a Golgi cell **(B)** and a Purkinje cell SS **(C)**.

the samples described in Vos et al. (1999) and Holtzman et al. (2006). Purkinje cell SSs we recorded had a mean firing rate of around 41 Hz. As our sample was better defined for the Golgi cells and Purkinje cell SSs, we decided to focus on these two groups for the rest of the analysis. The firing rate between the Golgi cells and Purkinje cell SSs was significantly different (*t*-test, $p < 0.05$).

Spike-LFP Relationship

We analyzed if the spikes coming from the different cells followed a specific firing pattern relative to the simultaneously recorded LFP oscillations. Of the overall sample, 34/46 Golgi cells were recorded with simultaneous LFP oscillations, and the same for 81/126 Purkinje cell SSs (see **Table 1**). Overall, using the spike-shuffled analysis to determine a phase-locking index or PLI, we determined that 74% (25/34) of Golgi cells and 54% (44/81) of Purkinje cell SSs had some degree of phase-locking with the simultaneous 4–12 Hz LFP oscillations (see **Table 2**). The average value of the PLI for Golgi cells was 0.65 (± 1.1; median of 0.36), while for the Purkinje cell SSs, the PLI had values of 0.32 (± 0.6; median of 0.10). Examples of LFP-triggered histograms (spike-LFP cross-correlograms) for a Golgi cell and Purkinje cell SS are given in **Figure 4**, showing a strong relationship for both. The Golgi cell would fire preferentially in-phase with the peak of the LFP (lag of +10 ms for this cell, PLI = 0.82, **Figure 4A**), while in another recording, the Purkinje cell SS would also fire close to in-phase (lag of −20 ms, PLI = 0.69, **Figure 4B**). For both LFP-triggered histograms, the modulation around the peak can be seen relative to the shuffled 2 SD thresholds. As is done customarily, the identified peak (or valley) was the one closest to zero lag, where the temporal relationship of the cross-correlation is the clearest, working on short timescales (Lamarre and Raynauld, 1965; Perkel et al., 1967; Frölich, 2016). When attempting to see if the phase would be matched at a group level, the averaged LFP-triggered counts for Golgi cells and Purkinje cell SSs (normalized to their average value across all bins) show only a weak modulation around the 0-time lag (**Figure 4C**). An implication is that these cell-LFP relationships could be different across cells, requiring a better-adapted method to capture the group response.

As a more precise way to assess the phase relation for the population, cells that were phase-locked were represented according to their peak in the LFP-triggered histogram. This can be seen in **Figure 5**, with the phase-locking peak in the time domain relative to the peak of the LFP, which was also converted to an angular distribution. The temporal distribution for the 25 Golgi cells is shown in **Figures 5A,B**, while the one for the 44 Purkinje cell SSs is given in **Figures 5C,D**. These graphs show a modulation of the spiking activity throughout the cycle, and the preferred phase for the units. For the Golgi cells, the units tended to discharge mostly in phase with the peak of the LFP (around the 10° angle for phase), which can also be seen in the time domain. As for the Purkinje cell SSs, the distribution is slightly more spread around, but it shows an overall tendency to fire during the up-phase of the cycle, close to the peak (circa 315°). The time-domain histogram shows a greater spread around the LFP peak than Golgi cells. These results imply that the Golgi cells and Purkinje cell SSs that are phase-locked with the 4–12 Hz LFP oscillations show a general tendency to fire around the peak of the LFP.

TABLE 2 | Properties of the two groups of units recorded, in phase-locking and in rate.

Group	Units with simultaneous LFP oscillations	Units with phase relation (PLI > 0)	Firing rate (spikes/s) for units with PLI > 0	Firing rate (spikes/s) for units with PLI = 0
Golgi	34	73.5% (25/34)	6.7 (± 4.7) median: 5.8 (n = 25)	8.5 (± 6.5)^{ns} median: 5.0 (n = 9)
Purkinje cell SS	81	54.3% (44/81)	30.5 (± 18.0) median: 23.8 (n = 44)	53.5 (± 24.4)^ median: 44.2 (n = 37)

We show the number of isolated units with a significant relationship with oscillatory LFPs, as defined by the phase-locking index (PLI) for the LFP-triggered cross-correlation. The average firing rate (spikes/s) was different between the Golgi cell and the Purkinje cell simple spike samples (Pcell SS, t-test $p < 0.05$). The firing rate for the Golgi cells between phase-locked and non-phase locked units was not different (K–W test, ns), Purkinje cells simple spikes firing rates did, however, show a difference concerning the phase-locking (^K–W test, $p < 0.05$).

We also looked at the distribution of the PLI values; for both types of units, it was clear they were not normally distributed (see **Figures 6A–C**), with the PLI skewed towards lower values. Certain units showed phase-locking (PLI > 0) for values less than 1, and as evidenced by the examples in **Figure 4**, and the insets in **Figure 6**, the modulation was appreciable. A comparison between the Golgi PLI and the Purkinje cell SS PLI revealed that the Golgi PLI was significantly higher (Kruskal–Wallis test: $\chi^2 = 5.54$, $p = 0.0186$, df = 1, see **Figure 6C**).

When comparing the firing rate properties for the units that were phase-locked vs. those that were not, a few differences can be noted. There was again a difference in firing rate between the Golgi cells and the Purkinje cells SSs (Kruskal–Wallis: $\chi = 62.6$, $p < 0.0001$, df = 1). Also, the firing rate for the phase-locked and non-phase-locked units was compared: for the Golgi cells, no firing rate difference could be noted (Kruskal–Wallis: $\chi^2 = 0.32$, $p = 0.57$, df = 1), while for the Purkinje cell SSs, the cells that were phase-locked showed a significantly slower firing rate than those that were not (Kruskal–Wallis: $\chi^2 = 21.32$, $p < 0.0001$, df = 1; see **Figure 6D**). This shows that the slower Purkinje cell SS firing could be better synchronized with the LFP rhythm while the firing rate did not limit phase-locking for Golgi cells. This frequency-specific capacity could be related to the cell's properties in following a local network resonance mechanism. The specific firing rates are given in **Table 2**.

Spiking Rhythmicity

As a significant proportion of units were found to be phase-locked with the LFP oscillations, it was also interesting to evaluate if the units had a rhythmic discharge. We did so by calculating the rhythm index (RI), based on the unit's autocorrelogram. Many units showed a rhythmic autocorrelogram, and examples are given in **Figure 7**. Some Golgi cells showed a rhythm in the 20 Hz range as the example in **Figure 7A** illustrates (period = 60 ms, for a rhythm of 16.7 Hz). Overall, 17/34 (50%) of our Golgi cells showed a RI > 0, and the RI overall for the Golgi cells was not normally distributed and had a median of 2.35. For the Purkinje cell SSs, 20/81 (24.7%) had a RI > 0, and the example is shown in **Figure 7B** shows a rhythmic cell (period = 125 ms, 8 Hz); their distribution was also strongly skewed to lower values, with a median set at 0. Comparing the distributions, it is clear that the RI was higher for the Golgi cells than for the Purkinje cell SSs (Kruskal–Wallis: $\chi^2 = 11.83$, $p = 0.0006$, df = 1). **Figure 7C** shows this disparity. Overall, this analysis shows that the Golgi cells had a greater tendency to show rhythmic properties.

Finally, we also explored if different factors would better predict which cells would have a greater rhythm index. For Golgi cells, there did not seem to be specific predictive properties, as firing rate or phase-locking did not seem to predict which cells were rhythmic. However, for Purkinje cell SSs, the firing rate was inversely related to the rhythm index, for cells that had a RI > 0 (see the correlation in **Figure 8A**, with the correlation values for the red dots, $r = -0.59$, $p = 0.006$). This means that cells with a higher firing rate would show a lower RI. Looking at the comparison from the opposite perspective, when we compare the firing rate for Purkinje cell SSs with no rhythmicity (RI = 0), from those with some rhythmicity, the firing rate shows lower values for the non-rhythmic units than for the rhythmic units (Kruskal–Wallis: $\chi^2 = 14.45$, $p = 0.0001$, df = 1, see **Figure 8B**), which can mostly be attributed to the larger range of firing rates shown across the group of rhythmic units. This can be interpreted as a potential rhythmic influence on the units to increase the firing rate variability for Purkinje cell SSs.

DISCUSSION

We show here that cerebellar Golgi cells and Purkinje cell SSs can show phase-locking activity with GCL LFP oscillations in the 4–12 Hz frequency range. The phase relationship for both the Golgi and Purkinje cell SSs was mostly around the peak of the LFP. The proportion of those cells that were phase-locked was greater for the Golgi cells than for the Purkinje cell SSs; this can be related to the optimal LFP oscillatory recordings being closer to the Golgi cells—within the GCL. However, the capacity to affect Purkinje cell SSs provide evidence of the capacity of GCL LFP oscillations to influence further elements of the cerebellar cortex networks. It seems fairly clear that the capacity of synaptic input that would stem from the 4–12 Hz rhythmic influence, as seen through the LFP oscillations, does not forcefully drive the Golgi cells or Purkinje cells to fire on each beat. The rhythmic synaptic input likely has a modulatory influence, influencing Golgi and Purkinje cell firing, even if not on every beat. LFP 4–12 Hz oscillations also show potential penetrability across the layers of the cerebellar cortex and have some predictive capacity in determining the timing of the firing of multiple units across the cerebellar cortex of the awake rodent.

GCL and Golgi Firing Under a 4–12 Hz Oscillatory Influence

Our results show that many Golgi cells tended to follow the 4–12 Hz LFP oscillations in a phase-specific way and that for the overall population, the tendency was to be aligned with

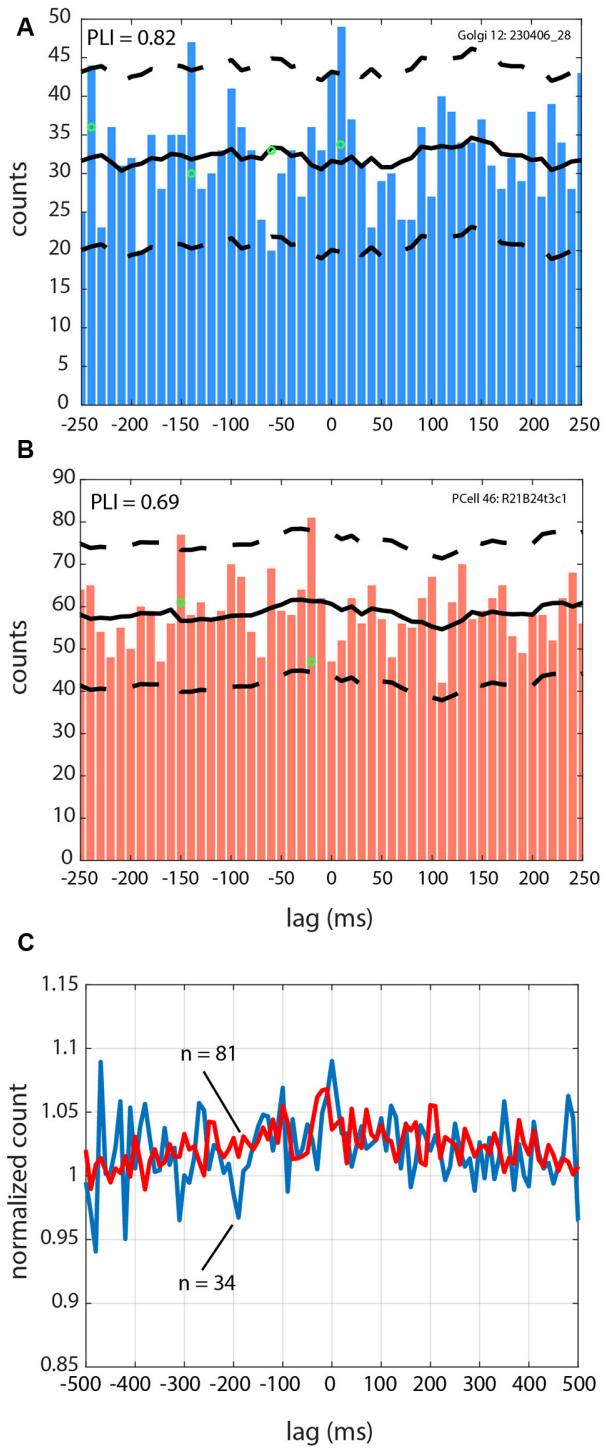

FIGURE 4 | Spike-LFP relationships for Golgi and a Purkinje cell during 4–12 Hz oscillatory LFPs. **(A)** LFP-triggered spike histogram for a Golgi cell, with a peak at +10 ms. **(B)** LFP-triggered spike histogram for a Purkinje cell SS, with a peak at −20 ms. **(C)** Averaged trace for the cells in the Golgi cell group (blue line), and the Purkinje cell SS group (red line). The averaged trace has been normalized across all bins to a value of 1 so they can be superimposed. For **(A–C)**, zero is the time of the LFP peak. For **(A,B)**, the average of the spike-shuffled control is shown with the full black line, and the ±2 SD is indicated with the dashed black line.

the peak of the LFP. These 4–12 Hz oscillations in the rodent are best recorded in the GCL (Hartmann and Bower, 1998; O'Connor et al., 2002), as are the 10–25 Hz cerebellar oscillations in the primate (Pellerin and Lamarre, 1997; Courtemanche et al., 2002). This layer specificity is such that during exploration and positioning of the microelectrodes, the oscillatory LFP signal corresponds well with multiunit firing in the GCL, as can be heard through the audio monitor when playing unit activity. This GCL multiunit activity, presumably coming from a combination of mossy fiber activity and granule cell firing is well correlated with the oscillatory epochs (Hartmann and Bower, 1998; Courtemanche et al., 2002). Our results show that Golgi cell firing is also related to these oscillations, potentially being triggered by an oscillatory afferent drive, and/or contributing to granule-Golgi resonance (Dugué et al., 2009; Robinson et al., 2017).

Golgi cells receive excitatory afferent input from mossy and parallel fibers (Llinás et al., 2004). This excitation gets to the Golgi cell through a feedforward inhibitory circuit (mossy fiber—Golgi cell) and a feedback inhibitory loop (mossy fiber—granule cell/parallel fiber—Golgi cell; Bell and Dow, 1967; Llinás et al., 2004). Both these circuits have potential resonance properties. Modeling has shown that the GCL does have 5–30 Hz resonance capacities (Maex and De Schutter, 2005; Dugué et al., 2009). These circuits constitute a potential mechanism for the Golgi cell phase locking to the LFP oscillations. Overall, this oscillatory pattern could correspond to a pattern of organization of the granule cells-Golgi cells network (Maex and De Schutter, 1998; D'Angelo et al., 2009, 2016), where GCL activity could gate oscillations, and perform group selection for resonance in the layer (Sudhakar et al., 2017). As such, GCL LFP oscillations in the 4–12 Hz range provide evidence of temporal windows of synaptic afferent input during which Golgi cell excitability could be enhanced, in agreement with Dugué et al. (2009).

Also, this pattern of activity could be enhanced by intrinsic properties of elements in the GCL, as both Golgi cell and granule cell-intrinsic properties could support these oscillations. Golgi cells provide rhythmic inhibition on granule cells and have pacemaking activity in the theta frequency range, with resonance for input frequencies of 4 Hz (Dieudonné, 1998; Forti et al., 2006; Solinas et al., 2007). The amount of synaptic noise *in vivo* might obscure the rhythm-generating capacity of Golgi cells; however, they are capable of responding to rhythmic input particularly well (Solinas et al., 2007). In our case, we also found some evidence of rhythmic firing in Golgi cells, as has been shown previously *in vivo*: in the awake animal (Edgley and Lidierth, 1987), in the anesthetized animal (Maex et al., 2000; Volny-Luraghi et al., 2002), with some studies showing strong rhythmicity (Vos et al., 1999; Huang et al., 2014). Golgi cell firing might thus follow network rhythmicity, even if skipping a few cycles; this skipping might be explained by the synaptic noise that prevents reaching the firing threshold in a synchronized way, while the membrane potential can follow baseline rhythmicity (Dugué et al., 2009). Golgi cell firing rhythmicity might require specific network conditions, such as synchronized afferent parallel fiber input (Maex et al., 2000). Also, their capacity to be electrically coupled would greatly influence the formation of Golgi populations

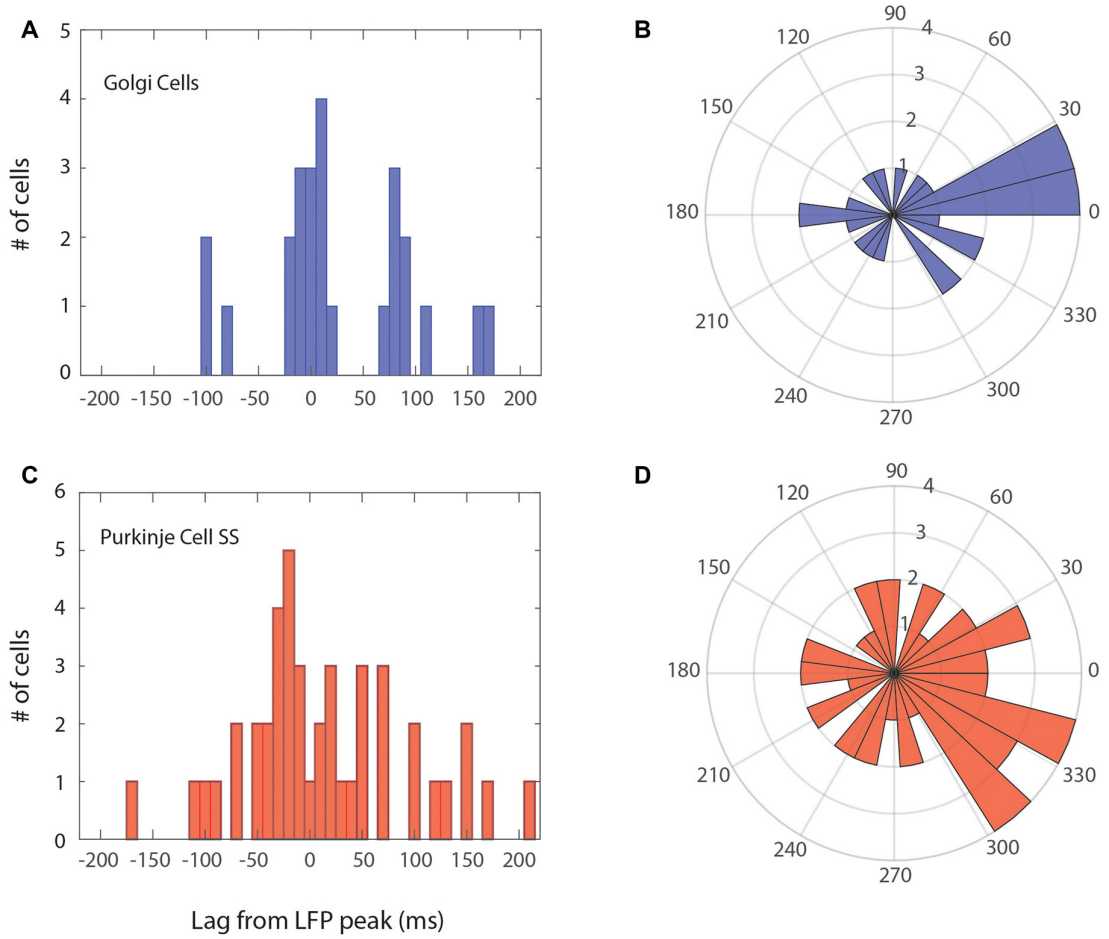

FIGURE 5 | Phase relationship for Golgi cells and Purkinje cell SSs within the LFP oscillation cycle. The main peak of the LFP-triggered histogram is taken to represent each cell. Left **(A,C)** peak alignment in the time domain; Right **(B,D)** angular (phase) relation, centered on the peak of the LFP (zero). **(A,B)** Relation of Golgi cells firing vs. the LFP cycle. Overall, the Golgi cells were more phase-locked with the peak of the LFP cycle or previous/subsequent cycles. **(C,D)** Relation of Purkinje cell SSs vs. the LFP cycle, who had more phase-locked cells with the ascending phase towards the peak, however, in a more variable manner.

following the rhythm (Dugué et al., 2009; Robinson et al., 2017). Granule cells also show specific properties of resonance at slow (best: ∼9 Hz) frequencies (D'Angelo et al., 2001), and their responsiveness to input is partially controlled by calcium conductances, modulating their firing rate (Gall et al., 2005). By controlling granular oscillations, Golgi cells could influence the spatio-temporal organization of information processing and storage in the GCL (D'Angelo, 2008; D'Angelo et al., 2009; Sudhakar et al., 2017) as the overall issue of the timing of population activity in the cerebellum gains increased interest (Bareš et al., 2019).

Extending Further Into the Cerebellar Cortex: Purkinje Cell Simple Spike Firing Under a 4–12 Hz Oscillatory Influence

As many Purkinje cell SSs were also phase-related to the oscillations, the 4–12 Hz oscillatory phenomenon could also influence neurons outside of the GCL. The proportion of Purkinje cells showing this influence is smaller than Golgi cells, but they do show potential "penetrability" of the 4–12 Hz oscillations up to the Purkinje cell layer. Under the strong oscillatory influence, units in the GCL and the Purkinje cell layer activity could fire in relation to the oscillation. In contrast with a network serving basic attentive immobility behavior, during movement, Purkinje cell SSs are related to sensorimotor parameters (Lamarre and Chapman, 1986; Thach et al., 1992; Heck et al., 2007); perhaps the oscillatory synaptic influence we witness through LFPs could provide baseline conditions for forming action-related networks. Information flow between the GCL and Purkinje cell layers has been established (Santamaria et al., 2007): while interneurons like Golgi, unipolar brush, and Lugaro cells influence GCL output to Purkinje cells (Barmack and Yakhnitsa, 2008), a spatio-temporal process must operate to ensure a coordinated activation of SSs. The GCL capacity to excite the Purkinje layer in such a coherent fashion could be due to the mossy fiber arrangement going to Purkinje cells, namely, those coming from the ascending portion of the granule

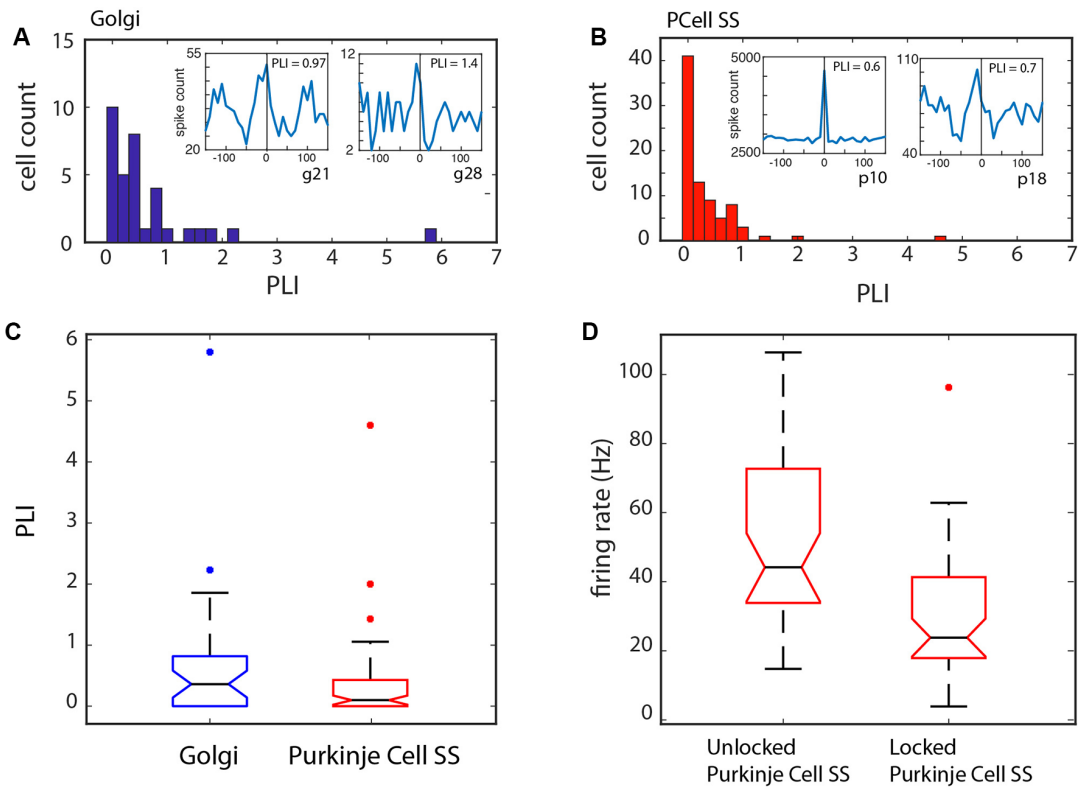

FIGURE 6 | Phase-locking over the samples of Golgi and Purkinje cell SSs. **(A)** Phase-locking index (PLI) distribution for the Golgi cells. Inset: two examples of Golgi cell LFP-triggered histograms. **(B)** PLI distribution for the Purkinje cell SSs. Inset: two examples of Purkinje cell SS LFP-triggered histograms. For both groups, the distribution is skewed towards lower values. A PLI > 0 was our criterion for phase locking. **(C)** Statistical difference between the two groups showing a higher PLI for the Golgi cells. **(D)** Relationship of phase-locking with Purkinje cell SS firing rate. Cells that were phase-locked with the LFP showed a slower firing rate than those that were not.

cell axon (Llinás et al., 1981; Gundappa-Sulur et al., 1999; Isope and Barbour, 2002; Lu et al., 2005), or *via* the spatial arrangement of the modulatory connections from the Golgi and Lugaro cells (Barmack and Yakhnitsa, 2008; Sillitoe et al., 2008). These connections could support a coherent temporal representation between the GCL and the Purkinje cell layer within circumscribed cerebellar zones. During GCL oscillations at rest, a coherent sagittal pattern of organization emerges (Courtemanche et al., 2009), which could potentially influence zonal organization at the level of the Purkinje cell layer: through strong anatomical and physiological evidence, the latter has shown heavy parasagittal modularity (Herrup and Kuemerle, 1997; Lang et al., 1999). In the case of our own Purkinje cell SS recordings, we compared GCL oscillations with Purkinje cell firing from a nearby electrode (e.g., from the same guide cannula, thus corresponding to the same sagittal and coronal location). This certainly would favor the phase-locking of Purkinje SS to GCL oscillations.

Extending Further In and Out of the Cerebellum

The oscillatory entrainment of the cerebellar cortex output cells also opens up the search for the influence outside of the cerebellar cortex and cerebellum, and we speculate on a few mechanisms here. Cerebellar inactivation influences patterns of rhythmic activity in the cerebral cortex (Popa et al., 2013), and Purkinje cell SS can be timed with cortical rhythms (McAfee et al., 2019). More specific to the cerebellar circuits, there are also examples of activity of rhythmic SS firing (Huang et al., 2014). It would be interesting to see how this relates to cerebellar nuclei activity. Indeed, synchronized Purkinje cell activity promotes the downstream activation in cerebellar nuclei (Person and Raman, 2012a,b). The particular "pauses" in the Purkinje cell firing to the deep cerebellar nuclei could be facilitated by the 4–12 Hz rhythm across the cerebellar cortex (De Schutter and Steuber, 2009), favoring synchronicity of firing towards the nuclei (Jaeger, 2011). Varying between 100 and 200 ms long, these pauses relate well with an underlying 5–10 Hz cerebellar cortex rhythmicity (Alviña et al., 2008), and they complement the pacemaker regularity of Purkinje cell firing, which have an important role in the coordinated circuitry (Walter et al., 2006). Besides, the 4–12 Hz rhythmicity also fits well with a recovery time constant of the channels CaV3.1 in those same neurons around 100 ms (Iftinca et al., 2006; De Schutter and Steuber, 2009; Tadayonnejad et al., 2010). Importantly as well, mutant mice that are without the calcium-sensitive BK channels in their Purkinje cells show

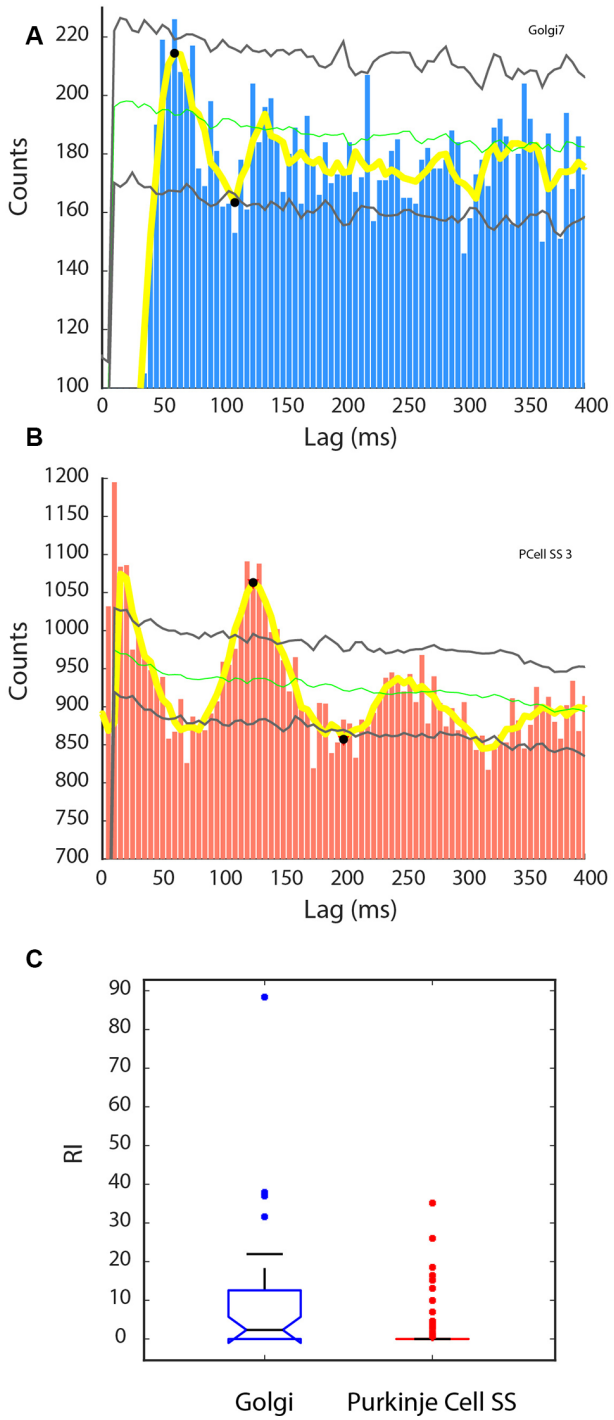

FIGURE 7 | Rhythmic activity in Golgi cells and Purkinje cell SSs. A rhythm index (RI) was calculated based on the unit's autocorrelogram, from the significant peaks and valleys exceeding the shuffled control for each cell. **(A,B)** Autocorrelograms for a sample Golgi cell (**A**, blue), and Purkinje cell SS (**B**, red). Also indicated are the mean of the shuffled control (green line) ±2 SD (gray lines). Yellow line: running average of the histogram. Black dots signify peaks higher and valleys lower than the shuffled control variability. **(A)** Golgi cell showing a 16.7 Hz rhythm. **(B)** Purkinje cell SS showing an 8 Hz rhythm. **(C)** Statistical difference between the two groups in RI, with the Golgi cell group showing larger RIs than the Purkinje cell SS group.

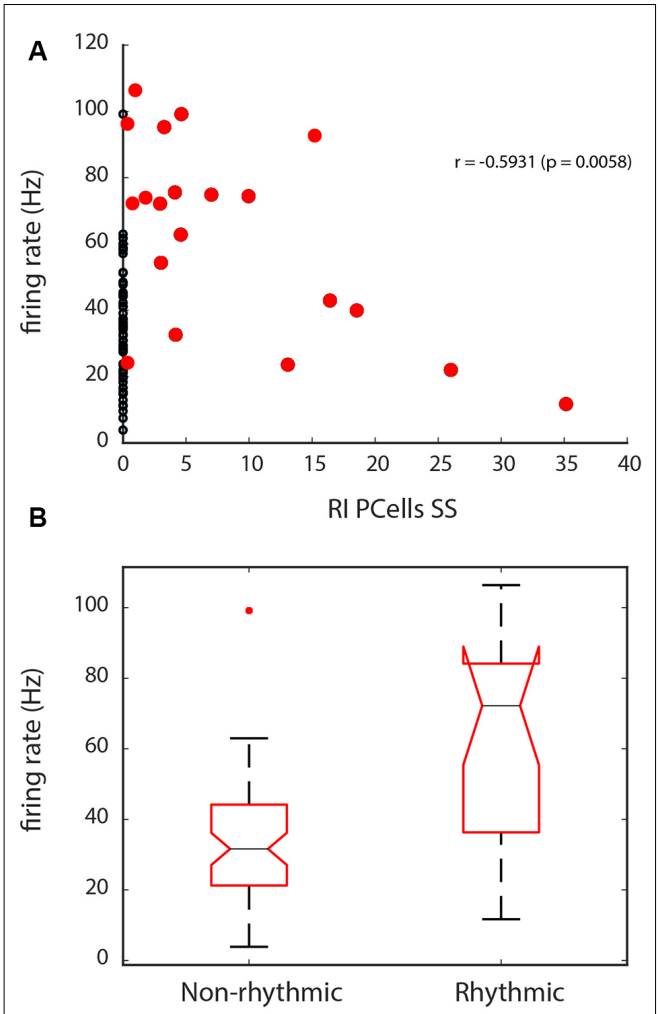

FIGURE 8 | Firing rate properties for Purkinje cell SSs in relation with the Rhythm Index (RI). **(A)** Correlation between the firing rate and the RI, for the units with a RI > 0 (red dots). Units with a RI = 0 are indicated with black dots. Note the inverse correlation with the RI, with lower rate spiking being related to higher RIs. **(B)** Statistical difference in firing rate seen between units with a RI = 0, and those that have a RI > 0. Overall, because of their lower range of firing rate, Purkinje cell's SSs with no rhythmicity show slower firing.

strong firing rhythmicity in SSs (Chéron et al., 2009) but also in the deep cerebellar nuclei, in the beta range, showing a transmittable rhythmic influence (Chéron et al., 2018). Together, these elements paint a picture that a rhythmic influence could coordinate the activity in the overall cerebellar circuitry under certain conditions, such as in movement preparation (Courtemanche et al., 2013).

Comparison With Other Cerebellar Cortex Slow Oscillatory Phenomena

Purkinje cell SS firing has been found to adapt to excitability state modulation and slow oscillations, including in a bistable manner (Loewenstein et al., 2005; Chen et al., 2009; Ros et al., 2009). This bistability in the awake animal has been

questioned (Schonewille et al., 2006), but could represent a mechanism influencing the firing patterns of Purkinje cell SSs. A depolarized state would favor the firing of the Purkinje cell SSs, and the state-switch from a hyperpolarized state could stem from afferent input/climbing fiber firing. Slow cerebellar oscillations which are around or less than one Hz could also affect cerebellar cortex firing (Chen et al., 2009; Ros et al., 2009). Slow oscillations in the cerebellar cortex of the anesthetized rat (∼1 Hz) and awake mouse (∼2–5 Hz) recorded by Ros et al. (2009) are tightly synchronized with the cerebral neocortical up-states and promote phase-related firing of Golgi cells, granule cells, and Purkinje cell complex spikes, but not for Purkinje cell SSs. It is unclear if slow and the 4–12 Hz cerebellar oscillations are related. Even slower oscillations (<0.1 Hz) have been recorded in the paramedian and Crus II lobules of the tottering mouse using optical imaging, which was related to Purkinje cell firing (Chen et al., 2009). The co-occurrence of these oscillatory processes, in various anesthetized and awake states and across species, has not been established. Also, as we find here that Purkinje cells SSs can show phasic relations with the GCL 4–12 Hz LFP oscillations, a comparison with the well-established olivocerebellar rhythms at similar frequencies (Lang et al., 1999; Llinás, 2009) would indeed be interesting (Courtemanche et al., 2013). An adapted methodology would have to be crafted to make a direct comparison; our small sample of Purkinje cell complex spikes, as well as our methods, could not allow for population-level analysis for olivocerebellar activity concerning GCL LFPs. Similarly, a comparison with faster oscillatory phenomena in the Purkinje cell layer would also warrant a specific methodology (Servais and Chéron, 2005; de Solages et al., 2008; Middleton et al., 2008).

Limitations

This study of course has certain limitations. In this study, we did not micro-map the local circuits, which would have required a denser arrangement of electrodes or recording channels (Buzsáki et al., 2012). This would have informed on the more exact span of coherence of our recorded GCL LFP oscillation and potential effects on units. Also, our methodology for determining the classification of units was based on indirect evidence, making our classified units putative Golgi cells and putative Purkinje cells. For Purkinje cells, it is customary to confirm SS identity with the co-recording of complex spikes (Welsh et al., 1999; Gao et al., 2011), which we did not systematically do here, focusing on obtaining both strong GCL LFP oscillations and well-isolated units. For any type of cell, the method of juxtacellular labeling using micropipettes is also quite advantageous in identifying cell types that are recorded from (Barmack and Yakhnitsa, 2008; Brown et al., 2018) but this exceeded the scope of our experimental methods. Here, we used the cell's location, its action potential as well as its firing pattern properties, especially the relation between the firing rate and its variability, as done previously (Vos et al., 1999). This approach has also been adapted and further perfected by others (Van Dijck et al., 2013). Finally, we did not fully monitor the animal's postural, jaw, limb, or whisker movements. However, as we encouraged the animals to be immobile but attentive—the optimal behavior to observe stronger oscillatory periods—we also selected these periods for recording, noted sudden movement, and inspected the traces offline for artifacts. Future experiments should indeed address the posture/movement interface quantitatively, especially with the potential of information-rich differential phase-coding in sensorimotor planning and execution.

In conclusion, in the context of awake immobility, we have found that the 4–12 Hz GCL oscillations can help predict the spike timing of Golgi cells and Purkinje cell SSs. The LFPs represent a measure of synaptic activity influencing the GCL, potentially modulating large portions of the cerebellar cortex. Information could flow better across circuits, here through the cerebellar layers, using an oscillatory influence (Akam and Kullmann, 2010). Also, LFP oscillations could help in the coordination of spike timing even if cells are not rhythmic (Bush and Burgess, 2019), as we show here that a greater proportion of Golgi or Purkinje cell SSs are phase-locked than are outright rhythmic. Our study has focused on normal circuits, but oscillatory flow could also have implications in pathological circuits, influencing cerebellar and extra-cerebellar connectivity (Bares et al., 2010; Georgescu et al., 2018). As oscillations flowing through circuits can represent time (Buzsáki and Llinás, 2017), the understanding of oscillatory flow and the timing of unit activity through the cerebellar cortex, and outward, is of particular interest.

DATA AVAILABILITY STATEMENT

The datasets generated for this study are available on request to the corresponding author.

ETHICS STATEMENT

The animal study was reviewed and approved by Concordia University Animal Research Ethics Committee.

AUTHOR CONTRIBUTIONS

ML and HG contributed equally to this work. ML, HG, CL, and RC designed and prepared the experiments. ML, HG, CS, CL, and RC acquired the data. ML, HG, JMPL, CL, and RC analyzed the data. ML, HG, CL, and RC wrote the manuscript, with all authors providing input. All authors contributed to the article and approved the submitted version.

FUNDING

Operating support for this work was provided by grants from NSERC (Canada), NAAR/Autism Speaks (USA), and Concordia FAS to RC, as well as from ANR (France) grants to CL. Infrastructure support was provided by an FRQS Group grant to the Groupe de Recherche en Neurobiologie Comportementale

(CSBN). ML received FRQS and NSERC scholarships, HG received ENS scholarships.

ACKNOWLEDGMENTS

We wish to thank S. Dieudonné for helpful discussions. Special thanks to L. Carmant for the usage of the microscope photographic equipment, and E. Zuccheroso for help in certain surgeries. CS is now at the Ontario Brain Institute, Toronto, ON, Canada.

SUPPLEMENTARY MATERIAL

The Supplementary Material for this article can be found online at: https://www.frontiersin.org/articles/10.3389/fnsys.2020.475948/full#supplementary-material.

REFERENCES

Akam, T., and Kullmann, D. M. (2010). Oscillations and filtering networks support flexible routing of information. *Neuron* 67, 308–320. doi: 10.1016/j.neuron.2010.06.019

Alviña, K., Walter, J. T., Kohn, A., Ellis-Davies, G., and Khodakhah, K. (2008). Questioning the role of rebound firing in the cerebellum. *Nat. Neurosci.* 11, 1256–1258. doi: 10.1038/nn.2195

Bareš, M., Apps, R., Avanzino, L., Breska, A., D'Angelo, E., Filip, P., et al. (2019). Consensus paper: decoding the contributions of the cerebellum as a time machine. From neurons to clinical applications. *Cerebellum* 18, 266–286. doi: 10.1007/s12311-018-0979-5

Bares, M., Lungu, O. V., Husárová, I., and Gescheidt, T. (2010). Predictive motor timing performance dissociates between early diseases of the cerebellum and Parkinson's disease. *Cerebellum* 9, 124–135. doi: 10.1007/s12311-009-0133-5

Barmack, N. H., and Yakhnitsa, V. (2008). Functions of interneurons in mouse cerebellum. *J. Neurosci.* 28, 1140–1152. doi: 10.1523/JNEUROSCI.3942-07.2008

Bell, C. C., and Dow, R. S. (1967). Cerebellar circuitry. *Neurosci. Res. Prog. Bull.* 5, 121–222.

Berryer, M. H., Chattopadhyaya, B., Xing, P., Riebe, I., Bosoi, C., Sanon, N., et al. (2016). Decrease of SYNGAP1 in GABAergic cells impairs inhibitory synapse connectivity, synaptic inhibition and cognitive function. *Nat. Commun.* 7:13340. doi: 10.1038/ncomms13340

Brown, A. M., White, J. J., Zhou, J., Jefferson, T., Lin, T., Sillitoe, R. V., et al. (2018). "*In vivo* loose-patch-justacellular labeling of cerebellar neurons in mice," in *Neuromethods 134: Extracellular Recording Approaches*, ed. R. V. Sillitoe (New York, NY: Humana Press), 1–18. doi: 10.1007/978-1-4939-7549-5_1

Bullock, T. H. (1997). Signals and signs in the nervous system: the dynamic anatomy of electrical activity is probably information-rich. *Proc. Natl. Acad. Sci. U S A* 94, 1–6. doi: 10.1073/pnas.94.1.1

Bush, D., and Burgess, N. (2019). Neural oscillations: phase coding in the absence of rhythmicity. *Curr. Biol.* 29, R55–R57. doi: 10.1016/j.cub.2018.11.056

Buzsáki, G. (2006). *Rhythms of the Brain.* New York, NY: Oxford University Press.

Buzsáki, G., Anastassiou, C. A., and Koch, C. (2012). The origin of extracellular fields and currents—EEG, ECoG, LFP and spikes. *Nat. Rev. Neurosci.* 13, 407–420. doi: 10.1038/nrn3241

Buzsáki, G., and Draguhn, A. (2004). Neuronal oscillations in cortical networks. *Science* 304, 1926–1929. doi: 10.1126/science.1099745

Buzsáki, G., and Llinás, R. (2017). Space and time in the brain. *Science* 358, 482–485. doi: 10.1126/science.aan8869

Chen, G., Popa, L. S., Wang, X., Gao, W., Barnes, J., Hendrix, C. M., et al. (2009). Low-frequency oscillations in the cerebellar cortex of the tottering mouse. *J. Neurophysiol.* 101, 234–245. doi: 10.1152/jn.90829.2008

Chen, L.-Y., Lévesque, M., Cataldi, M., and Avoli, M. (2018). Single-unit activity in the *in vitro* entorhinal cortex during carbachol-induced field oscillations. *Neuroscience* 379, 1–12. doi: 10.1016/j.neuroscience.2018.03.003

Chéron, G., Gall, D., Servais, L., Dan, B., Maex, R., and Schiffmann, S. N. (2004). Inactivation of calcium-binding protein genes induces 160 Hz oscillations in the cerebellar cortex of alert mice. *J. Neurosci.* 24, 434–441. doi: 10.1523/JNEUROSCI.3197-03.2004

Chéron, G., Sausbier, M., Sausbier, U., Neuhuber, W., Ruth, P., Dan, B., et al. (2009). BK channels control cerebellar Purkinje and Golgi cell rhythmicity *in vivo*. *PLoS One* 4:e7991. doi: 10.1371/journal.pone.0007991

Chéron, G., Márquez-Ruiz, J., Chéron, J., Prigogine, C., Ammann, C., Lukowski, R., et al. (2018). Purkinje cell BK channel ablation induces abnormal rhythm in deep cerebellar nuclei and prevents LTD. *Sci. Rep.* 8:4220. doi: 10.1038/s41598-018-22654-6

Courtemanche, R., Chabaud, P., and Lamarre, Y. (2009). Synchronization in primate cerebellar granule cell layer local field potentials: basic anisotropy and dynamic changes during active expectancy. *Front. Cell. Neurosci.* 3:6. doi: 10.3389/neuro.03.006.2009

Courtemanche, R., Fujii, N., and Graybiel, A. M. (2003). Synchronous, focally modulated beta-band oscillations characterize local field potential activity in the striatum of awake behaving monkeys. *J. Neurosci.* 23, 11741–11752. doi: 10.1523/JNEUROSCI.23-37-11741.2003

Courtemanche, R., and Lamarre, Y. (2005). Local field potential oscillations in primate cerebellar cortex: synchronization with cerebral cortex during active and passive expectancy. *J. Neurophysiol.* 93, 2039–2052. doi: 10.1152/jn.00080.2004

Courtemanche, R., Pellerin, J. P., and Lamarre, Y. (2002). Local field potential oscillations in primate cerebellar cortex: modulation during active and passive expectancy. *J. Neurophysiol.* 88, 771–782. doi: 10.1152/jn.2002.88.2.771

Courtemanche, R., Robinson, J. C., and Aponte, D. I. (2013). Linking oscillations in cerebellar circuits. *Front. Neural Circuits* 7:125. doi: 10.3389/fncir.2013.00125

Csicsvari, J., Hirase, H., Czurko, A., and Buzsaki, G. (1998). Reliability and state dependence of pyramidal cell-interneuron synapses in the hippocampus: an ensemble approach in the behaving rat. *Neuron* 21, 179–189. doi: 10.1016/s0896-6273(00)80525-5

D'Angelo, E. (2008). The critical role of Golgi cells in regulating spatio-temporal integration and plasticity at the cerebellum input stage. *Front. Neurosci.* 2, 35–46. doi: 10.3389/neuro.01.008.2008

D'Angelo, E., Nieus, T., Maffei, A., Armano, S., Rossi, P., Taglietti, V., et al. (2001). Theta-frequency bursting and resonance in cerebellar granule cells: experimental evidence and modeling of a slow K^+-dependent mechanism. *J. Neurosci.* 21, 759–770. doi: 10.1523/JNEUROSCI.21-03-00759.2001

D'Angelo, E., Antonietti, A., Casali, S., Casellato, C., Garrido, J. A., Rafael Luque, N., et al. (2016). Modeling the cerebellar microcircuit: new strategies for a long-standing issue. *Front. Cell. Neurosci.* 10:176. doi: 10.3389/fncel.2016.00176

D'Angelo, E., and de Zeeuw, C. I. (2009). Timing and plasticity in the cerebellum: focus on the granular layer. *Trends Neurosci.* 32, 30–40. doi: 10.1016/j.tins.2008.09.007

D'Angelo, E., Koekkoek, S. K. E., Lombardo, P., Solinas, S., Ros, E., Garrido, J., et al. (2009). Timing in the cerebellum: oscillations and resonance in the granular layer. *Neuroscience* 162, 805–815. doi: 10.1016/j.neuroscience.2009.01.048

Davidson, T. J., Kloosterman, F., and Wilson, M. A. (2009). Hippocampal replay of extended experience. *Neuron* 63, 497–507. doi: 10.1016/j.neuron.2009.07.027

De Schutter, E., and Steuber, V. (2009). Patterns and pauses in Purkinje cell simple spike trains: experiments, modeling, and theory. *Neuroscience* 162, 816–826. doi: 10.1016/j.neuroscience.2009.02.040

de Solages, C., Szapiro, G., Brunel, N., Hakim, V., Isope, P., Buisseret, P., et al. (2008). High-frequency organization and synchrony of activity in the Purkinje cell layer of the cerebellum. *Neuron* 58, 775–788. doi: 10.1016/j.neuron.2008.05.008

Destexhe, A., Contreras, D., and Steriade, M. (1999). Spatiotemporal analysis of local field potentials and unit discharges in cat cerebral cortex during natural wake and sleep states. *J. Neurosci.* 19, 4595–4608. doi: 10.1523/JNEUROSCI.19-11-04595.1999

De Zeeuw, C. I., Hoebeek, F. E., Bosman, L. W. J., Schonewille, M., Witter, L., and Koekkoek, S. K.. (2011). Spatiotemporal firing patterns in the cerebellum. *Nat. Rev. Neurosci.* 12, 327–344. doi: 10.1038/nrn3011

Dieudonné, S. (1998). Submillisecond kinetics and low efficacy of parallel fibre-Golgi cell synaptic currents in the rat cerebellum. *J. Physiol.* 510, 845–866. doi: 10.1111/j.1469-7793.1998.845bj.x

Dugué, G. P., Brunel, N., Hakim, V., Schwartz, E. J., Chat, M., Lévesque, M., et al. (2009). Electrical coupling mediates tunable low-frequency oscillations and resonance in the cerebellar Golgi cell network. *Neuron* 61, 126–139. doi: 10.1016/j.neuron.2008.11.028

Eccles, J. C., Ito, M., and Szentágothai, J. (1967). *The Cerebellum as a Neuronal Machine.* New York, NY: Spinger-Verlag.

Edgley, S. A., and Lidierth, M. (1987). The discharges of cerebellar Golgi cells during locomotion in the cat. *J. Physiol* 392, 315–332. doi: 10.1113/jphysiol.1987.sp016782

Fisher, N. I. (1995). *Statistical Analysis of Circular Data.* Cambridge, UK: Cambridge University Press.

Forti, L., Cesana, E., Mapelli, J., and D'Angelo, E. (2006). Ionic mechanisms of autorhythmic firing in rat cerebellar Golgi cells. *J. Physiol.* 574, 711–729. doi: 10.1113/jphysiol.2006.110858

Frederick, A., Bourget-Murray, J., Chapman, C. A., Amir, S., and Courtemanche, R. (2014). Diurnal influences on electrophysiological oscillations and coupling in the dorsal striatum and cerebellar cortex of the anesthetized rat. *Front. Syst. Neurosci.* 8:145. doi: 10.3389/fnsys.2014.00145

Fries, P. (2015). Rhythms for cognition: communication through coherence. *Neuron* 88, 220–235. doi: 10.1016/j.neuron.2015.09.034

Frölich, F. (2016). *Network Neuroscience.* London, UK: Academic Press.

Gall, D., Roussel, C., Nieus, T., Chéron, G., Servais, L., D'Angelo, E., et al. (2005). Role of calcium binding proteins in the control of cerebellar granule cell neuronal excitability: experimental and modeling studies. *Prog. Brain Res.* 148, 321–328. doi: 10.1016/S0079-6123(04)48025-X

Galliano, E., Mazzarello, P., and D'Angelo, E. (2010). Discovery and rediscoveries of Golgi cells. *J. Physiol.* 588, 3639–3655. doi: 10.1113/jphysiol.2010.189605

Gao, H., Solages, C. D., and Léna, C. (2011). Tetrode recordings in the cerebellar cortex. *J. Physiol. Paris* 106, 128–136. doi: 10.1016/j.jphysparis.2011.10.005

Georgescu, E. L., Georgescu, I. A., Mihaela Zahiu, C. D., Şteopoaie, A. R., Morozan, V. P., Pana, A. S., et al. (2018). Oscillatory cortical activity in an animal model of dystonia caused by cerebellar dysfunction. *Front. Cell. Neurosci.* 12:390. doi: 10.3389/fncel.2018.00390

Gerstein, G. L. (1999). "Correlation-based analysis methods for neural ensemble data," in *Methods for Neural Ensemble Recording*, eds S. A. Simon and M. A. L. Nicolelis (Boca Raton FL: CRC Press), 157–177.

Groth, J. D., and Sahin, M. (2015). High frequency synchrony in the cerebellar cortex during goal directed movements. *Front. Syst. Neurosci.* 9:98. doi: 10.3389/fnsys.2015.00098

Gundappa-Sulur, G., De Schutter, E., and Bower, J. M. (1999). Ascending granule cell axon: an important component of cerebellar cortical circuitry. *J. Comp. Neurol.* 408, 580–596. doi: 10.1002/(sici)1096-9861(19990614)408:4<580::aid-cne11>3.0.co;2-o

Hartmann, M. J., and Bower, J. M. (1998). Oscillatory activity in the cerebellar hemispheres of unrestrained rats. *J. Neurophysiol.* 80, 1598–1604. doi: 10.1152/jn.1998.80.3.1598

Heck, D. (2015). *The Neuronal Codes of the Cerebellum.* London, UK: Academic Press.

Heck, D. H., Thach, W. T., and Keating, J. G. (2007). On-beam synchrony in the cerebellum as the mechanism for the timing and coordination of movement. *Proc. Natl. Acad. Sci. U S A* 104, 7658–7663. doi: 10.1073/pnas.0609966104

Herrup, K., and Kuemerle, B. (1997). The compartmentalization of the cerebellum. *Ann. Rev. Neurosci.* 20, 61–90. doi: 10.1146/annurev.neuro.20.1.61

Holtzman, T., Rajapaksa, T., Mostofi, A., and Edgley, S. A. (2006). Different responses of rat cerebellar Purkinje cells and Golgi cells evoked by widespread convergent sensory inputs. *J. Physiol.* 574, 491–507. doi: 10.1113/jphysiol.2006.108282

Honda, T., Yamazaki, T., Tanaka, S., Nagao, S., and Nishino, T. (2011). Stimulus-dependent state transition between synchronized oscillation and randomly repetitive burst in a model cerebellar granular layer. *PLoS Comput. Biol.* 7:e1002087. doi: 10.1371/journal.pcbi.1002087

Huang, J.-J., Yen, C.-T., Tsao, H.-W., Tsai, M.-L., and Huang, C. (2014). Neuronal oscillations in Golgi cells and Purkinje cells are accompanied by decreases in Shannon information entropy. *Cerebellum* 13, 97–108. doi: 10.1007/s12311-013-0523-6

Iftinca, M., McKay, B. E., Snutch, T. P., McRory, J. E., Turner, R. W., Zamponi, G. W. (2006). Temperature dependence of T-type calcium channel gating. *Neuroscience* 142, 1031–1042. doi: 10.1016/j.neuroscience.2006.07.010

Isope, P., and Barbour, B. (2002). Properties of unitary granule cell→Purkinje cell synapses in adult rat cerebellar slices. *J. Neurosci.* 22, 9668–9678. doi: 10.1523/JNEUROSCI.22-22-09668.2002

Isope, P., Dieudonné, S., and Barbour, B. (2002). Temporal organization of activity in the cerebellar cortex: a manifesto for synchrony. *Ann. N Y Acad. Sci.* 978, 164–174. doi: 10.1111/j.1749-6632.2002.tb07564.x

Ito, M. (2006). Cerebellar circuitry as a neuronal machine. *Prog. Neurobiol.* 78, 272–303. doi: 10.1016/j.pneurobio.2006.02.006

Ito, M. (2010). "Cerebellar cortex," in *Handbook of Brain Microcircuits*, eds G. M. Shepherd and S. Grillner (New York, NY: Oxford University Press), 293–300.

Jaeger, D. (2011). Mini-review: synaptic integration in the cerebellar nuclei—perspectives from dynamic clamp and computer simulation studies. *Cerebellum* 10, 659–666. doi: 10.1007/s12311-011-0248-3

Lamarre, Y., and Chapman, C. E. (1986). Comparative timing of neuronal discharge in cortical and cerebellar structures during a simple arm movement in the monkey. *Exp. Brain Res. Series* 15, 14–27.

Lamarre, Y., and Raynauld, J. P. (1965). Rhythmic firing in the spontaneous activity of centrally located neurons. A method of analysis. *Electroenceph. Clin. Neurophysiol.* 18, 87–90. doi: 10.1016/0013-4694(65)90152-5

Lang, E. J., Sugihara, I., Welsh, J. P., and Llinás, R. (1999). Patterns of spontaneous Purkinje cell complex spike activity in the awake rat. *J. Neurosci.* 19, 2728–2739. doi: 10.1523/JNEUROSCI.19-07-02728.1999

Lévesque, M., Chen, L. Y., Hamidi, S., and Avoli, M. (2018). Dynamic interneuron-principal cell interplay leads to a specific pattern of *in vitro* ictogenesis. *Neurobiol. Dis.* 115, 92–100. doi: 10.1016/j.nbd.2018.04.004

Lévesque, M., Langlois, J. M. P., Lema, P., Courtemanche, R., Bilodeau, G.-A., and Carmant, L.. (2009). Synchronized gamma oscillations (30–50 Hz) in the amygdalo-hippocampal network in relation with seizure propagation and severity. *Neurobiol. Dis.* 35, 209–218. doi: 10.1016/j.nbd.2009.04.011

Lévesque, M., Herrington, R., Hamidi, S., and Avoli, M. (2016). Interneurons spark seizure-like activity in the entorhinal cortex. *Neurobiol. Dis.* 87, 91–101. doi: 10.1016/j.nbd.2015.12.011

Llinás, R. R. (2009). Inferior olive oscillation as the temporal basis for motricity and oscillatory reset as the basis for motor error correction. *Neuroscience* 162, 797–804. doi: 10.1016/j.neuroscience.2009.04.045

Llinás, R. R., Brookhart, J. M., and Mountcastle, V. B. (1981). "Electrophysiology of the cerebellar networks," in *Handbook of Physiology—The Nervous System II, Motor Control, Part 2*, ed. V. B. Brooks (Bethesda, MD: American Physiological Society), 831–876.

Llinás, R. R., Walton, K. D., and Lang, E. J. (2004). "Cerebellum," in *The Synaptic Organization of the Brain*, ed. G. M. Shepherd (New York, NY: Oxford University Press), 271–309.

Loewenstein, Y., Mahon, S., Chadderton, P., Kitamura, K., Sompolinsky, H., Yarom, Y., et al. (2005). Bistability of cerebellar Purkinje cells modulated by sensory stimulation. *Nat. Neurosci.* 8, 202–211. doi: 10.1038/nn1393

Lu, H., Hartmann, M. J., and Bower, J. M. (2005). Correlations between Purkinje cell single unit activity and simultaneously recorded field potentials in the immediately underlying granule cell layer. *J. Neurophysiol.* 94, 1849–1860. doi: 10.1152/jn.01275.2004

Maex, R., and De Schutter, E. (1998). Synchronization of Golgi and granule cell firing in a detailed network model of the cerebellar granule cell layer. *J. Neurophysiol.* 80, 2521–2537. doi: 10.1152/jn.1998.80.5.2521

Maex, R., and De Schutter, E. (2005). Oscillations in the cerebellar cortex: a prediction of their frequency bands. *Prog. Brain Res.* 148, 181–188. doi: 10.1016/S0079-6123(04)48015-7

Maex, R., Vos, B. P., and De Schutter, E. (2000). Weak common parallel fibre synapses explain the loose synchrony observed between rat cerebellar

Golgi cells. *J. Physiol.* 523, 175–192. doi: 10.1111/j.1469-7793.2000.t01-1-00175.x

Maris, E., Fries, P., and van Ede, F. (2016). Diverse phase relations among neuronal rhythms and their potential function. *Trends Neurosci.* 39, 86–99. doi: 10.1016/j.tins.2015.12.004

McAfee, S. S., Liu, Y., Sillitoe, R. V., and Heck, D. H. (2019). Cerebellar lobulus simplex and crus I differentially represent phase and phase difference of prefrontal cortical and hippocampal oscillations. *Cell Rep.* 27, 2328.e3–2334.e3. doi: 10.1016/j.celrep.2019.04.085

Middleton, S. J., Racca, C., Cunningham, M. O., Traub, R. D., Monyer, H., Knöpfel, T., et al. (2008). High-frequency network oscillations in cerebellar cortex. *Neuron* 58, 763–774. doi: 10.1016/j.neuron.2008.03.030

O'Connor, S., Berg, R. W., and Kleinfeld, D. (2002). Coherent electrical activity between vibrissa sensory areas of cerebellum and neocortex is enhanced during free whisking. *J. Neurophysiol.* 87, 2137–2148. doi: 10.1152/jn.00229.2001

Paxinos, G., and Watson, C. (1998). *The Rat Brain in Stereotaxic Coordinates*. 4th Edn. San Diego,CA: Academic Press.

Pellerin, J. P., and Lamarre, Y. (1997). Local field potential oscillations in primate cerebellar cortex during voluntary movement. *J. Neurophysiol.* 78, 3502–3507. doi: 10.1152/jn.1997.78.6.3502

Perez-Orive, J., Mazor, O., Turner, G. C., Cassenaer, S., Wilson, R. I., and Laurent, G.. (2002). Oscillations and sparsening of odor representations in the mushroom body. *Science* 297, 359–365. doi: 10.1126/science.1070502

Perkel, D. H., Gerstein, G. L., and Moore, G. P. (1967). Neuronal spike trains and stochastic point processes. II. Simultaneous spike trains. *Biophys. J.* 7, 419–440. doi: 10.1016/S0006-3495(67)86597-4

Person, A. L., and Raman, I. M. (2012a). Synchrony and neural coding in cerebellar circuits. *Front. Neural Circuits* 6:97. doi: 10.3389/fncir.2012.00097

Person, A. L., and Raman, I. M. (2012b). Purkinje neuron synchrony elicits time-locked spiking in the cerebellar nuclei. *Nature* 481, 502–505. doi: 10.1038/nature10732

Popa, D., Spolidoro, M., Proville, R. D., Guyon, N., Belliveau, L., and Léna, C. (2013). Functional role of the cerebellum in gamma-band synchronization of the sensory and motor cortices. *J. Neurosci.* 33, 6552–6556. doi: 10.1523/JNEUROSCI.5521-12.2013

Robinson, J. C., Chapman, C. A., and Courtemanche, R. (2017). Gap junction modulation of low-frequency oscillations in the cerebellar granule cell layer. *Cerebellum* 16, 802–811. doi: 10.1007/s12311-017-0858-5

Ros, H., Sachdev, R. N., Yu, Y., Sestan, N., and McCormick, D. A. (2009). Neocortical networks entrain neuronal circuits in cerebellar cortex. *J. Neurosci.* 29, 10309–10320. doi: 10.1523/JNEUROSCI.2327-09.2009

Santamaria, F., Tripp, P. G., and Bower, J. M. (2007). Feedforward inhibition controls the spread of granule cell-induced Purkinje cell activity in the cerebellar cortex. *J. Neurophysiol.* 97, 248–263. doi: 10.1152/jn.01098.2005

Schonewille, M., Khosrovani, S., Winkelman, B. H. J., Hoebeek, F. E., De Jeu, M. T. G., and Larsen, I. M. (2006). Purkinje cells in awake behaving animals operate at the upstate membrane potential. *Nat. Neurosci.* 9, 459–461; author reply 461.doi: 10.1038/nn0406-459

Senkowski, D., Schneider, T. R., Foxe, J. J., and Engel, A. K. (2008). Crossmodal binding through neural coherence: implications for multisensory processing. *Trends Neurosci.* 31, 401–409. doi: 10.1016/j.tins.2008.05.002

Servais, L., and Chéron, G. (2005). Purkinje cell rhythmicity and synchronicity during modulation of fast cerebellar oscillation. *Neuroscience* 134, 1247–1259. doi: 10.1016/j.neuroscience.2005.06.001

Sillitoe, R. V., Chung, S. H., Fritschy, J. M., Hoy, M., and Hawkes, R. (2008). Golgi cell dendrites are restricted by Purkinje cell stripe boundaries in the adult mouse cerebellar cortex. *J. Neurosci.* 28, 2820–2826. doi: 10.1523/JNEUROSCI.4145-07.2008

Simões de Souza, F. M., and De Schutter, E. (2011). Robustness effect of gap junctions between Golgi cells on cerebellar cortex oscillations. *Neural Syst. Circuits* 1, 1–19. doi: 10.1186/2042-1001-1-7

Solinas, S., Forti, L., Cesana, E., Mapelli, J., De Schutter, E., and D'Angelo, E.. (2007). Fast-reset of pacemaking and theta-frequency resonance patterns in cerebellar Golgi cells: simulations of their impact *in vivo*. *Front. Cell. Neurosci.* 1:4. doi: 10.3389/neuro.03.004.2007

Stratton, P., Cheung, A., Wiles, J., Kiyatkin, E., Sah, P., and Windels, F.. (2012). Action potential waveform variability limits multi-unit separation in freely behaving rats. *PLoS One* 7:e38482. doi: 10.1371/journal.pone.0038482

Sudhakar, S. K., Hong, S., Raikov, I., Publio, R., Lang, C., Close, T., et al. (2017). Spatiotemporal network coding of physiological mossy fiber inputs by the cerebellar granular layer. *PLoS Comput. Biol.* 13:e1005754. doi: 10.1371/journal.pcbi.1005754

Sugihara, I., Lang, E. J., and Llinás, R. (1995). Serotonin modulation of inferior olivary oscillations and synchronicity: a multiple-electrode study in the rat cerebellum. *Eur. J. Neurosci.* 7, 521–534. doi: 10.1111/j.1460-9568.1995.tb00657.x

Tadayonnejad, R., Anderson, D., Molineux, M. L., Mehaffey, W. H., Jayasuriya, K., and Turner, R. W.. (2010). Rebound discharge in deep cerebellar nuclear neurons *in vitro*. *Cerebellum* 9, 352–374. doi: 10.1007/s12311-010-0168-7

Thach, W. T., Goodkin, H. P., and Keating, J. G. (1992). The cerebellum and the adaptive coordination of movement. *Ann. Rev. Neurosci.* 13, 403–442. doi: 10.1146/annurev.ne.15.030192.002155

Van Dijck, G., Van Hulle, M. M., Heiney, S. A., Blazquez, P. M., Meng, H., Angelaki, D. E., et al. (2013). Probabilistic identification of cerebellar cortical neurones across species. *PLoS One* 8:e57669. doi: 10.1371/journal.pone.0057669

Vervaeke, K., Lorincz, A., Gleeson, P., Farinella, M., Nusser, Z., and Silver, R. A. (2010). Rapid desynchronization of an electrically coupled interneuron network with sparse excitatory synaptic input. *Neuron* 67, 435–451. doi: 10.1016/j.neuron.2010.06.028

Volny-Luraghi, A., Maex, R., Vos, B., and De Schutter, E. (2002). Peripheral stimuli excite coronal beams of Golgi cells in rat cerebellar cortex. *Neuroscience* 113, 363–373. doi: 10.1016/s0306-4522(02)00196-3

Voogd, J., and Glickstein, M. (1998). The anatomy of the cerebellum. *Trends Neurosci.* 21, 370–375. doi: 10.1016/s0166-2236(98)01318-6

Vos, B. P., Volny-Luraghi, A., and De Schutter, E. (1999). Cerebellar Golgi cells in the rat: receptive fields and timing of responses to facial stimulation. *Eur. J. Neurosci.* 11, 2621–2634. doi: 10.1046/j.1460-9568.1999.00678.x

Walter, J. T., Alviña, K., Womack, M. D., Chevez, C., and Khodakhah, K. (2006). Decreases in the precision of Purkinje cell pacemaking cause cerebellar dysfunction and ataxia. *Nat. Neurosci.* 9, 389–397. doi: 10.1038/nn1648

Welsh, J. P., Lang, E. J., Sugihara, I., and Llinás, R. (1995). Dynamic organization of motor control within the olivocerebellar system. *Nature* 374, 453–457. doi: 10.1038/374453a0

Welsh, J. P., Schwarz, C., and Nicolelis, M. A. L. (1999). "Multielectrode recording from the cerebellum," in *Methods for Neural Ensemble Recordings*, eds S. A. Simon and M. A. L. Nicolelis (Boca Raton, FL: CRC Press), 79–100.

Conflict of Interest: The authors declare that the research was conducted in the absence of any commercial or financial relationships that could be construed as a potential conflict of interest.

Advantages of publishing in Frontiers

OPEN ACCESS
Articles are free to read for greatest visibility and readership

FAST PUBLICATION
Around 90 days from submission to decision

HIGH QUALITY PEER-REVIEW
Rigorous, collaborative, and constructive peer-review

TRANSPARENT PEER-REVIEW
Editors and reviewers acknowledged by name on published articles

Frontiers
Avenue du Tribunal-Fédéral 34
1005 Lausanne | Switzerland

Visit us: www.frontiersin.org
Contact us: frontiersin.org/about/contact

REPRODUCIBILITY OF RESEARCH
Support open data and methods to enhance research reproducibility

DIGITAL PUBLISHING
Articles designed for optimal readership across devices

FOLLOW US
@frontiersin

IMPACT METRICS
Advanced article metrics track visibility across digital media

EXTENSIVE PROMOTION
Marketing and promotion of impactful research

LOOP RESEARCH NETWORK
Our network increases your article's readership